LOW-CYCLE FATIGUE PERFORMANCE OF STEEL H-PILES IN
INTEGRAL BRIDGES

A THESIS SUBMITTED TO
THE GRADUATE SCHOOL OF NATURAL AND APPLIED SCIENCES
OF
MIDDLE EAST TECHNICAL UNIVERSITY

BY

MEMDUH KARALAR

IN PARTIAL FULFILLMENT OF THE REQUIREMENTS
FOR
THE DEGREE OF DOCTOR OF PHILOSOPHY
IN
ENGINEERING SCIENCES

SEPTEMBER 2014

Approval of the thesis:

LOW-CYCLE FATIGUE PERFORMANCE OF STEEL H-PILES IN INTEGRAL BRIDGES

submitted by **MEMDUH KARALAR** in partial fulfillment of the requirements for the degree of **Doctor of Philosophy in Engineering Sciences Department, Middle East Technical University** by,

Prof. Dr. Canan Özgen   _____
Dean, Graduate School of **Natural and Applied Sciences**

Prof. Dr. Murat Dicleli   _____
Head of Department, **Engineering Sciences**

Prof. Dr. Murat Dicleli   _____
Supervisor, **Engineering Sciences Dept., METU**

Examining Committee Members:

Prof. Dr. Ahmet N. Eraslan   _____
Engineering Sciences Dept., METU

Prof. Dr. Murat Dicleli   _____
Engineering Sciences Dept., METU

Assoc. Prof. Dr.Alp Caner   _____
Civil Engineering Dept., METU

Assoc. Prof. Dr. Ferhat Akgül   _____
Engineering Sciences Dept., METU

Assist. Prof. Dr. Ö. Fatih Yalçın   _____
Civil Engineering Dept., İ.Ü

Date: .   .2014

I hereby declare that all information in this document has been obtained and presented in accordance with academic rules and ethical conduct. I also declare that, as required by these rules and conduct, I have fully cited and referenced all material and results that are not original to this work.

Name, Last name : Memduh Karalar

Signature :

ABSTRACT

LOW-CYCLE FATIGUE PERFORMANCE OF STEEL H-PILES IN
INTEGRAL BRIDGES

Karalar, Memduh

Ph.D., Department of Engineering Sciences

Supervisor: Prof. Dr. Murat Dicleli

September 2014, 323 pages

Integral bridges are jointless bridges where the superstructure is connected monolithically with the abutments. Due to seasonal temperature changes the abutments are pushed against the approach fill and then pulled away, causing lateral displacements at the top of the piles that support the abutments. This may result in the reduction of their service life due to low-cycle fatigue effects. In this research, both analytical and experimental studies are conducted to investigate the effect of thermal induced cyclic displacements/strains on the low cycle fatigue performance of steel H-piles at the abutments of integral bridges. First, a new cycle counting method is developed to determine the number and amplitude of large and small pile displacement/strain cycles due to seasonal and daily temperature fluctuations. Then, a new equation is developed to determine a displacement/strain cycle amplitude representative of a combination of a number of small and large amplitude cycles existing in a typical temperature induced

displacement/strain history in steel H-piles of integral bridges. Then, nonlinear finite element models (FEMs) of the steel H-pile specimens used in the experimental part of this research study are developed using the computer program ANSYS. Next, FEM of these test specimens are subjected to a loading similar to that is used in the experimental testing. The main purpose of conducting such nonlinear analyses is to identify potential problems that may be encountered during testing and to improve the test apparatus if necessary. Low cycle fatigue tests are then conducted to investigate the fatigue life of steel H-piles subjected to thermal induced cyclic strains/displacements. The tests are designed to study the effect of several parameters, namely; (i) pile size (ii) equivalent length of the pile, (iii) orientation of the pile (strong axis or weak axis bending), (iv) small amplitude cycles (displacement history with and without small amplitude cycles), iv) amplitude of the small displacement/strain cycles with respect to that of large displacement/strain cycles and (vi) the magnitude of the axial load applied on the pile. Furthermore, nonlinear FEMs of the steel H-pile specimens are developed using the program ANSYS to numerically predict their low cycle fatigue performance under cyclic thermal induced displacements/strains.

Keywords: Integral Bridge, Steel, Piles, low cycle Fatigue.

ÖZ

ENTEGRAL KÖPRÜLERDE ÇELİK H-KAZIKLARIN DÜŞÜK DEVİRDE YORULMA PERFORMANSI

Karalar, Memduh

Doktora, Mühendislik Bilimleri Bölümü

Tez Yöneticisi: Prof. Dr. Murat Dicleli

Eylül 2014, 323 sayfa

Integral köprüler geleneksel genleşme derzleri olmayan, üst yapı ile uç mesnetlerin monolitik olarak inşaa edildiği köprülerdir.Mevsimlik ısı değişimi nedeniyle monolitik uç mesnetleri, mesnet arkasında bulunan dolguyu yukarı doğru iterek kazık üst bölgesinde yanal değişimlere neden olabilirler. Bu periyodik değişimlerin büyüklüğü sıcaklık değişimlerinin, üst yapıda kullanılan malzeme tipinin ve köprünün uzunluğunun bir fonksiyonudur. İntegral köprü uzunluğu arttıkça, çelik H profilli kazıklarda meydana gelen kuvvet ve yerdeğiştirmelerde büyük olabilir. Bu durum, malzeme yorulmasından dolayı köprünün servis hayatının azalmasına neden olabilir. Bu çalışmada, çelik H profil kazıkların hem analitik hemde deneysel testler aracılığı ile sıcaklık değişimlerinin neden olduğu yerdeğiştirmelerin, çelik H profilli kazıklar üzerindeki etkileri incelenecektir. İlk olarak, mevsimlik ve günlük sıcaklık değişimlerinden dolayı, çelik H profil kazıkların küçük ve büyük periyotlu yer değiştirmelerinin büyüklüğünü ve sayısını elde etmek için yeni bir method geliştirilecektir. Daha sonra, integral köprülerdeki çelik kazıklarda sıcaklıktan dolayı yerdeğiştirmelerin neden olduğu küçük ve büyük ölçekli periyotların sayısının kombinasyonunu

sunan yeni bir denklem geliştirilecektir. Daha sonra, sonlu elemenlar yöntemi kullanılarak deneysel kısımda test edilecek olan çelik H profillerin ANSYS modeli geliştirilecektir. Bu modelin geliştirilmesindeki amaç, deneysel kısımda meydana gelebilecek olan problemleri öngörmek ve gerekli önlemleri almaktır. Bu çalışmanın deneysel kısmında ise sıcaklık değişimlerinden dolayı meydana gelen yerdeğiştirmelerin çelik H profilleri üzerindeki yorulma ömrünü incelemektir. Bu testler çeşitli parametlerin, kazık boyutu, kazık boyu, güçlü/zayıf eksen yönünde yerleştirilmesi, küçük periyotlu döngüler, büyük periyotlu döngülerin içinde yer alan küçük periyotlu döngüler, kazığın üzerine etki eden eksenel yükün büyüklüğü gibi parametrelerin etkisi incelenmiştir. Araştırmanın son kısmında ise, deneysel kısımdan elde edilen sonuçlar sonlu elemanlar yöntemi kullanılarak oluşturulan ANSYS modeli ile karşılaştırılıp, ilerki çalışmalarda çelik H profillerin malzeme yorulma performansı üzerinde çeşitli parametrelerin etkisini incelenmek için ANSYS modeli kullanılacaktır. Deneysel sonuçlara bakılarak, çelik H profillerin zayıf eksen yönünde, malzeme yorulması bakımından daha iyi sonuçlar verdiği görülmüştür. Ayrıca, eksenel yükün etkisi incelenerek, düşük strain degerlerinde eksenel yükün malzeme yorulmasını geciktirdiği, fakat yüksek strain değerlerinde (burkulmadan dolayı) ise eksenel yükün malzeme yorulmasını hızlandırdığı görülmüştür. Ayrıca, sonlu elemenlar yöntemi kullanılarak elde edilen sonuçlar, test sonuçları ile karşılaştırılmış ve yakın sonuçlar elde edilmiş olup, çelik HP profillerin yanal ve eksenel yükler altındaki davranışlarının, sonlu elemanlar yöntemi ile tahmin edilebileceği görülmüştür.

Anahtar Kelimeler: Entegral Köprü, Çelik, Kazıklar, Malzeme Yorulması.

To My Family,
For your endless support and love

ACKNOWLEDGEMENTS

I wish to offer my sincere thanks and appreciation to my supervisor Prof. Dr. Murat Dicleli for his precious help, invaluable suggestions, continuous support, guidance, criticisms, encouragements and patience throughout this study.

Secondly, I would like to thank Prof. Dr. M. Ruşen Geçit, and Prof. Dr. M. Polat Saka and for his helpful advices to me during my work life at Department of Engineering Sciences.

I wish especially thank Assoc. Prof. Dr. Gökhan Pekcan for his endless help, never-ending support and trust.

I should remark that without the sincere friendship of my roommate Fuat Korkut, this work would not have been realized. I strongly thank him for his amity. And many thanks to Serdar Çarbaş, Semih Erhan, Ferhat Erdal, Ferhat Celep, Hakan Bayrak, Alper Akın, and Refik Burak Taymuş for their excellent understanding and no end of aid at every stage of my thesis study.

I owe thanks to the most special person in my life Yasemin Kaya for her boundless moral support giving me joy of living. This life would have never been meaningful without her.

Last but not least, I can hardly find words to express my feelings about my parents Mahmut Karalar and Meryem Karalar, and my unique younger brother Selçuk Karalar for their lifetime support to compensate all the disadvantages in my life. I will always be indebted to their compassion and humanism no matter how hard I try to give back what they have given to me. They have priceless meaning for me. I feel very lucky to have them.

TABLE OF CONTENTS

xiv

LIST OF TABLES

TABLES

LIST OF FIGURES

FIGURES

xxvii

CHAPTER 1

INTRODUCTION

1.1. General Information

Integral bridges are jointless bridges where the superstructure is connected monolithically with the abutments supported on a single row of piles that provide the required flexibility to allow for longitudinal movement of the bridge under thermal effects. In these types of bridges, the road surfaces are continuous from one approach embankment to the other and the abutments are cast integral with the deck. The rigid connection between the superstructure and the abutments enables the bridge to act as a single structural unit and assures full moment transfer between them. The most common type of piles used at the abutments of integral bridges is steel H-piles. Cycle control joints are provided at the ends of the approach slabs to accommodate for the longitudinal movements of the bridge. A typical two-span, prestressed-concrete girder, integral bridge is shown in Figure1.1.

Integral bridges offer numerous advantages compared to traditional jointed bridges, especially from economical point of view. Integral bridges eliminate the problems associated with movement of joints and bearings. Furthermore, integral bridges have a smaller initial construction and maintenance cost than that of traditional jointed bridges due to the elimination of expansion joints and bearings.
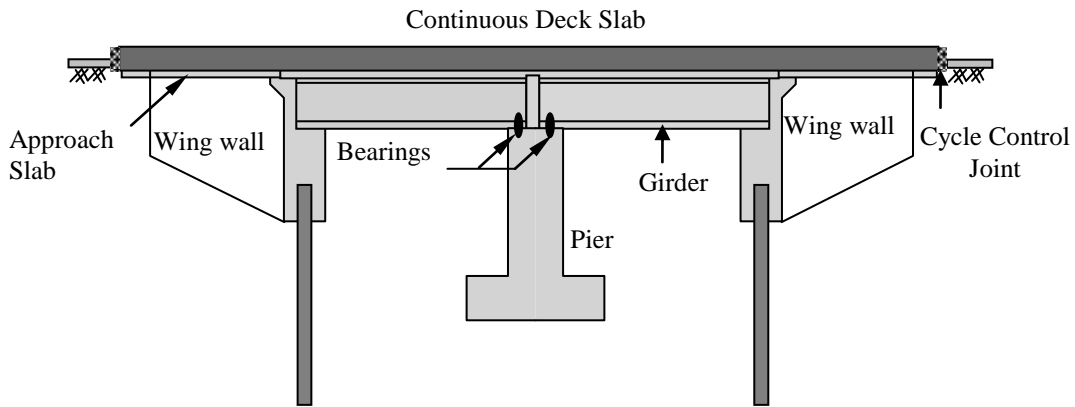
Figure 1.1. Typical two-span integral abutment bridge

The daily and seasonal temperature changes result in imposition of cyclic horizontal displacements on the continuous bridge deck of integral bridges and thus on the abutments, backfill soil, steel H-piles, and cycle control joints at the ends of the approach slabs. Due to these seasonal temperature changes the abutments are pushed against the approach fill and then pulled away, causing lateral deflections at the tops of the piles that support the bridge (Figure1.2).
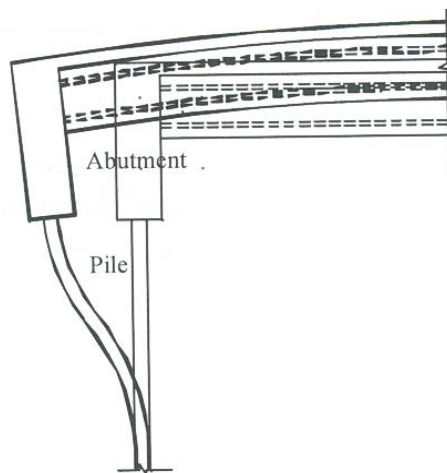
Figure 1.2. Pile displacement due to thermal changes.

The magnitude of these cyclic displacements is a function of the level of temperature variation, type of the superstructure material and the length of the bridge. As the length of the integral bridges gets longer, the temperature-induced cyclic displacements and forces in steel H-piles components may become larger as well. This may result in the reduction of their service life due to low-cycle fatigue effects. To minimize such detrimental effects, the length of integral bridges should be limited while the pile length must be kept above a certain length limit to accommodate thermal-induced longitudinal displacements of the bridge.

Recently numerous research studies have been conducted to estimate the length limits of integral bridges based on the performance of the abutments and piles under cyclic thermal loading (Dicleli and Albahisi, 2003; 2004a; 2004b; 2005). However, such research studies use low cycle fatigue models of structural members such as reinforcing steel (e.g. Shama et. al (2001)) to predict the low cycle fatigue performance of steel H piles. There is an urgent need of full scale experimental testing of steel H piles to determine their low cycle fatigue performance under thermal induced cyclic displacements/strains. Accordingly, in this research study, first full–scale experimental testing of various steel H piles used in integral bridge construction is conducted to estimate their low cycle fatigue life and behavior under thermal induced cyclic displacements/strains. The experimental study also included investigation of the effect of several parameters on the low cycle fatigue performance of steel H-piles. These parameters are; (i) pile size (ii) equivalent length of the pile, (iii) orientation of the pile (strong axis or weak axis bending), (iv) small amplitude cycles (displacement history with and without small amplitude cycles), iv) amplitude of the small displacement/strain cycles with respect to that of large displacement/strain cycles and (vi) the magnitude of the axial load applied on the pile. Additional tests are conducted on piles with improved structural details with and without the abutments to delay low cycle fatigue failure. Furthermore, nonlinear FEMs of the steel H-pile specimens are developed using the program ANSYS to numerically predict their low cycle fatigue performance under cyclic thermal induced displacements/strains. The numerical study includes sensitivity analyses to establish a FEM that best

3

represents the experimental low cycle fatigue behavior of the steel H-pile specimens. These FEMs could be used in further research studies to investigate the effect of various parameters on low cycle fatigue performance of steel H-piles.

1.2. Objective

The main objectives of this research study are;

- To develop a cycle counting technique to accurately predict the cyclic thermal effects on integral bridge piles.

- To investigate the low cycle fatigue behavior of steel H piles typically used in integral bridge construction via full–scale experimental testing.

- To experimentally investigate the effect of pile size and orientation, equivalent length of the pile, axial load level acting on the pile, the small amplitude cycles, the relative amplitude of small cycles with respect to that of large cycles as well as pile connection detail with the abutment on the low cycle fatigue performance of steel H piles .

- To compare results between FEMs and experimental tests in terms of fatigue life in the steel H-pile specimens for various lateral displacements and axial load values

1.3. Scope of Study

The research study is limited to steel H-piles typically used in integral bridge construction. The piles are assumed to have adequate ultimate shear capacity to allow for the formation plastic flexural hinges is normally the case in steel sections under thermal induced cyclic displacements (Dicleli and Bruneau, 1996). In the analytical parts of this research study, the pile is assumed to be an end-bearing pile.

1.4. Research Outline

1.4.1. Phase 1

As a first step, an extensive literature review is conducted on the historical background, design standards, design practice as well as attributes and limitations of integral bridges. Next, a literature review is conducted on the amplitude and the number of temperature induced cycles on integral bridge piles. Furthermore, a literature review is conducted on low-cycle fatigue performance of steel-H piles and similar steel sections.

1.4.3. Phase 2

In the second phase of the research, the field measurements obtained for integral bridges are used to determine the amplitude and the number of temperature induced cycles on steel H-piles in integral bridges. Using the obtained measurements, the number of large strain cycles per year due to seasonal temperature changes and the number and relative amplitude (relative to the amplitude of large displacement/strain cycles, i.e. β=small strain cycle amplitude / large strain cycles amplitude) of small strain cycles per year due to daily or weekly temperature changes are determined. Additionally, the number of small cycles between the maximum and minimum cycle above and/or under the large strain cycles is counted. Using the available data on the number and amplitude of temperature induced displacement-strain cycles, a new cycle counting method is developed to determine the number and amplitude of large and small displacement/strain cycles. Then, a new equation is obtained to determine a displacement/strain cycle amplitude representative of a number of small amplitude cycles existing in a typical temperature induced displacement/strain history in steel H-piles of integral bridges.

1.4.4. Phase 3

In the third phase of the research, nonlinear finite element models of the steel H-pile specimens that will be used in the experimental part of this research study is developed using the computer program ANSYS. Then, the numerical model of these test specimens are subjected to a lateral displacements similar to that is used in the experimental tests. The main purpose of conducting such nonlinear analyses is to identify potential problems that may be encountered during testing and to improve the test apparatus if necessary.

1.4.5. Phase 4

In this phase of the research study, experimental testis are conducted to investigate the effect of cyclic thermal induced displacements / strains on the low cycle fatigue behavior and performance of steel H-piles used in integral bridges. These tests include 35 steel H-piles of two different sizes, HP220x57 and HP260x75, oriented to bend about their strong and weak axes and subjected to various cyclic flexural strain amplitudes. The experimental tests are designed to investigate the effect of following parameters on the low cycle fatigue performance of steel H-piles; (i) pile size (ii) equivalent length of the pile, (iii) orientation of the pile (strong axis or weak axis bending), (iv) small amplitude cycles (displacement history with and without small amplitude cycles), iv) amplitude of the small displacement/strain cycles with respect to that of large displacement/strain cycles and (vi) the magnitude of the axial load applied on the pile.

1.4.6. Phase 5

In the last phase of the research, nonlinear FEMs of the steel H-pile specimens are developed using the program ANSYS to numerically predict their low cycle fatigue performance under cyclic thermal induced displacements/strains. The numerical study includes sensitivity analyses to establish a FEM that best represents the experimental low cycle fatigue behavior of the steel H-pile specimens. These FEMs could be used in further research studies to investigate the effect of various parameters on low cycle fatigue performance of steel H-piles.

1.4.7. Important Contributions of This Thesis

1. Development of a methodical approach in experimental testing by simulating the experimental set-up via complex finite element model and analyses to identify potential problems that may be encountered during testing and to improve the test apparatus if necessary.

2. Development of a new cycle counting method to estimate the low cycle fatigue life of steel H-piles.

3. First research study in the literature to determine low cycle fatigue performance of steel H-piles (or I sections) and tom study the effect of several parameters on the fatigue life of st6eel H-piles.

4. Development of a stiffener detail to enhance the low cycle fatigue life of steel H-piles.

1.5. Review of Previous Studies

1.5.1. Maximum Integral Bridge Length as Determined by Low Cycle Fatigue Performance of Steel H-Piles

Increasing the length of integral bridges results in larger cyclic lateral displacements of steel piles supporting the abutments. As a result, the piles may be subjected to cyclic plastic deformations. Consequently, the service life of integral bridges may decrease due to low-cycle fatigue effects in steel H piles. Thus, the lengths of integral bridges must be limited to avoid such potential problems. Because of the fact that deformations due to temperature variations are proportional to bridge lengths, cyclic lateral displacements capacities of piles are an important factor for the determination of maximum integral bridge length limits. In the literature only a few research study has been found on this particular topic.

Dicleli and Albahisi (2003; 2004a; 2004b; 2005) presented length limits of integral bridges as a function of the ability of steel H-piles supporting the abutments to sustain thermal induced cyclic lateral displacements and flexural capacity of the abutment. The research study of Dicleli and Albahisi (2003) was based on the cyclic temperature induced pile strain data from the field measurements of two different integral bridges in Iowa, USA. Additionally, the length limits were determined based on a fatigue damage model which was not particularly obtained for steel H piles. Dicleli and Albahisi (2003) suggested that the maximum length limit for steel integral bridges should range between 80 m and 145 m in cold climates and 125 m and 220 m in moderate climates, whereas, the maximum length limit for concrete integral bridges should range between 150 m and 265 m in cold climates and 180 m and 320 m in moderate climates for various pile sizes.

1.5.2. The Number of Small Amplitude Cycles and Their Relative Amplitude With Respect to the Large Cycles

Field studies have been conducted by numerous researches to investigate the cyclic thermal induced displacement/strain history in steel H piles of integral bridges. One of these field studies was performed by Girton et al. (1991) in Iowa, USA. Girton et al. instrumented two integral bridges, the Boone Bridge and the Maple Bridge, from January 1987 to February 1989. This study showed that both bridges exhibited one large strain cycle per year due to seasonal temperature changes and about 52 small strain cycles per year due to weekly temperature fluctuations. The amplitude of the small strain cycles ranged between 17% (i.e. the ratio of the small to large strain amplitudes, $\beta=0.17$) and 34% (i.e. $\beta=0.34$) of the large amplitude cycle.

Another field test was performed by French et al. (2004). French et al. used the data obtained from a reinforced-concrete integral bridge in Minnesota, USA to investigate the behavior of integral bridges due to temperature variations. This bridge demonstrated one large strain cycle per year due to seasonal temperature changes and about 120 small strain cycles per year due to more frequent (daily and/or weekly) temperature fluctuations. The amplitude of the small strain cycles ranged between 19% and 42% of the large amplitude cycle.

Examination of the strain versus time records of instrumented steel H piles of two integral bridges in the state of Iowa (Abendroth et al., 2005) revealed that both bridges exhibited one large strain cycle per year due to seasonal temperature changes and about 49 small strain cycles per year due to weekly temperature fluctuations. The amplitude of the small strain cycles ranged between 20% and 45% of the large amplitude cycle.

According to another research performed by Abendroth et al. (2007), the steel H-piles of Tama county bridge in Iowa, USA, exhibited one large strain cycle per year due to seasonal temperature changes and about 81 small strain cycles per

year due to more frequent temperature fluctuations. The amplitude of the small strain cycles ranged between 17% and 34% of the large amplitude cycle.

Breña et al. (2007) reported the results from the field measurement of an integral bridge (Orange-Wendell bridge, in Massachusetts, USA) where the bridge was monitored for a period of three years from January 2002 through December 2004. In the first phase of the field measurement of Breña et al.(2007), in 2002, Orange-Wendell bridge exhibited one large strain cycle due to seasonal temperature changes and about 233 small strain cycles per year due to more frequent temperature fluctuations. In 2003, the bridge demonstrated one large strain cycle due to seasonal temperature changes and about 205 small strain cycles per year due to more frequent temperature fluctuations. In the last measurement of the same bridge by Breña et al. (2007), in 2004, the same bridge exhibited one large strain cycle due to seasonal temperature changes and about 256 small strain cycles per year due to more frequent temperature fluctuations. The amplitude of the small strain cycles ranged between 12% and 25% of the large amplitude cycle.

1.5.3. Low-Cycle Fatigue Effects

Low-cycle fatigue may occur in piles due to lateral cyclic displacements induced by temperature variations. Although bridge engineers (Dicleli 2000) have already predicted that low cycle fatigue may occur in the steel H piles of integral bridges due to thermal effects, only a few research studies have been found on this topic in the literature.

Shama et al. (2001) has extrapolated the low-cycle fatigue behavior of reinforcing bars to predict the low-cycle fatigue behavior of steel H-Piles under cyclic lateral seismic loading. The analytical predictions were compared to experimental results and a reasonably good agreement was found. Then, Dicleli and Albahisi (2004b) have formulated the low-cycle fatigue behavior of steel H piles based on the fatigue damage model of Shama et al. (2001) and the strain measurements performed for the piles of two integral bridges located in Iowa, USA. The

equation developed by Dicleli and Albahisi (2004b) is a function of the number of large and small strain amplitudes in steel H piles induced by cyclic thermal variations, the ratio, β, of the small to large strain amplitudes and the parameters used in the low cycle fatigue damage equation of Shama et al. (2001). Using the developed equation, Dicleli and Albahisi (2004) recommended a simple equation which is a function of the pile width in the direction of the cyclic displacement, to determine pile curvature limits under cyclic thermal displacements.

Arsoy et al. (2004) experimentally investigated the low-cycle fatigue behavior of three pile types (steel H, steel pipe and reinforced concrete) subjected to cyclic thermal induced displacement reversals. Arsoy et al suggested that steel H-piles oriented in weak axis bending exhibit the best performance against low cycle fatigue.

French et al. (2004) used three different methods namely, General Strain Life Equations, Manson's Universal Slope Equation and Extrapolated S-N Curves, to calculate the fatigue resistance of various steel H-piles used in integral bridges and compared the results obtained from these three methods. At the end of these comparisons, French et al. (2004) suggested that low-cycle fatigue failure of steel H- piles may not be considered for the design of most integral bridges shorter than 100 m. However, French et al. suggested that if the integral bridge length is very long, low-cycle fatigue failure should be considered.

Hällmark (2006) investigated if, how and when low-cycle fatigue failure is a possible failure mode in piles supporting integral bridges. The varying pile strains, as a result of thermal-induced moments, traffic loads, etc, are simulated to achieve a strain-time sequence during the bridge service lifetime. Hällmark (2006) discussed the effect of varying bridge temperatures in integral bridges and described factors influencing bridge temperatures. Low-cycle fatigue was described and some methods of predicting the fatigue life were briefly mentioned. Hällmark (2006) suggested that low-cycle fatigue does not seem to be a problem, at least, as long as the length of the bridge does not exceed 100m.

11

CHAPTER 2

THERMAL EFFECTS ON INTEGRAL BRIDGE PILES

A change in temperature causes a material to change its length. This property of materials is accountable for expansion and contraction of the integral bridge superstructures. Each daily variation in temperature completes a cycle of expansion and contraction and the cycles repeat over time. The maximum expansion occurs during summer days while the maximum contraction forms during winter nights. The extreme lateral displacements of integral bridges are controlled by these extreme temperature changes. To better understand the effect of thermal fluctuations on integral bridges, field test results of several integral bridges in the US are studied. The details of these bridges are given in the following subsection.

2.1. Bridges with Available Field Test Results Considered in This Study

The effects of primary and secondary small cycles are investigated for different integral bridges. Details of these integral bridges are given as fallows;

The Guthrie County Bridge is a three-span-continuous, 318-ft long, PC girder bridge with a right-side-ahead, 30-deg., skew angle as shown in Figure 2.1. This bridge has a U-shaped abutment with a single row of ten, HP 10 x 42, steel piles under the reinforced-concrete (RC) backwall, and an HP10x42 pile under each wingwall. The piles under the RC backwall are oriented with their webs parallel to the abutment face. The wingwall piles are oriented with the webs perpendicular to the longitudinal axis of the bridge. The piles were driven to a depth of at least 45 ft into shale bedrock at the south abutment and to a depth of at least 40 ft into

shale bedrock at the north abutment. Pre-bored holes that were filled with bentonite slurry were specified for the piles at this bridge.

The Story County Bridge is a three-span-continuous, 201 ft - 4 in. long, PC girder bridge with a right-side-ahead, 15-deg. skew angle as shown in Figure 2.2. Each RC abutment is supported on a single row of seven, HP10 x 42, steel piles that are oriented with their webs parallel to the abutment face. The wingwalls are cantilevered from the abutment backwall. The abutment piles are driven to bedrock or to a minimum bearing strength of 34 tons. The specified length of the abutment piles was 40 ft. An 8-ft deep, pre-bored hole that was filled with sand was provided for each abutment pile. The two, pedestal-type piers have a single line of twelve, HP10 x 42, steel piles that are encased by concrete. The bridge superstructure is supported at the piers, which are fixed piers, by 1-in. thick, neoprene pads.
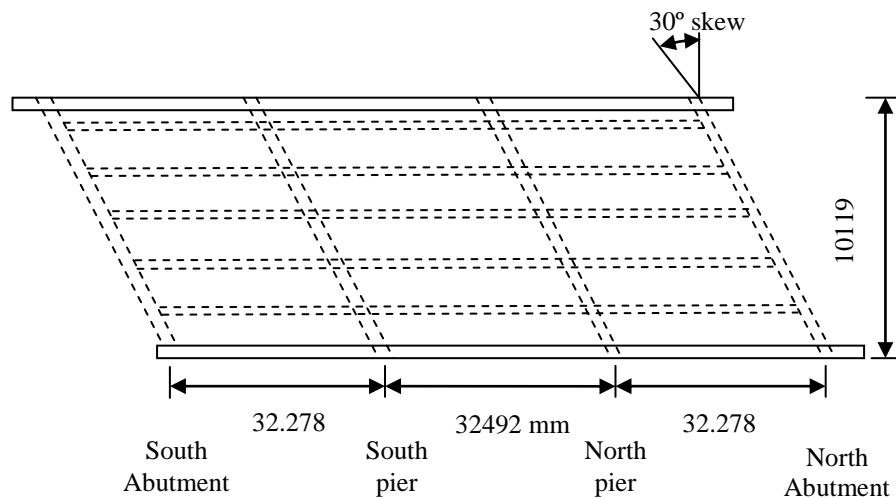
(a)

Figure 2.1. (a) Guthrie County Bridge, (b) Plan view of the south abutment for the
Guthrie County Bridge

14

4712
2133
2578
212
914
405
9 spaced at
914
All dimensions in
millimeter
1010
914
509
457
481
159
30º skew
213
205
418

(b)

Figure 2.2. (Continued)

15

10058 mm

19507 mm
22250 mm
19507 mm

East
Abutment
East
pier
West
pier
North
Abutment
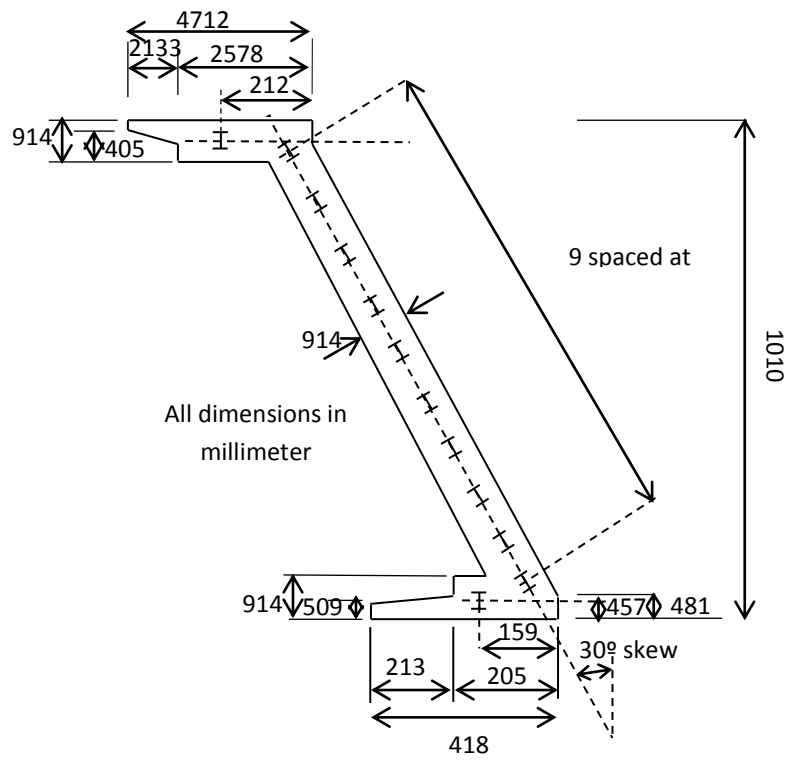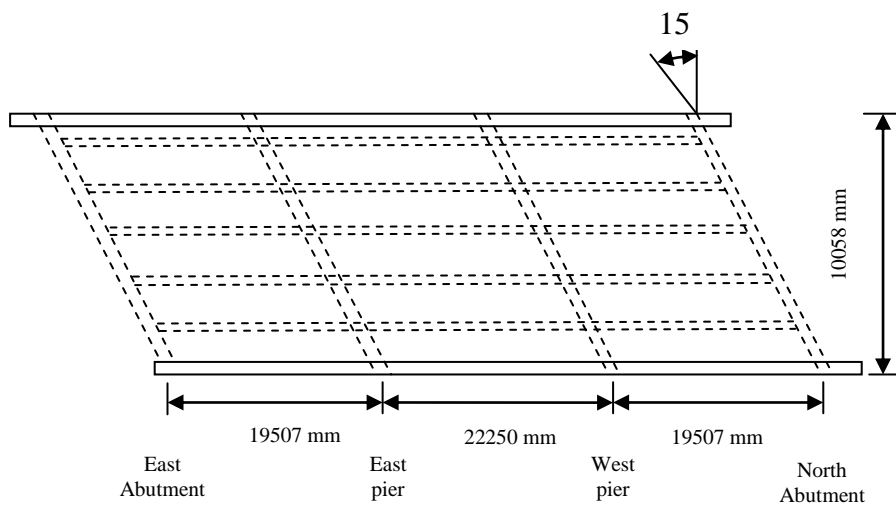
Figure 2.3. Story County Bridge

15

Minnesota Department of Transportation (Mn/DOT) Bridge #55555, in Olmsted County was constructed on CR 104, 1.5 miles south of CSAH 25, to span the south fork of the Zumbro River. The bridge elevation and cross section are shown in Figure 2.3 and 2.4. The bridge was a three-span prestressed concrete bridge with a total length of 216.6 ft. Each span consisted of four 72 ft. long Type 45M prestressed girders with a center-to-center spacing of 11 ft. The length of single span between the centerlines of bearings was 70.75 ft. The total bridge width was 39.33 ft, including two Jersey barriers and one lane of shoulder in each direction. At the piers, the girders were supported by a curved plate-bearing assembly to achieve a simple support. A 2-inch gap was set between the adjacent girders. The continuity of the superstructure over the piers was provided by a 9- in. thick reinforced concrete deck.

Figure 2.4. Bridge #55555 in Olmsted County, Minnesota over the Zumbro River
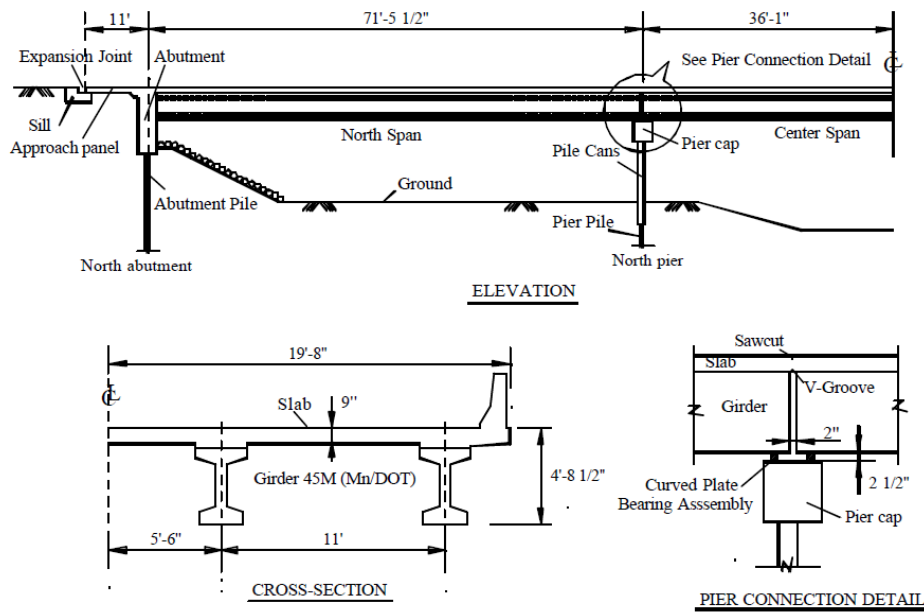
Figure 2.5. Bridge elevation and cross section

The Boone River Bridge, located in central Iowa, is a concrete-deck, prestressed-girder bridge, 40 ft. wide, that spans 324.5 ft. The bridge is a continuous four-span bridge. Two of the piers are located approximately 80 ft. from each abutment, and the third pier is located in the center of the bridge. The prestressed girders are not integral with the piers but sit on neoprene pads approximately 1 in. thick. The rest of the structure is monolithically constructed. The skew angle of the bridge is 45°. The 7.5-in. deck is of reinforced concrete with a compressive strength of 3,000 psi.

The Maple River Bridge, located in northwest Iowa, is a composite concrete-deck, steel-girder bridge, 320 ft. long by 32 ft. wide. The bridge is a continuous three-span bridge with two piers located proximately 98 ft. from each abutment. The Maple River Bridge has a skew angle of 30°. The abutments and girders were integrally cast with the deck to form a monolithic structure. The 8.5-in. deck is of reinforced concrete with a concrete compressive strength of 3,500 psi. The steel girders are welded plate girders approximately 49 in. deep and placed on bearing

17

pads over the piers. The piles were driven in a predrilled hole approximately 12 ft. deep with the strong axis parallel to the longitudinal direction of the bridge.

The Orange–Wendell Bridge is located over Millers River on Wendell Depot road in Orange, MA. The bridge has a total length of 270 ft. and a 32 ft. width as shown in Figure 2.5. Exterior spans are 80 ft. long and the interior span is 110 ft. long. The span is perpendicular to the abutments. The north end is exposed to direct sunlight, while the south span is predominantly shaded. The superstructure consists of an 8 in. concrete deck supported on four 48 in. deep steel plate girders. The girders are evenly spaced every 8.67 ft. across the bridge starting at 3.00 ft. from the deck edge on each side. Concrete guardrails are provided along both sides of the bridge deck. A 5.33 ft. sidewalk is provided along the east side of the bridge deck. The steel girders are embedded into the abutment walls at both ends of the bridge, and supported on elastomeric bearing pads on the two interior concrete bents. Each abutment wall is supported on 8 HP 10x57 steel piles equally spaced every 4.1 ft. The pile tops are embedded approximately 2 ft. into the bottom of the abutment and driven approximately 60 ft. into the ground.
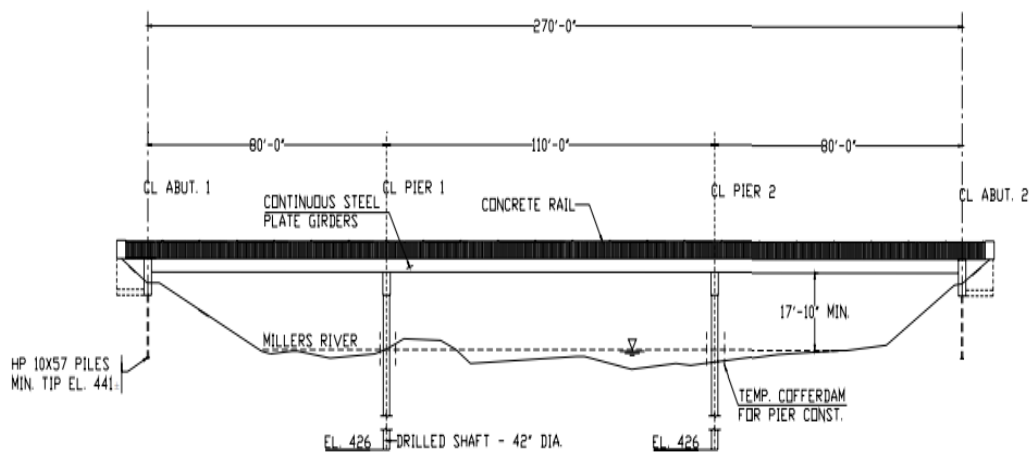
Figure 2.6. Orange–Wendell Bridge

18

2.2. Thermal Displacements/strains versus Time Pattern in Integral Bridges

The measured displacements at the pile of the Maple river bridge in Iowa, USA due to temperature variations are shown in Figure 2.6. It is clearly observed from Figure 2.6 that the bridge displacements are composed of more frequent minor amplitude cycles and seasonal large amplitude cycles.
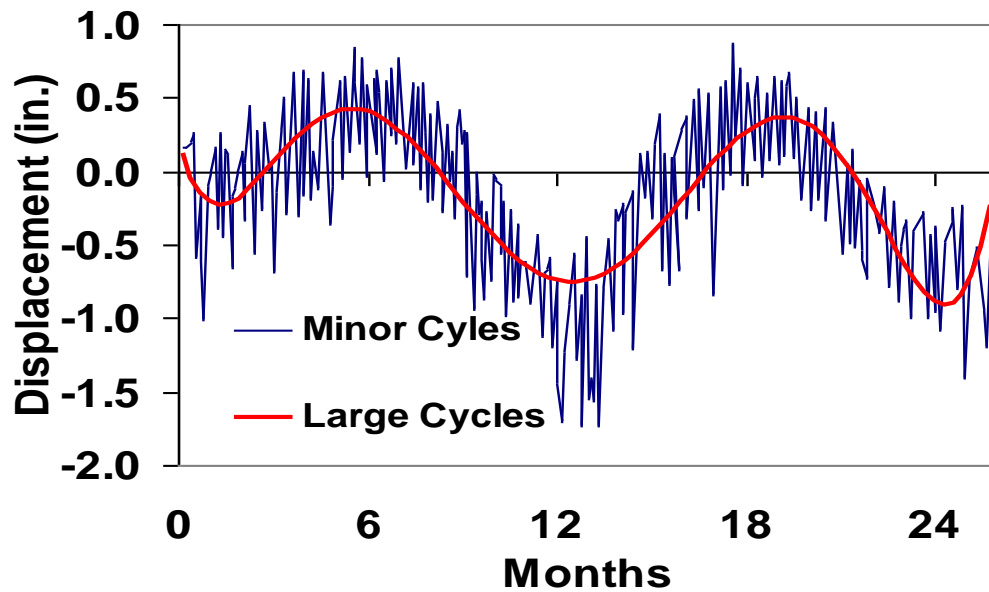
Figure 2.7. Measured pile displacements Girton et al. (1991).

The field test records demonstrate that the strain amplitude of the small cycles in the piles supporting the abutments fall within 20% to 40% range of the strain amplitude from the large cycles. Similar findings were reported by Lawyer et al. (2000) and Dicleli et al. (2003). The net difference between the seasonal and construction temperatures may be disparate in the summer and winter times based on the climatic conditions of the area where the bridge is located. Therefore, the amplitudes of the positive (ε_{ap}) and negative (ε_{an}) strain cycles corresponding to the summer and winter time may not be equal as observed from Figure 2.7. However, as the range of strain amplitudes rather than the strain amplitude itself

19

defines the extent of fatigue damage in steel H-piles, the positive and negative strain amplitudes are assumed to be equal (Dicleli et al. 2003).

In this research study, it is observed that the small cycles can be divided into two types as primary and secondary. The primary cycle is defined as a cycle that crosses the backbone of the large amplitude cycle and the secondary cycle is a smaller amplitude cycle that does not cross the backbone of the large amplitude cycle as observed from Figure 2.8.
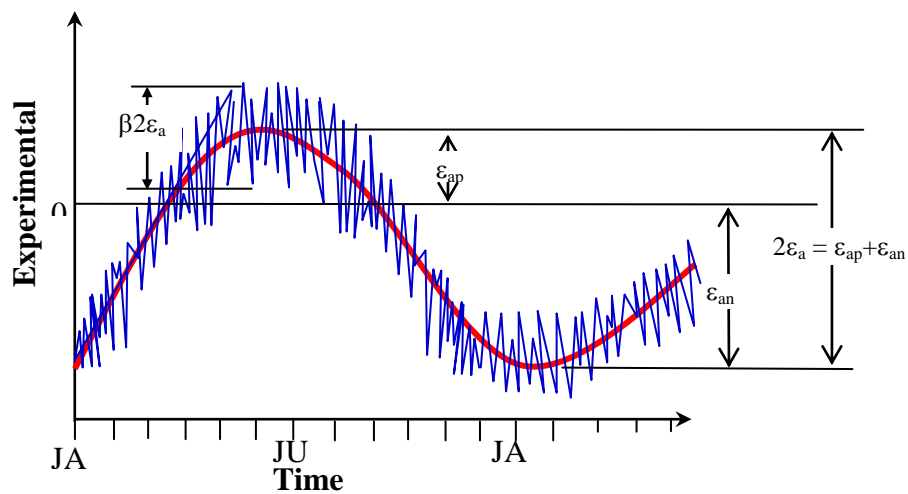
Figure 2.8. General experimental versus time for bridges (Dicleli and Albhaisi (2004)).
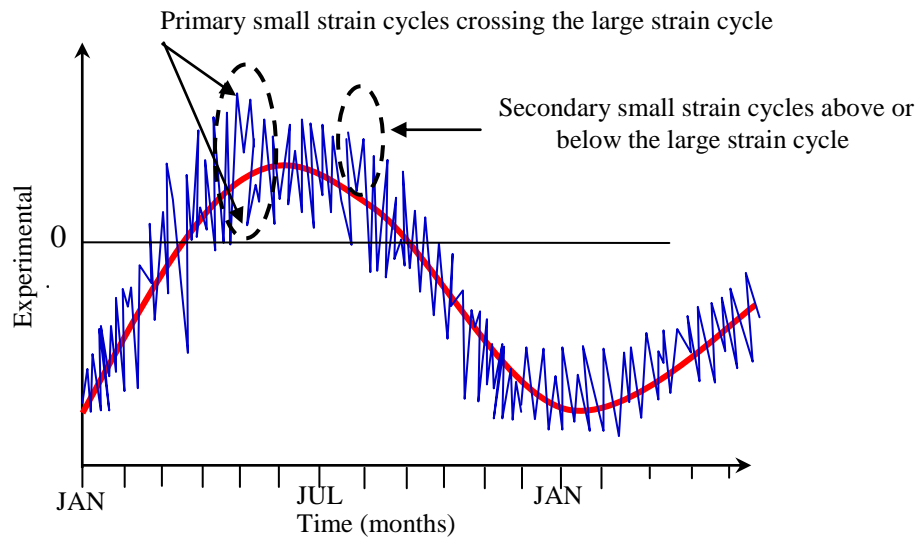
Figure 2.9. General experimental strain versus time for bridges (2004).

In the earlier research studies conducted by Dicleli and Albahisi (2003-2004) and French et al. (2004) to study the low cycle fatigue effects on steel H piles due to temperature induced strain cycles, the numbers of primary small and large amplitude strain cycles throughout the service life of the bridge were taken into account. However, the secondary small strain cycles above and/or under the backbone of the large amplitude cycle were not considered in these earlier research studies. From Figures 2.9 and 2.10, it can be noticed that the secondary small strain cycles cause the steel H-pile to behave in a mixture of plastic and elastic cyclic behavior. For this reason, the secondary small amplitude strain cycles are conservatively assumed to result in low cycle fatigue.
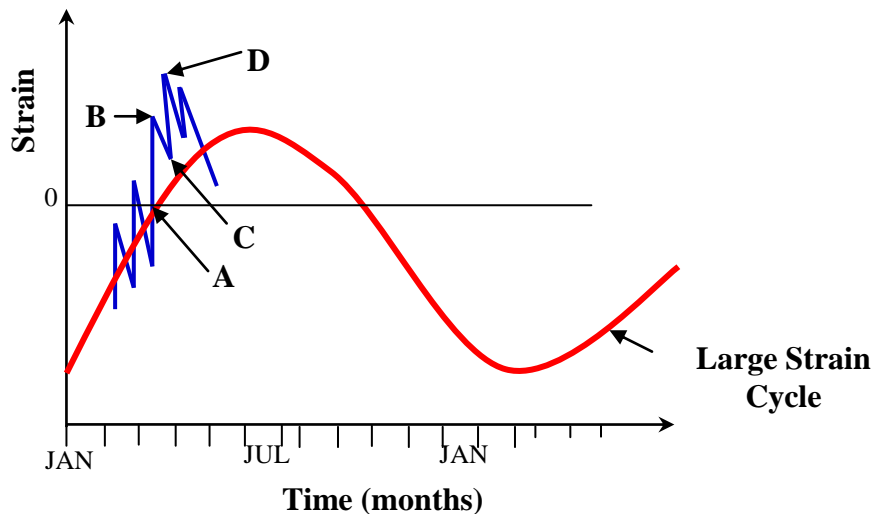
Figure 2.10. Loading and unloading due to secondary small cyclic strain versus time.
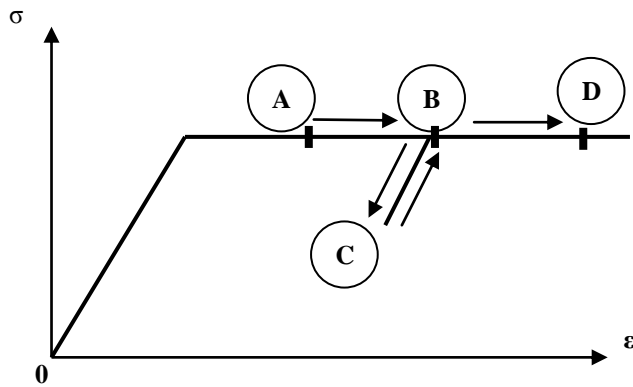
Figure 2.11. Stress and strain relationship corresponding to the same loading versus time points.

Consequently, the secondary small amplitude cycles should also be considered in studying the low cycle fatigue effects in steel H-piles. Because of the fact that secondary small strain cycles are part of low-cycle fatigue and the fact that their effect was not considered in earlier research studies, a new cycle counting method is developed to take into consideration the effect of secondary small amplitude cycles.

2.1. Development of Cycle Counting Method for Thermal Induced Strains in Integral Bridge Piles

Cycle counting methods have been developed for the study of fatigue damage generated in structures. Level Crossing counting (ASTM, 2005), Peak counting (ASTM, 2005), Simple range counting (ASTM, 2005) and Rainflow counting (ASTM, 2005) methods are those using the stress and deformation range to count the number of cycles. Although various methods may still be in use, Rainflow counting is the most favorable one among all. However, the primary and secondary small strain cycles mentioned earlier are not counted in these methods. Because of the fact that these small strain cycles are part of the low-cycle fatigue effects on steel H piles and these methods are not considering the effect of these small strain cycles, a new cycle counting method is developed. The procedure of the new cycle counting method is explained as follows;

- First, the cyclic displacements/strain data obtained from field measurements are used in a nonlinear minimum least square curve fitting technique to formulate a sixth degree polynomial curve representing the large amplitude cycles, due to seasonal temperature variations. The main reason for using a sixth degree polynomial function is to simulate the shape of the large amplitude cycle as accurately as possible. The solid line plotted in Figure 2.11 shows the large amplitude cycle obtained through such a process. The amplitude of the large displacement/strain cycle is determined as the average of the absolute maximum

and minimum amplitudes obtained from the sixth degree polynomial function. The number of large amplitude cycles per year is equal to one.

- To determine the amplitude and the number of primary small amplitude cycles, first, the corresponding amplitude of the large cycle (polynomial curve) is subtracted from each recorded data point to obtain the relative amplitude of the small amplitude cycles with respect to the large amplitude cycle. The maximum positive and absolute negative relative amplitudes before the relative amplitude changes sign, determines the positive and negative amplitudes of a specific primary small cycle as observed from Figure 2.12 and Table 2.1. In the figure the points designated by '*' indicates the amplitudes of the primary cycles. The rest of the points (other than those indicated by'*') are taken as the secondary small amplitude cycles. The average of the absolute values of the positive and negative relative amplitudes obtained through the process described above determines the amplitude of a constant amplitude primary small cycle that can be used for studying the performance of steel H piles under cyclic thermal effects. The number (n_{s1}) of these primary small cycles is calculated as the number of positive and negative amplitudes determined through the process described above divided by two. The amplitude of these primary small amplitude cycles relative to that of the large amplitude cycles (β_1) is defined as;

$$\beta_1 = \frac{\text{Amplitude of the primary small amplitude cycles}}{\text{Amplitude of the large amplitude cycle}} \qquad (1)$$
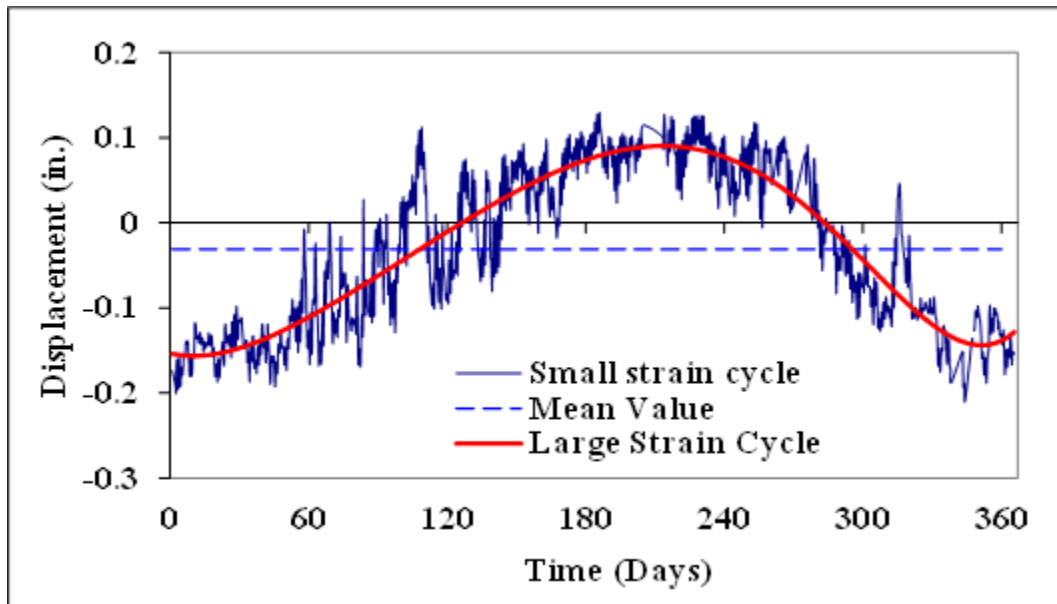
Figure 2.12. Experimental Bridge Displacement versus Time for Orange–
Wendell Bridge
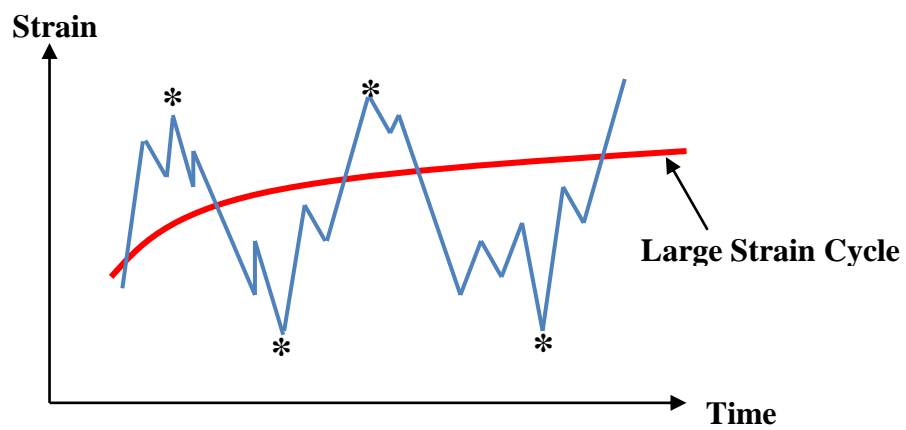
Figure 2.13. The maximum positive and negative amplitudes of primary small
cycles.

Table 2.1. Determination of the maximum positive and negative amplitudes of primary small cycles from Tama County Bridge.

Time (month)	Displacement (inc.)	Six Degree Polynomial	Difference	Absolute Value
2.1180	0.1955	0.2185	-0.0230 [x]	0.023
2.0928	0.3070	0.2151	0.9190 [x]	0.919
2.1423	0.5048	0.2219	0.2829	0.2829
2.3728	0.4037	0.2569	0.1467	0.1467
2.5011	0.5869	0.2787	0.3082	0.3082
2.6835	0.6181	0.2087	0.4094	0.4094
2.8478	0.3057	0.3438	-0.0381	0.0381
3.0926	-0.1084	0.3941	-0.5020 [x]	0.5025
3.57	0.2828	0.4983	-0.2156	0.2156
3.4602	0.8513	0.4739	0.3774	0.3774
3.5836	0.6389	0.5014	0.1375	0.1375
3.5816	0.8979	0.5009	0.3970 [x]	0.3970
4.0274	0.5122	0.6006	-0.0884	0.0884
4.3268	0.4397	0.6662	-0.2260 [x]	0.2265
4.0566	0.7172	0.6071	0.1101	0.1101

- To determine the amplitude and the number of secondary small amplitude cycles, first, the set of data points above or below the polynomial curve are used in a linear minimum least square curve fitting technique to formulate a linear function representing the mean of the secondary small amplitude cycles as shown in Figure 2.13. Next, the linear function obtained in the previous step is subtracted

26

from each recorded data point to obtain the relative amplitude of the secondary small amplitude cycles with respect to the linear function representing the mean values. The maximum positive and absolute negative relative amplitudes before the relative amplitude changes sign with respect to the linear mean function, determines the positive and negative amplitudes of a specific secondary small cycle as observed from Figure 2.14 and Table 2.2. In the figure the points designated by '+' indicate the amplitudes of the secondary small cycles. The average of the absolute values of the positive and negative relative amplitudes obtained through the process described above determines the amplitude of a constant amplitude secondary small cycle that can be used for studying the performance of steel H piles under cyclic thermal effects. The number (n_{s2}) of these secondary small cycles is calculated as the number of positive and negative amplitudes determined through the process described above divided by two. The amplitude of these secondary small amplitude cycles relative to that of the large amplitude cycles (β_2) is defined as;

$$\beta_2 = \frac{\text{Amplitude of the secondary small amplitude cycles}}{\text{Amplitude of the large amplitude cycle}}$$

(2)

The measured displacements at the pile of the integral bridge, namely Orange–Wendell Bridge, Guthrie County Bridge, Story County Bridge, Bridge #55555, Maple River Bridge, and Tama County Bridge, in USA due to temperature variations are shown in through Figure 2.15-2.19 (a). The amplitude of these primary small amplitude cycles relative to that of the large amplitude cycles (β_1) is also obtained from these measured displacement by using above procedure as shown in through Figure 2.15-2.19 (b).
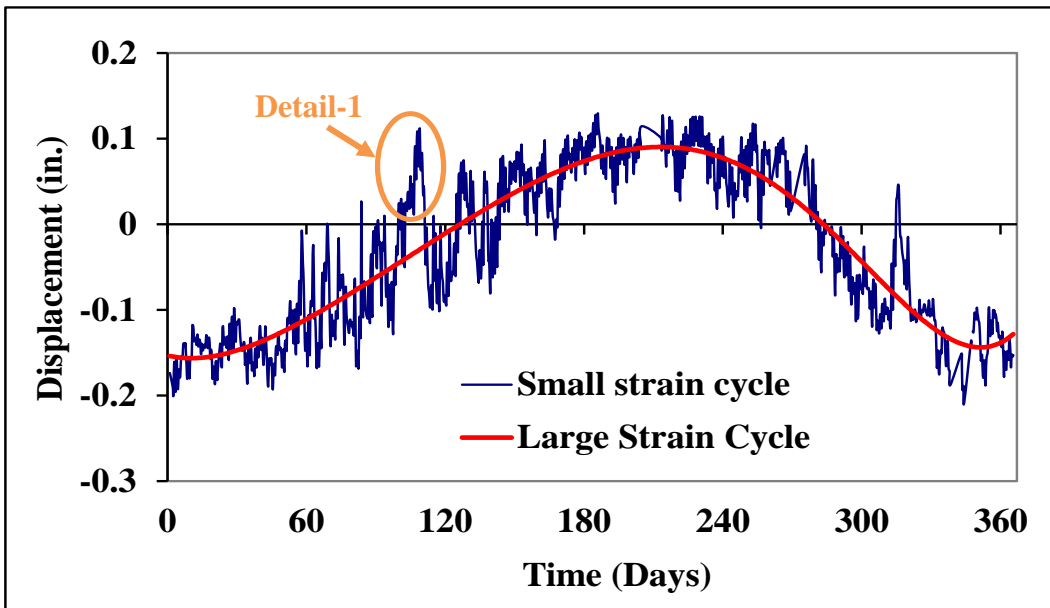
(a)
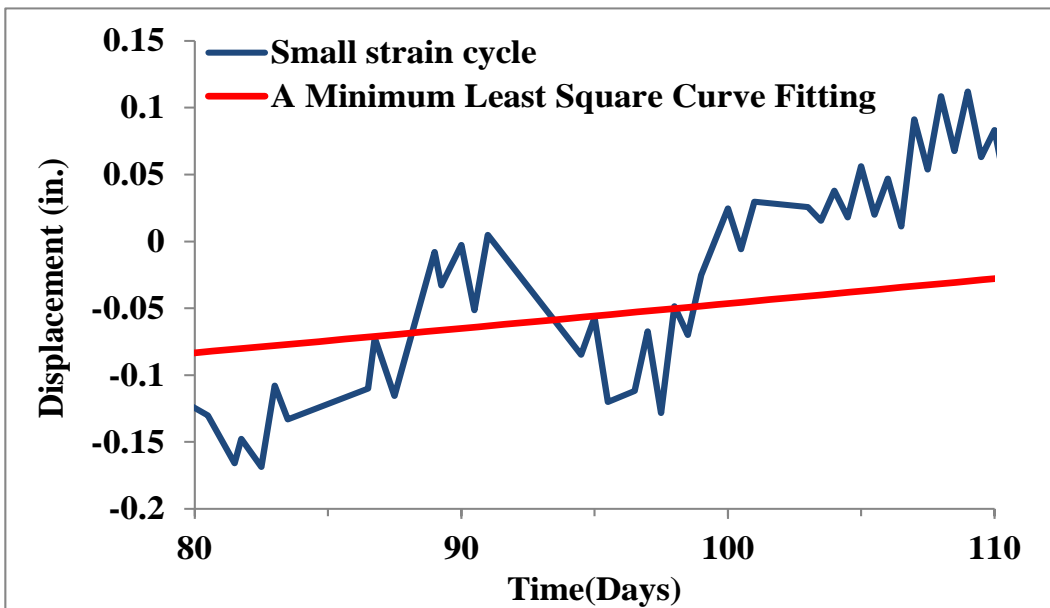
(b)

Figure 2.14. (a) Experimental Bridge Displacement versus Time for Orange–
Wendell Bridge, (b) Detail-1

28

Strain

A minimum least square curve fitting

Large Strain Cycle

Time

Strain

(+)

(+)

(+)

(+)

(+)

(+)

A Minimum Least Square Curve Fitting
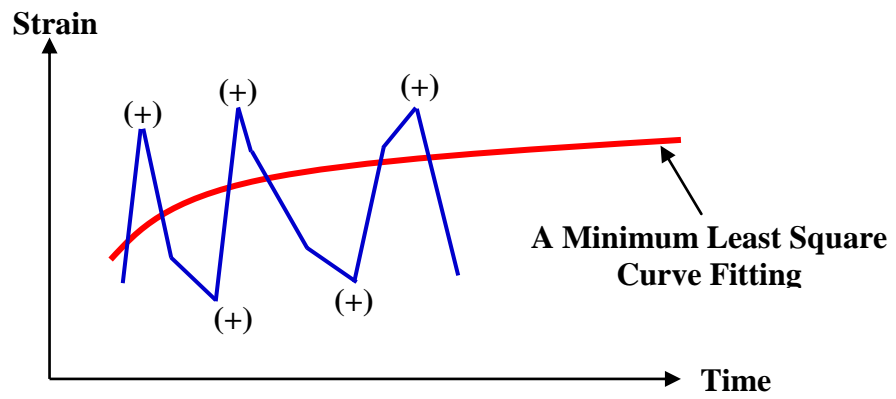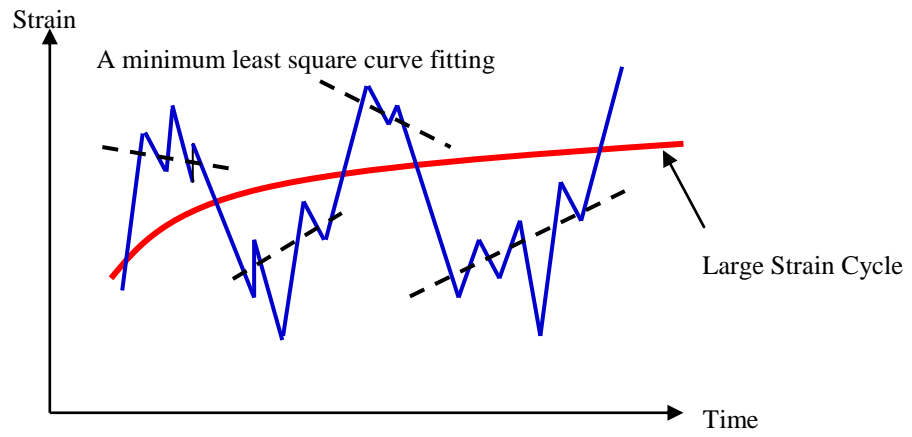
Time

Figure 2.15. The positive and negative small strain amplitudes obtained from least square curve fitting.

Table 2.2. Determination of positive and negative amplitudes.

Time (month)	Displacement (inc.)	Six Degree Polynomial	Difference
0.1176	112.23	100.19	12.04 (+)
0.1554	70.059	98.41	-28.350
0.1696	66.00	97.98	-31.98 (+)
0.5392	89.09	88.31	0.775 (+)
0.5523	95.178	88.018	7.159
0.6359	85.54	86.20	-0.656
0.6367	78.188	86.18	-7.996 (+)
0.9254	83.27	80.65	2.620
0.9886	83.99	79.91	4.080 (+)
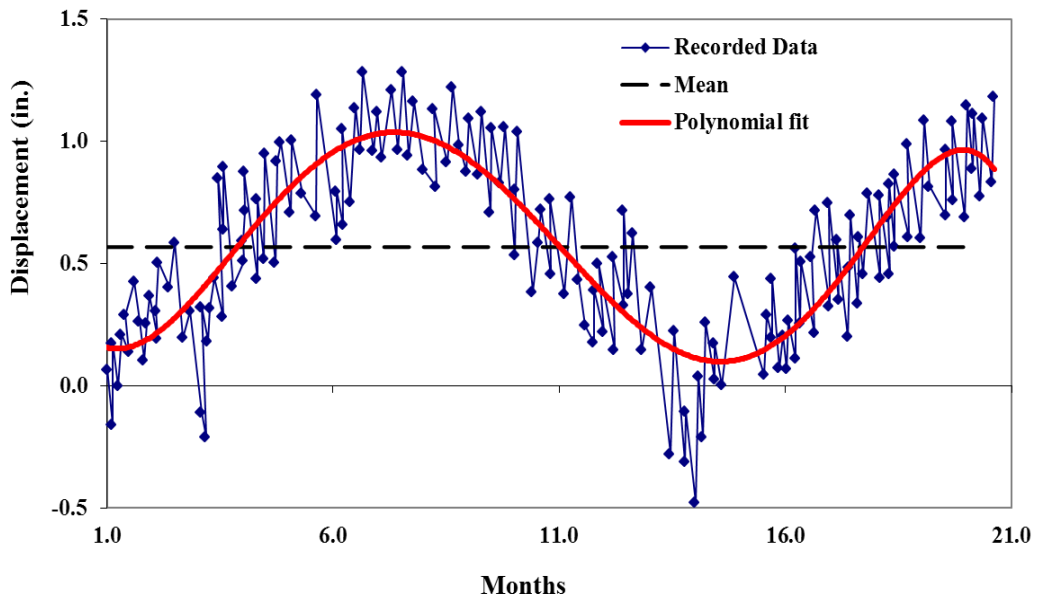
(a)
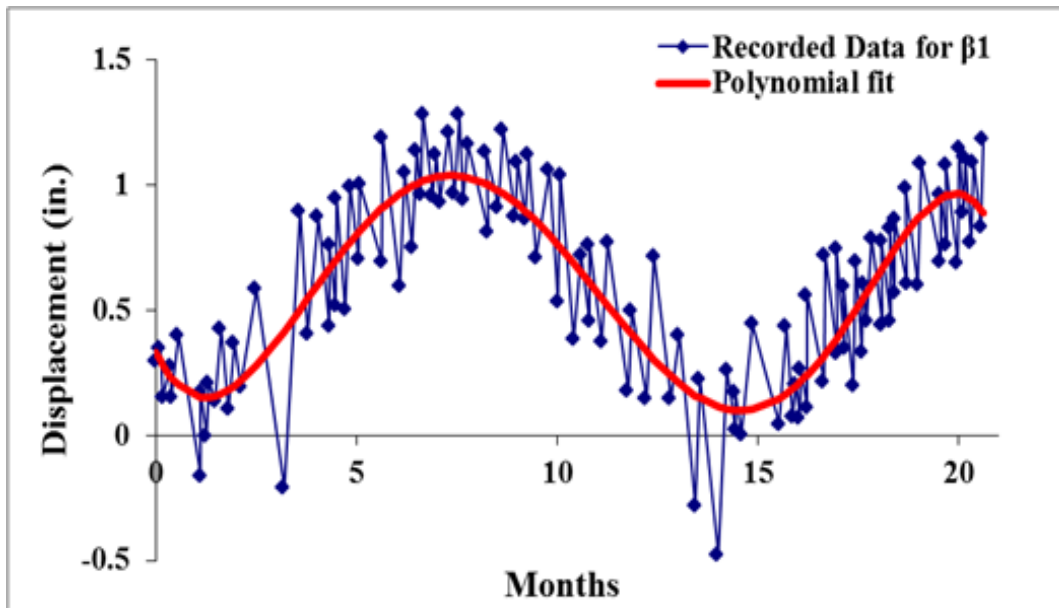
(b)

Figure 2.16. (a) Experimental Bridge Displacement versus Time for Guthrie County Bridge from December 1998 to April 1999, (b) The amplitude of these primary small amplitude cycles

31
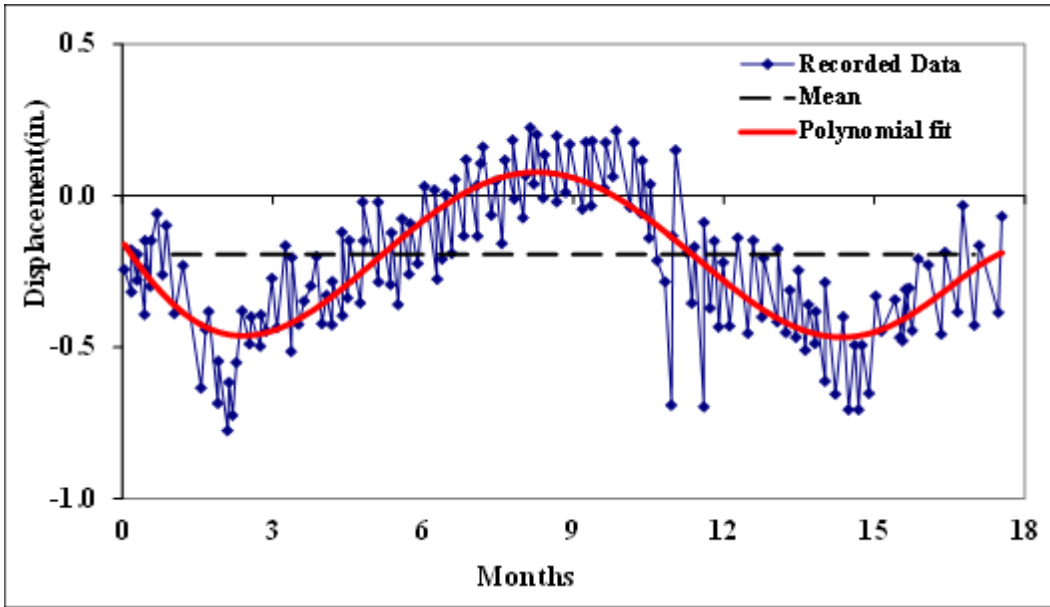
(a)
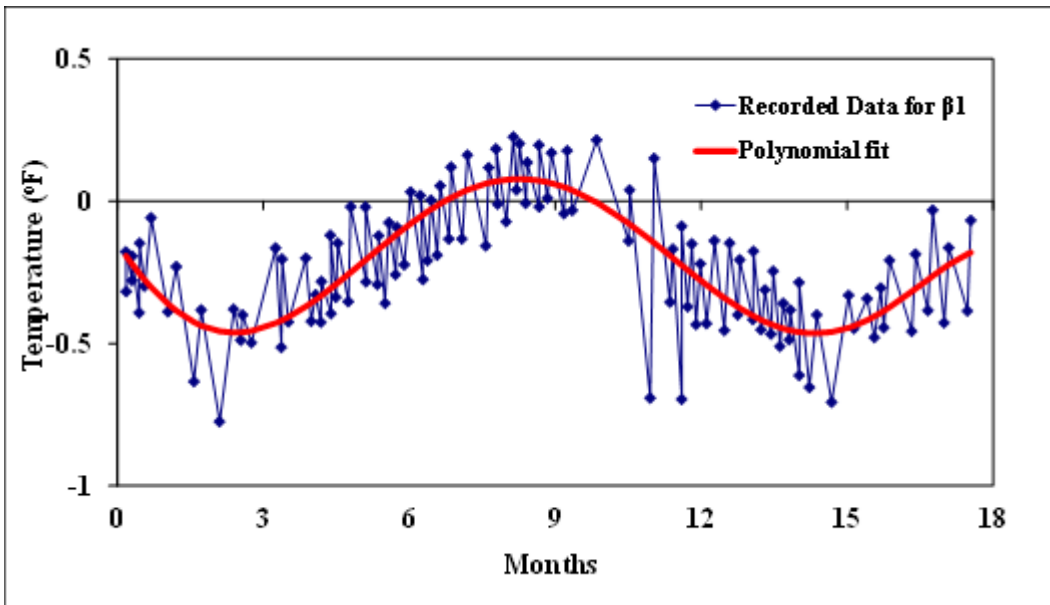
(b)

Figure 2.17. (a) Experimental Bridge Displacement versus Time for Story County
Bridge from December 1998 to April 1999, (b) The amplitude of
these primary small amplitude cycles

32
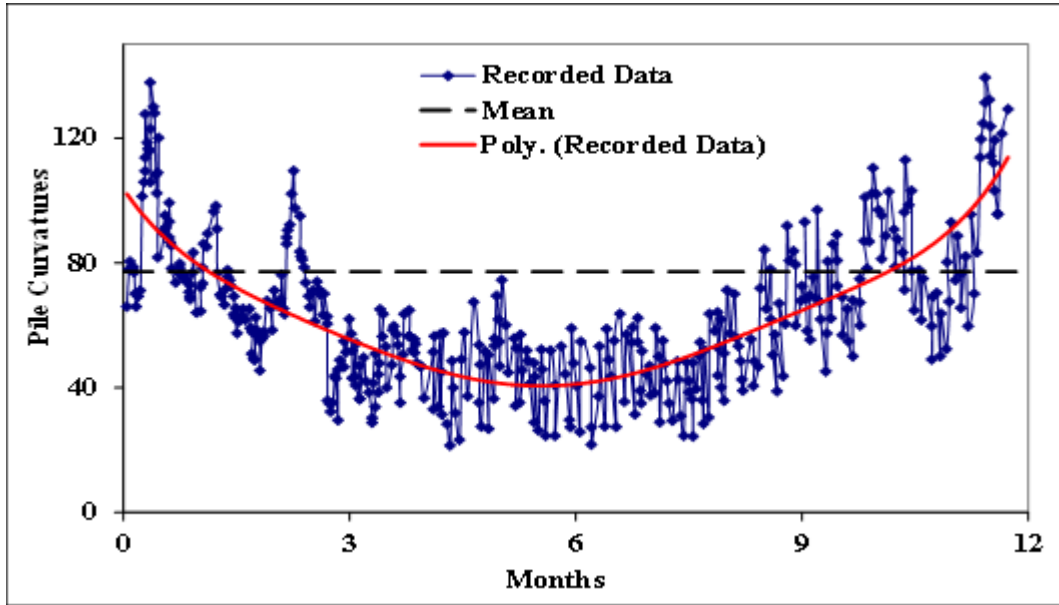
(a)
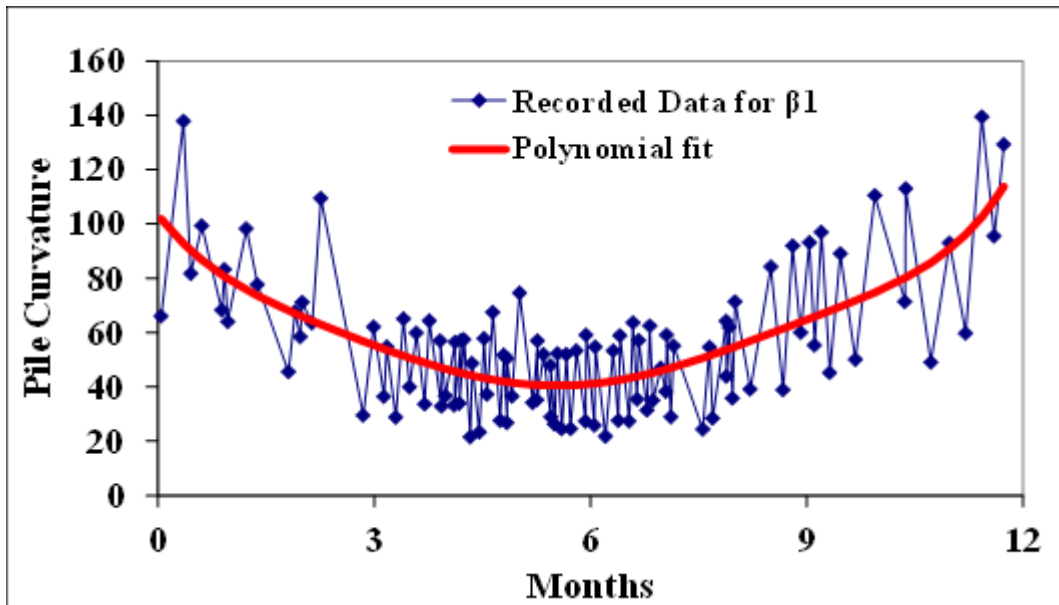
(b)

Figure 2.18. (a) Experimental Bridge Displacement versus Time for Bridge #55555, (b) The amplitude of these primary small amplitude cycles
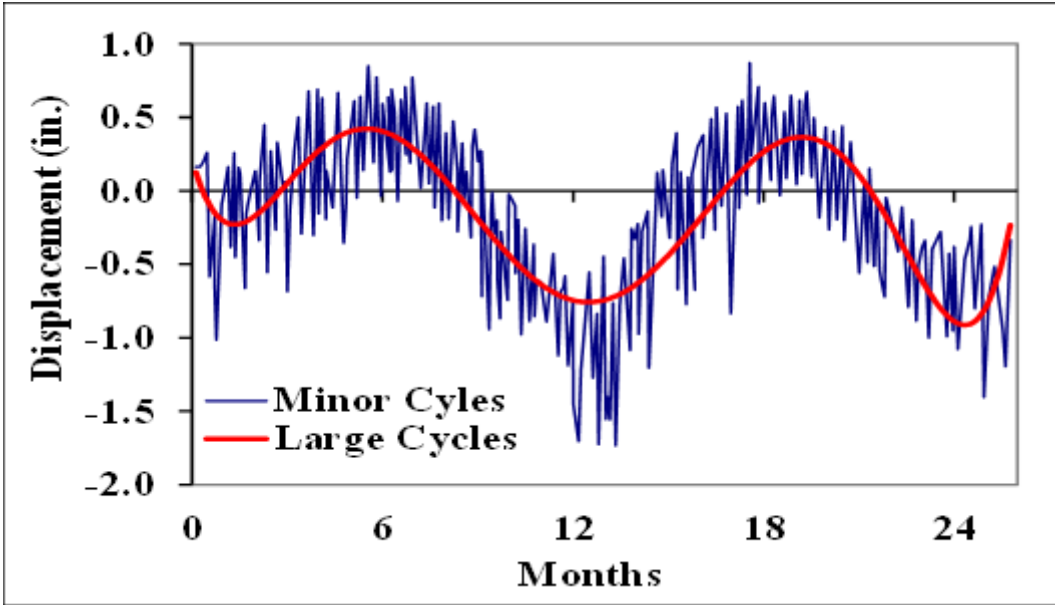
(a)
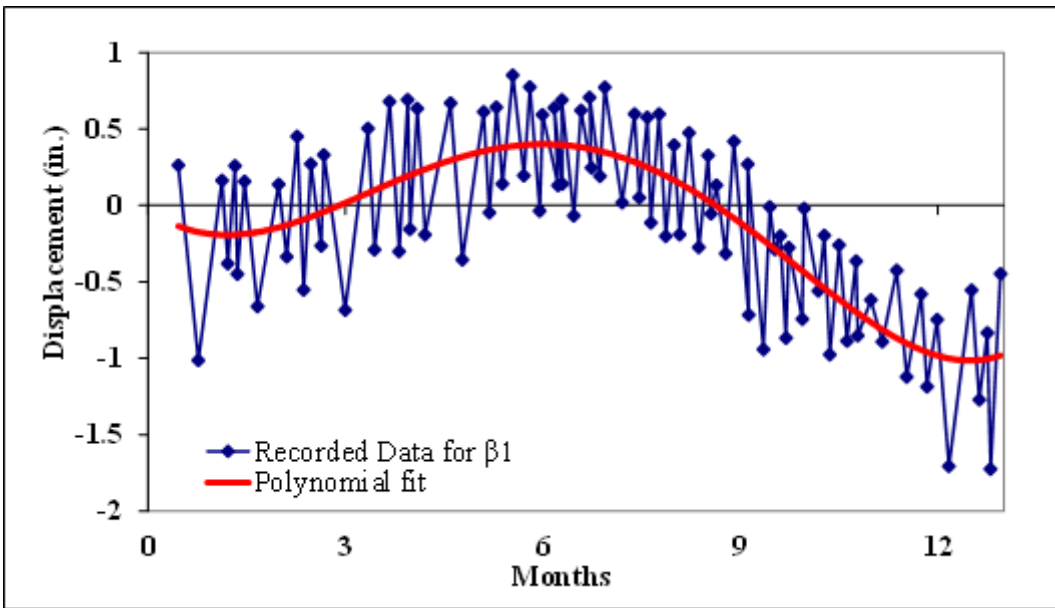
(b)

Figure 2.19. (a) Experimental Bridge Displacement versus Time for Maple River Bridge, (b) The amplitude of these primary small amplitude cycles

34
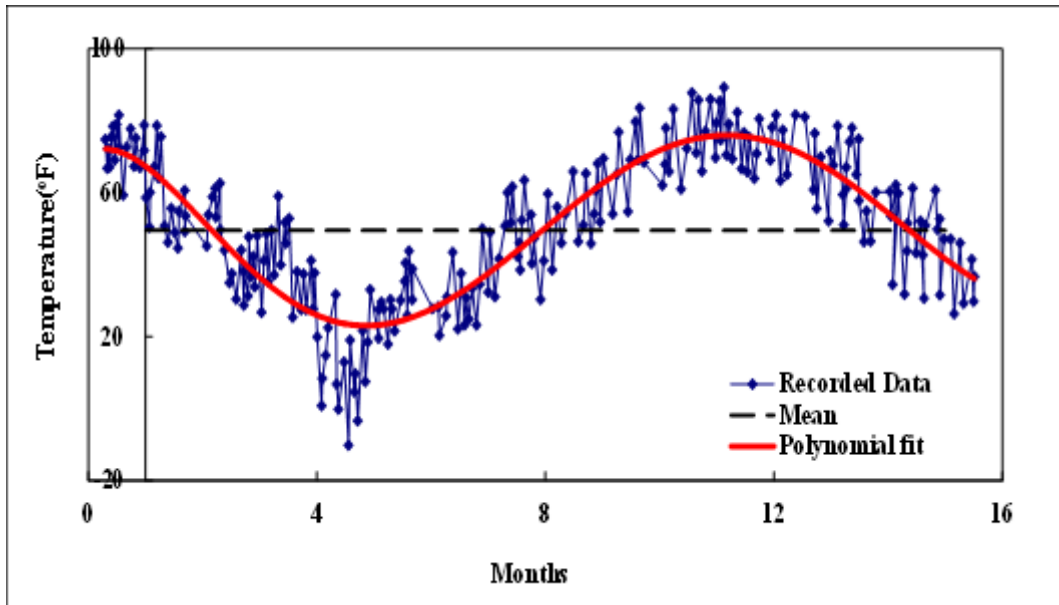
(a)
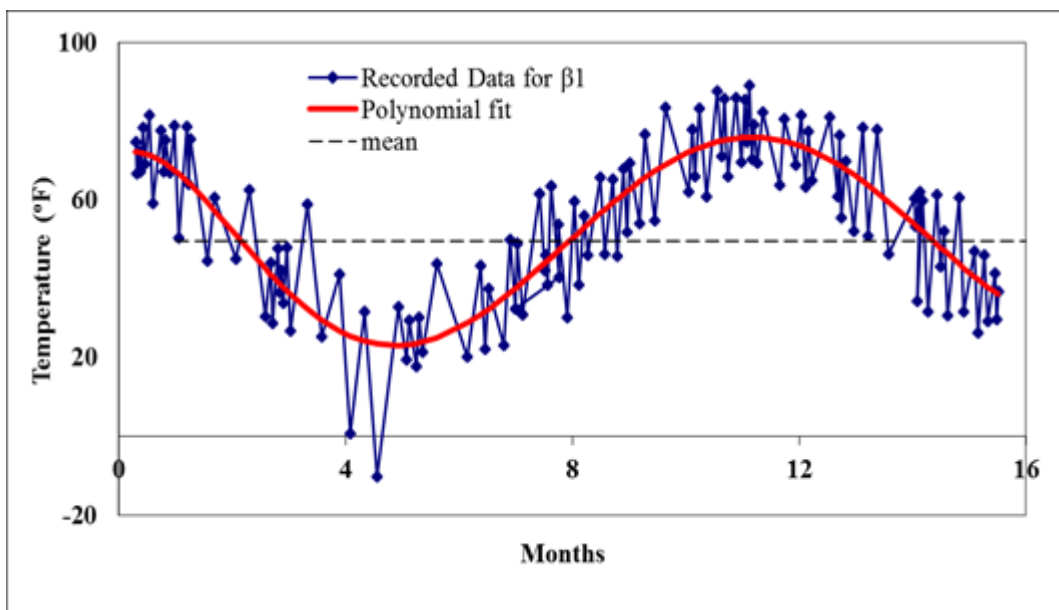
(b)

Figure 2.20. (a) Experimental Bridge Displacement versus Time for Tama
County Bridge, (b) The amplitude of these primary small
amplitude cycles

35

2.2. Application of the Developed Cycle Counting Method

In this section using the β_1 and β_2 values obtained from field measurements of integral bridges available in the literature and the cycle counting method developed above, the effect of primary and secondary small amplitude strain cycles on the low cycle fatigue performance of steel H piles is studied. For this purpose, the equation proposed by Koh and Stephens' (1991) is used together with Miner's rule (1945) to estimate the amplitude (ε_a) of the large flexural strain cycles required for low cycle fatigue failure of steel H–piles by including and excluding the effect of primary and secondary small amplitude strain cycles.

Koh and Stephens proposed an equation to calculate the number of constant amplitude strain cycles to failure for steel sections under low cycle fatigue. This equation is based on the constant strain amplitude, ε_a, and expressed as follows:

$$\varepsilon_a = M.\left(2N_f\right)^m \tag{3}$$

where M = 0.0795; m=-0.448 and N_f is the number of cycles to failure. The above equation is used for the estimation of the large strain amplitude that the steel H-piles can sustain before their failure takes place due to low-cycle fatigue effects within the service life of the bridge.

The temperature induced strains in steel H-piles are assumed to have variable amplitudes consisting of large and small cycles as illustrated in Fig. 2.6. Therefore, Eq. (3), which is derived for constant amplitude strain cycles, cannot be used directly to obtain the large strain amplitude a pile may sustain. Conservatively assuming that both the large and small amplitude strain cycles induce low cycle fatigue damage in the steel H-piles, Miner's rule may be used in

36

combination with Eq. (3) to obtain the maximum strain amplitude a pile may sustain.

Miner (1945) have formulated an expression of fatigue damage in a structure. The equation is presentation below;

$$\sum_{i=1}^{n} \frac{n_i}{N_{fi}} \leq 1 \tag{4}$$

Where N_{fi} is the number of cycles to failure with certain stress/strain amplitude and n_i is the number of times that a cycle with the same amplitude is repeated. This equation can be used to calculate for a structure' the fatigue life that has been consumed. In the case of the steel H-piles in integral bridges, this expression may be written in a different form as follows;

$$\frac{n_L}{N_L} + \frac{n_{S1}}{N_{S1}} + \frac{n_{S2}}{N_{S2}} \leq 1 \tag{5}$$

where, n_L is the number of large amplitude strain cycles, n_{S1} and n_{S2} are the numbers of respectively the primary and secondary small amplitude strain cycles due to temperature variations through the service life of the integral bridge and N_{s1}, N_{s2} and N_L are the total number of cycles to failure for the corresponding primary small, secondary small and large amplitude strain cycles, respectively. For a bridge with 'n' years of service life, the number of large amplitude strain cycles is $n_l=n$, the number of primary small-amplitude strain cycles is $n_{s1}=k_{s1}$ n and the number of secondary small-amplitude strain cycles is $n_{s2}=k_{s2}$ n.

Using Eq. (3), the small and large amplitude strains are then expressed as:

$$\varepsilon_{as1} = M.\left(2N_{fs1}\right)^m \tag{6}$$

$$\varepsilon_{as2} = M.\left(2N_{fs2}\right)^m \tag{7}$$

$$\varepsilon_{al} = M.\left(2N_{fl}\right)^m \tag{8}$$

The small strain amplitude, ε_{a1}, may be expressed as a fraction of the large strain amplitude, ε_a, as follows;

$$\varepsilon_{as1} = \beta_1.\varepsilon_a \tag{9}$$

$$\varepsilon_{as2} = \beta_2.\varepsilon_a \tag{10}$$

Substituting Eq. (9) and (10) into Eq. (6) and (7) and solving for N_{fs} and N_{fl}, the numbers of small and large amplitude cycles to failure are obtained as follows;

$$N_{fs1} = \left(\frac{\varepsilon_a.\beta_1}{M}\right)^{\frac{1}{m}}.\frac{1}{2} \tag{11}$$

$$N_{fs2} = \left(\frac{\varepsilon_a.\beta_2}{M}\right)^{1/m}.\frac{1}{2} \tag{12}$$

Substituting Eqs. (11) and (12) into Eq. (6) and (7) and rearranging the following damage equation is obtained:

$$\frac{n_l}{N_L} + \frac{2.n_{s1}}{\left(\frac{\varepsilon_a.\beta_1}{M}\right)^{1/m}} + \frac{2.n_{s2}}{\left(\frac{\varepsilon_a.\beta_2}{M}\right)^{1/m}} = 1 \tag{13}$$

Rearranging the above equation to have a common term $\left(\dfrac{\varepsilon_a}{M}\right)^{1/m}$ in the denominator, the following equation is obtained;

$$\frac{2n_l}{\left(\dfrac{\varepsilon_a}{M}\right)^{1/m}} + \frac{2.n_{s1}}{\beta_1^{1/m}.\left(\dfrac{\varepsilon_a}{M}\right)^{1/m}} + \frac{2.n_{s2}}{\beta_2^{1/m}.\left(\dfrac{\varepsilon_a}{M}\right)^{1/m}} = 1 \qquad (14)$$

The large strain amplitude, ε_a, required for the low cycle fatigue failure of the steel H-pile is then obtained as;

$$\varepsilon_a = M.\left[2.n_l + \frac{2.n_{s1}}{\beta_1^{1/m}} + \frac{2.n_{s2}}{\beta_2^{1/m}}\right]^m \qquad (15)$$

Using the value of M and m, as 0.0795 and -0.448 in Eq. (16), ε_a, is obtained in the following final form;

$$\varepsilon_a = \frac{1}{6.289\left[n_L + 2.23n_{S1}\beta_1 + 2.23n_{S2}\beta_2\right]^{0.448}} \qquad (16)$$

Next, the effect of primary and secondary small cycles are investigated for different integral bridges by using the field measurement results obtained by Breña et al. (2007), Abendroth et al. (2005, 2007), French et al. (2004) and Girton et al. (1991). Finally, the values of ε_{al} for different small and large amplitude cycle combinations are tabulated (Table 2.4-Table 2.16) and it seems that small amplitude cycles do not have a very significant effect on the low cycle fatigue life of steel H-piles as shown in Figure 2.20 and Tables 2.4 – 2.16 (difference ranges between 2% and 9%). These will be verified experimentally.

Table 2.3. The values of β_1, β_2, β, n_{s1}, n_{s2}, n_s for different integral bridges.

	Bridge	β_1	β_2	β	n_{s1}	n_{s2}
Abendroth et.al. (2005)	Story County Bridge	0.4506	0.2673	0.4107	40	11
Abendroth et.al. (2005)	Guthrie County Bridge	0.3775	0.2075	0.3304	34	13
Abendroth et.al. (2007)	Tama County Bridge	0.3443	0.1748	0.2842	52	29
Girton et.al. (1991)	Boone River	0.2959	0.1733	0.3083	39	6
Girton et.al. (1991)	Maple River	0.3864	0.1132	0.3425	44	5
French et. al. (2004)	Bridge #55555	0.4238	0.1955	0.2965	53	67
Brena et.al. (2002)	North Pile Orange–Wendell Bridge	0.2620	0.1590	0.2220	126	81
Brena et.al. (2002)	South Pile Orange–Wendell Bridge	0.2843	0.1398	0.2000	102	157
Brena et.al. (2003)	North Pile Orange–Wendell Bridge	0.1710	0.1078	0.1427	124	101
Brena et.al. (2003)	South Pile Orange–Wendell Bridge	0.2543	0.1276	0.2036	111	74
Brena et.al. (2004)	North Pile Orange–Wendell Bridge	0.2497	0.0864	0.1700	130	123
Brena et.al. (2004)	South Pile Orange–Wendell Bridge	0.2750	0.1042	0.1900	130	128
Average		**0.3146**	**0.1547**	**0.2584**	**82**	**66**
Average+S.D		**0.3934**	**0.2047**	**0.3368**	**121**	**117**
Average-S.D		**0.2358**	**0.1047**	**0.1800**	**43**	**15**

Table 2.4. Values of ε_{al} for different β combination and service life of Story County Bridges.

SERVICE LIFE	Large Amplitude Cycles + Primary and Secondary Small Amplitude Cycles	Large Amplitude Cycles + Primary Small Amplitude Cycles	Only Large Amplitude Cycles
50	0.003908	0.003980	0.004036
75	0.003259	0.003319	0.003366
100	0.002865	0.002917	0.002959

Table 2.5. Values of ε_{al} for different β combination and service life of Guthrie County Bridges.

SERVICE LIFE	Large Amplitude Cycles + Primary and Secondary Small Amplitude Cycles	Large Amplitude Cycles + Primary Small Amplitude Cycles	Only Large Amplitude Cycles
50	0.004804	0.004926	0.004972
75	0.004006	0.004108	0.004147
100	0.003522	0.003611	0.003645

Table 2.6. Values of ε_{al} for different β combination and service life of Tama County Bridges.

SERVICE LIFE	Large Amplitude Cycles + Primary and Secondary Small Amplitude Cycles	Large Amplitude Cycles + Primary Small Amplitude Cycles	Only Large Amplitude Cycles
50	0.004396	0.004566	0.004591
75	0.003666	0.003807	0.003829
100	0.003223	0.003347	0.003366

Table 2.7. Values of ε_{al} for different β combination and service life of Boone River Bridges.

SERVICE LIFE	Large Amplitude Cycles + Primary and Secondary Small Amplitude Cycles	Large Amplitude Cycles + Primary Small Amplitude Cycles	Only Large Amplitude Cycles
50	0.005280	0.005625	0.005709
75	0.004403	0.004691	0.004761
100	0.003870	0.004124	0.004185

Table 2.8. Values of ε_{al} for different β combination and service life of Maple River Bridges.

SERVICE LIFE	Large Amplitude Cycles + Primary and Secondary Small Amplitude Cycles	Large Amplitude Cycles + Primary Small Amplitude Cycles	Only Large Amplitude Cycles
50	0.004426	0.004439	0.004713
75	0.003691	0.003701	0.003930
100	0.003245	0.003254	0.003455

Table 2.9. Values of ε_{al} for different β combination and service life of Bridge #55555 Bridges.

SERVICE LIFE	Large Amplitude Cycles + Primary and Secondary Small Amplitude Cycles	Large Amplitude Cycles + Primary Small Amplitude Cycles	Only Large Amplitude Cycles
50	0.003515	0.003783	0.003813
75	0.002931	0.003155	0.003180
100	0.002577	0.002773	0.002795

Table 2.10. Values of ε_{al} for different β combination and service life of North Pile Orange–Wendell Bridge (2002).

SERVICE LIFE	Large Amplitude Cycles + Primary and Secondary Small Amplitude Cycles	Large Amplitude Cycles + Primary Small Amplitude Cycles	Only Large Amplitude Cycles
50	0.003837	0.003937	0.004136
75	0.003200	0.003283	0.003449
100	0.002813	0.002886	0.003032

Table 2.11. Values of ε_{al} for different β combination and service life of South Pile Orange–Wendell Bridge (2002).

SERVICE LIFE	Large Amplitude Cycles + Primary and Secondary Small Amplitude Cycles	Large Amplitude Cycles + Primary Small Amplitude Cycles	Only Large Amplitude Cycles
50	0.003756	0.003950	0.004183
75	0.003132	0.003294	0.003788
100	0.002753	0.002896	0.003066

Table 2.12. Values of ε_{al} for different β combination and service life of North Pile Orange–Wendell Bridge (2003).

SERVICE LIFE	Large Amplitude Cycles + Primary and Secondary Small Amplitude Cycles	Large Amplitude Cycles + Primary Small Amplitude Cycles	Only Large Amplitude Cycles
50	0.005365	0.005480	0.005833
75	0.004474	0.004570	0.004864
100	0.003933	0.004017	0.004276

Table 2.13. Values of ε_l for different β combination and service life of South Pile Orange–Wendell Bridge (2003).

SERVICE LIFE	Large Amplitude Cycles + Primary and Secondary Small Amplitude Cycles	Large Amplitude Cycles + Primary Small Amplitude Cycles	Only Large Amplitude Cycles
50	0.004232	0.004429	0.004453
75	0.003529	0.003693	0.003713
100	0.003103	0.003246	0.003264

Table 2.14. Values of ε_{al} for different β combination and service life of North Pile Orange–Wendell Bridge (2004).

SERVICE LIFE	Large Amplitude Cycles + Primary and Secondary Small Amplitude Cycles	Large Amplitude Cycles + Primary Small Amplitude Cycles	Only Large Amplitude Cycles
50	0.004122	0.004259	0.004580
75	0.003437	0.003552	0.003819
100	0.003022	0.003122	0.003357

Table 2.15. Values of ε_{al} for different β combination and service life of South Pile Orange–Wendell Bridge (2004).

SERVICE LIFE	Large Amplitude Cycles + Primary and Secondary Small Amplitude Cycles	Large Amplitude Cycles + Primary Small Amplitude Cycles	Only Large Amplitude Cycles
50	0.003755	0.003917	0.004137
75	0.003131	0.003266	0.003452
100	0.002752	0.002871	0.003033

Table 2.16. Values of ε_{al} for different β combination and service life from the average of all the data considered.

SERVICE LIFE	Large Amplitude Cycles + Primary and Secondary Small Amplitude Cycles	Large Amplitude Cycles + Primary Small Amplitude Cycles	Only Large Amplitude Cycles
50	0.003929	0.003931	0.004170
75	0.003276	0.003278	0.003477
100	0.002880	0.002882	0.003057
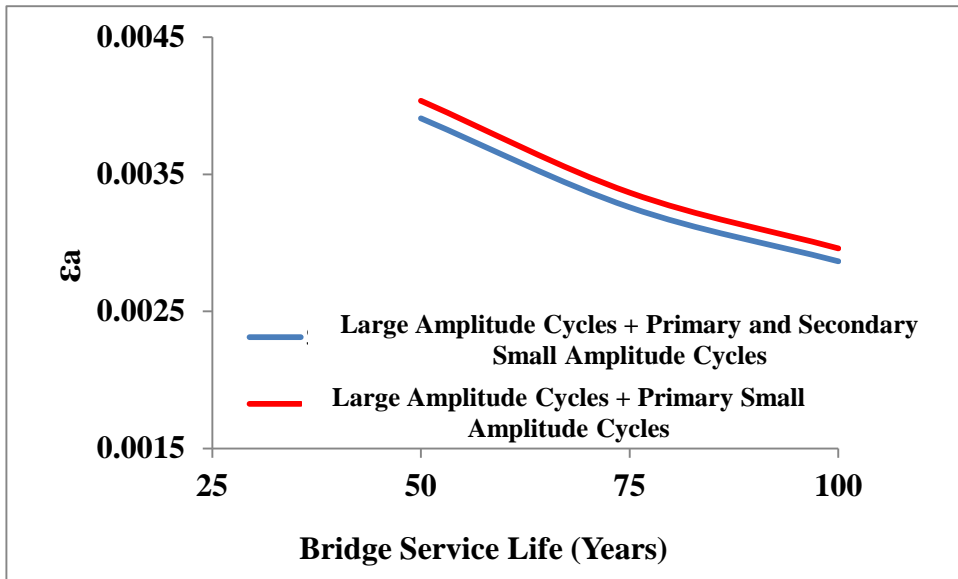
(a)
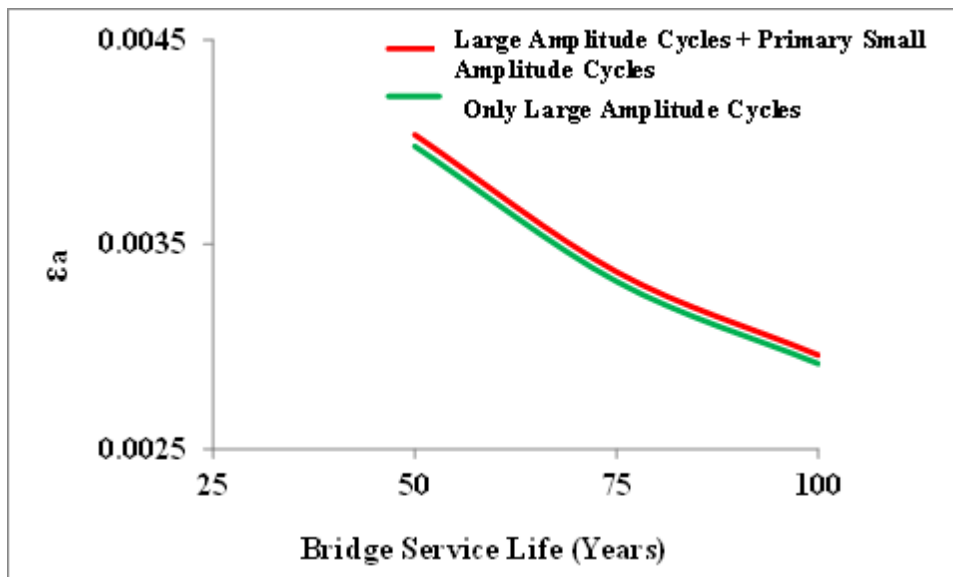
(b)

Figure 2.21. Values of ε_a for different combination of β, β_1 and $\beta_1+\beta_2$ and bridge service life.

CHAPTER 3

DISPLACEMENT CAPACITY AND STABILITY OF STEEL H PILES

3.1. Displacement Capacity of Steel H-Piles under Monotonic Loading

As mentioned earlier, the daily and seasonal temperature changes result in imposition of cyclic horizontal displacements on the continuous deck of integral bridges and thus on the steel H-piles. As the length of the integral abutment bridges becomes longer, the temperature-induced displacements in the steel H-piles may become larger as well. Consequently, the piles may experience deformations beyond their elastic limit. The ability of steel H-piles to accommodate such large displacements is an important factor that affects the maximum length of an integral bridge.

The displacement capacity of steel members is affected by their buckling instability. Instability in steel structural members includes local buckling of the plates forming the cross-section of the member as well as lateral-torsional and global buckling of the steel member. Local buckling instability in steel H piles may occur in either the flange or web or both depending on the width to thickness ratios of the flange and web plates. Lateral torsional buckling, which occurs when steel members are subjected to bending about their strong axis, is critical for steel sections with relatively narrow flanges and is not of a much concern in steel H piles that have wider flanges. Furthermore, as the steel H-piles in integral bridges are laterally supported by the surrounding soil, the lateral- torsional or global buckling instability need not be considered. Thus, the local buckling is the only instability type that will be considered when determining the displacement capacity of steel H-piles.

3.1.1. Local Buckling of Steel Sections

The width to thickness ratios of the flanges and the web for steel H-piles must be limited to prevent local buckling. Many researchers worked out limits for the width to thickness ratios of web and flange to prevent local buckling effects and hence to ensure a ductile behavior of the steel member. Most of these researches have been implemented in design codes such as the AISC (American Institute of Steel Construction) Load and Resistance Factor Design (LRFD) Manual for steel structures (1996), and the CISC (Canadian Institute of Steel Construction) Design Manual for steel structures (1993). In the following sub sections, two approaches that account for the local buckling of HP sections are presented. The first approach is the LRFD approach (AISC, 1996) and the second is the web-flange interaction approach presented by Kato (1998).

3.1.1.1. AISC Load and Resistance Factor Design Approach to Local Buckling

AISC LRFD design manual (1996), divides the steel sections into three categories based on their ability to reach a certain compressive stress level and deform without experiencing local buckling problems. These are compact sections, non-compact sections, and sections with slender plate elements. Compact sections are capable of developing full plastic flexural capacity. Non-compact sections cannot develop full plastic capacity, but are capable of developing yield stress in compression elements. The third category covers steel sections with slender plate elements that experience local buckling before the yield stress is achieved. The dividing lines between these three categories are defined by slenderness parameters λ_p and λ_r that define the limiting width to thickness ratios for compact and non-compact sections respectively. For compact sections, the width to thickness ratios for the web and flange are smaller than λ_p. For non-compact sections, they are larger than λ_p but smaller than λ_r and for slender sections, they are larger than λ_r. Table 3.1 displays the expressions for λ_p and λ_r for web and flange under monotonic loading.

Table 3. 1. Limiting width to thickness ratios for compression elements in steel sections (LRFD, 2010).

Width-Thickness Ratio	Limiting Width-thickness Ratios	
	λ_p	λ_r
b_f/t_f	$\dfrac{0.38}{\sqrt{E/F_Y}}$	$0.83\sqrt{E/(F_Y-69)}$
d_w/t_w	For $P_U/\phi_b P_Y \leq 0.125$	$5.7\sqrt{\dfrac{E}{F_Y}\left(1-0.74\dfrac{P_U}{\Phi_b P_Y}\right)}$
	$\dfrac{3.76}{\sqrt{E/F_Y}}\left(1-\dfrac{2.75P_U}{\phi_b P_Y}\right)$	
	For $P_U/\phi_b P_Y \rangle 0.125$	
	$\dfrac{1.12}{\sqrt{E/F_Y}}\left(2.33-\dfrac{P_U}{\phi_b P_Y}\right)\geq 1.49\sqrt{E/F_Y}$	

In the above table, b_f is the flange width, d_w is the clear height of the web plate between flanges, t_f and t_w are respectively the flange and web thickness, P_u and P_y are the required and yield axial Forces, and F_y is the yield stress in ksi.

3.1.1.2. Kato's (1998) Web-Flange Interaction Approach to Local Buckling of Steel HP Sections

Kato (1998) introduced a web-flange interaction approach to calculate the local buckling strength of steel HP-sections commonly used as piles (steel H-piles). Kato (1998) defined the local buckling strength of an HP-section considering the interaction between the web and flanges since the web restrains the buckling of the flanges and vice versa the flanges restrain the buckling of the web.

Using a total of 68 test data on stub-columns made of HP sections, Kato (1998) developed the following linear regression formula to relate the maximum stress,

σ_u, that an HP section can undergo without local buckling, to the yield stress, σ_y, of the material.

$$\frac{1}{s} = 0.6003 + \frac{1.600}{\alpha_f} + \frac{0.1535}{\alpha_w} \tag{17}$$

Where s is the normalized critical stress = σ_u/σ_y and, and are the slenderness parameters for the flange and web respectively. The slenderness parameters, and are defined as functions of the geometric and material properties of the HP-sections as follows;

$$\alpha_f = \frac{E}{\alpha_y}\left(\frac{t_f}{b_f/2}\right)^2 \tag{18}$$

$$\alpha_y = \frac{E}{\alpha_y}\left(\frac{t_w}{d_w}\right)^2 \tag{19}$$

where, E is *the* Young's modulus, b_f is the flange width, d_w is the clear height of the web plate between flanges and t_f and t_w are, respectively, the flange and web thickness.

3.1.2. Local Buckling Assessment of HP-Sections

Tables 3.2-3.3 and 3.4 display properties, the width to thickness ratios of the webs and flanges of the HP-sections as well as the parameters used to assess the local buckling of HP sections for both AISC's (2005) and Kato's (1998) methods. The data presented in the tables exhibit a close agreement between the AISC's and Kato's (1998) methods for local buckling. That is, for HP sections with s > 1, the width to thickness ratios for the web and flange are either smaller than or very

50

close to λ_p. The sections with s values less than 1.0 are anticipated to experience local buckling problems before the yielding of the material takes place and therefore, cannot withstand large deformations. Such sections may not be suitable for long integral bridges, where large amount of rotation and displacement is expected in the piles that support the abutments.

Table 3. 2. Dimensions of HP-piles.

Designation	Axis X-X				Axis Y-Y			
	I_x (10^6 mm^4)	S_x (10^3 mm^3)	r_x (mm)	Z_x (10^3 mm^3)	I_y (10^6 mm^4)	S_y (10^3mm^3)	r_y (mm)	Z_y (10^3 mm^3)
HP220x57	57.29	545	88	613	20.7	185.2	53.4	285
HP260x75	106.5	855	105	958	37.3	281.7	62.5	435
HP305x88	184.2	1221	128	1360	59.8	388.9	73.1	595
HP305x95	200.4	1320	128	1474	65.2	423	73.5	648
HP305x110	235.6	1531	129	1720	77.0	496.2	74.2	761
HP305x126	274.1	1755	130	1986	90.0	575.4	74.9	885
HP320x88	187.4	1237	129	1379	56.3	370.6	70.7	572
HP320x103	220.5	1437	129	1611	67.0	438.2	71.5	677
HP320x117	254.8	1638	130	1849	78.1	507.5	72.3	785
HP320x147	326.7	2048	132	2338	101.6	6513	73.7	1011
HP360x109	306.3	1769	148	1956	109.9	592.3	89	902
HP360x133	379.8	2158	149	2406	136.8	731.9	89.9	1119

Table 3.3. Properties of HP-piles.

Designation	Dead Load (Kg/m)	Total Area (10^3mm^2)	Depth (mm)	Flange		Web	
				Width (mm)	Thick. (mm)	Depth (mm)	Thick. (mm)
HP220x57	57.2	7.29	210	245	11.0	188	11.0
HP260x75	75	9.55	249	265	12.0	225	12.0
HP305x88	88	11.2	301	307	12.3	277	12.4
HP305x95	94.9	12.1	303	308	13.3	277	13.3
HP305x110	110	14.0	307	310	15.4	277	15.3
HP305x126	126	16.1	312	312	17.6	277	17.5
HP320x88	88.5	11.3	303	304	12.0	279	12.0
HP320x103	103	13.1	307	306	14.0	279	14.0
HP320x117	117	15.0	311	308	14.0	279	16.0
HP320x147	147	18.7	319	312	20.0	279	20.0
HP360x109	109	13.9	346	371	12.9	320	12.8
HP360x133	133	16.9	352	373.8	15.7	320	15.6

Table 3. 4. $\left(P_u = 0.3P_y\right)$

Designation	σ_y	1/s	s	b/t$_f$	h/t$_w$	b/t	$0.38\sqrt{\dfrac{E}{F_Y}}$	h/t$_w$	$3.76\sqrt{\dfrac{E}{F_Y}}$	h/t$_w$	$3.76\sqrt{\dfrac{E}{F_Y}}\left(1-\dfrac{2.75P_U}{P_Y}\right)$
HP220x57	235	0.848	1.18	20.4	17.09	20.4	11.08	17.09	109.69	17.09	19.19
HP220x57	*300*	0.917	**1.09**	20.4	17.09	20.4	9.81	17.09	97.08	17.09	16.989
HP220x57	320	0.938	1.06	20.4	17.09	20.4	9.5	17.09	94	17.09	16.45
HP305x88	235	0.984	1.01	25.02	22.34	12.51	11.08	22.34	109.69	22.34	19.19
HP305x88	300	1.09	0.92	25.02	22.34	12.51	9.81	22.34	97.08	22.34	16.989
HP305x88	320	1.123	0.89	25.02	22.34	12.51	9.5	22.34	94	22.34	16.45
HP305x95	235	0.93	1.07	23.21	20.83	11.6	11.08	20.83	109.69	20.83	19.19
HP305x95	300	1.02	0.98	23.21	20.83	11.6	9.81	20.83	97.08	20.83	16.989
HP305x95	320	1.052	0.95	23.21	20.83	11.6	9.5	20.83	94	20.83	16.45
HP260x75	235	0.89	1.12	22.08	18.75	11.04	11.08	18.75	109.69	18.75	19.19
HP260x75	*300*	0.97	**1.03**	22.08	18.75	11.04	9.81	18.75	97.08	18.75	16.989
HP260x75	320	0.99	1.0	22.08	18.75	11.04	9.5	18.75	94	18.75	16.45
HP305x110	235	0.85	1.17	20.17	18.11	10.08	11.08	18.1	109.69	18.1	19.19
HP305x110	300	0.92	1.08	20.17	18.11	10.08	9.81	18.1	97.08	*18.1*	*16.989*
HP305x110	320	0.94	1.06	20.17	18.11	10.08	9.5	18.1	94	18.1	16.45
HP305x126	235	0.79	1.26	17.78	15.83	8.89	11.08	15.83	109.69	15.83	19.19
HP305x126	300	0.847	*1.18*	17.78	15.83	8.89	9.81	15.83	97.08	*15.83*	*16.989*
HP305x126	320	0.864	1.16	17.78	15.83	8.89	9.5	15.83	94	15.83	16.45
HP 320x88	235	0.99	1.0	25.33	23.25	12.67	11.08	23.25	109.69	23.25	19.19
HP 320x88	300	1.11	0.9	25.33	23.25	12.67	9.81	23.25	97.08	23.25	16.989
HP 320x88	320	1.14	0.87	25.33	23.25	12.67	9.5	23.25	94	23.25	16.45

The two main column groups are **Kato's Limitations** (σ$_y$, 1/s, s, b/t$_f$, h/t$_w$) and **AISC -LRFD Limitations** (b/t, $0.38\sqrt{E/F_Y}$, h/t$_w$, $3.76\sqrt{E/F_Y}$, h/t$_w$, $3.76\sqrt{E/F_Y}(1-2.75P_U/P_Y)$).

Table 3.5. ($P_U = 0.3P_Y$) (Cont.'d).

Designation	σ_y	1/s	s	b/t$_f$	h/t$_w$	b/t	$0.38\sqrt{\dfrac{E}{F_Y}}$	h/t$_w$	$3.76\sqrt{\dfrac{E}{F_Y}}$	h/t$_w$	$3.76\sqrt{\dfrac{E}{F_Y}}\left(1-\dfrac{2.75P_U}{P_Y}\right)$
HP320x103	235	0.896	1.12	21.86	19.92	10.93	11.08	19.92	109.69	19.92	19.19
HP320x103	300	0.978	*1.02*	21.86	19.92	10.93	9.81	19.92	97.08	*19.92*	*16.989*
HP320x103	320	1.0	0.996	21.86	19.92	10.93	9.5	19.92	94	19.92	16.45
HP320x117	235	0.83	1.20	19.25	17.44	19.92	11.08	17.44	109.69	17.44	19.19
HP320x117	300	0.892	*1.12*	19.25	17.44	19.92	9.81	17.44	97.08	*17.44*	*16.989*
HP320x117	320	0.91	1.096	19.25	17.44	19.92	9.5	17.44	94	17.44	16.45
HP320x147	235	0.749	1.33	15.6	13.95	7.8	11.08	13.95	109.69	13.95	19.19
HP320x147	300	0.79	1.26	15.6	13.95	7.8	9.81	13.95	97.08	*13.95*	*16.989*
HP320x147	320	0.803	1.24	15.6	13.95	7.8	9.5	13.95	94	13.95	16.45
HP360x109	235	1.103	0.91	28.75	25.04	14.38	11.08	25.04	109.69	25.04	19.19
HP360x109	300	1.24	0.80	28.75	25.04	14.38	9.81	25.04	97.08	25.04	16.989
HP360x109	320	1.28	0.778	28.75	25.04	14.38	9.5	25.04	94	25.04	16.45
HP360x133	235	0.943	1.06	23.8	20.55	11.9	11.08	20.55	109.69	20.55	19.19
HP360x133	300	1.04	0.96	23.8	20.55	11.9	9.81	20.55	97.08	20.55	16.989
HP360x133	320	1.066	0.94	23.8	20.55	11.9	9.5	20.55	94	20.55	16.45

3.1.3. Lateral Torsional Buckling

Lateral torsional buckling, which occurs when steel members are subjected to bending about their strong axis, is critical for steel sections with relatively narrow flanges and is not of a much concern in steel H piles that have wider flanges. Furthermore, as the steel H-piles in integral bridges are laterally supported by the surrounding soil, the lateral-torsional or global buckling instability need not be considered. Additionally, in the experimental set up, lateral supports will be used to prevent lateral torsional buckling.

Lateral buckling capacity for an HP section may be expressed as;

$$M_U = \frac{S}{w}\sqrt{\sigma_1^2 + \sigma_2^2} \tag{20}$$

where;

$$\sigma_1 = \frac{140000}{Ld/A_F}$$
$$\sigma_2 = \frac{1700000}{\left(L/r_t\right)^2} \tag{21}$$

In the above equations, A_f denotes the area of one flange and r_t is the radius of gyration about the y axis of a tee section made up of the compression flange and one-sixth of the web. For members subjected to uniformly distributed transverse loads $w=1.0$, whereas for members subjected to a moment gradient, w is calculated as;

$$w = 0.6 + 0.4\frac{M_{f1}}{M_{f2}} \leq 1 \tag{22}$$

where, M_{f1} and M_{f2} are the smaller and larger bending moments at the two points of lateral support. The flexural capacity of a steel section considering lateral buckling is then calculated as;

$$M_r = 1.15\phi M_P \left(1 - \frac{0.28M_P}{M_U}\right) \leq \phi M_P \qquad (23)$$

At the end of the assessment mentioned above, two HP sections; HP220x57 and HP260x75 are selected for experimental testing. These sections are selected based on their common use as integral bridge piles as well as their availability from the manufacturer. As mentioned above, the sections with s values less than 1.0 are anticipated to experience local buckling problems before the yielding of the material takes place and therefore, cannot withstand large deformations. Thus, steel sections with s values that will be used in the experimental part of this research study are chosen as bigger than 1.0. However, local buckling problem may be expected in these sections as their s values are nearly equal to 1.0 (s=1.09 for HP 220x57 and s=1.03 for HP 260x75).

CHAPTER 4

PRELIMINARY NUMERICAL STUDIES FOR EXPERIMENTAL PHASE

4.1. Selection of HP Sections for Experimental Testing

Two HP sections; HP220x57 and HP260x75 are selected for experimental testing. These sections are selected based on their common use as integral bridge piles as well as their availability from the manufacturer. Two different sizes are selected to study size effect on low cycle fatigue performance. The lateral torsional buckling checks of these sections are conducted to make sure that no such problems would occur during the tests.

4.2. Simulation of Pile Behavior in Experimental Testing

The behavior of piles at the abutments of integral bridges under thermal induced horizontal displacements is shown in the figure below (Dicleli and Albhaisi 2003, 2004). Results from past research studies indicated that the maximum moment occurs at the steel H-pile top at the abutments under thermal induced horizontal displacements as shown in the figure below and there is a point of zero moment (inflection point) at some distance below the abutment. The length L_e, of the pile between the pile top and inflection point is called the equivalent pile length. Accordingly, in the experimental testing the low cycle fatigue performance of the pile under cyclic displacements/strains could be simulated using a simple inverted cantilever as shown in Figure 4.1. In the following subsection, the equivalent length of the pile, L_e, which will be used in the experimental set up, will be determined.

(a)   (b)
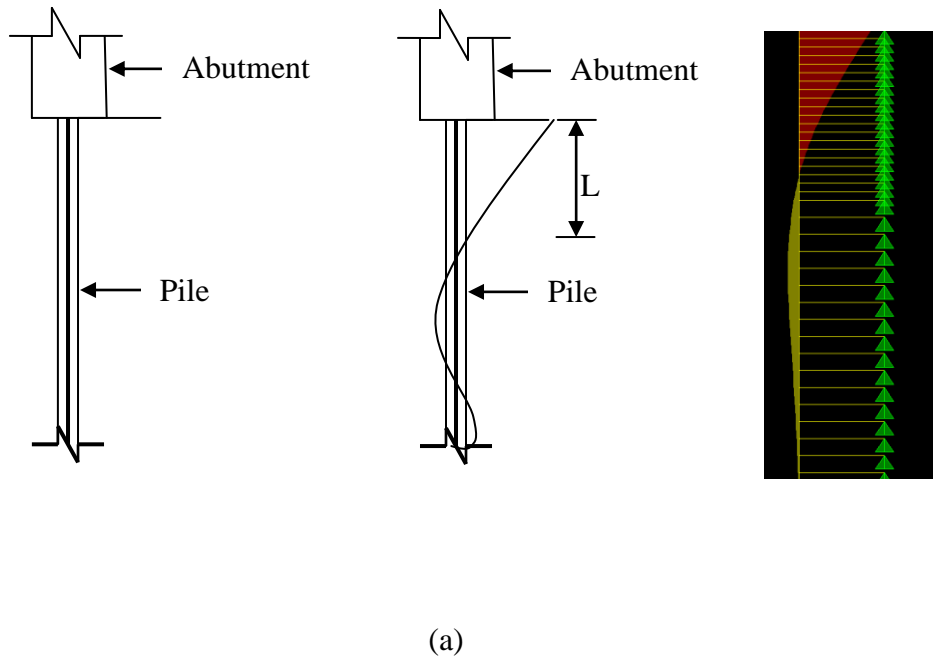
Figure 4. 1. (a) The equivalent pile length, (b) The equivalent pile length on SAP
2000
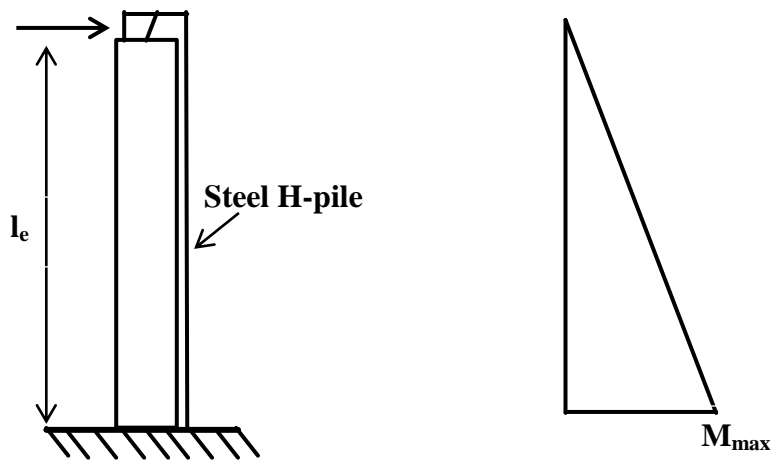
Figure 4. 2. Distribution of Moment for steel H-piles

4.3. Determination of Equivalent Length of Pile via Pushover Analyses

4.3.1. Definition of Integral Bridges and Parameters Used in the Pushover Analyses

Two symmetrical integral bridges are considered to determine the equivalent length of pile specimens, L_e that will be used in experimental testing. The bridges are chosen such that the study covers a wide range of deck and abutment stiffness properties. One of the bridges is located in Illinois, USA and the other is located in Ontario, Canada. The total lengths of the bridges are modified for the purpose of this study. Both bridges are assumed to have a total length of 120 m. This is done to include a realistic effect of axial deformation of the bridge decks on the lateral displacements of the piles. The first bridge is referred to as the small bridge. It represents those bridges with relatively smaller deck and abutment stiffness. It has six 20 m long spans and represents those bridges with relatively smaller deck and abutment stiffness. The bridge deck is composed of a 190 mm thick concrete slab supported on steel W760x173 girders spaced at 2400 mm. The thickness of the abutments is 1000 mm. The second bridge is referred to as the large bridge. It represents those bridges with relatively larger deck and abutment stiffness. It has three 40 m long spans. The bridge deck is composed of a 225 mm thick concrete slab. The thickness of the abutments is 1500 mm. The properties of both bridges are summarized in Table 4.1.

Table 4.1. Properties of Integral Bridges Used in Study.

Properties	Small Bridge	Large Bridge
Location	Illinois, USA	Ontario, Canada
Total Length (m)	120	120
Number of Spans	6	3
Span Length (m)	20	40
Deck Type	Slab-on-girder	Slab-on-girder
Girder Spacing (mm)	2400	2400
Girder Type	Steel	Prestressed Concrete
Girder Size	W760x173	AASHTO VI
Slab Thickness (mm)	190	225
Abutment Thickness (mm)	1000	1500
Concrete Strength (MPa)	30	30
Type of bearings over piers	Elastomeric	Laminated Elastomeric
Number of Piles per girder	1	1

Static pushover analyses of the bridges are conducted to determine the length of the steel H-piles' that will be used in the experimental part of this research study. For this purpose, the piles, *HP220X57* and *HP260X75* that will be used in the experimental study are used in each bridge model to obtain the equivalent pile length for the experimental set up. The equivalent pile length is defined as the length from the fixed pile top to the point of contra flexure (point of zero moment) as shown in Figure 4.1. Orientation of the piles for bending about their strong and weak axes is also considered in the analyses. The soil stiffness is anticipated to affect the equivalent pile length. Accordingly, four different clay stiffnesses are included in the analyses. However, the average of the results from all the analyses cases is used to determine the equivalent pile length for experimental testing.

.

4.3.2. Structural Model for Nonlinear Static Pushover Analyses

Nonlinear structural models of the two bridges incorporating the response of the soil to bridge movement are built and analyzed using the finite element based software SAP2000 (2007). Only half of the bridges are modeled due to their symmetrical configuration, symmetrical nature of the thermal effects and assumption of identical soil properties at both ends of the bridge. The structural model of the bridge is illustrated in Figure 4.3.

The abutment is modeled using beam elements. The deck-abutment joint is modeled using a horizontal and a vertical rigid elastic beam element. The pile is modeled using beam elements with nonlinear frame-hinges to simulate the inelastic deformation of the steel H-piles under thermal effects.
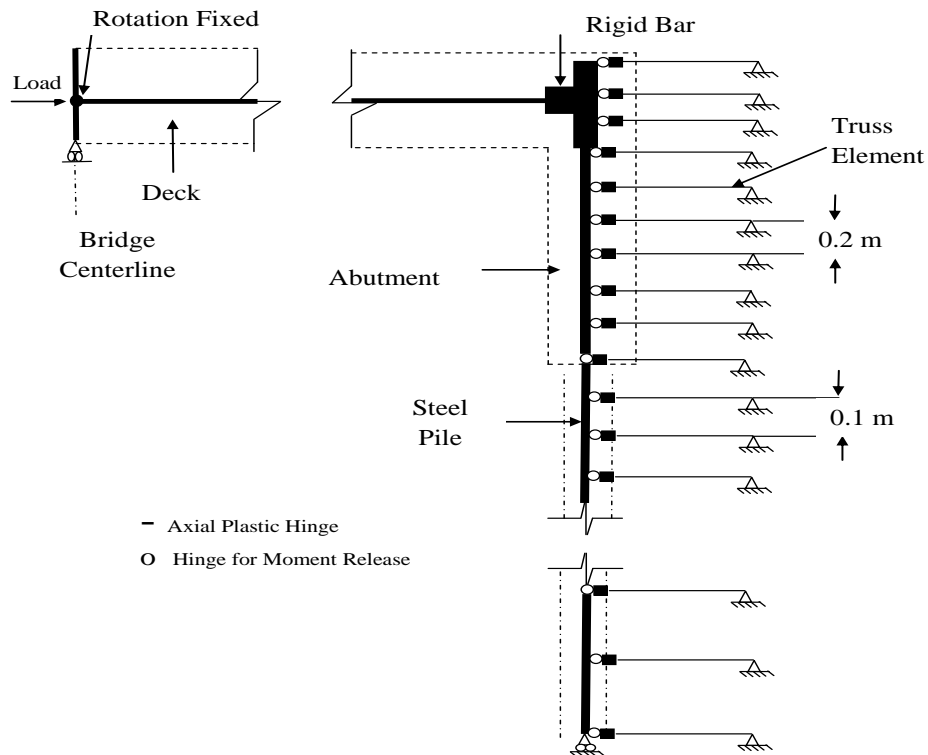
Figure 4. 3. Nonlinear Structural Model of the Bridge

61

4.3.3. Static Pushover Analyses Results

A total of 128 static pushover analyses are conducted to estimate the equivalent cantilever length of the steel H-piles used in experimental study. Figure 4.4 shows static pushover analyses cases. The analyses results are presented in Tables 4.2 and 4.3 for the push direction and in Tables 4.4 and 4.5 for the pull direction.
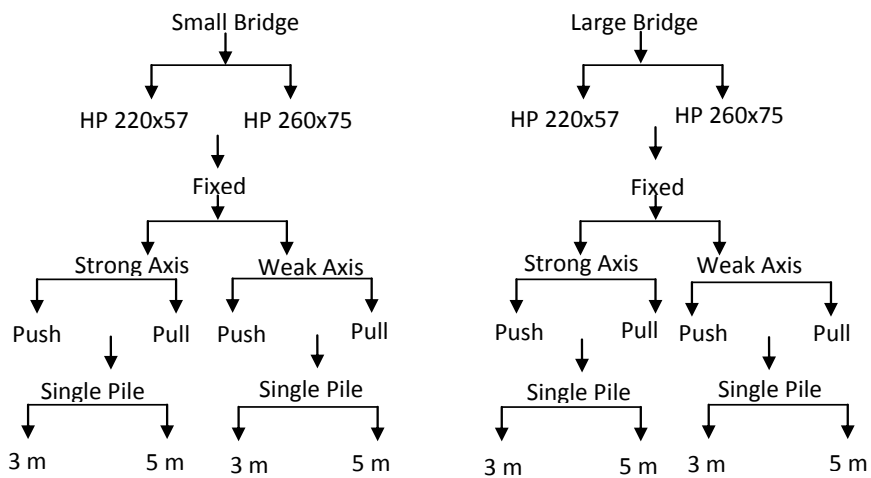
Figure 4.4. Static Pushover Analyses Scheme.

Table 4.2. Equivalent cantilever pile length subjected to moment gradient (strong axis+thermal expansion).

Sand Stiffness	Small Bridge				Large Bridge			
	Abutment H=3 m		Abutment H=5 m		Abutment H=3 m		Abutment H=5 m	
	HP 220x57	HP 260x75	HP 220x57	HP 260x75	HP 220x57	HP 260x75	HP 220x57	HP 260x75
Loose	2.8 m	3.0 m	2.4 m	2.6 m	2.2 m	2.4 m	2.2 m	2.4 m
Medium	2.0 m	2.4 m	1.9 m	2.0 m	1.8 m	1.9 m	2.0 m	2.2 m
Medium Dense	1.8 m	2.0 m	1.8 m	1.9 m	1.6 m	1.6 m	1.8 m	2.0 m
Dense	1.7 m	1.8 m	1.4 m	1.6 m	1.4 m	1.5 m	1.6 m	1.8 m
Average	**2.0 m**	**2.3 m**	**1.8 m**	**2.0 m**	*1.7 m*	*1.8 m*	*1.9 m*	*2.1 m*

Strong Axes average= 1.95 m

Table 4.3. Equivalent cantilever pile length subjected to moment gradient (weak axis + thermal expansion).

Sand Stiffness	Small Bridge				Large Bridge			
	Abutment H=3 m		Abutment H=5 m		Abutment H=3 m		Abutment H=5 m	
	HP 220x57	HP 260x75	HP 220x57	HP 260x75	HP 220x57	HP 260x75	HP 220x57	HP 260x75
Loose	1.8 m	2.0 m	1.7 m	1.8 m	1.7 m	1.8 m	1.8 m	1.8 m
Medium	1.5 m	1.7 m	1.4 m	1.5 m	1.3 m	1.4 m	1.4 m	1.5 m
Medium Dense	1.3 m	1.5 m	1.3 m	1.4 m	1.2 m	1.2 m	1.2 m	1.3 m
Dense	1.2 m	1.3 m	1.1 m	1.2 m	1.1 m	1.1 m	1.0 m	1.1 m
Average	**1.4 m**	**1.6 m**	**1.3 m**	**1.4 m**	*1.3 m*	*1.3 m*	*1.3 m*	*1.4 m*

Weak Axes average= 1.40 m

Table 4.4. Equivalent cantilever pile length subjected to moment gradient (strong axis+ thermal contraction).

Sand Stiffness	Small Bridge				Large Bridge			
	Abutment H=3 m		Abutment H=5 m		Abutment H=3 m		Abutment H=5 m	
	HP 220x57	HP 260x75	HP 220x57	HP 260x75	HP 220x57	HP 260x75	HP 220x57	HP 260x75
Loose	1.4 m	1.7 m	1.4 m	1.5 m	1.6 m	1.7 m	1.5 m	1.7 m
Medium	1.2 m	1.3 m	1.2 m	1.3 m	1.4 m	1.4 m	1.3 m	1.4 m
Medium Dense	1.0 m	1.1 m	1.0 m	1.0 m	1.2 m	1.2 m	1.1 m	1.2 m
Dense	0.9 m	0.9 m	0.8 m	0.8 m	0.9 m	0.9 m	0.8 m	0.9m
Average	1.1 m	1.2 m	1.1 m	1.1 m	1.3 m	1.3 m	1.2 m	1.3 m

Strong Axes average= 1.2 m

Table 4.5. Equivalent cantilever pile length subjected to moment gradient (weak axis+ thermal contraction).

Sand Stiffness	Small Bridge				Large Bridge			
	Abutment H=3 m		Abutment H=5 m		Abutment H=3 m		Abutment H=5 m	
	HP 220x57	HP 260x75	HP 220x57	HP 260x75	HP 220x57	HP 260x75	HP 220x57	HP 260x75
Loose	1.1 m	1.2 m	1.1 m	1.2 m	1.0 m	1.1 m	1.2 m	1.2 m
Medium	0.9 m	1.0 m	0.8 m	0.9 m	0.8 m	0.9 m	1.0 m	1.1 m
Medium Dense	0.7 m	0.8 m	0.7 m	0.8 m	0.6 m	0.7 m	0.8 m	0 .9m
Dense	0.6 m	0. 7 m	0.5 m	0.6 m	0.5 m	0.6 m	0.6m	0.7 m
Average	0.8 m	0.9 m	0.8 m	0.8 m	0.7 m	0.8 m	0.9 m	0.9 m

Weak Axes average= 0.8 m

Table 4.6. Average values.

		HP220x57	*HP260x75*	*Average*
Push Direction	**Strong axis**	1.85 m	2.05 m	1.95 m
	Weak axis	1.33 m	1.43 m	1.38 m
Pull Direction	**Strong axis**	1.18 m	1.23 m	1.21 m
	Weak axis	0.80 m	0.85 m	0.83 m
Strong axes $\dfrac{Push + Pull}{2}$		1.52 m	1.64 m	1.58 m
Weak axes $\dfrac{Push + Pull}{2}$		1.07 m	1.14 m	1.11 m
Average		1.29 m	1.39 m	1.34 m

Based on the pushover analyses results, the average equivalent pile length that will be used in the experimental part of this research study is determined as 1.35 m. However both HP220x57 and HP260x75 piles are cut in 1.90 m length where the 0.4 m part is encased in a steel base fixture to provide fixity and the load is applied at approximately 0.15 m from the top of the pile (the centerline of the load is at 0.15 m from the pile top). The cutting process of the test specimens from 12 m long HP sections is shown in Figure 4.5.
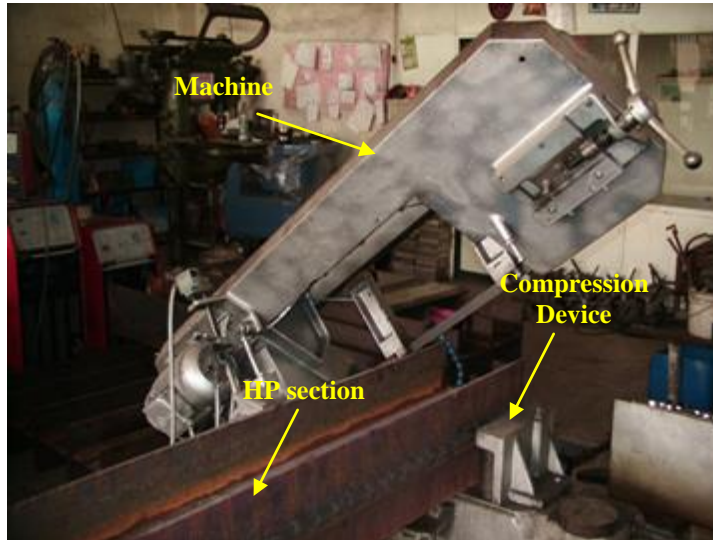
(a)
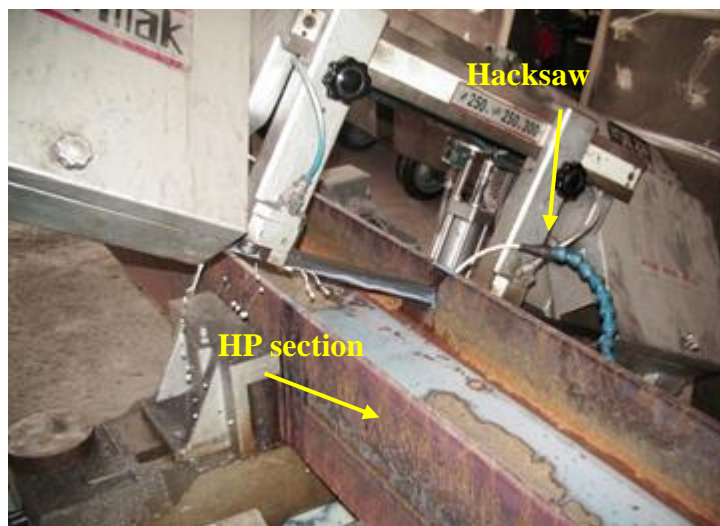
(b)

Figure 4.5. Cutting process, (a) before cutting, (b) cutting with hacksaw.

4.4. FINITE ELEMENTS ANALYSIS TO REFINE THE PRELIMINARY TEST SET UP

4.4.1. Proposed test set up

A cantilever steel H-pile will be tested to simulate cyclic behavior of such piles under thermal effects in integral bridges. Thus, the equivalent system has upside down geometry of the pile/pile cap system under an integral bridge as shown in Figure 4.6. The cantilever length chosen approximately corresponds to the length of the pile effective in resisting the movement.
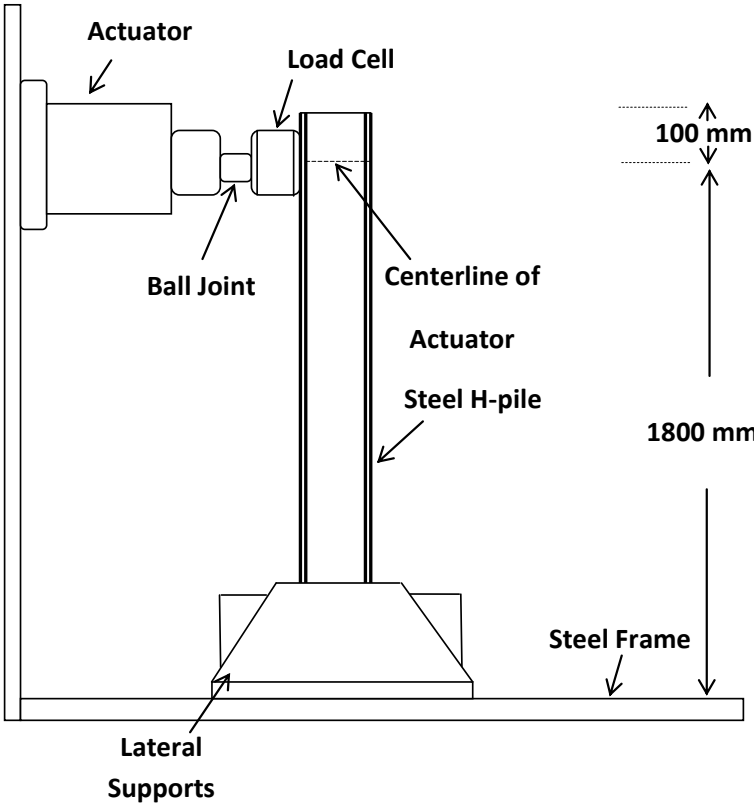
Figure 4.6. The equivalent system

4.4.2. Purpose of Finite Element Modeling and Analyses of the proposed test set up

In this part of the research study, linear and nonlinear finite element models of the steel H-pile specimens used in the experimental part of this research study are developed using the computer program ANSYS to identify potential problems that may be encountered during testing and to improve the test apparatus if necessary. First, linear finite element models of the steel H-pile specimens are built to determine maximum stress concentrations occurring in the HP sections and the steel base fixture used for fixing the pile to the testing frame. From these linear analyses results; the locations of stress concentrations in the HP sections are identified. Using these results, the test set up is modified to decrease the stress concentrations (as in the case of piles embedded in concrete abutment). Then, nonlinear finite element analyses of the steel H-pile specimens are repeated on the modified specimen model to observe the distribution of stresses and strains in the steel HP sections and the steel base fixture. Based on these analyses results, proper locations for the installment of strain gages in the HP sections are also determined.

4.4.3. Linear Finite Element Model

The main objective of the linear finite element analyses is to determine stress concentrations occurring in the HP sections and the steel base fixture. First, linear finite element models of the steel H-pile specimens are developed using the computer program ANSYS. Figure 4.7 shows the linear finite element model for the *HP260x75* section. The *HP260x75* section for bending about the strong axis is modeled. Figure 4.8 demonstrates the 400 mm-high steel base fixture. The steel base fixture is attached to the testing frame using 30 mm diameter bolts. The steel base fixture-pile interaction is modeled using the frictionless contact algorithm in ANSYS. In the finite element model, the *HP260x75* section is meshed using ANSYS's automatic mesh generation feature. However, the automatically

68

generated mesh sizes are modified manually in ANSYS to obtain a more accurate simulation of the stress distribution (the mesh size is taken as 25 mm within contact regions and 50 mm within the rest of the model). The model consists of 63,897 tetrahedron elements and 20,657 nodes. Further details on the linear finite element modeling of the test specimen are presented in the following subsections.
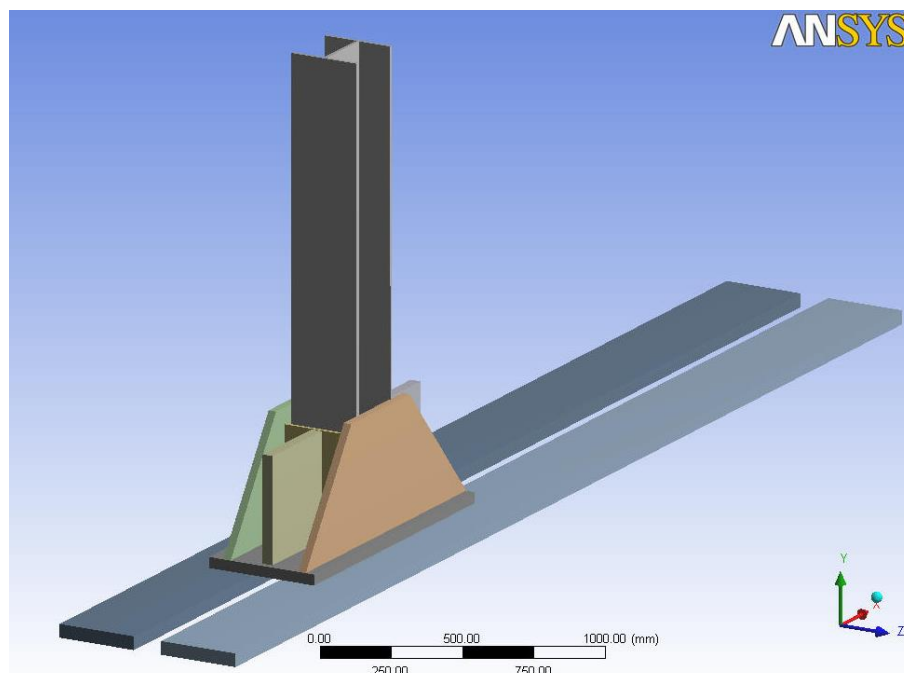
Figure 4. 7. Finite element model for the *HP 260x75* section.
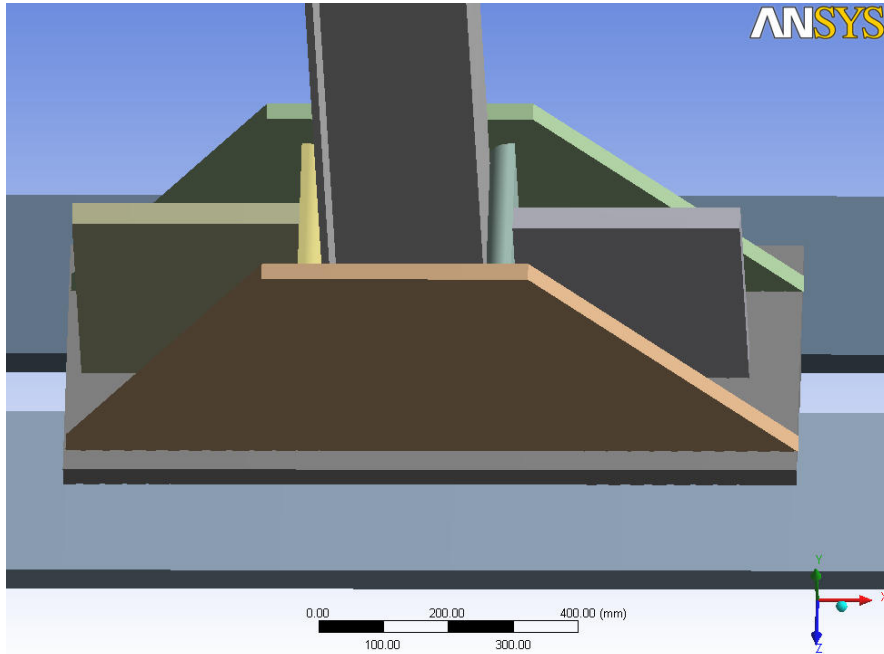
Figure 4.8. 400 mm-high two lateral supports.

4.4.3.1. Element Model

In the finite element model, a structure is divided into small and simple elements. To perform finite element analysis on a structure, first element type (bar, beam, shell…etc) should be chosen for the analysis. The finite elements used in the model are composed of 10-node high-order tetrahedron elements as shown in Figure 4.9. Every node has three degrees of freedom: translations in the nodal x, y and z directions. The element has a quadratic displacement behavior and is well suited to modeling irregular meshes.
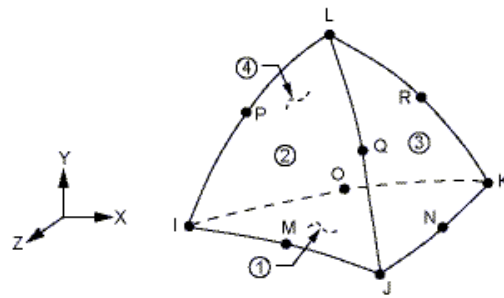
Figure 4.9 .Solid187 geometry**.**

For the contact elements, CONTA174 is used to represent contact and sliding between 3-D "target" surfaces and a deformable surface. The element is applicable to 3-D structural and coupled field contact analyses. This element is located on the surfaces of 3-D solid or shell elements with mid-side nodes. It has the same geometric characteristic as the solid or shell element face, to which it is connected as shown Figure 4.10. Contact occurs when the element surface penetrates one of the target segment elements on a specific target surface.
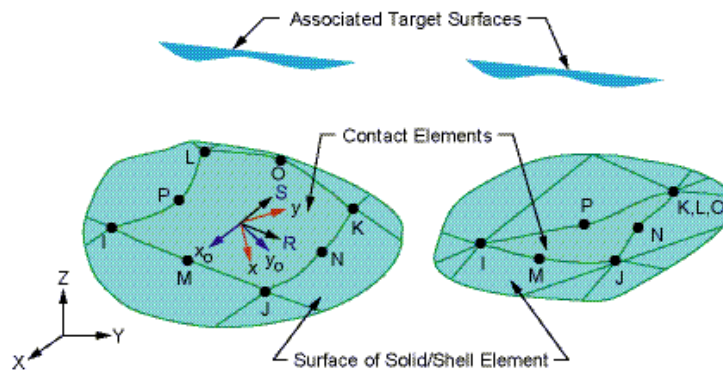
Figure 4.10. Contact Element Geometry.

For the target segment elements, TARGE170 is used to represent various 3-D "target" surfaces for the associated contact elements as shown Figure 4.11. The contact elements themselves overlay the solid, shell or line elements describing the boundary of a deformable body and are potentially in contact with the target surface, defined by TARGE170. This target surface is discretized by a set of target segment elements and is paired with its associated contact surface via shared real constant set.
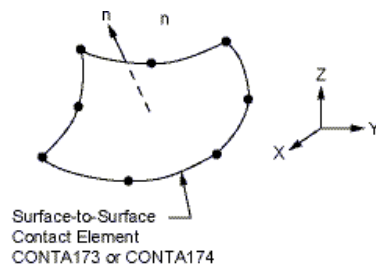
Figure 4. 11.Target Element Geometry.

Mesh size and type are important for accurate stress values. For this purpose, four meshing options were tested and compared in the finite element model: Automatic, Tetrahedrons, Hex Dominant and Sweep meshing options. Shown in Figure 4.12 are different meshes of finite element model. The first option, automatically-generated mesh, consists of 13,626 elements and 40,826 nodes. Tetrahedrons mesh consists of 62,303 elements and 20,207 nodes. The other mesh properties are shown in Table 4.7. Based on these mesh properties, Tetrahedrons meshing option is chosen because the obtained mesh has a better size distribution across the model, as shown in Figure 4.13. The selected meshing type, the tetrahedron mesh, is tested using various sizing mesh starting with 250 mm and reducing the mesh size until the results become stable. When the stress values are stable, this mesh sizing can be applicable for FEM analysis. As shown in Figure 4.14, the maximum stress value in the HP section remains nearly constant for both 50 mm and 25 mm mesh sizes (526 MPa and 529MPa, respectively). Thus, the

72

mesh sizes are input manually and taken as 25 mm within contact regions and 50 mm within the rest of the model. Consequently, an accurate simulation of the linear elastic behavior is obtained.

Table 4. 7.Numbers of Nodes and Elements for different mesh type.

Mesh Type	Number of Nodes	Number of Elements
Tetrahedrons	20207	62303
Automatic	40826	13626
Hex Dominant	47052	16026
Sweep	43922	14658
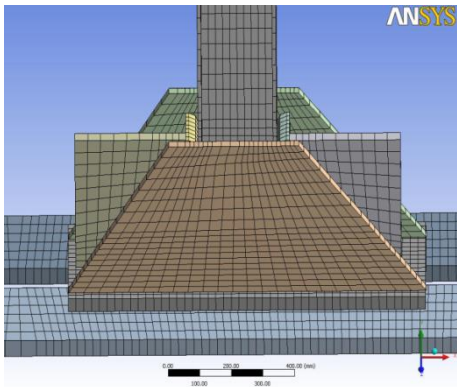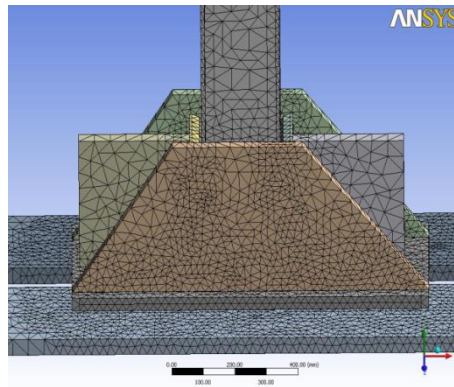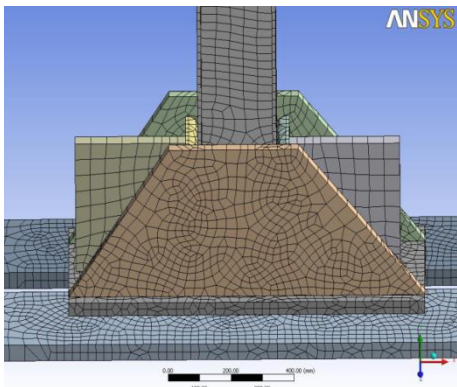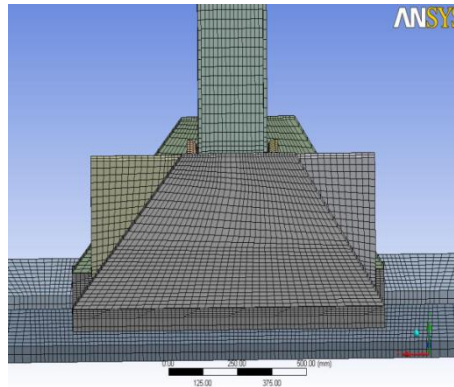
Figure 4.12. Mesh options, (a) Automatic Mesh generation, (b) Tetrahedrons Mesh, (c) Hex Dominant Mesh, (d) Sweep Mesh.
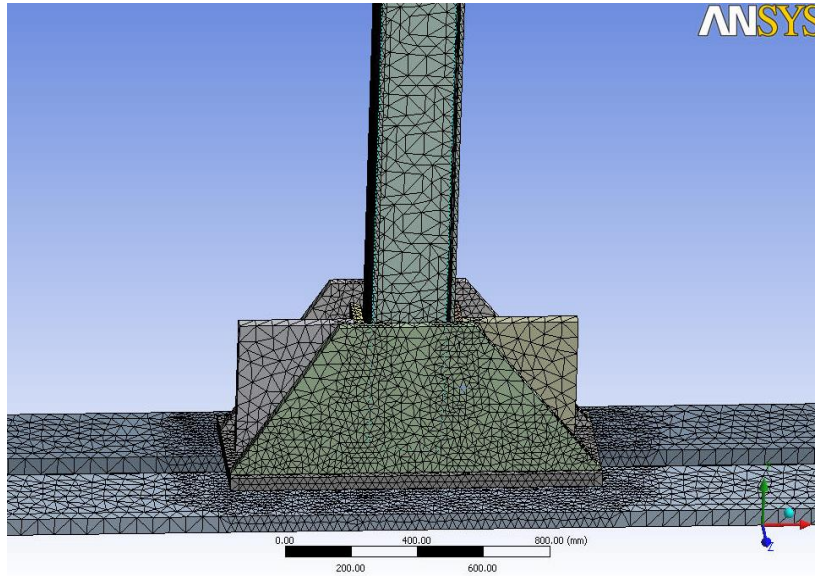
Figure 4.13. Tetrahedrons Mesh Model.
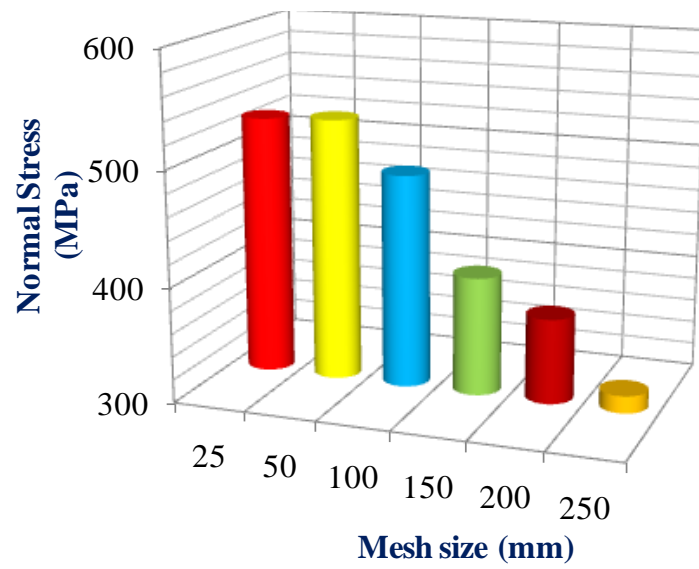
Figure 4.14. Stress value for different mesh size.

4.4.3.2. Material Model

Material properties are extracted from material library, which covers standard concrete, steel and has the ability to create user defined custom materials for non-standard applications. Linear elastic material model is used for steel HP sections with Young's modulus of 200,000 MPa, Poisson's ratio 0.3, tensile yield stress 350 MPa and tensile ultimate stress 460 MPa.

4.4.4. Setting Contact Analysis Parameters

4.4.4.1. Introduction

Contact surfaces in ANSYS allow representing a wide range of different types of interaction between components in a model. In the present finite element model, there exists contact between HP section and the plates of the steel base fixture. Thus, it is important to investigate the nature of interaction between two contacting bodies (HP section and connection plates) and the ANSYS solution procedure to understand the simulation of the contact behavior.

4.4.4.2. Identification of Contact and Target Surface

The contact between the HP section and the steel plates of the base fixture is a surface-to-surface contact type. This contact type is established when a surface of one body comes in contact with the surface of another body. This contact type is commonly used for arbitrary bodies that have large contact areas. It is very efficient for bodies that experience large amounts of relative sliding with friction, such as a block sliding on a plane. The chosen contact and target surfaces are shown in Figure 4.15.
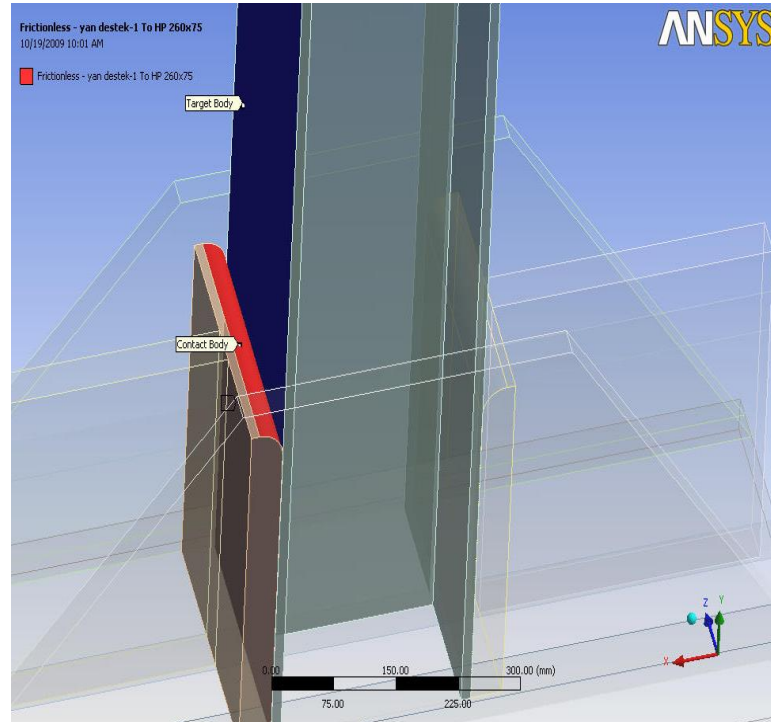
Figure 4.15. Contact and Target Surface.

4.4.4.3. Types of Surface-to-Surface Contact Elements

Contact surface has different types of behavior according to different characteristics of contact. There are several kinds of contact used in ANSYS: Frictional, Frictionless, Rough, Bonded, No Separation.

Bonded contact: In bonded type contact, no sliding or separation between faces or edges is allowed. In Figure 4.16, neither (a) nor (b) can occur. This type of contact allows for a linear solution since the contact length/area will not change during the application of load.

No separation: This contact setting is similar to bonded case. It only applies to regions of faces. Separation of faces in contact is not allowed, but small amounts

77

of frictionless sliding can occur along contact faces. That means, referring to Figure 4.16, (a) is possible but (b) is not.

Frictionless: This setting models standard uni-lateral contact; that is, normal pressure equals zero if separation occurs. Thus depending on the loading, gaps between bodies can form. This solution is nonlinear because the area of the contact may change as the load is applied. A zero coefficient of friction is assumed, thus allowing free sliding.

Rough contact: Similar to the frictionless setting, as shown in Figure 4.16 (c), this setting models perfectly rough frictional contact where there is no sliding. By default, no automatic closing of gaps is performed.

Frictional Contact: Two contacting faces can carry shear stresses up to a certain magnitude across their interface before they start sliding relative to each other as shown in Figure 4.16 (a).

(a)   (b)

(c)
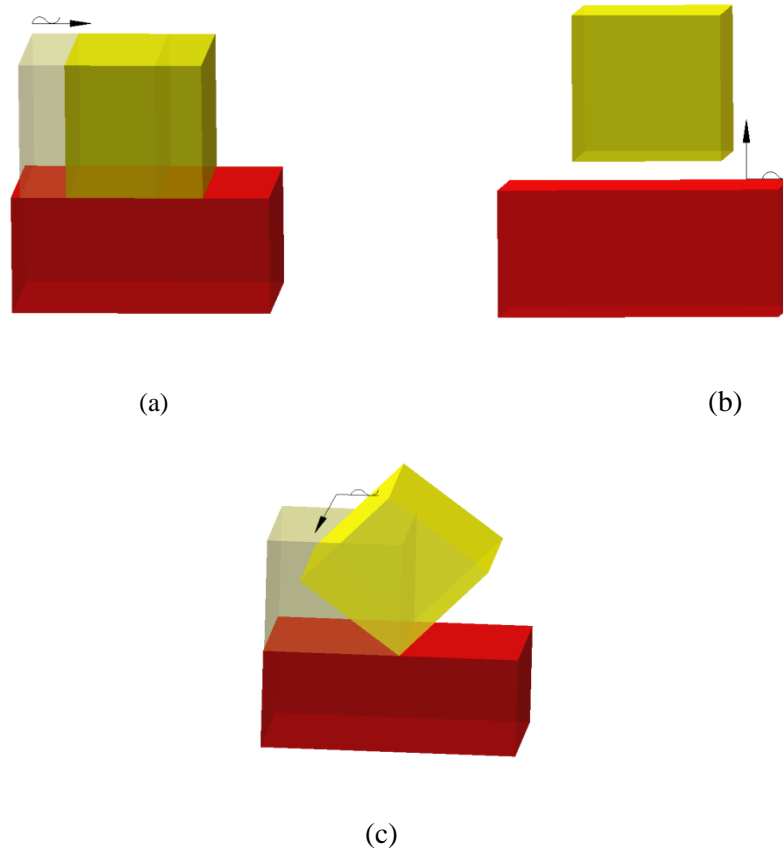
Figure 4.16. Contact Types.

In this study, frictionless contact is chosen between the HP section and connection plates as gaps form in the model between contacting bodies. For the remainder of the model, bonded contact is chosen (for the contact with the side plates of the steel base fixture).

4.4.4.4. Behavior of Contact

Several types of contact behavior are available in ANSYS, namely, symmetric, asymmetric, and auto asymmetric. In asymmetric contact one face is chosen as contact and the other face as target, creating a contact pair. Asymmetric contact is usually the most efficient way to model face-to-face contact for solid bodies. Symmetric contact means that there exists both contact and target elements on the same surface. Auto asymmetric contact option allows the program to automatically identify and generate an asymmetric contact pair. This can significantly improve performance in some instances. When it is chosen, during the solution phase the solver will automatically choose the more appropriate contact face designation. In this study, asymmetric contact is chosen between two contact surfaces of the model.

4.4.4.5. Contact Analysis Algorithm

Several analysis algorithms are available in ANSYS, namely, Penalty Method, Augmented Lagrangian, Pure Lagrangian, Multipoint Constraint and so on. Characteristic of each algorithm are presented in the following.

Penalty method: The penalty method uses a contact "spring" to establish a relationship between the two contact surfaces. The penalty method has short computation time and is fastest among all the algorithms. Furthermore, in this method, large penetration may be produced.

Augmented Lagrangian: The Agumented Lagrangian Method is an iterative series of penalty methods. Compared to the Penalty method, the agumented lagrangian method usually leads to better conditioning and is less sensitive to the magnitude of contact stiffness. However, the agumented lagrangian method needs additional iterations when mesh becomes too distorted.

Pure Lagrangian: The Pure Lagrangian Method does not require contact stiffness. Instead, it requires penetration control factor and maximum allowable tensile contact pressure. However, this method has long computational time.

Multipoint Constraint: Another method, multipoint constraint algorithm, is used in conjunction with bonded contact and no separation contact to model several types of contact assemblies and kinematic constraints.

In this study, the augmented lagrangian method is chosen because it usually leads to better conditioning and is less sensitive to the magnitude of contact stiffness.

4.4.5. Definition of Static Structural Analysis Settings

Before proceeding to the solution, analysis options should be defined including boundary conditions, analysis type and stepping controls. Analysis setting is about the load to be applied to the structure, including load steps, load magnitude and load direction. For a static structural analysis, there can be one or several load steps. Furthermore, for each load step, several sub-steps might be required to make the solution converge better and results more accurate. Figure 4.17 shows one example of how analysis settings are defined in ANSYS Workbench. The total number of steps, number of sub-steps for the initial step and maximum allowable number of sub-steps are set to 10, 10 and 100 sub-steps, respectively. A maximum force of 269.6 KN is applied to the structure. Having 10 steps, at each step a 26.96 KN incremental load is applied to the structure as shown in Figure 4.17. The software uses the Newton-Raphson iterative algorithm for the solution of equations.

Figure 4.17. Analysis Setting.

Correct definition of boundary conditions is of great importance in the finite element analysis and, depending on the structure, can greatly affect the behavior. Defined boundary conditions are shown in Figure 4.18. 'Fixed Support' in Figure 4.19, means that any movement of the body is restrained. Having made all the above mentioned definitions, the finite element model is ready for solution.
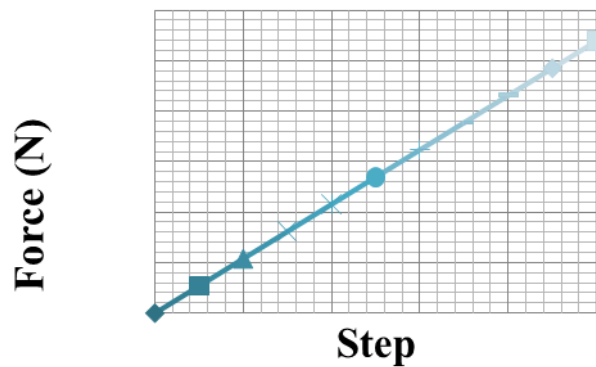
Figure 4.18. Load Diagram for HP260x75 section.
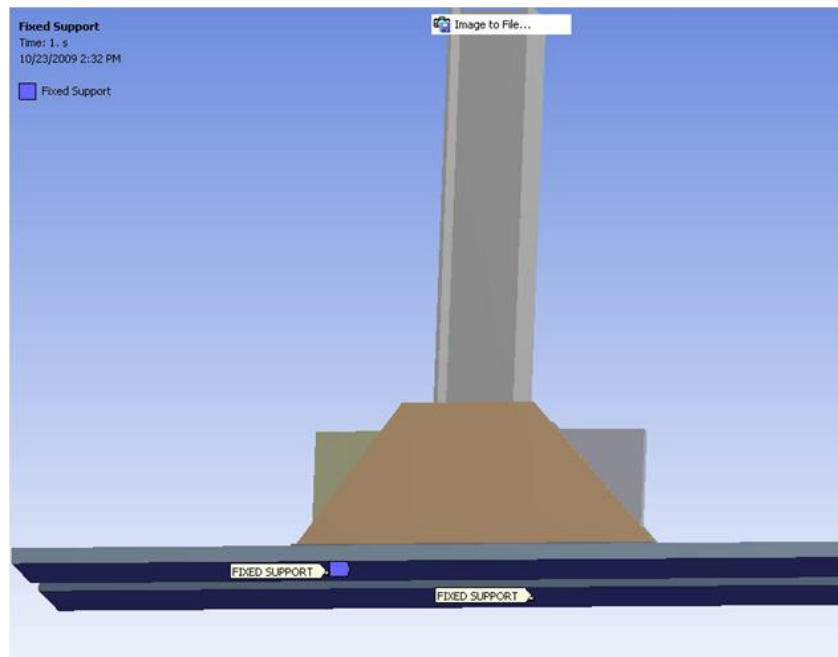
Figure 4.19. Boundary Condition.

4.4.6. Analysis Results

The results obtained from the linear three dimensional finite element analyses are evaluated for the HP220x57 and HP 260x75 sections. The distributions of the axial stresses are shown in Figure 4.20 for the HP260x57 section. The analyses results revealed that high axial stress concentrations exist around the connections of the HP 260x75 section and the 400 mm-high plate of the steel base fixture. The magnitude of these stresses is very high on HP section as noted from the 589 MPa stress value. This is indicative of local damage to HP section. Such local damages may be amplified under cyclic loading. To prevent these local damages (which do not occur in the case of steel H-piles embedded in concrete abutment), steel blocks are used between flanges of the HP section within the steel base fixture and the finite element model is modified accordingly. In the case of the modified finite element model, the presence of the steel blocks between the flanges of the HP section within the steel base fixture results in a more even distribution of stresses as shown in Figure 4.21. This results in a more uniform stress distribution over the

flanges of the steel HP sections (e.g. the stress is reduced from from 676 to 338 MPa for the   HP220x57 section as shown in Figure 4.22). Consequently, it is expected that the modified-test set up with steel blocks between flanges of the HP section will offer a better experimental set up for the HP220x57 and HP 260x75 sections. Stress distributions for these sections are shown in Figure 4.23 - 4.28.
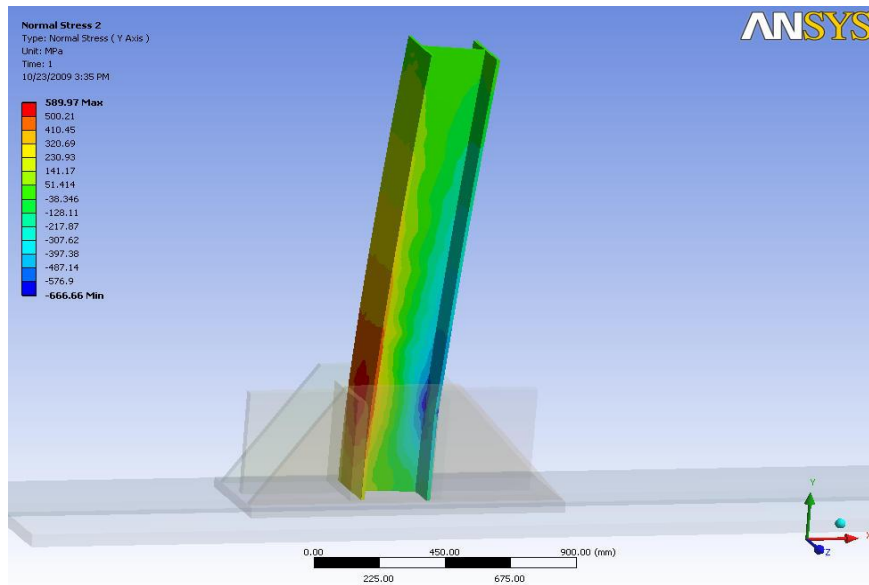
(a)
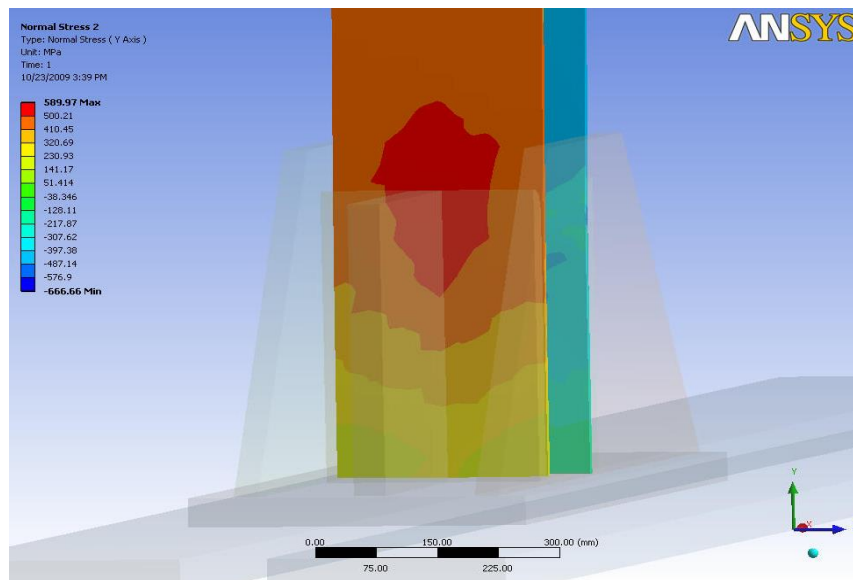
(b)

Figure 4. 20. Axial stresses on HP 260x75 section without blocks at the location of the connection with a maximum stress of 589 Mpa; (a) side view, (b) front view.
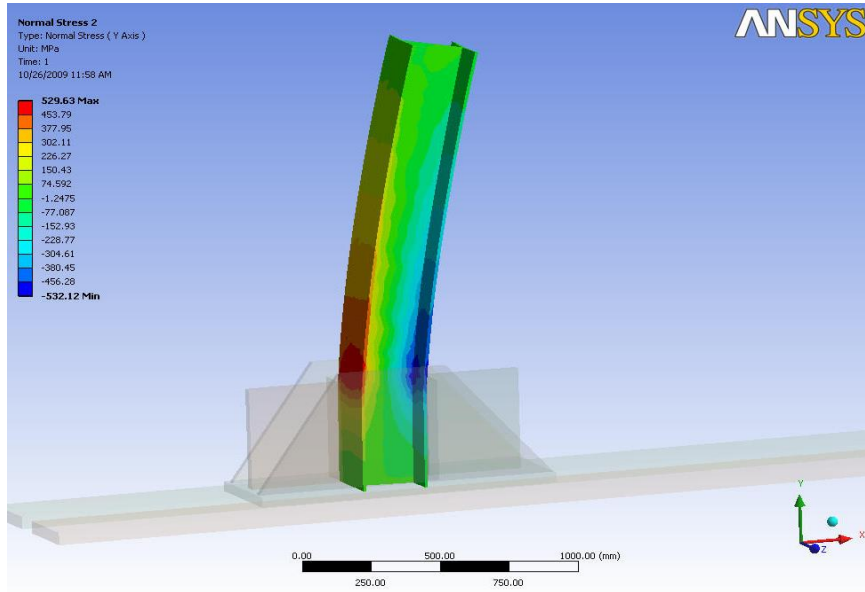
(a)
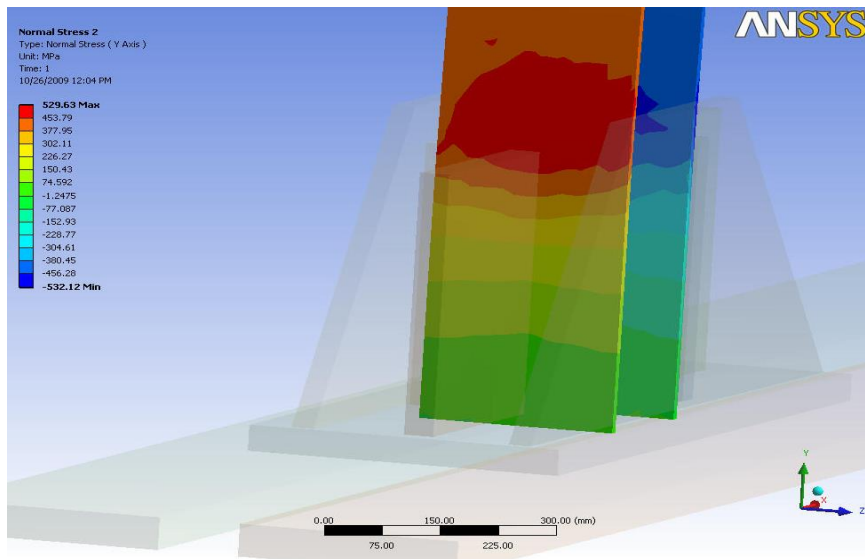
(b)

Figure 4. 21.Axial stresses on HP 260x75 section with block at the location of the connection with a maximum stress of 529 Mpa; (a) side view, (b) front view.

86
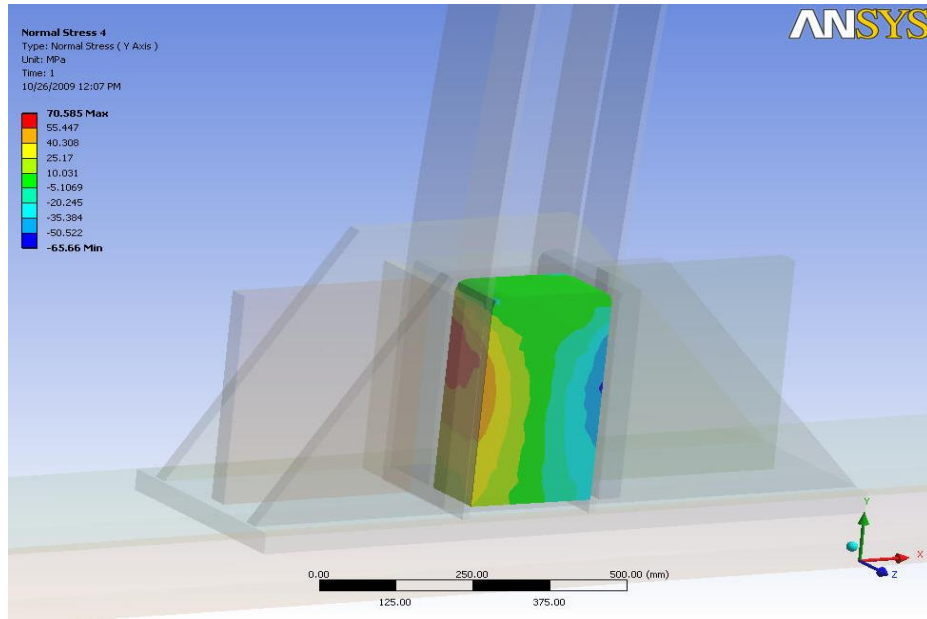
(a)
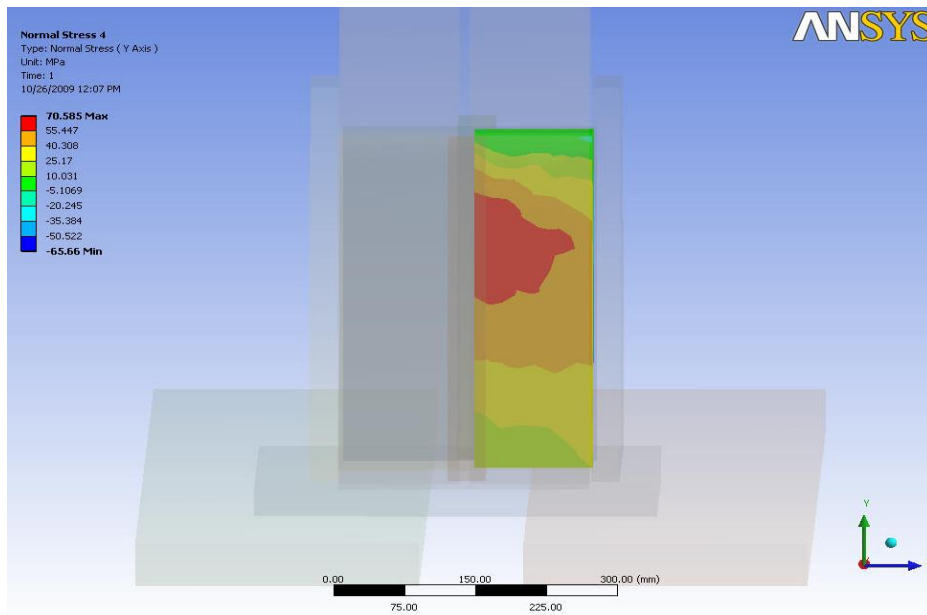
(b)

Figure 4.22. Axial stresses on block at the between flanges for HP 260x75; (a) side view, (b) front view.

(a)   (b)
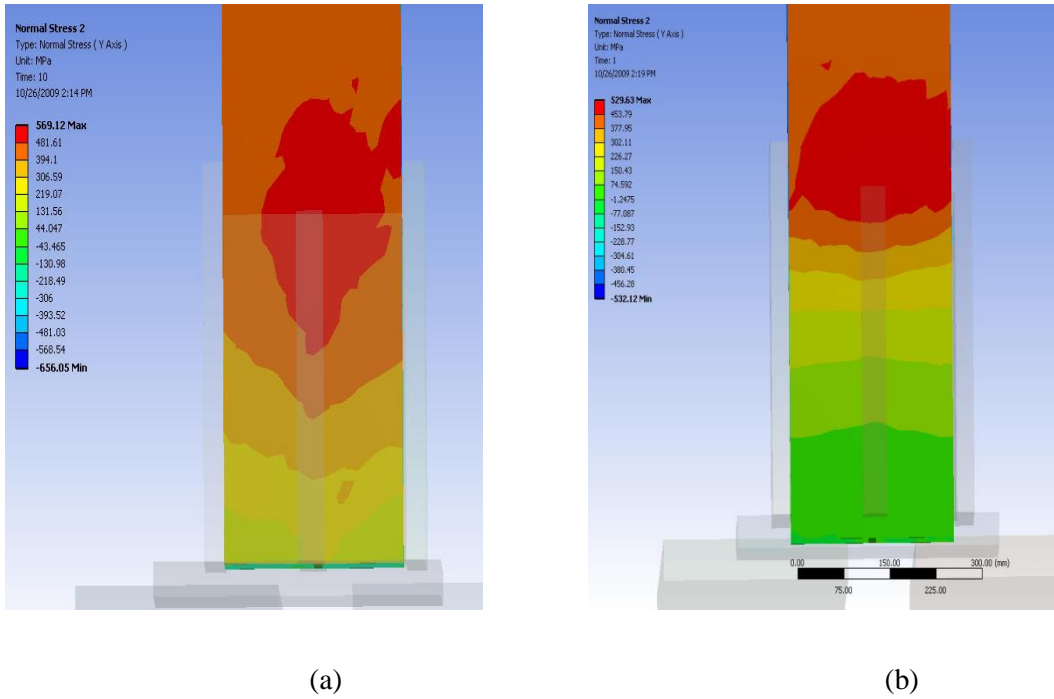
Figure 4.23. Comparison of the axial stresses; (a) HP section without block, (b)
HP section with block.
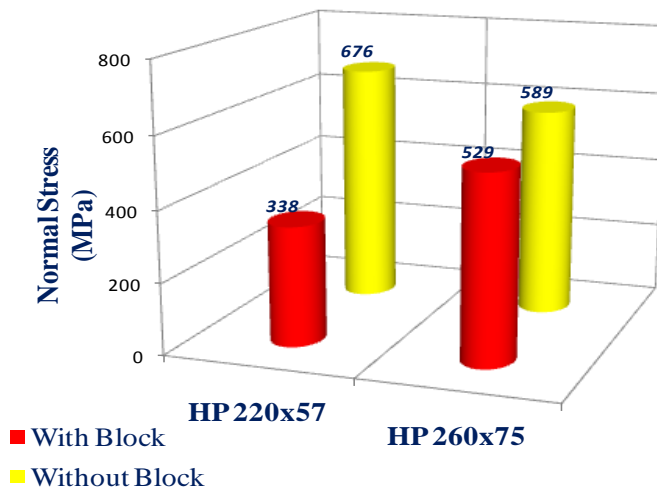
Figure 4.24. Comparison of finite element analyses results with block and
without block.
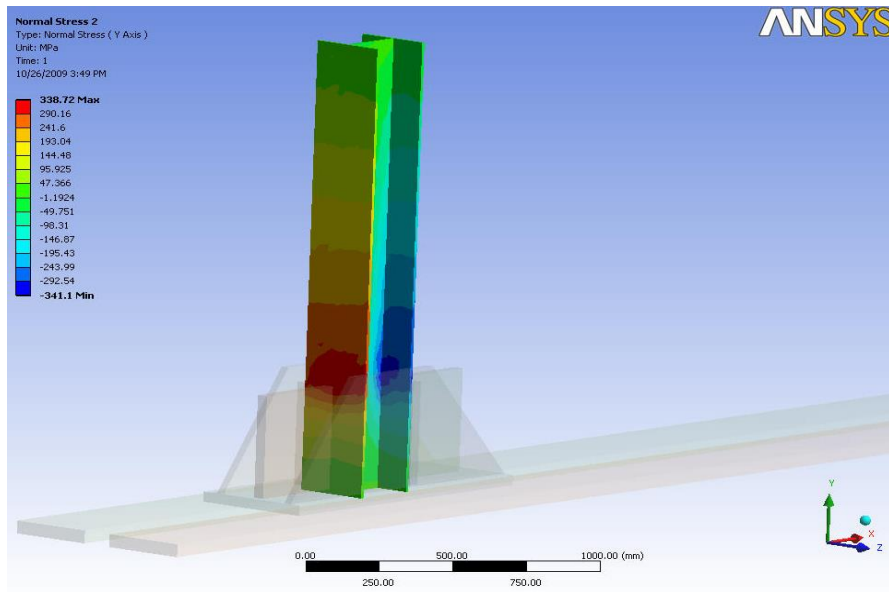
(a)
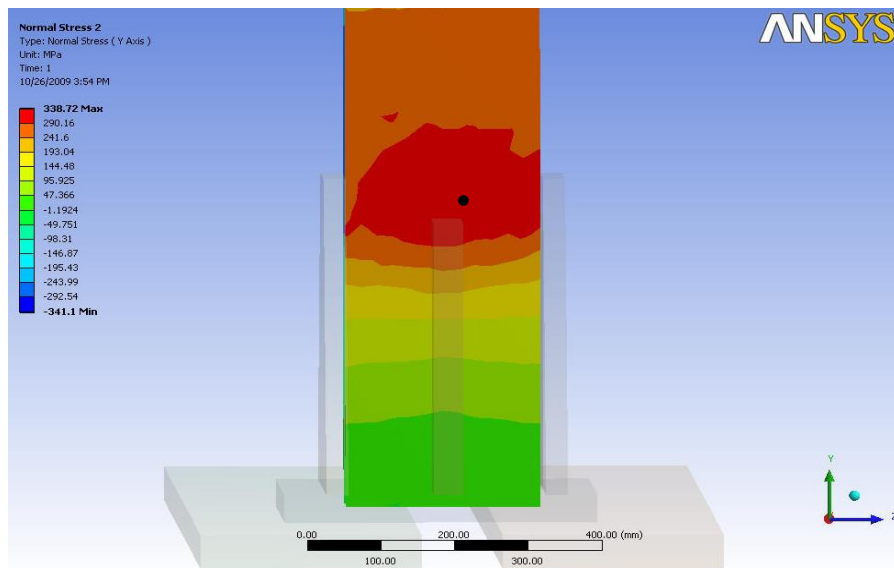
(b)

Figure 4.25.   Axial stresses on HP 220x57 section at the location of the connection with a maximum stress of 338 Mpa; (a) side view, (b) front view.
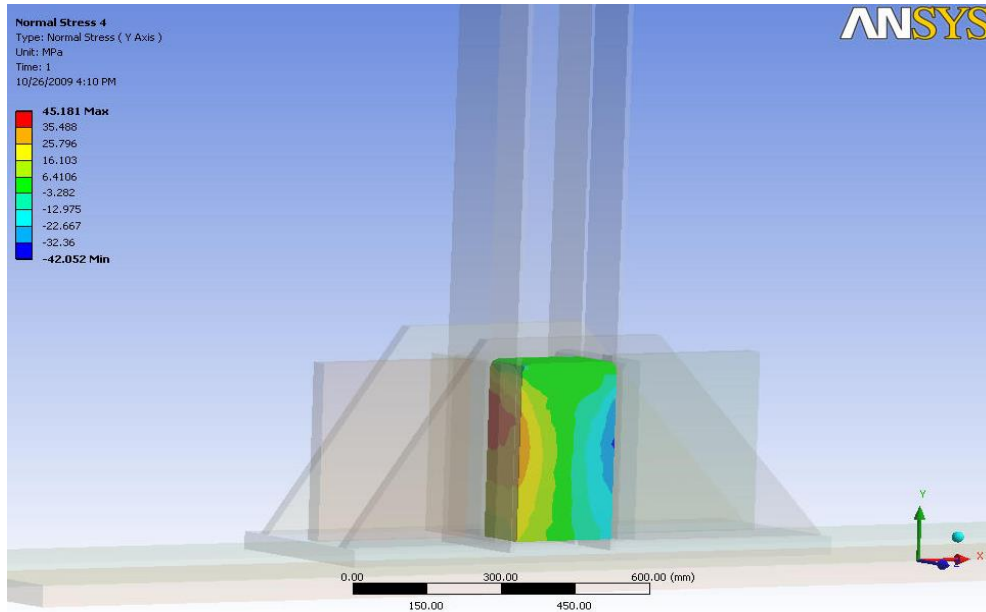
(a)
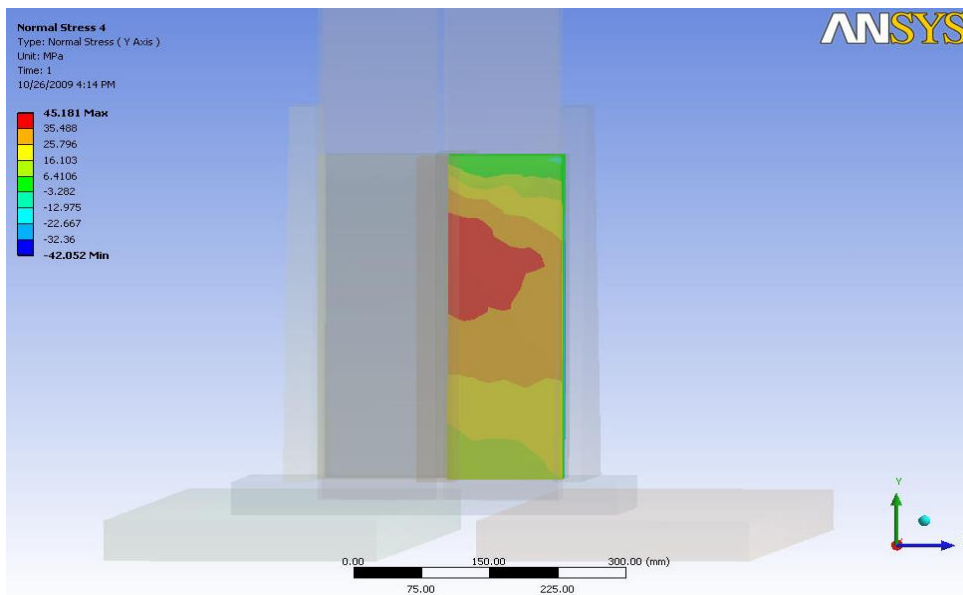
(b)

Figure 4.26. Axial stresses on block at the between flanges for HP220x57; (a) side view, (b) front view.
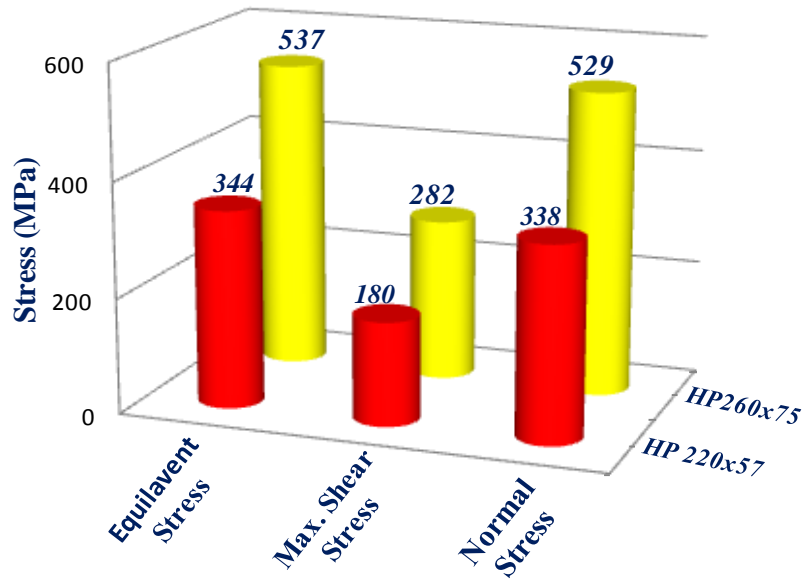
Figure 4.27. Finite element analyses results for different HP sections.
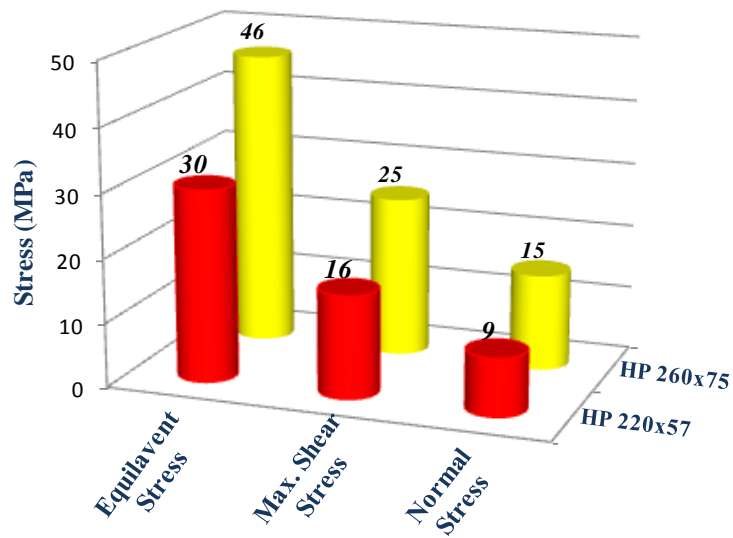
Figure 4.28. Finite element analyses results for different on lateral support.

4.4.7. Nonlinear Finite Element Model

The main objective of the nonlinear finite element analyses is to determine stress, strain and displacements in the HP sections and the steel base fixture. Among the two major types of nonlinearity, namely, material nonlinearity and geometric nonlinearity, material nonlinearity is considered in this study. Nonlinear static analyses produce more accurate stress results than linear static analyses for models where the loading results in concentrated stress values beyond the material yield point. Based on these analyses results, proper locations for the installment of strain gages in the HP sections are determined.

A finite element modeling procedure similar to that of linear finite element model is followed. However, the material model is chosen to define the yield point and post-yield behavior of the steel. Details about the material model used in the analyses are given below.

4.7.1. Material model

There are many material models to describe the elasto-plastic behavior of the materials. Each model has its characteristic. Because of this, it is very important to understand the theory associated with each model before using it in ANSYS. Followings are the bilinear/multi-linear material models used in ANSYS.

Bilinear Kinematic Hardening: The Bilinear Kinematic Hardening option assumes the total stress range is equal to twice the yield stress, so that the Bauschinger effect is included. This option is recommended for general small-strain use for materials that obey von Mises yield criteria. It is not recommended for large-strain application.

Multilinear Kinematic Hardening: The Multilinear Kinematic Hardening option uses the Besseling model so that the Bauschinger effect is included.

Bilinear Isotropic Hardening: The Bilinear Isotropic Hardening model uses the von Mises yield criteria coupled with an isotropic hardening assumption. It is called bilinear because just two lines define the stress-strain curve; one to describe the linear elastic region and another to describe the plastic region as shown Figure 4.28. This option is often preferred for large strain analysis.

Multilinear Isotropic Hardening: The Multilinear Isotropic Hardening option is like the bilinear isotropic hardening option, except that a multilinear curve is used instead of a bilinear curve. This option is not recommended for cyclic or highly non-proportional load histories in small-strain analyses. It is, however, recommended for large strain analyses.

In this study the Bilinear Isotropic Hardening model is used because just two lines define the stress-strain curve; one to describe the linear elastic region and another to the plastic and it is recommended for large strain analyses, which is the case in this research study. In the material model, the yield strength is assumed as 340 MPa (as obtained from the tensile tests of the steel coupons cut from the pile specimens) with a post-elastic hardening of 4%
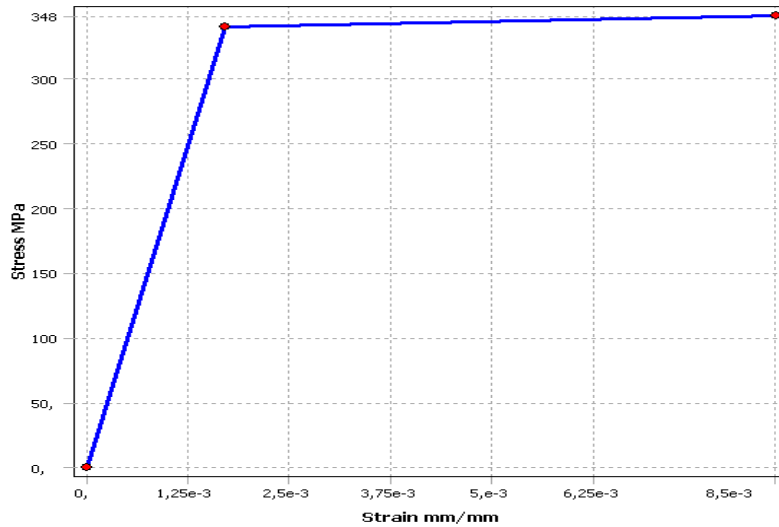
Figure 4.29. Bilinear isotropic hardening.

4.4.8. Definition of Structural Analysis Settings

To apply the displacement on the top of the HP profile, a lateral displacement is implemented over the entire top surface of the HP profile in the ANSYS software. The lateral displacement can be simulated using the ANSYS displacement step option. Displacement step option may be used when the incremental displacement is considered. The number of displacement steps depends on the user's definition. In this case, displacements are defined according to the actual displacement steps that will be applied during the test. A solution is obtained by solving several sub-steps in each displacement step to attain convergence. In each sub-step, an iteration procedure is carried out until providing a convergent solution before moving to the next sub-step. The number of the sub-steps taken in the analysis may improve the accuracy of the solution. It will, however, sometimes be very time-consuming when too many sub-steps are taken. To avoid this problem, ANSYS offers an alternate automatic time step option to reduce the computational time required in the analysis. Accordingly, this option is selected sue to the advantage it offers. When the automatic time step option is selected, it will automatically resize the number of sub-steps in each load step when it fails to

94

reach a convergent solution. This process keeps repeating until it provides a convergence value.

Figure 4.30 shows one example of how analysis settings are defined in ANSYS. The total number of steps, number of sub-steps for the initial step and maximum allowable number of sub-steps are set to 12, 12 and Auto Time Stepping, respectively. A maximum displacement of 120 mm is applied to the structure. Having 12 steps, at each step a 10 mm incremental displacement is applied to the structure.
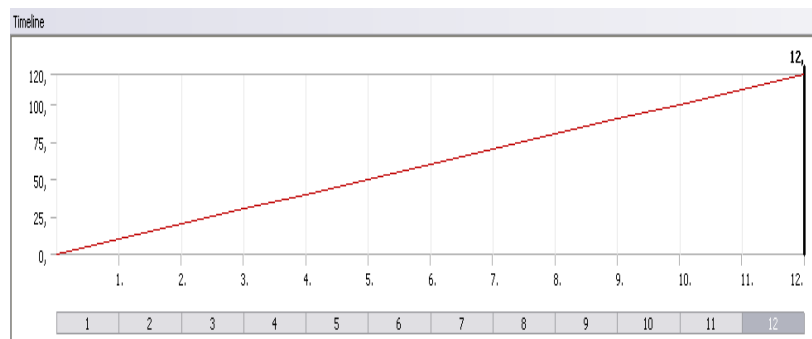
Figure 4.30. Analysis Setting

The results obtained from the nonlinear three dimensional finite element analyses for the HP 260x75 sections are shown in Figures 4.30 - 4.42 in terms of the equivalent Von-Misses stresses. As observed from the figures, flexural yielding occurs (the maximum stress occurs just above the base fixture when strain hardening is considered) just above the base fixture and penetrates further down. This yielding phenomenon had already been expected. The placement of strain gauges will be done accordingly where they will be placed on the steel H-pile just above the base fixture.
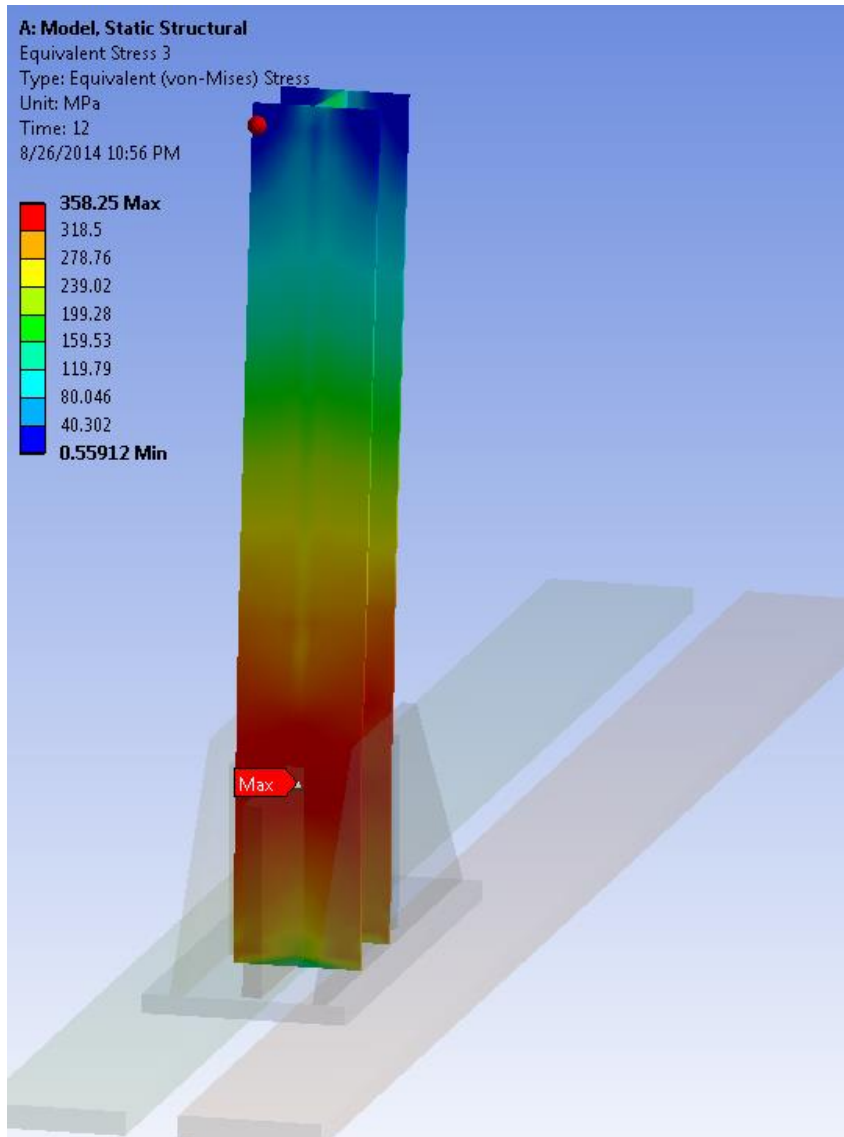
(a)

Figure 4.31. Equivalent (Von-Mises) stress on HP 260x75 section; (a) front view.

96
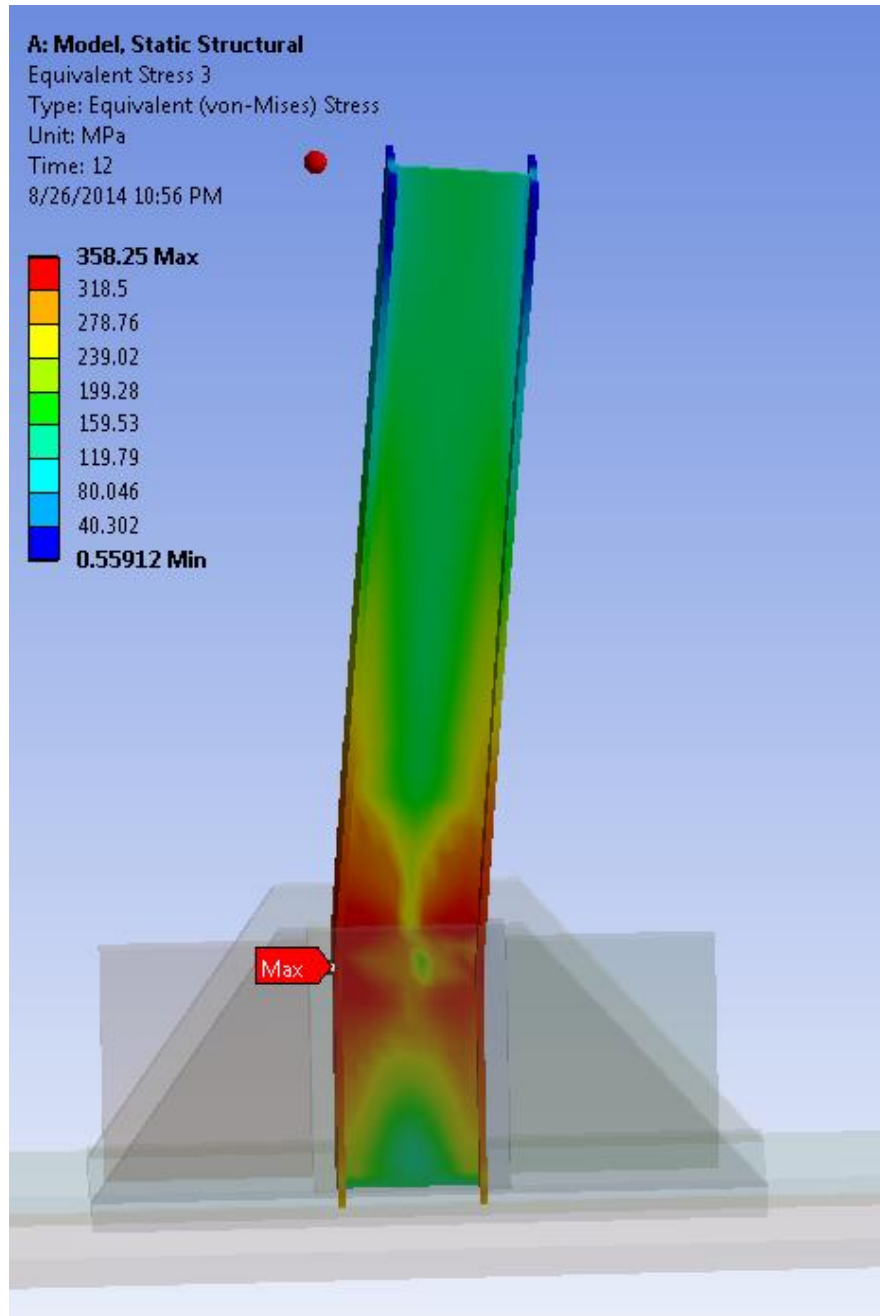
Figure 4.32. Equivalent (Von-Mises) stress on HP 260x75 section; (b) side view.
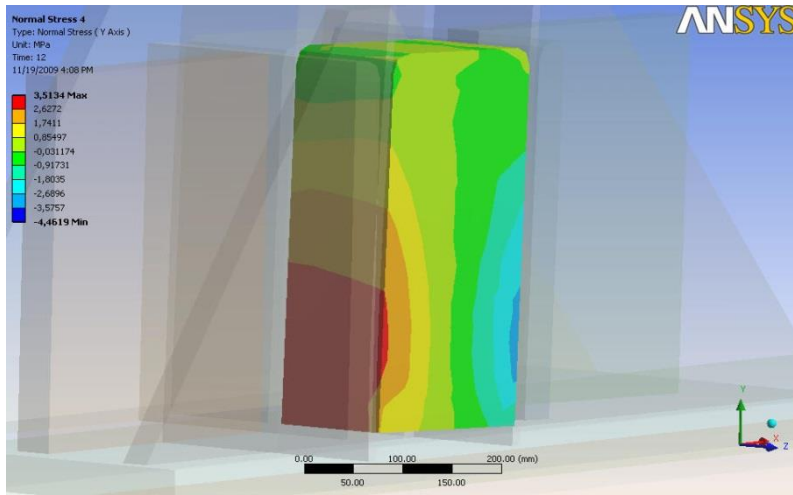
Figure 4.33. Normal stress on block at the between flanges for HP260x75.
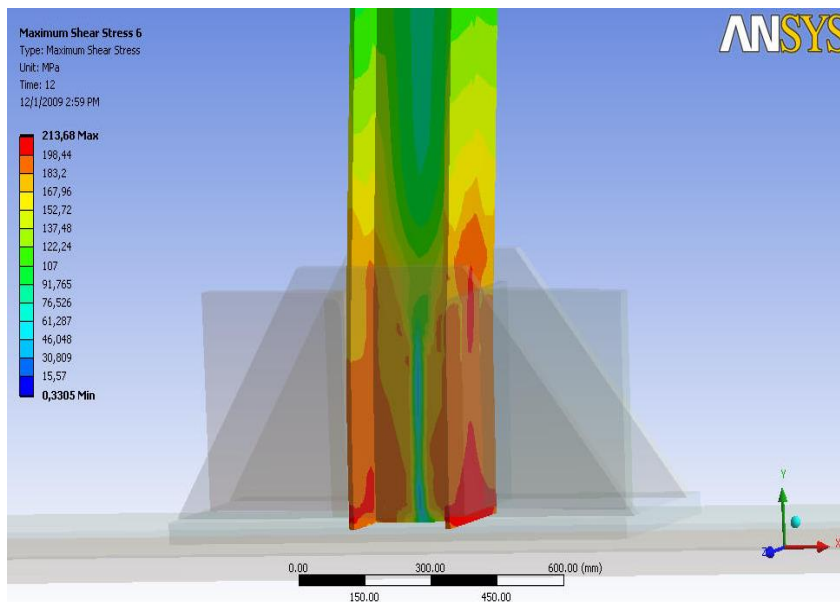
Figure 4.34. Maximum shear stress on HP 260x75.
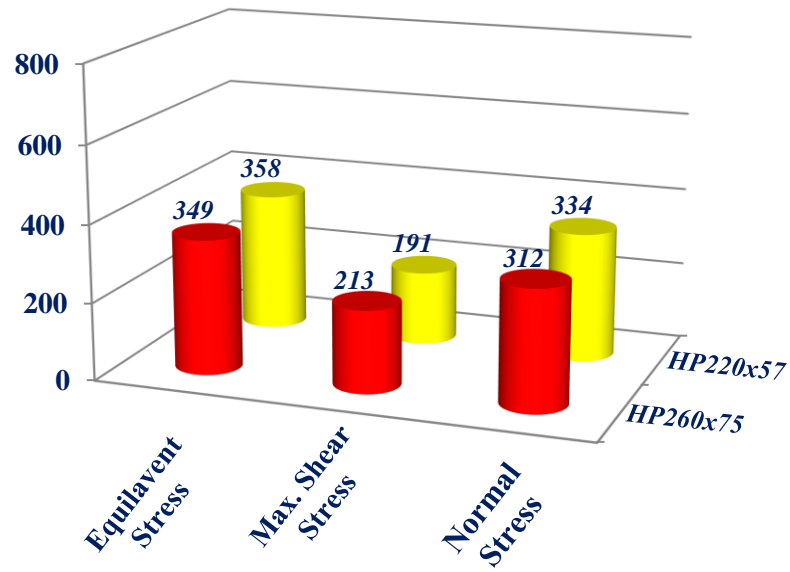
Figure 4.35. Finite element analyses results for different HP sections.
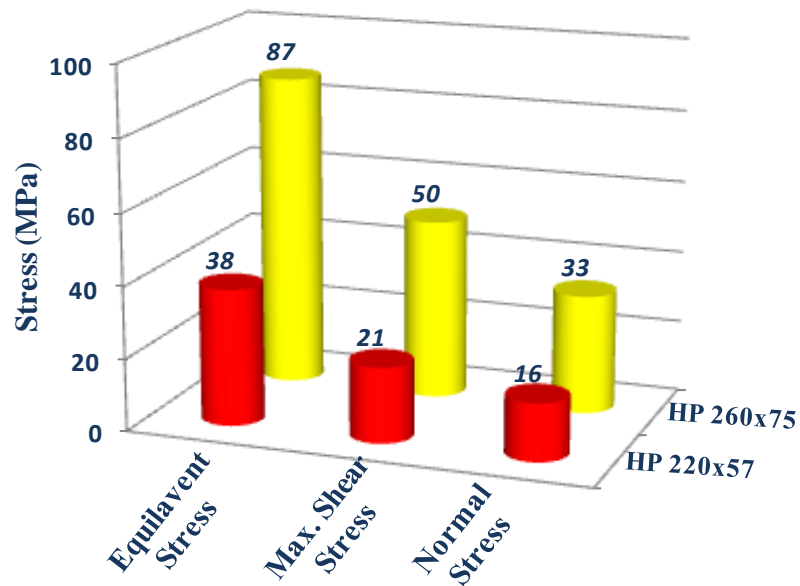
Figure 4.36. Finite element analyses results for lateral support.

CHAPTER 5

TENSILE TESTS

Tensile tests of the HP sections are conducted to determine the mechanical (material) properties for the numerical studies. The mechanical properties of materials used in engineering are determined by tests performed on small specimens of the material. The tensile test is the most widely used test to determine the mechanical properties of materials. Although many important mechanical properties of a material can be determined from this test, it is used primarily to determine the relationship between the average normal stress and average normal strain in many engineering materials such as metals, ceramics composites. To perform the tension test, a specimen of the material (steel coupon) is made into a *"standard"* shape and size.

5.1. Test Specimen Geometry

Standard tensile test is performed according to ASTM E 8M–04, "Standard Test Methods for Tension Testing of Metallic Materials". These specimens can be machined into cylindrical samples or flat plate samples. Test samples must have a specific ratio of length to width or diameter in the test area to produce repeatable results and comply with standard test method requirements. According to the standard; recommended dimensions for test specimens are presented in Figure 5.1 and Table 5.1.
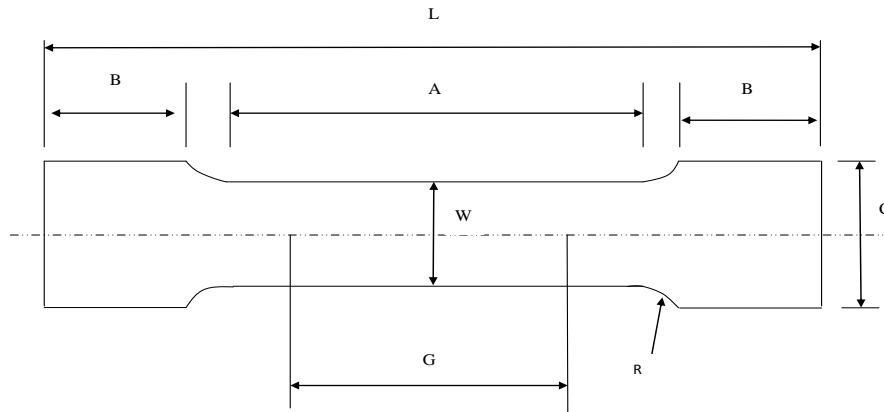
Figure 5. 1. Rectangular Tension Test Specimen.

Table 5. 1. Tension Test Dimensions.

	DIMENSIONS			
	Standard Specimens		Subsize Specimen	
	Plate Type, 40-mm Wide			
	200-mm Gauge Length	**50-mm Gauge Length**	**Sheet- type, 12.5-mm Wide**	**6-mm Wide**
G-Gauge Length	200±0.25	50±0.10		
W-Width	40+3 -6	40+3 -6	12.5±0.25	6.25±0.05
T-Thickness	Thickness of Material			
R-Radius of fillet	13	13	13	6
L-Overall length	450	200	200	100
A-Length of reduced section	225	60	60	32
B-Length of grip section	75	50	50	32
C-Width of grip section	50	50	20	10

Test- specimens with the above defined geometry are cut from the web and flanges of the HP sections used in the experimental study. The cutting process of the test specimens from the HP sections using CNC (Computer Numerical Control) method using laser cutting technology are shown in Figure 5.2. The test specimens as shown Figure 5.3 are rectangular sections of 400 mm total length and a gage length of 200 mm of S275 steel.

Figure 5.2. Cutting process of standart test speciment with CNC method.

(a)   (b)

Figure 5.3. Tension Test Specimen, (a) HP220x57, (b) HP260x75.

5.2. Test Setup and Equipment

The universal testing machine TF-H1000 (Figure 5.4), is used for testing of the specimens. The machine is used for testing metallic and composite materials in either tension or compression and has a testing capacity of 1000 kN, a crosshead speed range of 5 to 40 mm/min with an accuracy of 0.1%. Other equipment used are; digital calipers and data acquisition system.

Figure 5.4. Universal Testing Test Machine.

5.3. The Objective of Tension Test

The objective of this experiment is to determine the following properties for the two different steel HP sections (HP220x57 and HP260x75) using standard test specimens cut from the test speciments. These parameters are;

- The tensile strength (UTS)
- Yield strength or yield point (σ_y)
- Elastic modulus (E)
- Percent elongation ($\Delta L\%$)

5.4. Test Procedure

The testing is carried in accordance with ASTM E 8M–04 as shown Figure 5.5. The procedure is as follows;

- Identify the material for each specimen.
- Mark off nearly 10-cm gage length on each specimen
- Measure the initial dimensions of each specimen.
- Fixing the specimen in the tensile machine using standard mechanical pneumatic clamps of universal testing machine TF-H1000, attaching the extensometer, recording applied load and resulting deflection and load at failure.
- The speed of test (velocity of separation of the cross heads of the testing machine) is set to a constant speed of 5 mm/min and then the tension test is started.
- Load, stress and strain data for each tensile test are recorded so that a plot of the stress-strain curve can be generated.
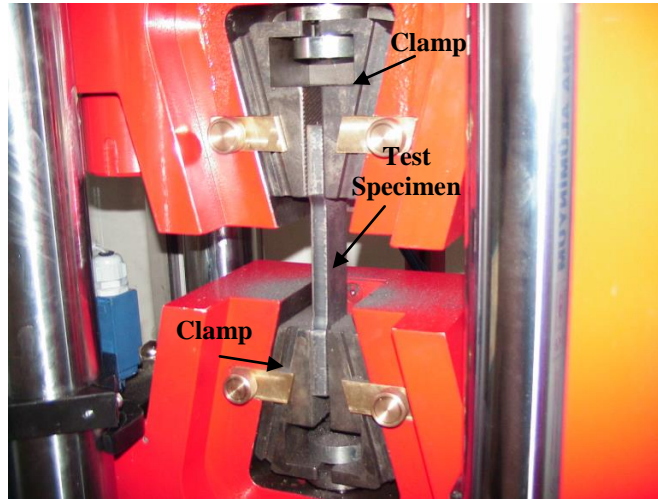
Figure 5.5. Tensile test specimen.

5.5. Test Results

The load and strain data are taken until the failure of the specimens take place. Figure 5.6 shows the geometric configurations of the broken sheet specimen at the end of the test. These data are used to calculate the ultimate tensile strength of the specimens, and at the same time, converted into stress vs. strain graphs. These graphs are then used in determination of the modulus of elasticity of the specimens. For this purpose, the slope of the elastic region of these curves is determined by fitting a straight line, with the minimum least-square method. Stress-strain graphs plotted in MS Excel Software are shown Figure 5.7. Using the stress-strain graphs, in this study, average value of elasticity modulus is determined as 200,000 Mpa. The yield strength is determined as 306 MPa for HP220x57 steel section and 340 MPa for HP260x75 steel section (Figure 5.8). The ultimate strength is determined as 421 MPa for HP220x57 steel section and 443MPa for HP260x75 steel section (Figure 5.8).

Figure 5.6. Tension test specimen after test.

(a) (b)
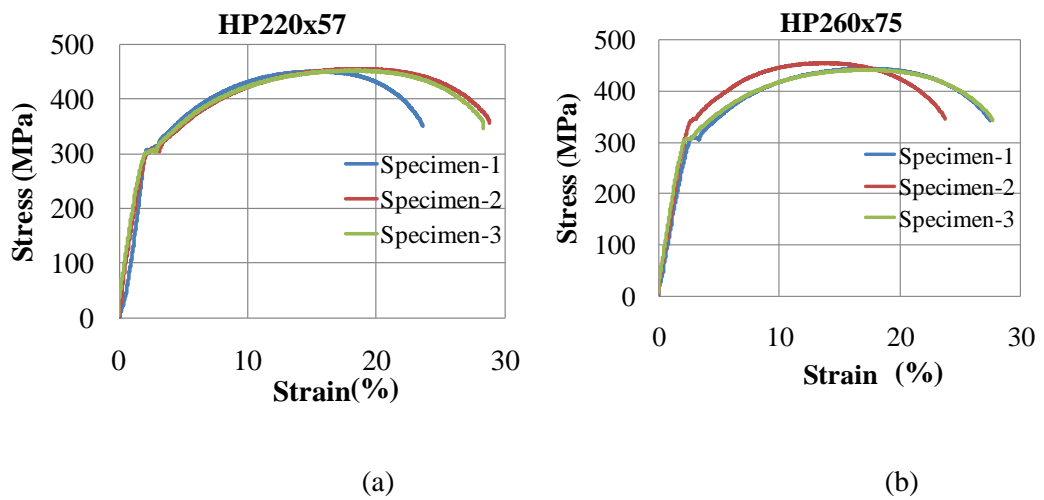
Figure 5.7. Stress-Strain Graph of Tensile Test; (a) HP220x57, (b) HP260x75.

107
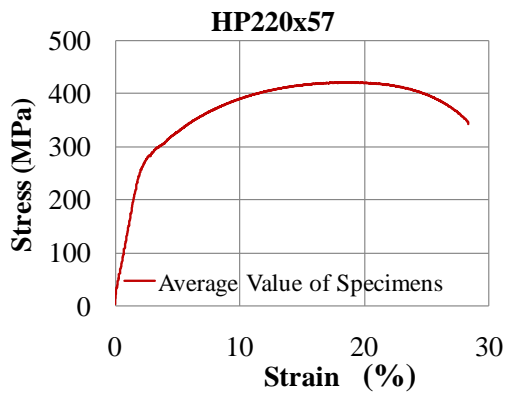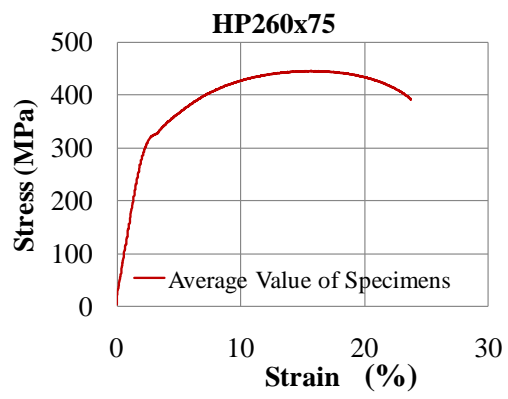
Figure 5.8. Average Value of Stress-Strain Graph of Tensile Test; (a) HP220x57, (b) HP260x75.

CHAPTER 6

FATIGUE TESTS OF HP PILES

This chapter describes the numerical studies conducted to estimate the displacement of the steel H-pile specimens required to determine the stroke of the actuator for the experimental test setup and the test set up itself. Accordingly, in the following subsections, first the details and results of the aforementioned numerical study is presented. This is followed by a detailed description of the test setup, the fatigue rated actuator system used to apply the lateral cyclic loading, the instrumentation plan, the data acquisition equipment and the data analysis techniques. Next, the types of low cycle tests and test parameters are described. Subsequently, the test results are presented in detail.

6.1. Moment Curvature Relationships

In this phase of the research study, first the moment-curvature relationships (MCR) of the steel HP sections used in the experimental testing are obtained. The obtained MCRs are used to estimate the displacement capacity of the steel H-piles under cyclic loading. In the development of MCR, the round corners at the intersection of the web and flanges are assumed as straight. This resulted in an error of less than 1 % in the geometric properties such as cross-section area and plastic modulus. MCRs are obtained for both strong and weak axis bending under an axial load that ranges between 0 to 60 percent of the axial yield capacity, P_y, of the steel H-pile section. Then, a MATLAB code is developed to obtain the moment-curvature relationships for the steel H-pile sections used in the experimental testing. Further details of the moment-curvature relationships are presented in the following subsections.

6.1.1. Section Division

The pile's cross-section is divided into 600 small rectangular strips as shown in Figure 6.1. To estimate the MCR for bending about the strong axis each flange is divided into 150 strips and the web is divided into 300 strips. In the case of bending about the weak axis, each of the flanges is divided into 100 strips above and below the web and the web is divided into 50 strips including portions from the flanges.

6.1.2. Procedure of Moment Curvature Calculation

A total of twenty thousand strain increments are applied at the centroid of the outermost strip on the compression side of the section. The strain at one of the outermost strips, ε_1, is gradually increased from zero to a strain equal to 0.25 at the total of twenty thousand increments.
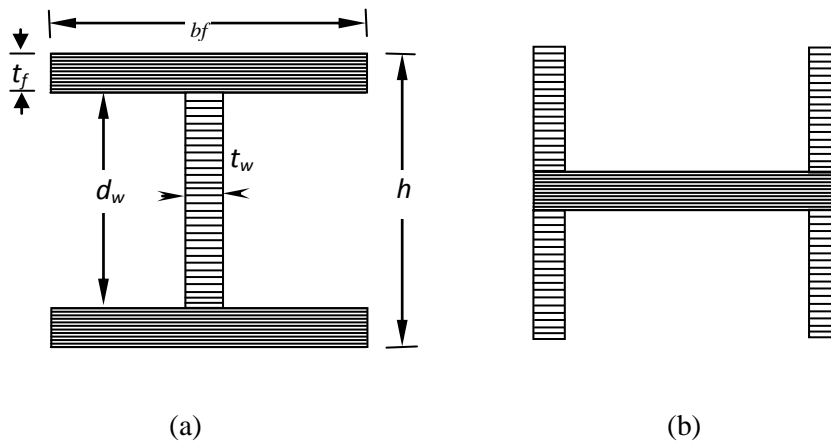
Figure 6.1. Divided sections, (a) Strong axis orientation, (b) weak axis orientation.

At each strain level, strain at the other outermost strip is changed between -0.25 to 0.25 at a total of twenty thousand increments. At each of these assumed strain distributions, stress at each fiber is calculated using monotonic stress-strain data obtained from the tests. Once the stress distribution over the section is at hand, sectional axial force and bending moments are calculated using the following equations:

$$F_i = \sum_{i=1}^{600} A_i * \sigma_i \tag{1}$$

$$M = \sum_{i=1}^{600} \sigma_i * A_i * d_i \tag{2}$$

In which A_i, d_i, σ_i are area, distance from central axis and stress at the ith strip. The results are presented in a large table containing strains at two outermost strips, curvatures, axial force and bending moment values. Using this table, bending moment can be calculated at any assumed value of axial load and curvature through interpolation. The flow chart depicting the above steps for the calculation of moment-curvature relationship is presented in Figure 6.2. The moment-curvature relationship is influenced by the existence of the axial force P. Figure 6.3 shows a series of strain and stress diagrams that correspond to three stages of loading including elastic (no yielding), primary plastic (yielding in compression zone only), and secondary plastic (yielding in both compression and tension zones). The axial force has no effect on the moment-curvature relationship when the section is elastic (Case 1). However, as soon as the section starts to yield, the moment-curvature relationship will be affected by the presence of the axial force (Case 2 and Case 3).

Step1:
Divide section to 600 segments each flange 150, and the Web 300

Step2.a:

Divide the ultimate strain into 20000 increments

Step2.b:
Apply the strain at the compression side gradually starting from 0 to 0.25 strain

Step2.c:

The strain in the other side gradually starting from -0.25 to 0.25 strain

Step3:
Find the stress corresponding to the strain at each segment from σ&ε diagram

Step 4:

Calculate Force F_i at each segment $F_i = A_i * \sigma_i$

Step 5:

Calculate $M = \sum_{i=1}^{600} F_i * d_i$

Step 6: Calculate ϕ

$$\phi_{strong-axis} = \frac{\varepsilon_{top} - \varepsilon_{bot}}{h} \text{ or}$$

$$\phi_{weak-axis} = \frac{\varepsilon_{top} - \varepsilon_{bot}}{b}$$

Step 7: Output
Table containing M, P, ϕ, strains at two extreme strips

Step 8:
For axial load values $=n*P_y$
n=0.0, 0.1, 0.2, 0.3, 0.4, 0.5, and 0.6

Add 0.1Py axial force increment

Add the next increment of strain

Figure 6.2. Flowchart for MCR calculations.

112

STRAIN

$\varepsilon_c < \varepsilon_y$

CENTROIDAL
AXIS

ε

ε_0

Φ

NEUTRAL
AXIS

$\varepsilon_t < \varepsilon_y$

STRESS

$\sigma_c < \sigma_y$

σ

h/2

h/2

M

P

$\sigma_t < \sigma_y$

y

(a) Case 1

STRAIN

$\varepsilon_c > \varepsilon_y$ ε

CENTROIDAL
AXIS

ε

y

$\hat{h}$

ε_0

Φ

NEUTRAL
AXIS

$\varepsilon_t < \varepsilon_y$

STRESS

$\sigma_c = \sigma_y$

σ_y

σ

h/
2

h/
2

M

P

$\sigma_t < \sigma_y$

(b) Case 2

STRAI

$\varepsilon_c > \varepsilon_y$

CENTROIDAL
AXIS

ε

ε

y

$\hat{h}$

ε_0

Φ

$\breve{g}$

NEUTRAL
AXIS

$\varepsilon_t > \varepsilon_y$

STRES

$\sigma_c = \sigma_y$

σ

σ

h/
2

h/
2

M

P

$\sigma_t = -\sigma_y$

(c) Case 3
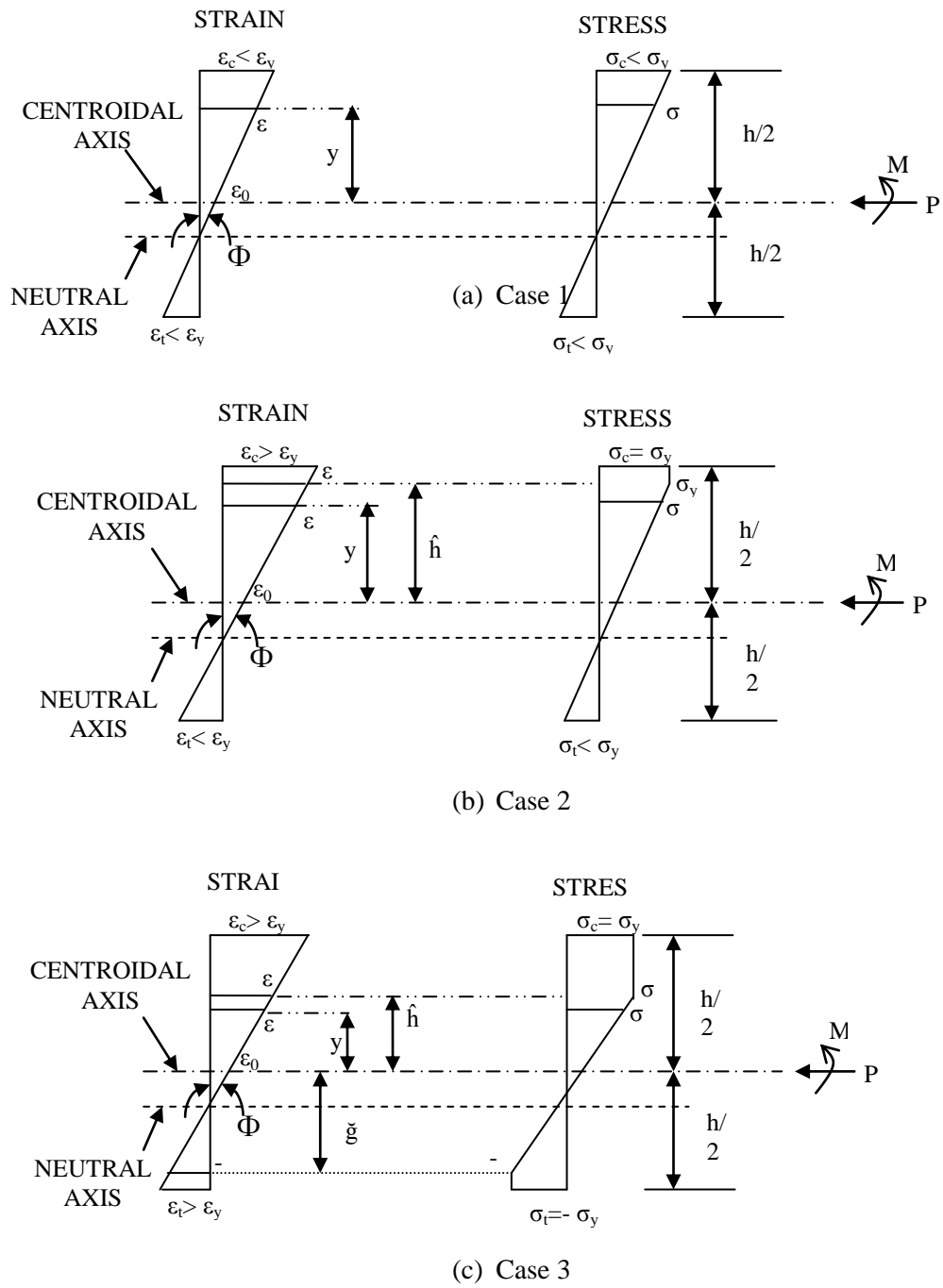
Figure 6.3. Stress and strain diagram.

113

6.2. MCR Results and Analysis

The moment-curvature relationships for both strong and weak axes bending under axial loads ranging from 0 to 60 percent of the axial yield capacity, P_y, of the section are obtained for the two steel HP sections; HP220x57 and HP260x75. The moment-curvature relationships are shown in Figure 6.4-Figure 6.15. Figs.6.4 and 6.7 show the MCR for the HP220x57 section under varying axial loads for bending about the strong and the weak axis, respectively. As expected, both figures imply that the axial load decreases the ultimate moment capacity of the section. Moreover, the reduction in the moment capacity is more critical in bending about the strong axis than it is for bending about the weak axis. For example, for bending about the strong axis, the ultimate bending moment capacity of the pile decreases from 150 kN.m, in case of no axial load, to 62 kN.m under $0.6P_y$ axial load (56 % reduction). However, for bending about the weak axis, the ultimate bending moment capacity decreases from 77 kN.m, in case of no axial load, to 62 kN.m under $0.6P_y$ axial load. This is only a 23 % reduction in the bending moment capacity due to the presence of a large axial load. Fig 6.10 displays the MCR for strong axis bending of the HP260x75 pile section. The above observations are also valid for this section. Figs.6.16 and 6.17 show plastification of the clamped end of the column in the case of HP220x57 section for bending about the strong and the weak axes.

The calculated moment-curvature relationships are employed in moment-area method to obtain the inelastic displacement of the steel H-pile specimens as a function of maximum flexural strain as shown in Figures 6.6, 6.9, 6.12 and 6.15 for various axial load levels. These figures are then used to determine the stroke of the actuator for a predetermined strain level. This allowed us to determine (i) if the stroke capacity of the actuator is adequate for a given strain level, (ii) the level of displacement expected for an assumed strain level while setting up the test at the initial stage.
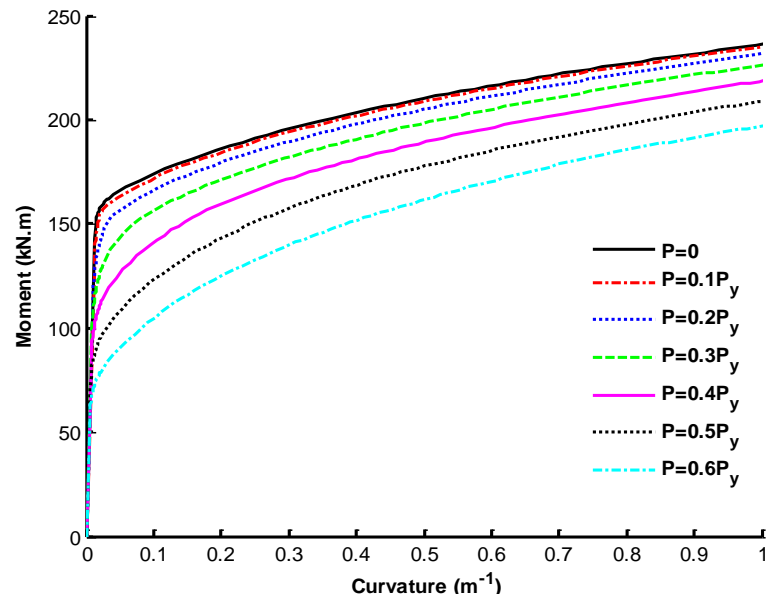
Figure 6.4. The moment-curvature relationship for HP220x57 (Strong axis bending).
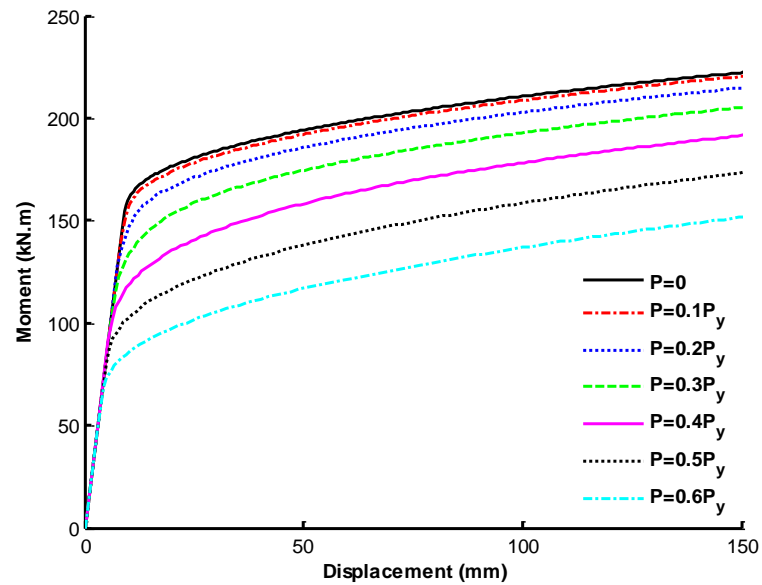
Figure 6.5. The moment-displacement relationship for HP220x57 (Strong axis bending).
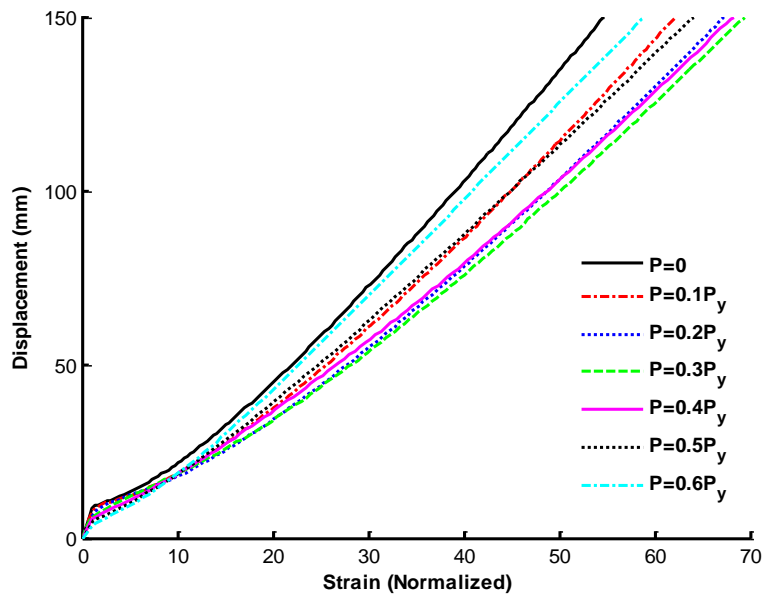
Figure 6.6. The displacement-strain relationship for HP220x57 (Strong axis bending).
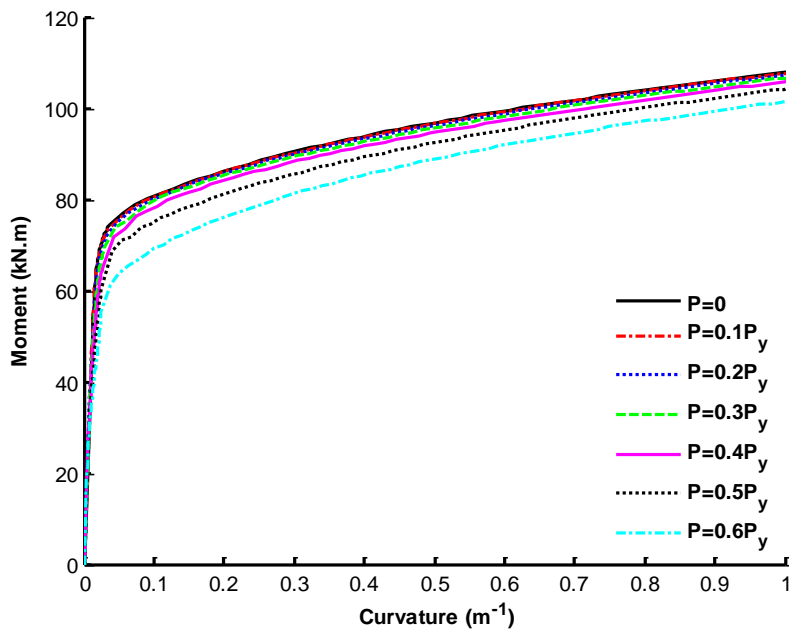
Figure 6.7. The moment-curvature relationship for HP220x57 (Weak axis bending).
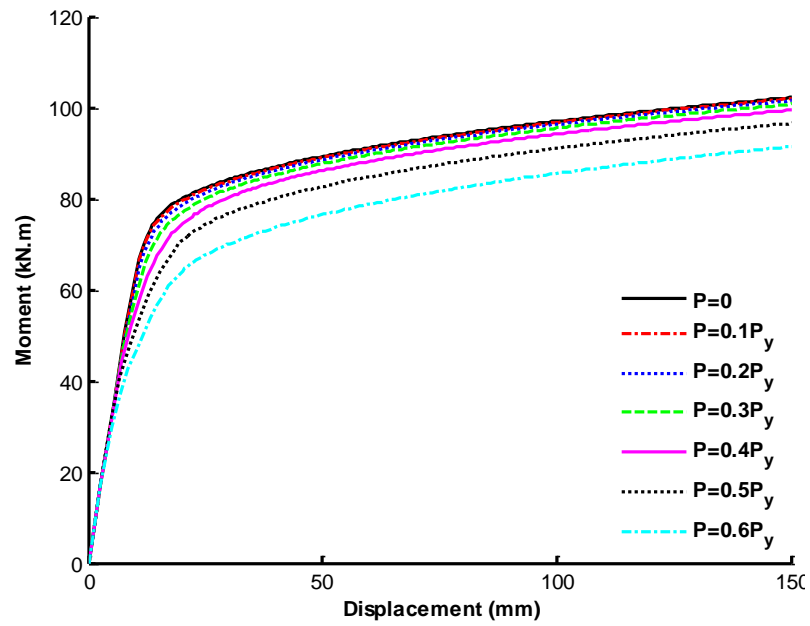
Figure 6.8. The moment-displacement relationship for HP220x57 (Weak axis bending).
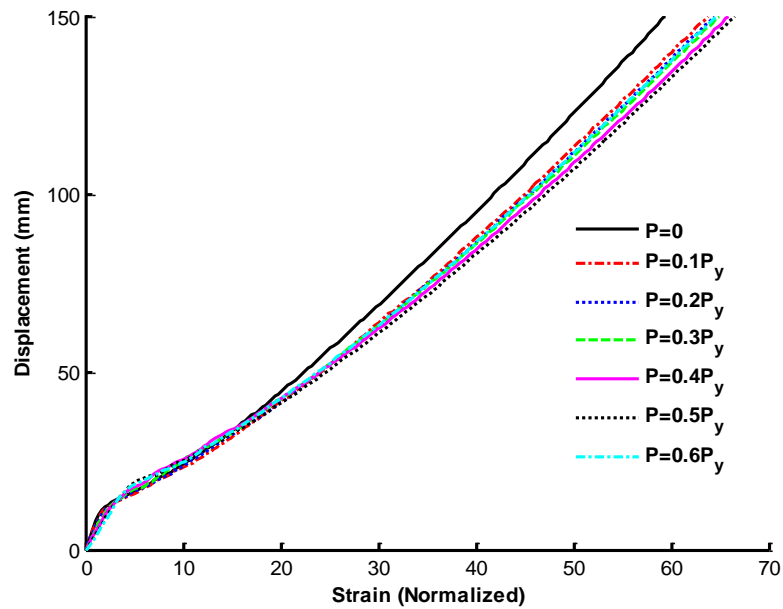
Figure 6.9. The displacement-strain relationship for HP220x57 (Weak axis bending).
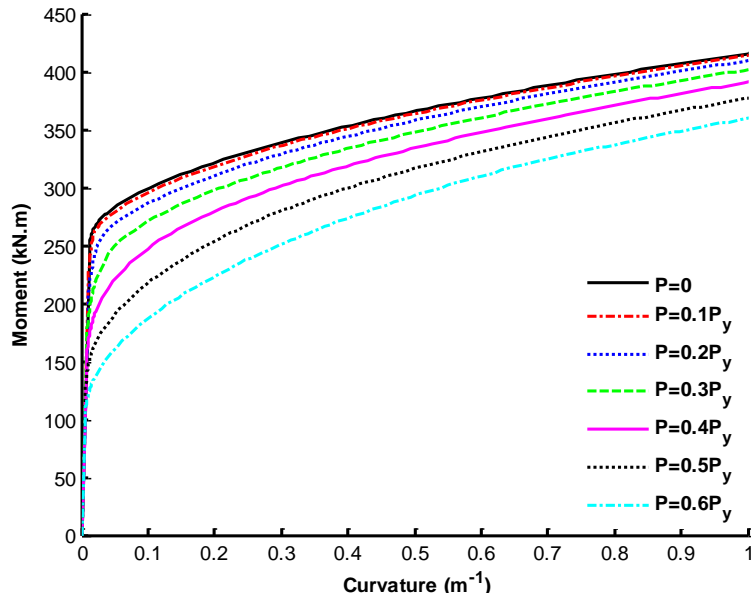
Figure 6.10. The moment-curvature relationship for HP260x75 (Strong axis bending).
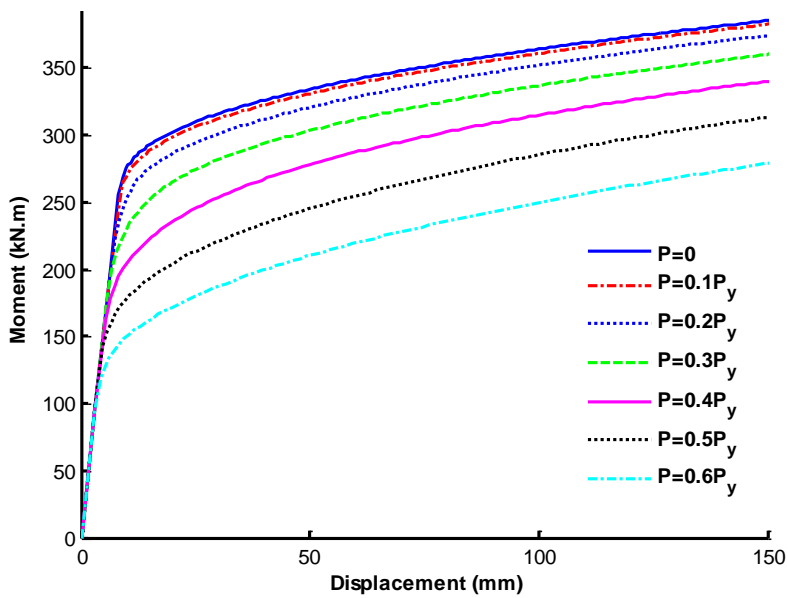
Figure 6.11. The moment-displacement relationship for HP260x75 (Strong axis bending).
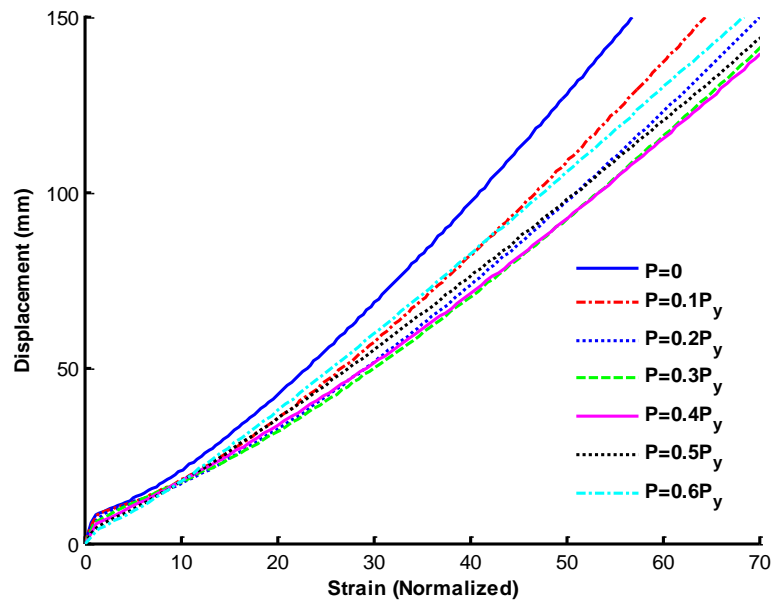
Figure 6.12. The displacement-strain relationship for HP260x75 (Strong axis bending).
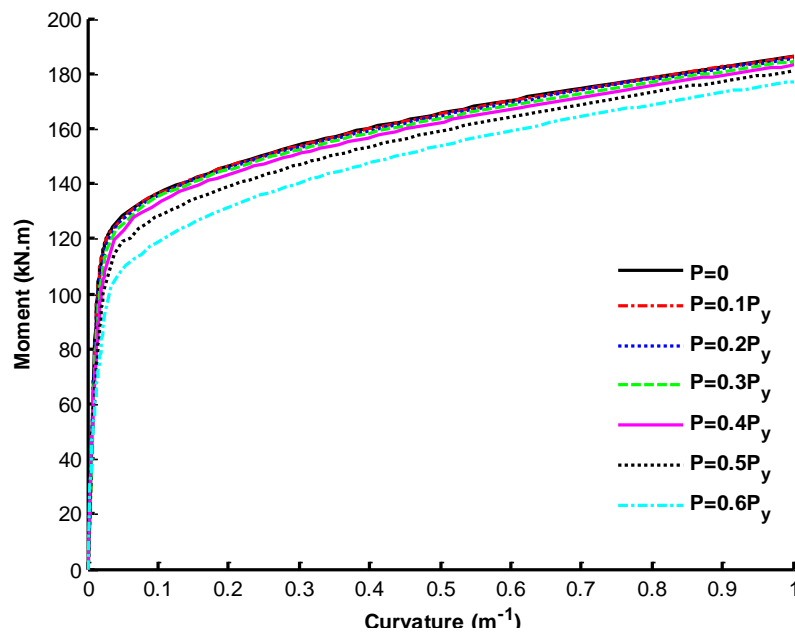
Figure 6.13. The moment-curvature relationship for HP260x75 (Weak axis bending).
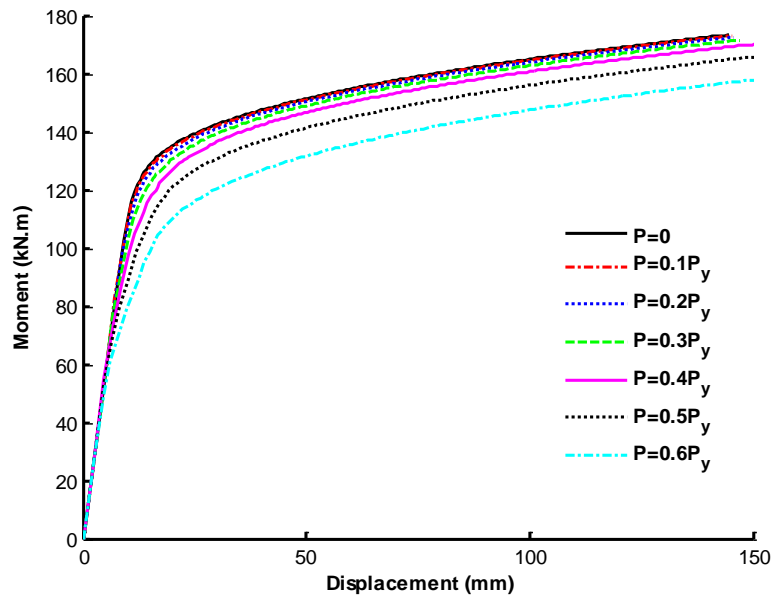
Figure 6.14. The moment-displacement relationship for HP260x75 (Weak axis bending).
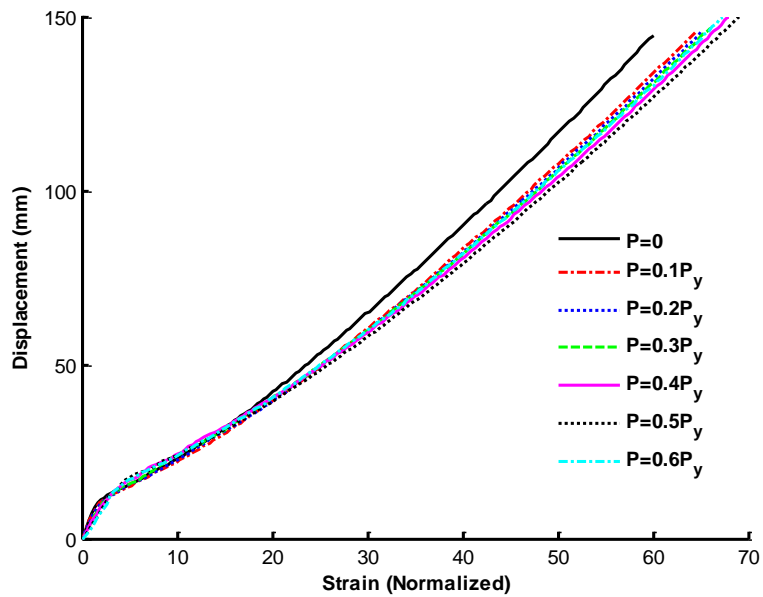
Figure 6.15. The displacement-strain relationship for HP260x75 (Weak axis bending).
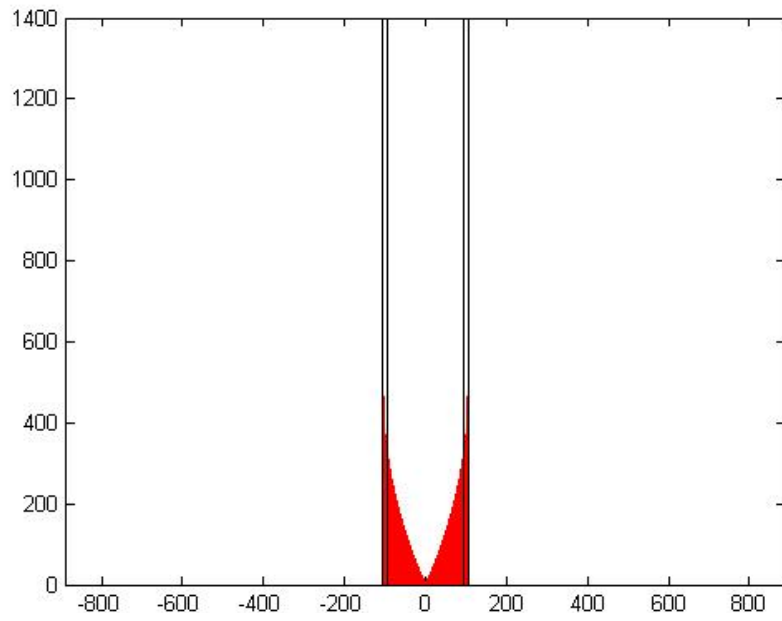
Figure 6.16. Plastic hinge for HP220x57 (Strong axis bending) at 130 mm displacement.
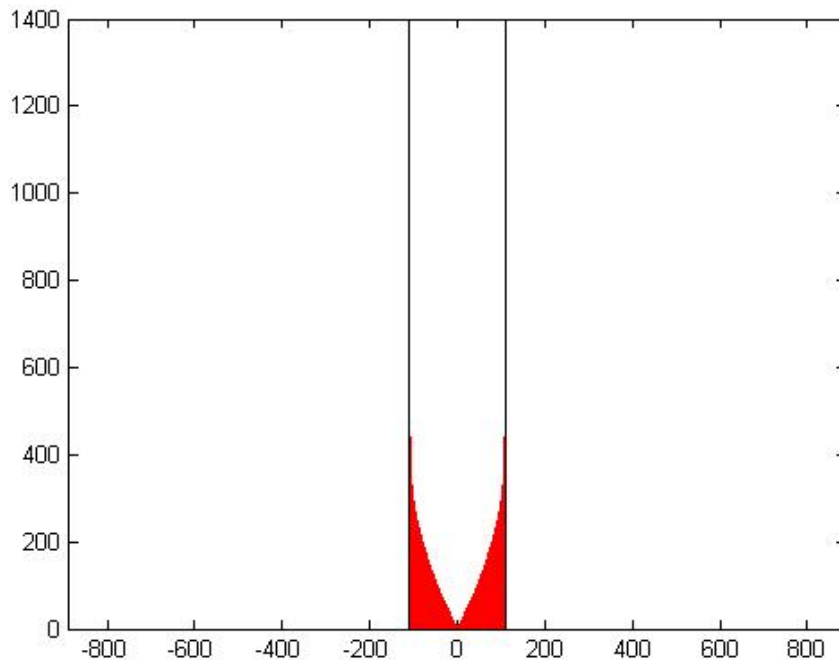
Figure 6.17. Plastic hinge for HP220x57 (Weak axis bending) at 130 mm displacement.

6.3. Test Setup

Preparation of the test setup consists of four main steps;

- Mounting the HP specimens onto the stiff steel base fixture,
- Setting up the lateral cyclic loading system,
- Setting up the vertical static loading system,
- Instrumentation.

6.4. Mounting the HP Specimens onto the Stiff Steel Base Fixture

The present 20 mm diameter holes in the flanges of the testing frame are enlarged to fit the 30 mm diameter bolts as shown in Figure 6.18. The 30 mm diameter bolts are shown in Figure 6.19. Then, the 400 mm-high steel base fixture is attached to the testing frame using 30 mm diameter bolts. The 400-mm-high steel base fixture consists of stiffening steel plates with 50-mm thickness. The 400 mm-high support and bolts pattern are shown in Figure 6.20. The HP section is mounted into the steel base fixture using the available 3 ton crane. The small space between the HP pile and the inner surface of the steel base fixture is eliminated by inserting thin steel sheets.
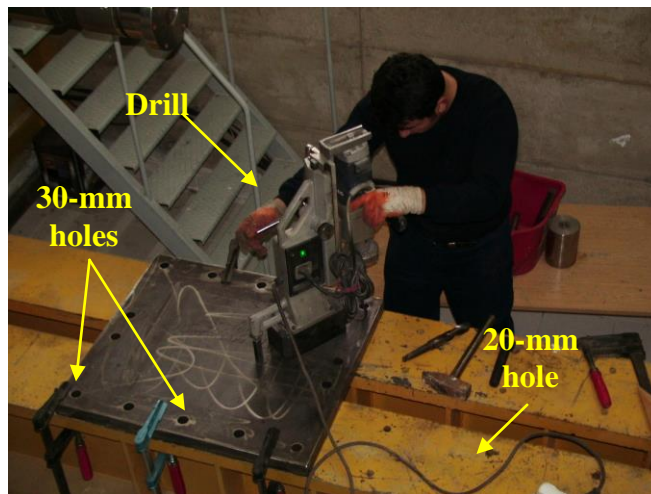
Figure 6.18. Enlarging process.

Figure 6.19. 30 mm diameter bolt.

(a)

(b)

Figure 6.20. Support assembly; (a) side view, (b) upper view.

6.5. Setting up the Lateral Cyclic Loading System

A computer controlled hydraulic actuator capable of applying ±500 KN of load and a stroke of ± 125 mm is used to impose lateral cyclic load. A view of the actuator is shown in Figure 6.21. The system is capable of applying both push and pull forces. The actuator can be used with either load or displacement control.
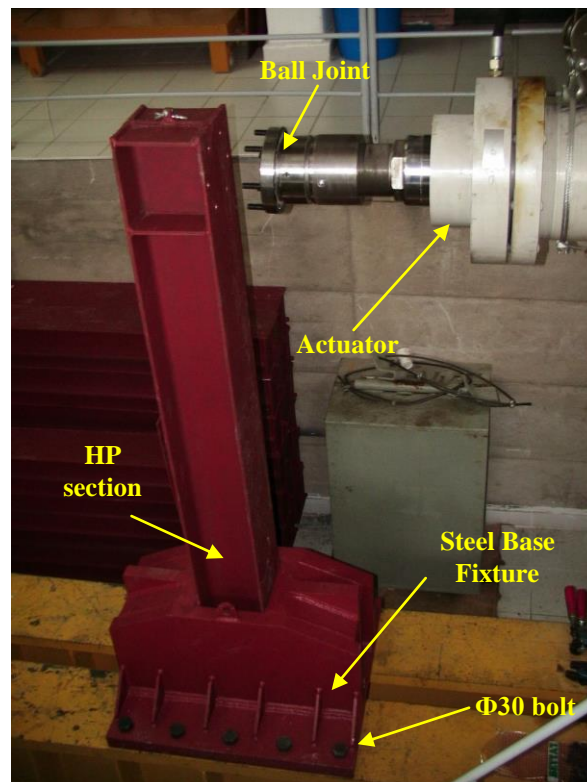
Figure 6.21. Test equipment in laboratory.

A ball joint is designed at the head of the actuator rod to create a three dimensional hinge connection at the column end.

6.6. Setting up the vertical static loading system

The application of the vertical load is obtained through a specially designed system. The vertical load system is consists of four components as shown in Figure 6.22.

- A stiff steel frame
- A single-acting hydraulic ram
- Roller and thin plate
- Vertical load control unit

A stiff steel frame is used to support the vertical loading ram. Vertical load is applied by a single acting hydraulic ram. A single acting hydraulic ram capable of applying +1000 KN of vertical load and a stroke of ± 250 mm is used to impose vertical load. A roller and thin plate with 50-mm thickness mechanism are placed between the HP specimen and vertical load ram.
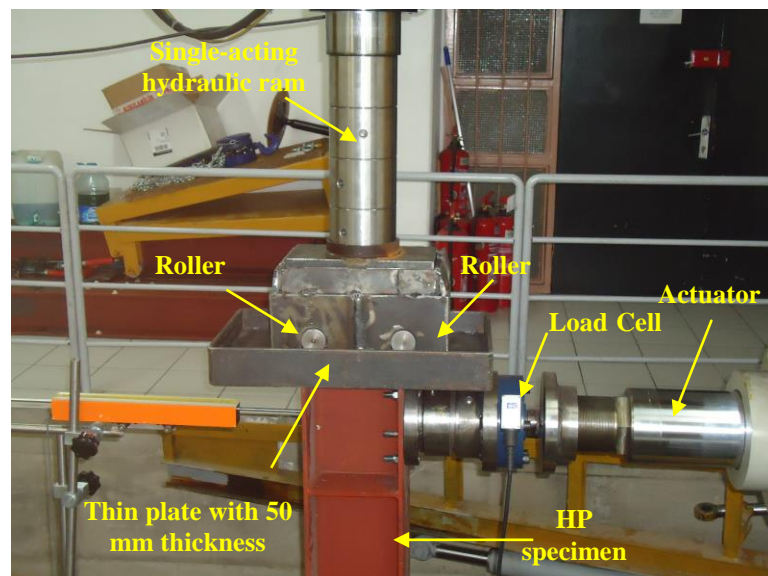
Figure 6.22. Vertical static loading system.

6.7. Instrumentation

In this phase of the research study, a description of the data acquisition equipment and data analysis techniques is presented. Firstly, detailed characteristics of strain gauges, data acquisition system, displacement transducers and load cell are given. Then, test setup producer is presented.

6.7.1. Strain Gauge

The strain gauge is one of the most important instruments of the electrical measurement techniques. As their name indicates, they are used for strain measurement. As a technical term, 'strain' consists of tensile and compressive strain distinguished by a positive or negative sign. Thus, strain gauges can be used to pick up expansion as well as contraction. Strains in a body are always caused by an external influence or an internal effect.

In the experiments, strain gauges are used to measure the strains on the surface of the steel H-piles at the most critical points, which are identified from 3D Finite element ANSYS results. Strain gauges with resistances of 120 and 350 ohms are commonly used in the experimental stress analysis. In this research, "BF120-10AA" type strain gauges having 120 ohm resistances are used. Although strain gauges are available in many shapes and sizes, the fundamental working principle of them is the same. The uniaxial strain gauge is shown in Figure 6.23. The figure also demonstrates the overall length, overall width, matrix length, matrix width and the gridline direction. The characteristics of the strain gauges used on surface of the steel H-piles are presented in Table 6.1.
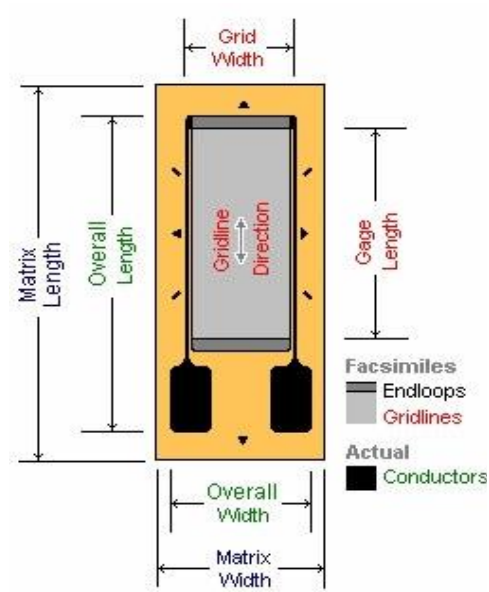
Figure 6.23. Strain gauges detail.

Table 6.1. Strain gauge specifications.

Dimensions	Pattern (mm)	Length	10.0
		Width	0.8
		Over length	12.9
		Over width	2.4
	Matrix (mm)	Length	14.4
		Width	4.0

Strain measurements rarely involve quantities larger than a few millistrain. Therefore, strain measurement requires accurate measurement of very small changes in resistance. To measure such small changes in resistance, strain gauges are almost always used in a bridge configuration with a voltage excitation source. Strain gauge configurations are arranged to form a Wheatstone bridges. The general Wheatstone bridge is illustrated Figure 6.24. There are three types of Strain gauge configurations: quarter-bridge, half-bridge, and full-bridge. The number of active element legs in the Wheatstone bridge determines the type of bridge configuration. Table 6.2 shows the number of active elements at each configuration. In this research, a Quarter–bridge type is used to the strains on the surface of the steel H-piles at the most critical points, which are identified from 3D finite element ANSYS results.
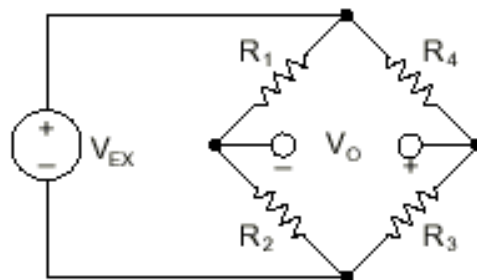
Figure 6.24. The Wheatstone bridge.

Table 6.2. Strain gauge configuration.

Configuration	Number of active elements
Quarter-bridge	1
Half-bridge	2
Full-bridge	4

6.7.2. Data Acquisition System

Principal components of data acquisition system used in the experimental part of this research study consist of a data logger, a computer with related data acquisition software, an adapter between computer and data logger, quarter bridge completion cables connecting strain gauges to data logger. The components of data acquisition system are shown in Figure 6.25.
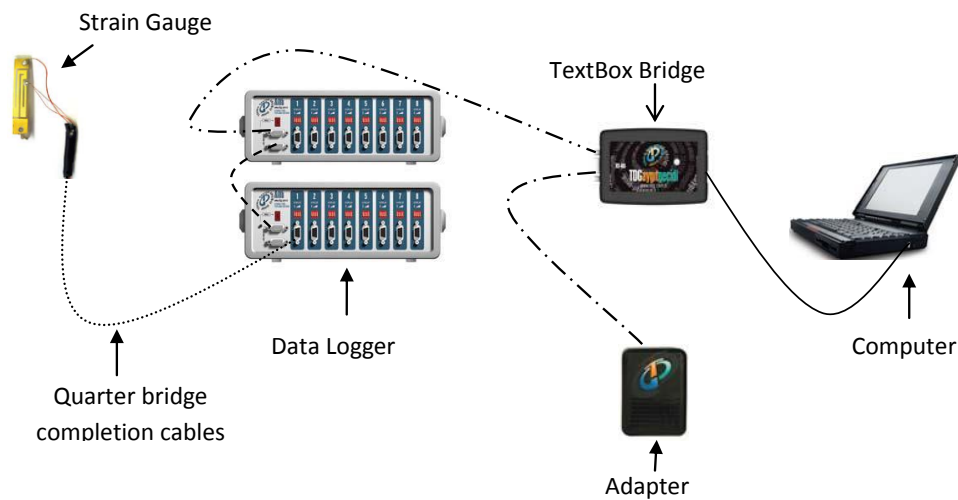
Figure 6.25. Data Acquisition system.

The "TDG Ai8b" data logger, shown in Figure 6.26, is used to convert analog signals from strain gauges to digital signals. Data logger has 8 channels to which strain gauges can be connected as shown in Figure 6.28. Two data loggers are used in series which lead to 16-channeled system. The strain values can be recorded at least in 0.125 s intervals by the data acquisition system. The sampling frequency in this research study is set to 2 samples per second.

Figure 6.26. 8-channel data logger.
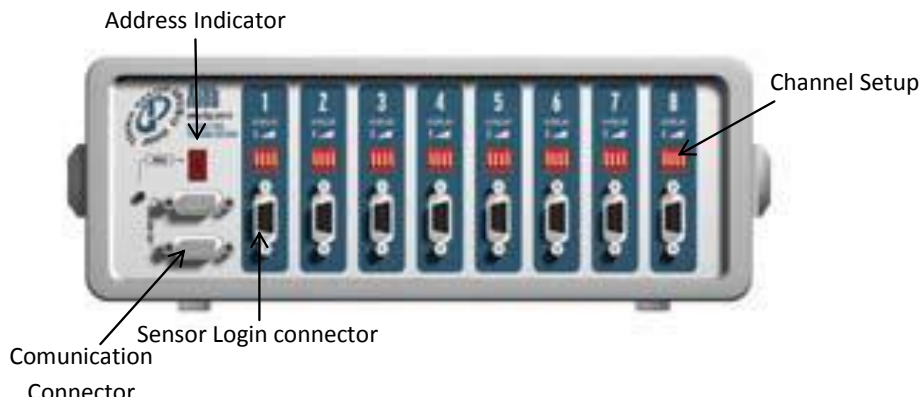
Figure 6.27. 8-channel data logger.

6.7.3. Displacement Transducer

There are five types of displacement transducers with stroke lengths of 5 mm, 10 mm, 25 mm, 50 mm, and 100 mm. The accuracy offered is ±0.1 % for strokes up to 25 mm and ± 0.15 % for strokes above 25 mm. Transducer having stroke lengths of 25 mm is used in the experimental part of this research study as shown in Figure 6.28. Details of transducer are presented in Figure 6.29 and Table 6.3.

130

Figure 6.28. Displacement Transducer.
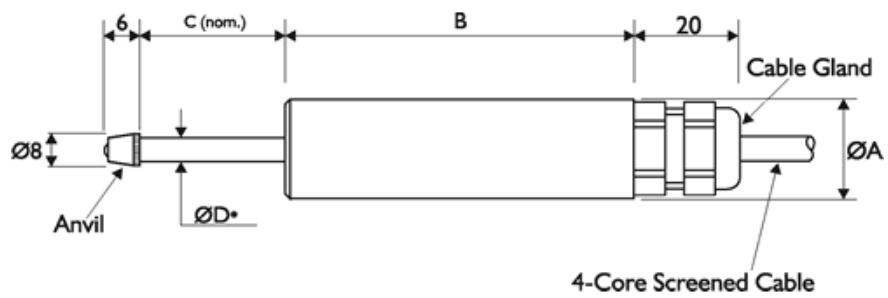
Figure 6.29. Transducer diagram.

Table 6.3. Transducer specification.

Stroke range	ØA	B	C	ØD
5 mm	17.4	88.8	6	4.8
10 mm	17.4	88.8	11	4.8
25 mm	17.4	104.5	26	4.8
50 mm	17.4	157	51	4.8
100 mm	25.4	264	102	4.8

6.7.4. SPD-D Displacement Transducer

The SPD-D displacement transducer is an axial type transducer with a measuring range of 200 mm or 300 mm. It can work at a large displacement range and make stable measurement over a long period of time. Details of SPD-D Displacement Transducer are presented in Figure 6.30 and Table 6.4. SPD-300D displacement transducer having stroke lengths of 317 mm is used in the experimental part of this research study as shown in Figure 6.31.
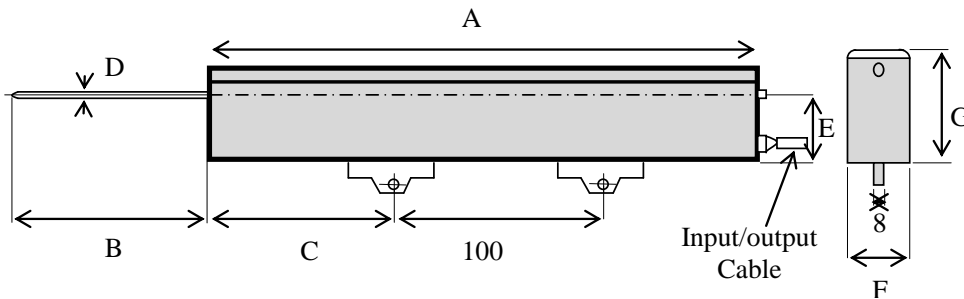
Figure 6.30. SPD-D Displacement Transducer diagram.

Table 6.4. SPD-D Displacement Transducer specification.

Dimension	TYPE	
	SPD-200D	**SPD-300D**
A	300	400
B	216	317
C	100	150
D	Ø6	Ø8
E	32	35
F	37	42
G	42	51

132
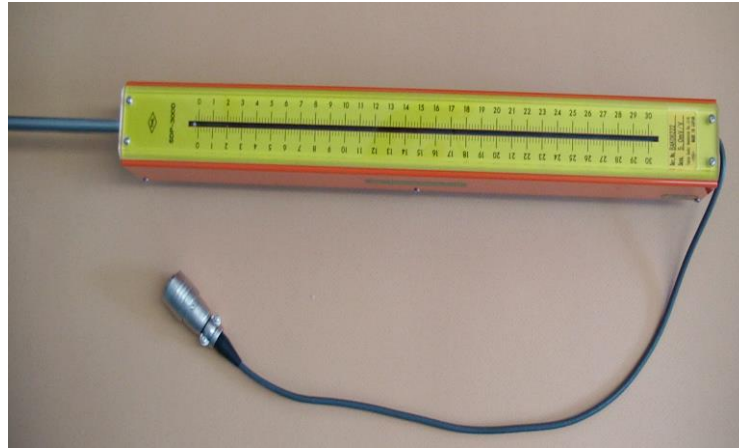
Figure 6.31. SPD-D Displacement Transducer.

6.7.5. Load Cell

A load cell is a force measurement device which uses strain measurements for indirect measurement of forces. It can convert compressive, tensile or shear forces into a proportional analog electric signal. This signal is processed to determine the forces acting on the load cell. There are many mechanical configurations for load cells: compression, s-beam, platform, single point, compression/tension, low profile, bending beam and canister load cell. In this research study, two types of load cells are used to measure lateral and vertical loads: compression load cell and compression/tension load cell. Compression/tension load cell used in the experimental part of this research study, shown in Figure 6.32, has 500 kN capacity. This load cell is used to measure lateral loads. Furthermore, compression load cell used in the experiments, shown in Figure 6.33 has 1000 kN capacity. Compression load cell is used to measure vertical loads.

Figure 6.32. Compression/tension load cell.

Figure 6.33. Compression load cell.

6.7.6. Test Setup Configuration

Test setup configuration is shown in Figure 6.34 with HP steel section vertically erected and instrumented with twelve strain gauge and three displacement transducer (LVDT). The plan configuration of the strain gauge is shown in Figure 6.35 and Figure 6.36. Strain measurements are required to correlate fatigue life of HP steel section with the intensity of strains. Therefore, strain measurement should be performed at the critical section where fatigue failure occurs. Theoretically, this section is located exactly above the 400 mm-high steel base fixture. Therefore, one row of strain gauges is considered at this location as shown in Figure 6.37. However, in order to have a fuller view of strain distribution over this region and neighborhood, a second row of strain gauges are attached at the 50 mm above this level as shown in Figure 6.38.
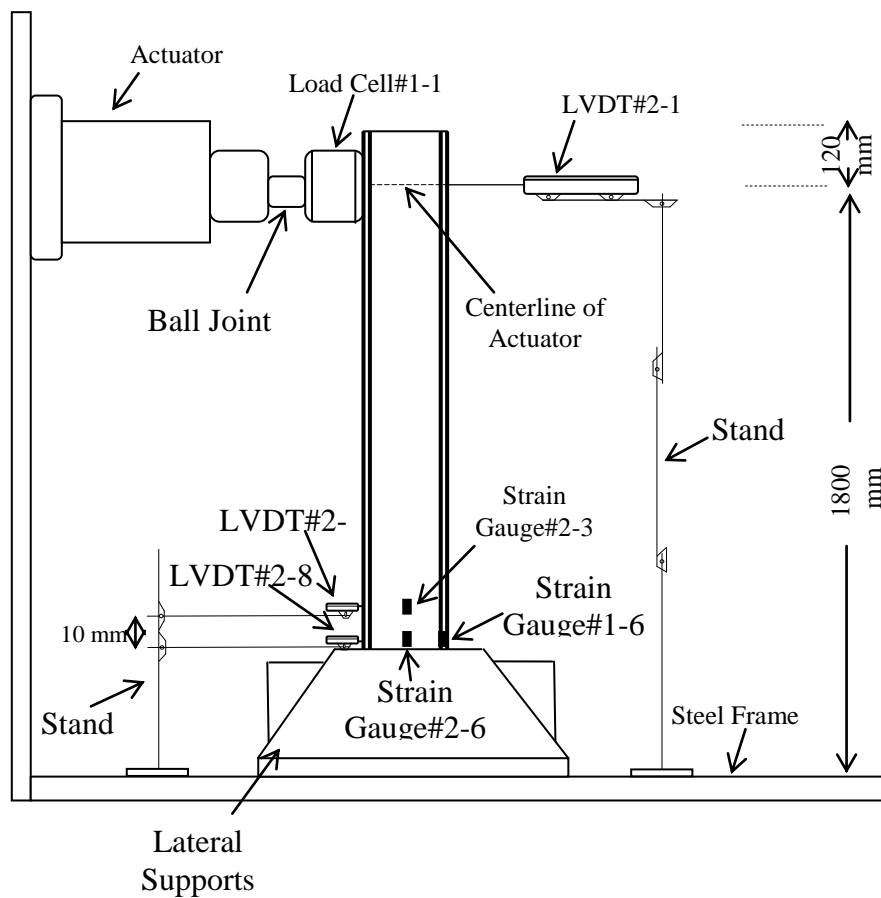
Figure 6.34. Location of the strain gauges and LVDT.
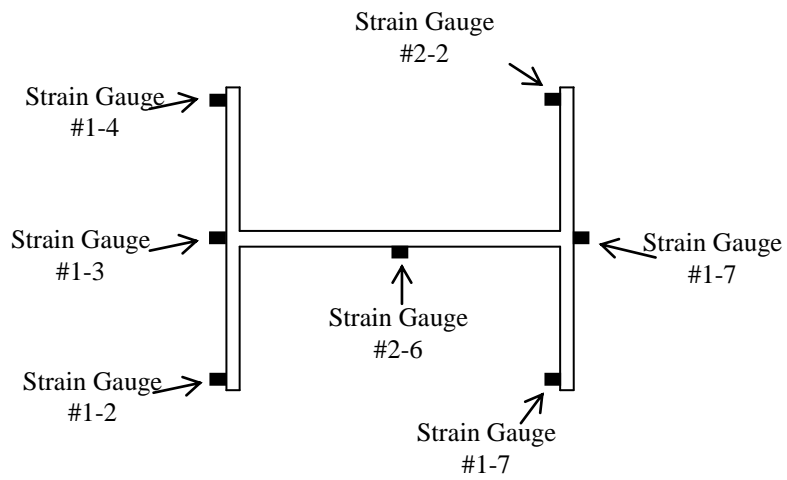
Figure 6.35. Strain gauge arrangement at upper level of the 400 mm-high steel base fixture.
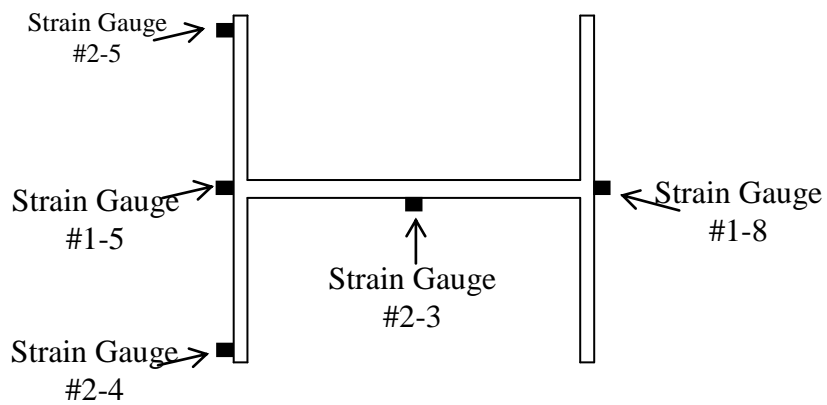
Figure 6.36. Strain gauge arrangement at 50 mm distance from the upper level of the 400 mm-high steel base fixture.
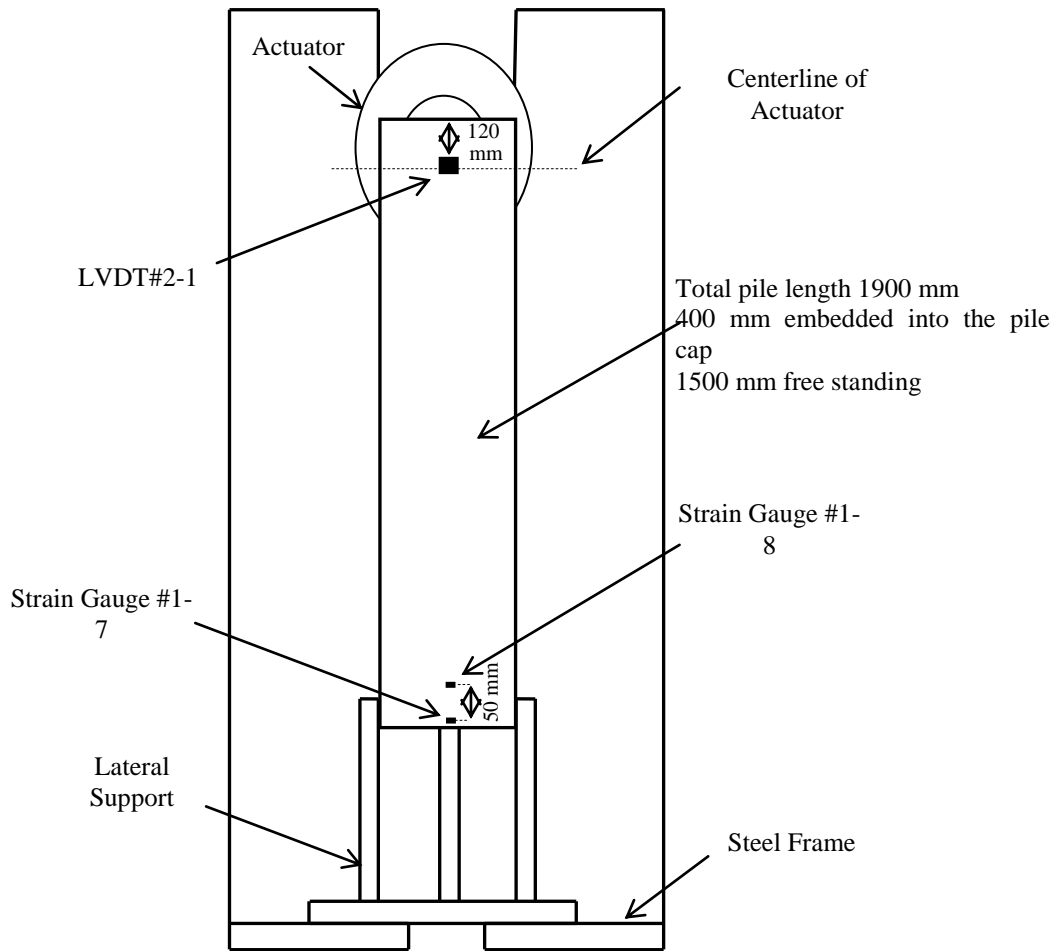
Figure 6.37. Location of the strain gauges and LVDT.
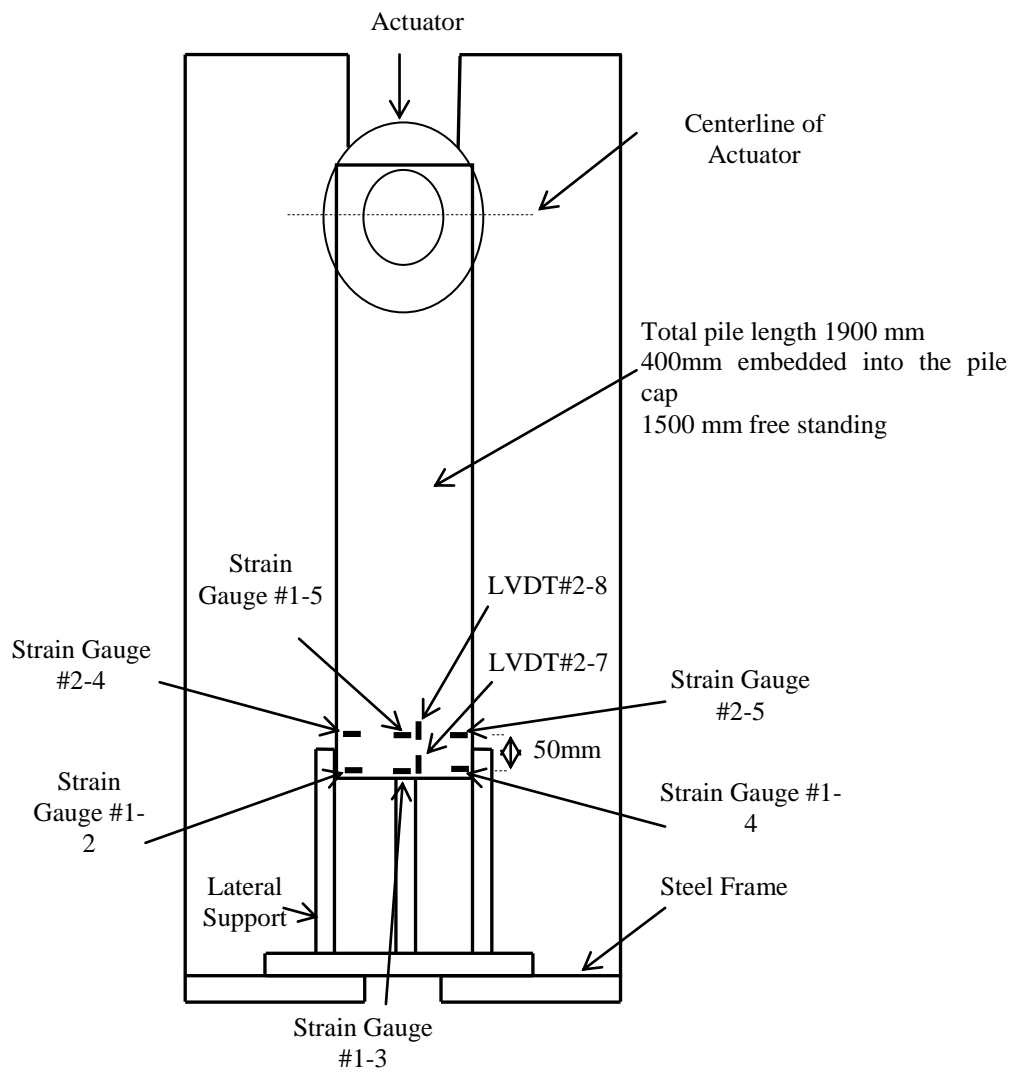
Figure 6.38. Location of the strain gauges and LVDT.

6.8. Instrumentation Procedure

Before installation of any measurement devices, HP steel section is mounted onto the stiff steel base fixture as shown in Figure 6.39.

Figure 6.39. HP test specimen mounted onto the stiff steel base fixture.

After the placement of HP steel section, strain gauges are installed to measure the strains at twelve different locations on the steel H-piles. Strain gauge points are chosen with the aid of nonlinear finite element analyses results using ANSYS.

After determination of the strain gauge locations, Strain gauges are strongly glued with the chemical cohesive on steel HP pile. Preparation of the strain gauges consists of four main steps;

- The surface preparation,
- Placement of the strain gauges,
- Gluing,
- Soldering the cable.

Figure 6.40 shows the HP steel section with strain gauges which is glued on. One side of the cable is soldered to the strain gauge and the other side is going through the connector by the quarter bridge completion cable as shown in Figure 6.41. Furthermore, the other side of the quarter bridge completion cable is connected to the data logger as shown in Figure 6.42. All of these processes are done for twelve strain gauges on HP steel section.
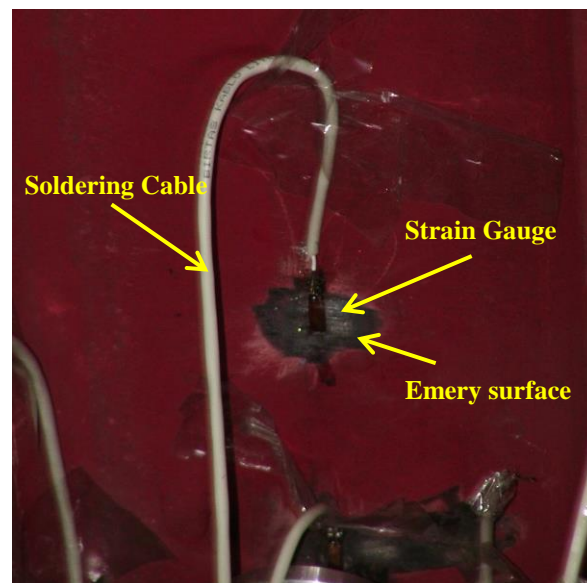
Figure 6.40. Strain gauges glued on the HP steel section.
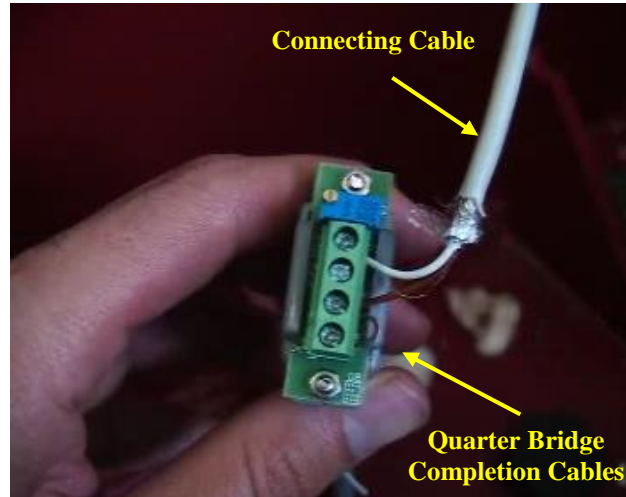
Figure 6.41. One side of the Quarter Bridge completion cable.
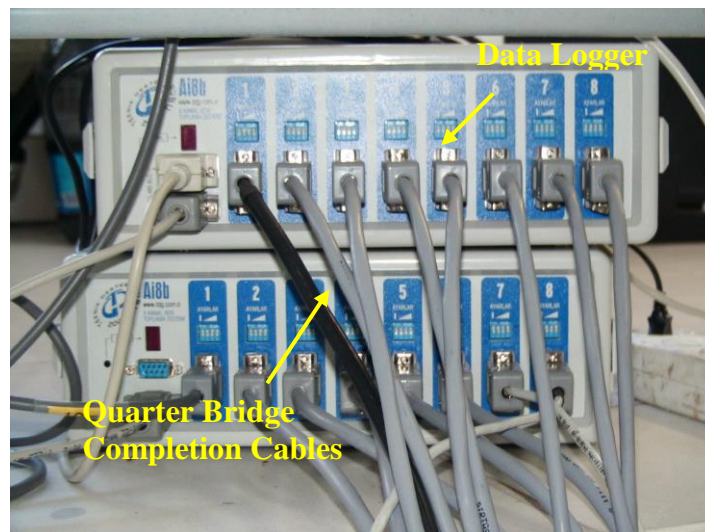
Figure 6.42. The other side of Quarter Bridge completion cable.

After attachment of all strain gauges, instrumentation is continued by installation of LVDTs. Three LVDTs are used in the experiments; One 350 mm capacity at top and two 25 mm capacity LVDTs at bottom. The upper 350mm-capacity LVDT is located at 120 mm distances from the top, coaxial with the actuator as

141

shown in Figure 6.43 and Figure 6.44. One of the lower 25 mm-capacity LVDTs is located at 1400 mm distances from the top. Additionally, the other 25 mm-capacity LVDT is located at 1300 mm distances from top as shown in Figure 6.45. The two lower LVDTs allow for measurement of the amount of rigid-body rotation of the HP steel section due to presence of clearances at base fixture.
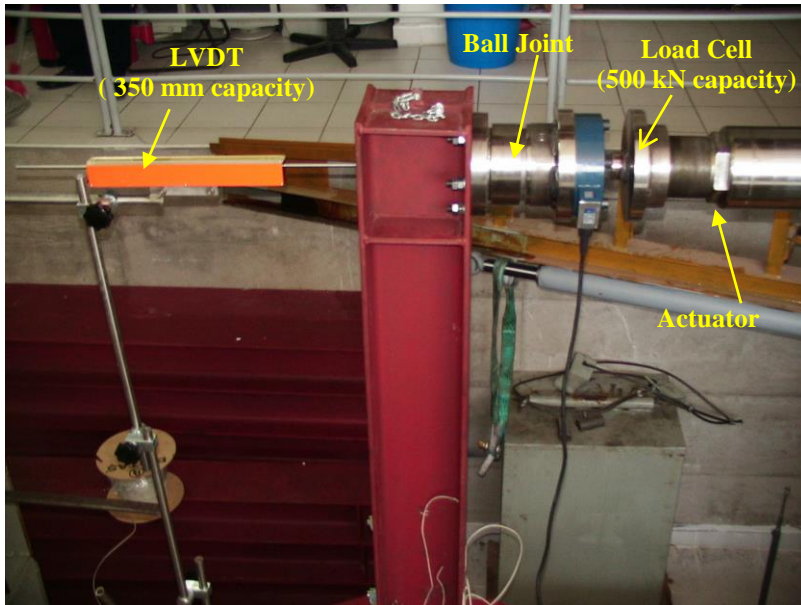
Figure 6.43. LVDT and Load Cell.
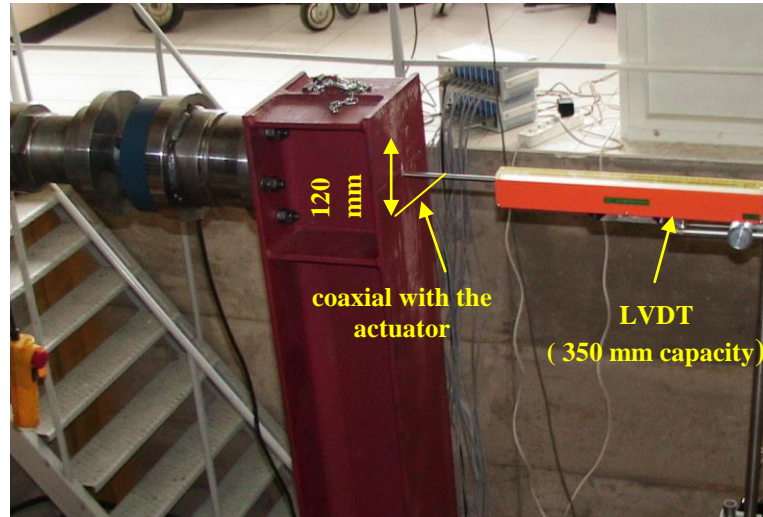
Figure 6.44. Side view of LVDT.
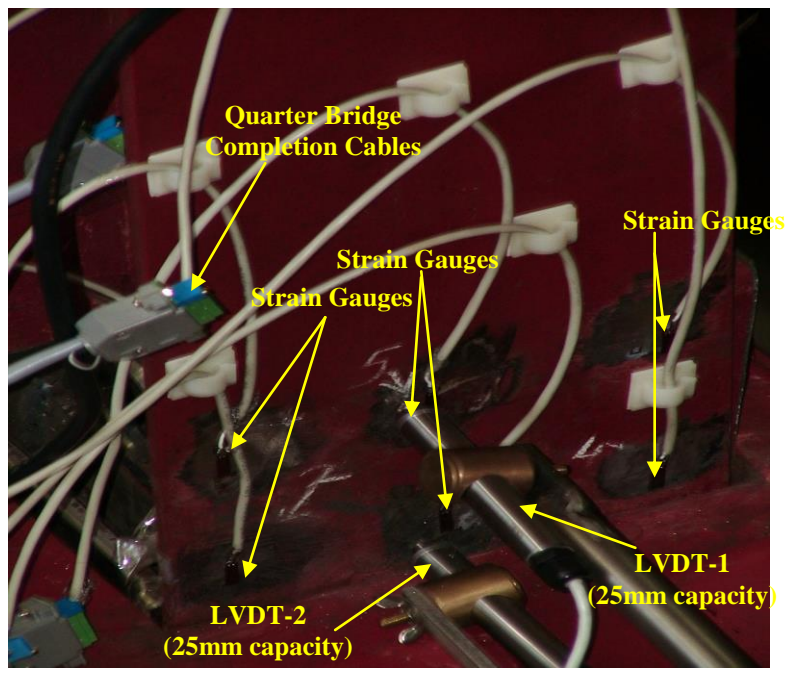
Figure 6.45. lower LVDTs.

After the strain gauges, LVDT and load cell are connected to the data logger and calibrated. Computer and actuator unit are shown in Figure 6.46.
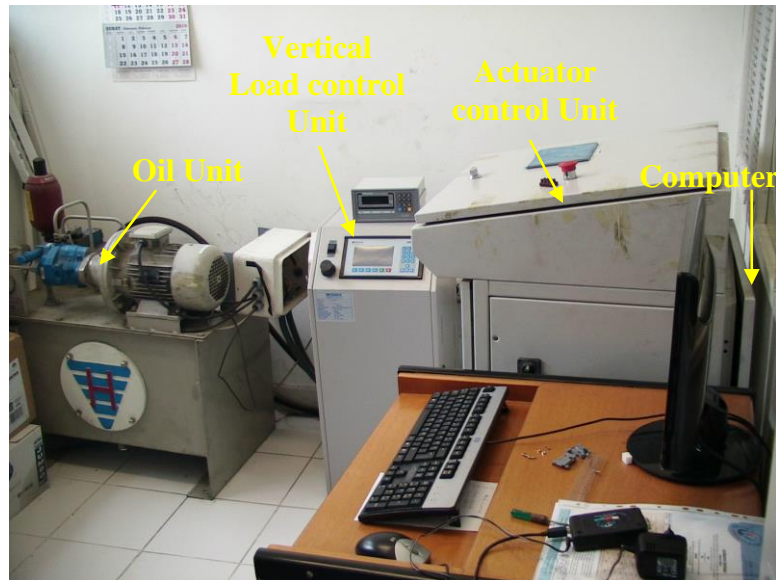
Figure 6.46. Computer and actuator unit.

6.9. Experimental Test Setup and Types of Tests

A total of 35 different tests will be conducted to study the effects of various parameters such as pile size and orientation, pile length, axial load level, small amplitude cycles as well as the strain amplitude. Details about these tests are given below.

1- Effect of pile size, orientation (Strong and Weak axis) and axial level:

$$HP220x57 \rightarrow StrongAxis \rightarrow P\begin{cases} \rightarrow 0 \\ \rightarrow 0.075P_Y \\ \rightarrow 0.11Py \\ \rightarrow 0.16P_Y \end{cases}$$

$$HP220x57 \rightarrow WeakAxis \rightarrow P\begin{cases} \rightarrow 0P_y \\ \rightarrow 0.11P_Y \end{cases}$$

$$HP260x75 \rightarrow P = 0.075P_Y \rightarrow \begin{pmatrix} \rightarrow StrongAxis \\ \rightarrow WeakAxis \end{pmatrix}$$

2- Effect of small amplitude cycles:

$$HP220x57 \rightarrow StrongAxis\begin{cases} \rightarrow P = 0 \rightarrow \begin{cases} \beta = 0.15 \\ \beta = 0.3 \end{cases} \\ \rightarrow P = 0.075P_Y \rightarrow \begin{cases} \beta = 0 \\ \beta = 0.15 \end{cases} \end{cases}$$

3- Effect of strain amplitude:

HP 260x75:

Strong Axis

$$\left.\begin{array}{l} \varepsilon_a = 2\varepsilon_y \\ \varepsilon_a = 5\varepsilon_y \\ \varepsilon_a = 10\varepsilon_y \\ \varepsilon_a = 15\varepsilon_y \\ \varepsilon_a = 20\varepsilon_y \end{array}\right\} \rightarrow 8$$

Weak Axis

$$\left.\begin{array}{l} \varepsilon_a = 2.5\varepsilon_y \\ \varepsilon_a = 5\varepsilon_y \\ \varepsilon_a = 10\varepsilon_y \\ \varepsilon_a = 15\varepsilon_y \\ \varepsilon_a = 20\varepsilon_y \end{array}\right\} \rightarrow 6$$

HP 220x57:

Strong Axis

$$\left.\begin{array}{l} \varepsilon_a = 2\varepsilon_y \\ \varepsilon_a = 5\varepsilon_y \\ \varepsilon_a = 10\varepsilon_y \end{array}\right\} \rightarrow 12$$

Weak Axis

$$\varepsilon_a = 5\varepsilon_y \} \rightarrow 2$$

4- Effect of pile length (moment gradient):

HP 220x57: L=1.30 mm (200 mm shorter)

CHAPTER 7

TEST RESULTS

After preparation of test set up as mentioned above, experimental tests are conducted as follows;

7.1. Specimen-1: A Maximum Strain of $\varepsilon_a = \pm 5\varepsilon_y$ in Bending about Strong Axis with No Axial Load

This specimen which is subjected to no vertical load, is tested under cyclic lateral load normal to its strong axis. Using a servo hydraulic actuator operated in displacement control, the amount of cyclic displacement is controlled such that a maximum strain of 0.0076 equivalent to five times yield strain ($\varepsilon_a=5\varepsilon_y$) is developed as shown in Figure 7.1. The maximum compression and tension forces 160 kN, and 160 kN respectively are applied during the push of first cycle, and mounted at a height of 1900 mm above the base as shown in Figure 7.2. Figure 7.3 shows HP220x57 section under cyclic lateral load normal to its strong axis.

Total 140 mm displacement is applied on the push and pull side to obtain five times yield strain. Due to presence of 2 mm clearance on both sides, the required displacements are larger than the theoretical value calculated based on fixed-support conditions. Thin plates are inserted between the specimen and the base supports to eliminate reduce the effect of these gaps.

The cracks firstly developed in the intersect lines of flanges and webs, and then expanded with the following cycles. Finally the specimen fractured due to the low cycle fatigue when the steel HP220x57 is reached to 200 cycles. The mentioned fractures are shown in Figure 7.4, Figure 7.5 and Figure 7.6. Front and side view

147

of the fracture occurring exactly above the 400 mm-high steel base fixture are shown in Figure 7.50 and Figure7.7. Additionally, the fracture on the other side of the HP220x57 section is displayed in Figure 7.8.
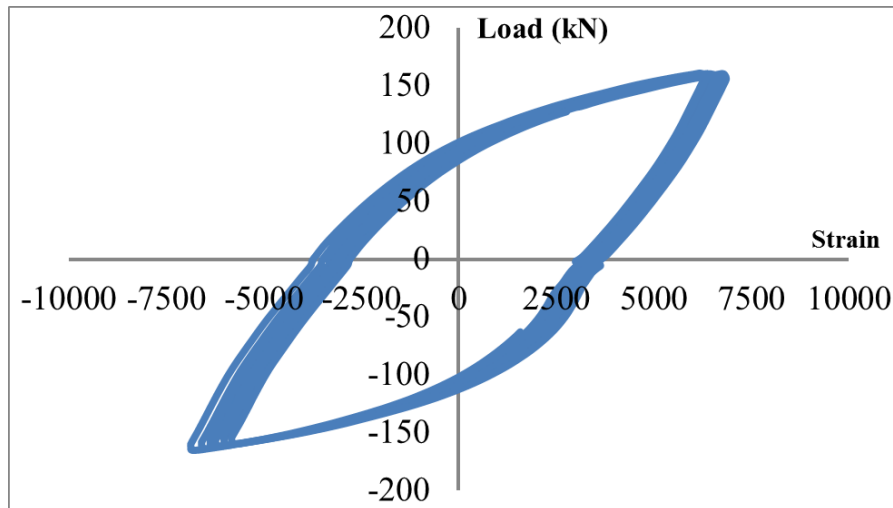
Figure 7.1. HP220x57 pile specimen-1 Lateral Load-Micro strain Relationship.
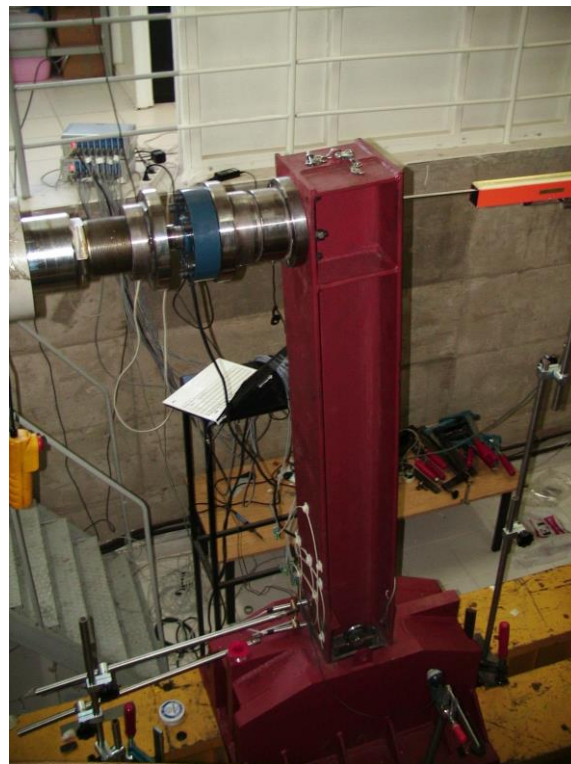
Figure 7.2. HP220x57 pile specimen-1

148
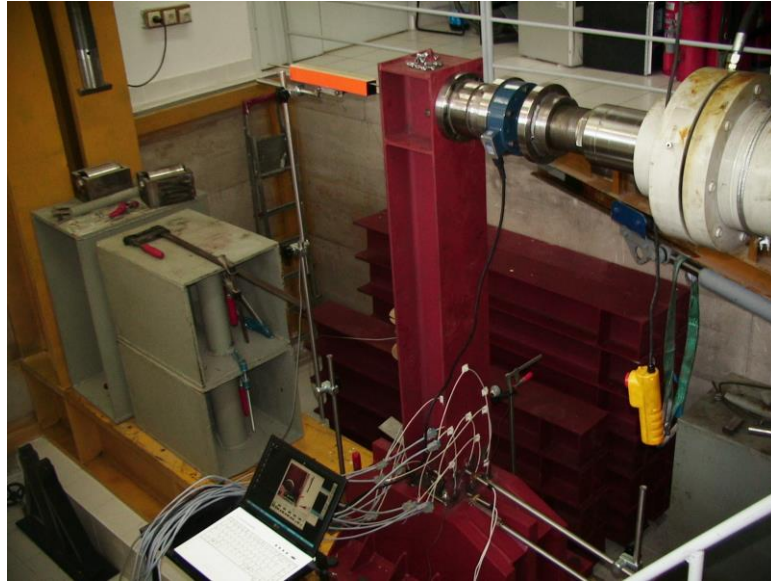
Figure 7.3. Specimen-1 under cyclic lateral load normal to its strong axis.

Figure 7.4. Front view of fracture occurs exactly above the 400 mm-high steel
base fixture.

Figure 7.5. Side view of fracture occurs above the 400 mm-high steel base fixture.
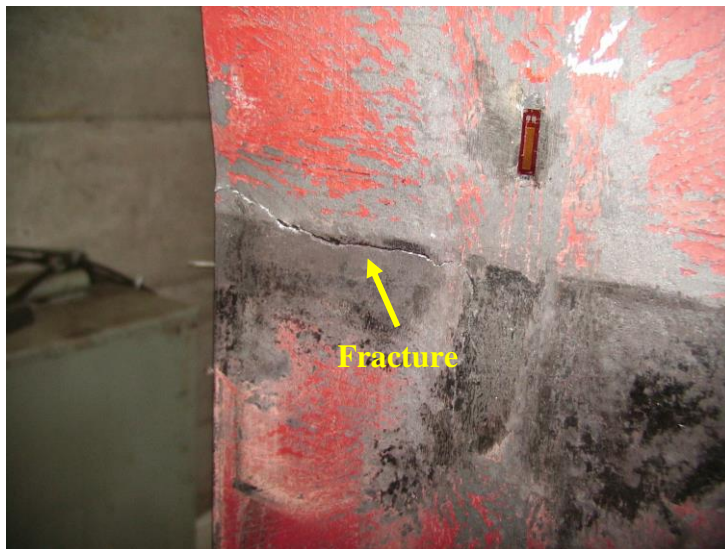
Figure 7.6. Fracture occurs above the 400 mm-high steel base fixture in other side of HP220x57 specimen.

7.2. Specimen-2: A Maximum Strain of εa = ±5εy in Bending about Strong Axis with No Axial Load

This specimen is tested before under the same conditions as specimen-1. The lateral actuator is mounted at a height of 1900 mm above the base as shown in Figure 7.7. Same displacements are applied on the push and pull side to obtain five times yield strain as specimen-1. To reach these displacements, maximum compression and tension forces 165 kN, and 160 kN respectively are applied during the push and pull of first cycle as shown in Figure 7.8. Thin plates are inserted between the specimen and the base supports to eliminate reduce the gaps. First fracture begins 220 cycles as shown in Figure 7.9. The cracks firstly developed in the intersect lines of flanges and web. After 220 cycles, fracture started to expand as shown in Figure 7.10. Finally, 239 cycles are completed until low cycle fatigue in steel HP220x57 section is reached as shown in Figure 7.11.

Figure 7.7. HP220x57 pile specimen-2
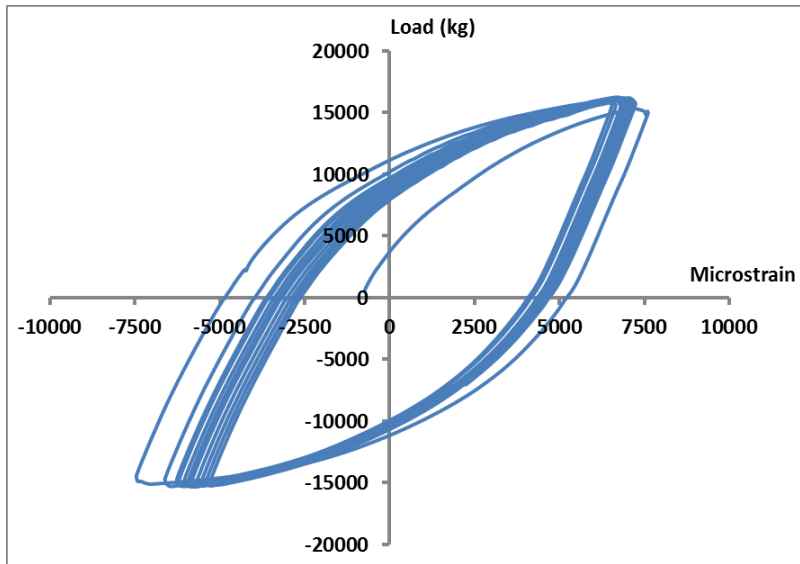
Figure 7.8. HP220x57 pile specimen-2 Lateral Load-Micro strain Relationship.

Figure 7.9. First fracture occurs 220 cycles.

Figure 7.10. First fracture begins expansion after 220 cycles.

Figure 7.11. Front view of fracture occurs exactly above the 400 mm-high steel
base fixture.

7.3. Specimen-3: A Maximum Strain of $\varepsilon_a = \pm 5\varepsilon_y$ in Bending about Strong Axis with No Axial Load

This specimen is tested before under the same conditions as specimen-1 and specimen-2 to investigate the number of cycles until fracture. During the tests, applied lateral force and corresponding pile displacement at the point of lateral force application are measured by LVDTs and Load cell. To obtain five times yield strain ($\varepsilon_a = \pm 5\varepsilon_y$), same lateral displacements are applied on the push and pull side. To reach these displacements, maximum compression and tension forces 163 kN, and 167 kN respectively are applied during the push and pull of first cycle. First fracture begins 232 cycles. After 232 cycles, fracture starts to expand and finally, low cycle fatigue occurs when steel HP220x57 section is reached to the 285 cycles.

7.4. Specimen-4: A Maximum Strain of $\varepsilon_a = \pm 2.5\varepsilon_y$ in Bending about Strong Axis with No Axial Load

This specimen is tested under cyclic lateral load normal to its strong axis; no vertical loads are applied to the pile. Using a servo hydraulic actuator operated in displacement control, the amount of cyclic displacement is controlled such that a maximum strain (0.0038) is developed as equal to the two and a half times yield strain ($\varepsilon_a = 2.5\varepsilon_y$) as shown in Figure 7.12. The maximum compression and tension forces 90 kN, and 90 kN respectively are applied during the push of first cycle, and mounted at a height of 1900 mm above the base. Total 87 mm displacements are applied on the push and pull side to obtain two and a half times yield strain. First fracture begins 1695 cycles as shown in Figure 7.13. After 1695 cycles, fracture starts to expand as shown in Figure 7.14. Finally, low cycle fatigue occurs when steel HP220x57 section is reached to the 2134 cycles as shown in Figure 7.15 and 7.16.
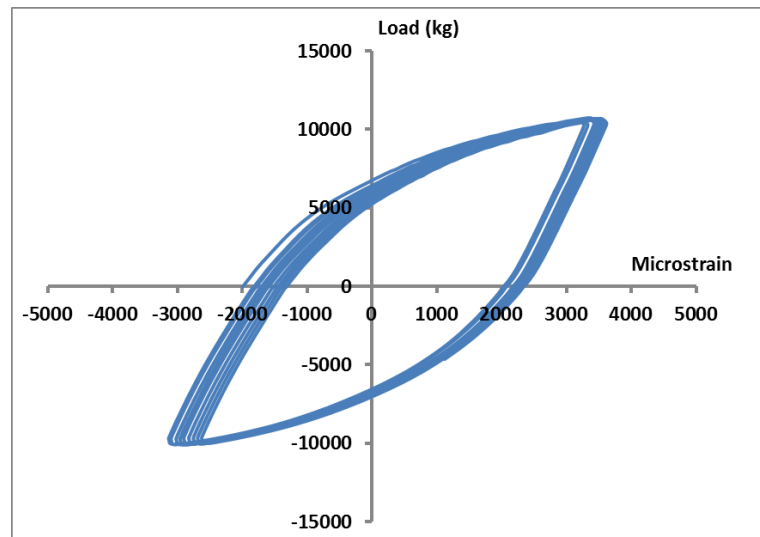
Figure 7.12. HP220x57 pile specimen-4 Lateral Load-strain Relationship.
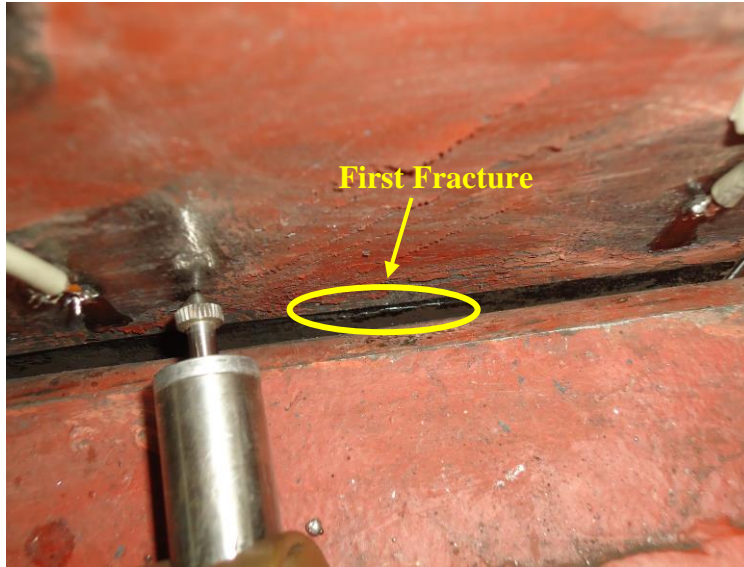
Figure 7.13. First fracture occurs 1695 cycles.
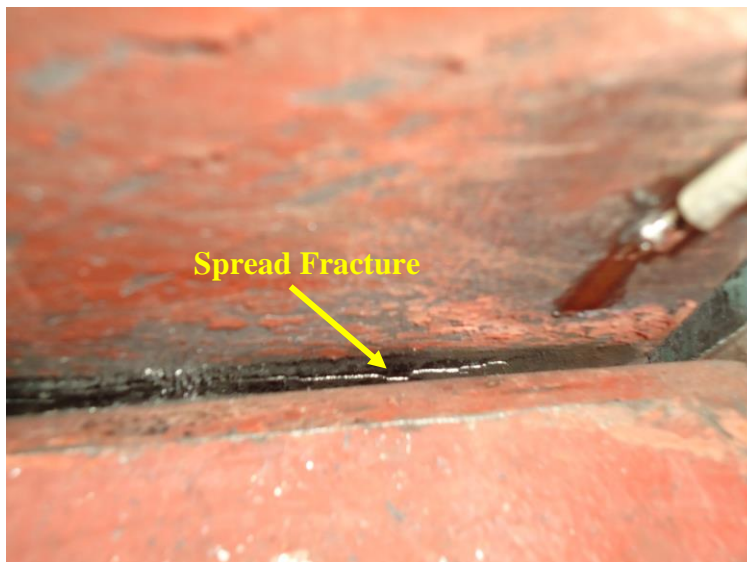
Figure 7.14. First fracture begins expansion after 1695 cycles.

Figure 7.15. Front view of fracture occurs exactly above the 400 mm-high steel
base fixture.

Figure 7.16. Fracture occurs on flange and web above the 400 mm-high steel base
fixture.

7.5. The Effect of Axial Load together with Lateral Load

In this phase of the research study, the effect of axial load together with lateral load on HP steel section is investigated. For this purpose, three different existing integral bridges with one, two and three spans are considered. The considered integral bridges are illustrated in Figs. 7.17-19. The single span integral bridge illustrated in Figure 7.20 is located in Illinois, USA (IL.Route 4 Over Sugar Creek Bridge). The two span integral bridge illustrated in Figure 7.21 is located in Ontario, Canada (Hwy 400 Underpass at Major Mackenzie Drive) while the three span integrals bridge illustrated in Figure 7.22 is located in Illinois, USA (IL. 4/13 Over Illinois Central Railroads). The single span integral bridge has a span length of 34 m, a width of 13 m and its 195 mm. Thick slab is supported by steel plate girders spaced at 2.24 m. The two spans integral bridge has span lengths of 41 m each, a width of 35 m and its 225 mm. Thick slab is supported by AASHTO Type VI prestressed concrete girders spaced at 2.38 m. The three span integral bridge has span lengths of 15.7, 20.7 and 15.7 m, a width of 13 m and its 190 mm thick slab is supported by W760x173 steel girders spaced at 2.26 m. More details about these bridges are given in Table 7.1.

The axial load ratios of Steel H piles of these bridges are calculated to determine the amount of axial load level of H-pile of integral bridge. The calculated axial load ratios from three different existing integral bridges are then used to determine the effects of axial load levels on the low cycle fatigue failure in steel H piles of integral bridges. The axial load percentage for one, two and three spans bridge are calculated as 8%, 15% and 10.8% respectively. Thus, in the further experiments, the effect of axial load levels on the low cycle fatigue failure is investigated using calculated axial load levels together with lateral loads.
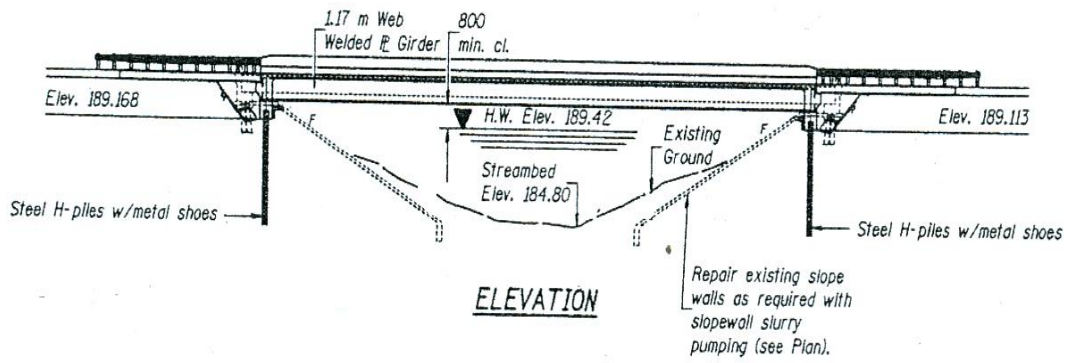
Figure 7.17. IL. Route 4 Over Sugar Creek Illinois.
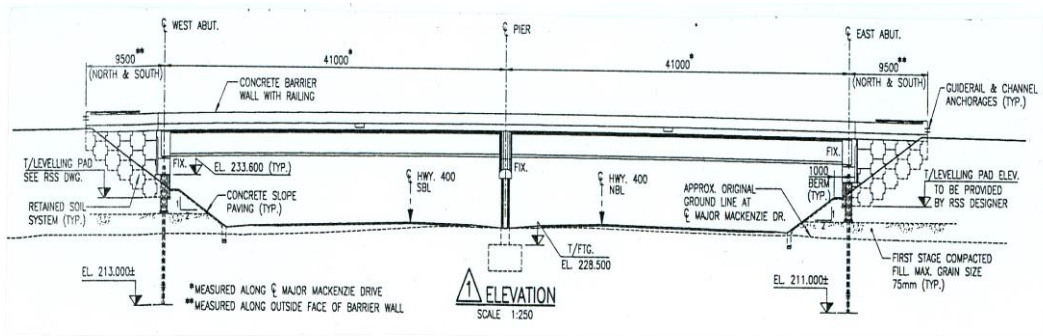
Figure 7.18. Hwy 400 Under Pass at Major Mackenzie Drive Ontario/Canada
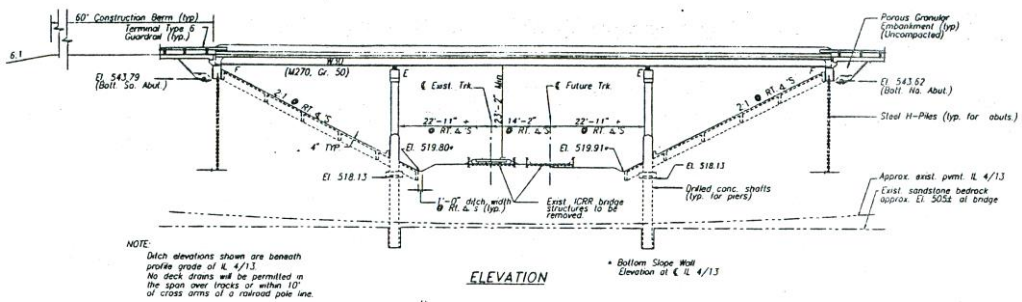
Figure 7.19. IL. 4/13 Over Illinois Central Railroad

Table 7.1. Properties of existing IBs considered.

Bridge Properties	Bridge 1	Bridge 2	Bridge 3
Number of Span	1	2	3
Span Length (m)	34.25	41, 41	15.7, 20.7, 15.7
Width (m)	13	35	13
Girder Type	Steel (I) Plate Girder (Flanges: 408x51 mm, Web: 1170x12 mm)	Prestress Concrete AASHTO VI	Steel (I) W 760x173
Girder Spacing (m)	2.24	2.38	2.26
Pile Type	HP 310x125	HP 310x110	HP 250x63
Number of Piles	7	22	6
Abutment Height (m)	2.67	4	2.12
Abutment Thickness (m)	0.76	1.5	0.76
Pier Type	N/A	Multiple Column bent	Multiple Column bent
Pier Foundation	N/A	Pile	Pile

7.6. Specimen-5: A Maximum Strain of $\varepsilon_a=\pm5\varepsilon_y$ in Bending about Strong Axis with Axial Load ($P=0.11P_y$)

This specimen is tested under cyclic lateral load normal to its strong axis; vertical loads are also applied to the pile to investigate the effect of axial load together with lateral load. Using a servo hydraulic actuator operated in displacement control, the amount of cyclic displacement is controlled such that a maximum strain of 0.0076 which is equal to five times yield strain ($\varepsilon_a = 5\varepsilon_y$), is developed. The maximum compression and tension forces 177 kN, and 171 kN respectively are applied during the push of first cycle, and mounted at a height of 1900 mm above the base. In addition, axial loads are also applied as 360 kN, 156 kN and 280 kN during the push, normal and pull direction together with the lateral loads. Average value of axial load is determined as 250 kN (*P=0.11P_y*) as shown in Figure 7.20. HP220x57 section under cyclic lateral load and axial load are shown

in Figure 7.21. Additionally, axial load setup is shown in Figure 7.22. Total 125 mm lateral displacements are applied on the push and pull side to obtain five times yield strain as shown in Figure 7.23. The results obtained from experimental test on HP220x57 section demonstrate that first fracture begins 341 cycles as shown in Figure 7.24. After 341 cycles, fracture starts to expand as shown in Figure 7.25. Finally, low cycle fatigue occurs when steel HP220x57 section is reached to the 508 cycles as shown in Figure 7.26.

The result obtained from experimental test on HP220x57 section reveals that local buckling occurs exactly above the 400 mm-high steel base fixture as shown in Figure 7.27.
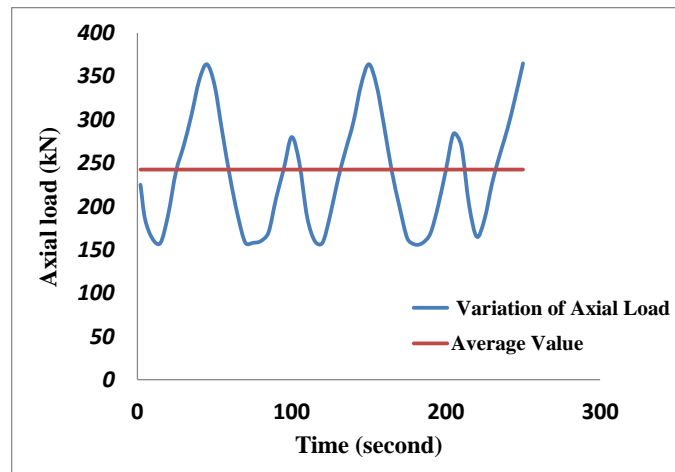
Figure 7.20. Average value of axial load.

Figure 7.21. Specimen-5 under cyclic lateral load and axial load.
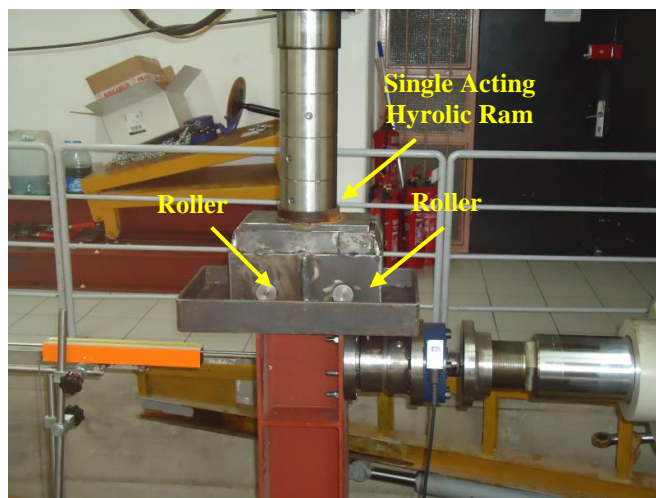
Figure 7.22. Axial load setup.
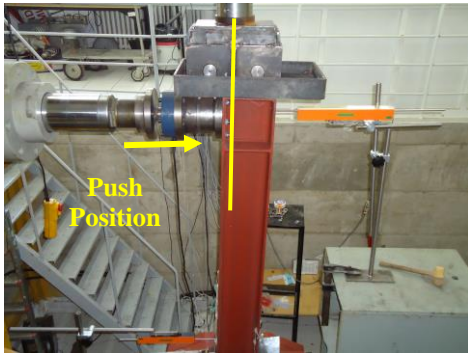
(a)
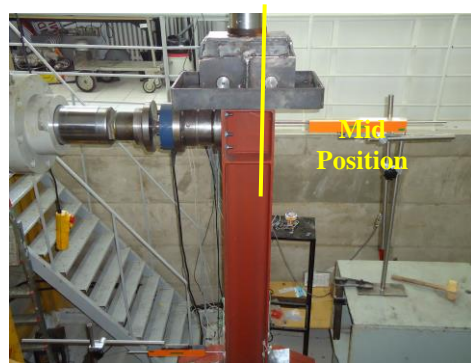
(b)
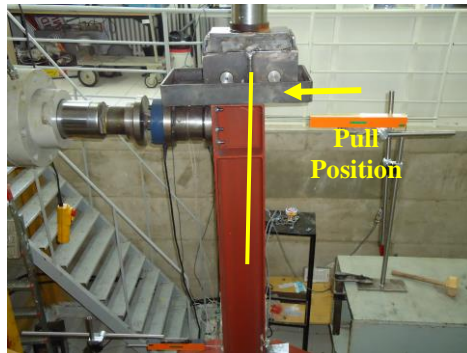
(c)

Figure 7.23. (a) Push direction, (b) Mid-position, (c) Pull direction.

Figure 7.24. First fracture occurs 341 cycles.

Figure 7.25. First fracture begins expansion after 341 cycles.

Figure 7.26. Front view of fracture occurs exactly above the 400 mm-high steel base fixture.

Figure 7.27. Local Buckling.

7.7. Specimen-6: A Maximum Strain of $\varepsilon_a=\pm5\varepsilon_y$ in Bending about Strong Axis with Axial Load (P=0.11Py)

This specimen is tested before under the same conditions as specimen-5 to investigate the number of cycles until fracture. To obtain five times yield strain ($\varepsilon_a=\pm5\varepsilon_y$), total 120 mm lateral displacements are applied on the push and pull side. To reach these displacements, maximum compression and tension forces 176 kN respectively are applied during the push and pull of first cycle as shown in Figure 7.28. In addition, axial loads are also applied as 364 kN, 158 kN and 280 kN during the push, normal and pull direction together with lateral load as shown in Figure 7.29. Average value of axial load is determined as 250 kN ($P=0.11P_y$).

The results obtained from experimental test on HP220x57 section demonstrate that first fracture begins 329 cycles as shown in Figure 7.30. After 341 cycles, fracture starts to expand as shown in Figure 7.31. Finally, low cycle fatigue occurs when steel HP220x57 section is reached to the 548 cycles as shown in Figure 7.32. Local buckling occurred exactly above the 400 mm-high steel base fixture is illustrated in Figure 7.33.
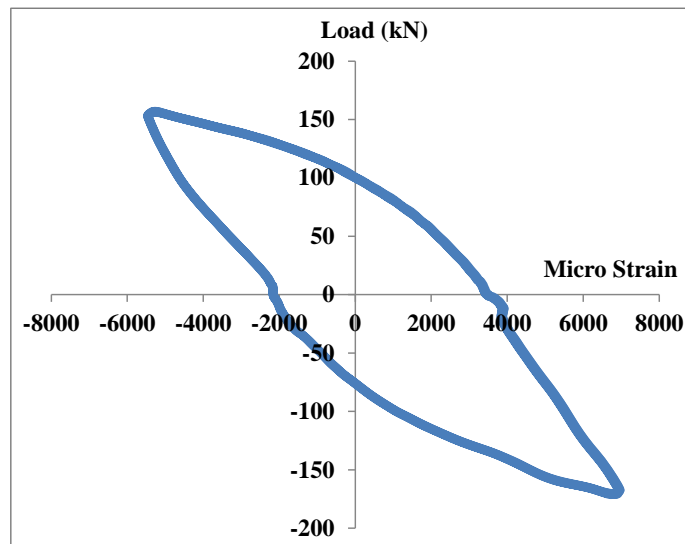
Figure 7.28. HP220x57 pile specimen-6 Lateral Load-strain Relationship.

166
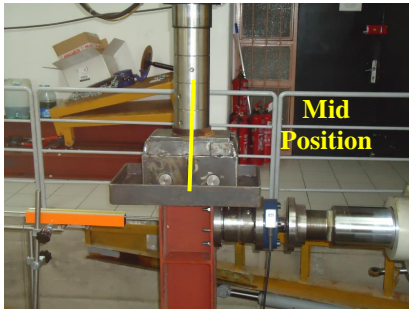
(a)
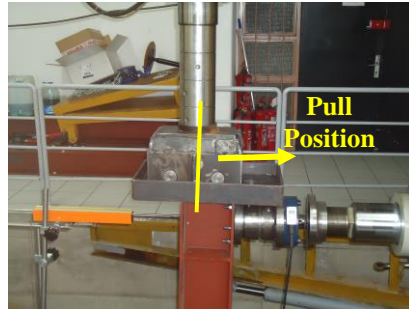
(b)
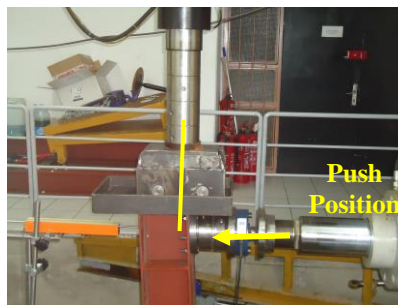
(c)

Figure 7.29. (a) Push direction, (b) Mid-position, (c) Pull direction.
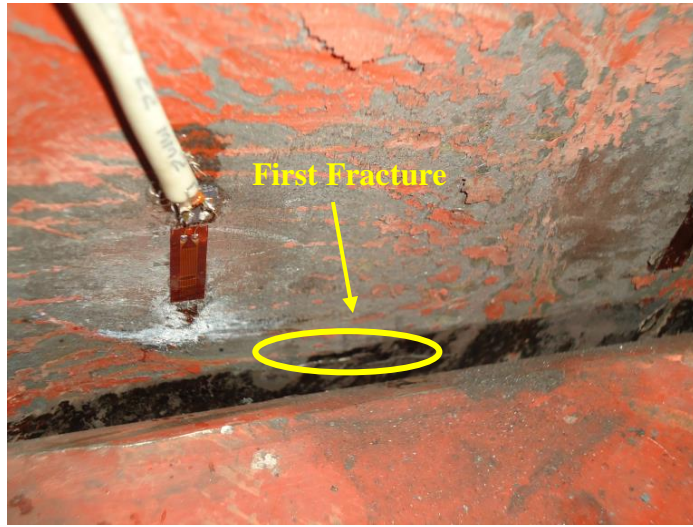
Figure 7.30. First fracture occurs.
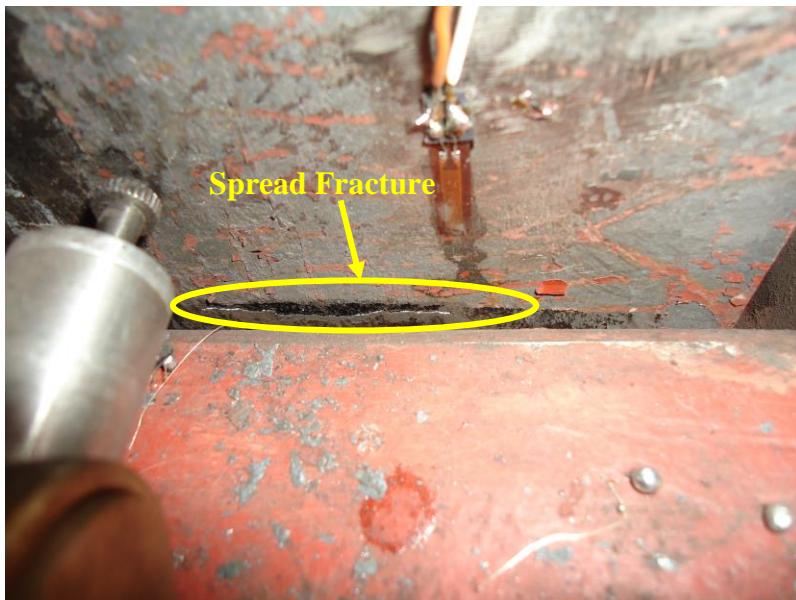
Figure 7.31. First fracture begins expansion after 329 cycles.

Figure 7.32. Fracture complete after 548 cycles.
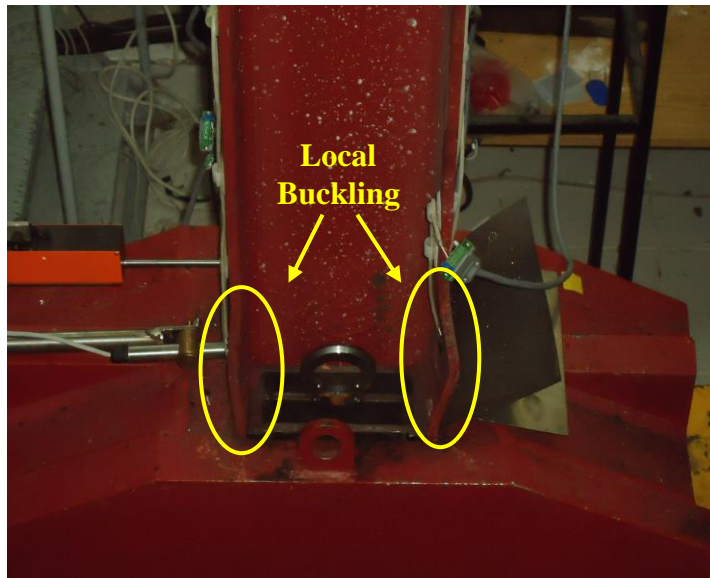
Local
Buckling

Figure 7.33. Local Buckling.

Consequently, from comparison between the HP220x57 section with axial load and the HP220x57 section without axial load, the effect of axial load is found to increase the number of cycles until fracture as shown in Figure 7.34.
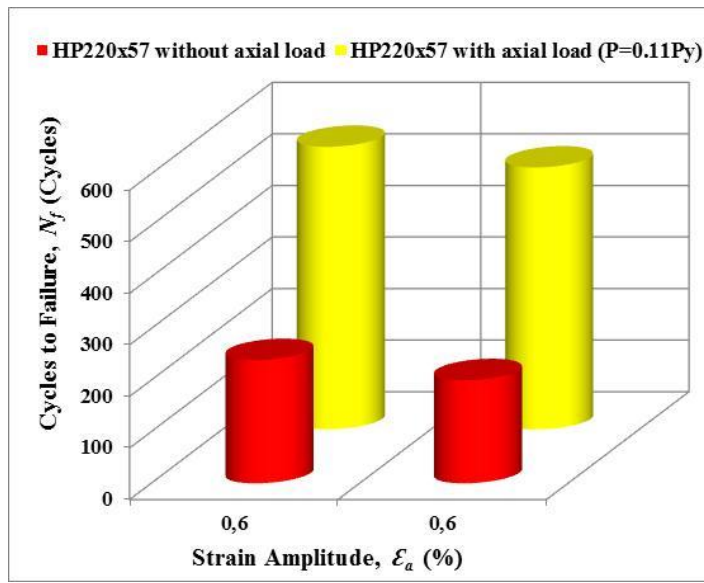
Figure 7.34. Comparison between the section with axial load and the section without axial load.

7.8. Specimen-7: A Maximum Strain of $\varepsilon_a = \pm 5\varepsilon_y$ in Bending about Strong Axis with Axial Load (P=0.075Py)

In the previous two experiments (specimen-5 and specimen-6), the effect of axial load is investigated for ($P=0.11P_y$). The results obtained from previous two experiments on HP220x57 section demonstrate that 508 and 548 cycles are completed until low cycle fatigue in steel HP220x57 section is reached. In this experiment, different axial load level ($P=0.075P_y$) is applied on HP220x57 steel section to investigate the effect of axial load level. For this purpose, the applied axial load is varied as 290 kN, 70 kN and 250 kN during the push, normal and

pull direction respectively. Average value of axial load is determined as 170 kN ($P=0.075P_y$) as shown in Figure 7.35. While axial load is applied, lateral displacements are also applied on the push and pull side to obtain five times yield strain ($\varepsilon_a=\pm5\varepsilon_y$) as shown in Figure 7.36. For this purpose, 60 mm and 65 mm lateral displacements are applied on the push and pull side. To reach these displacements, maximum compression and tension forces 178 kN, and 182 kN respectively are applied during the push and pull of first cycle.

The results obtained from experimental test on HP220x57 section demonstrate that first fracture begins 229 cycles as shown in Figure 7.37-(a). After 229 cycles, fracture starts to expand as shown in Figure 7.37-(b). Finally, low cycle fatigue occurs when steel HP220x57 section is reached to the 351 cycles as shown in Figure 7.38.

Consequently, the experimental test results obtained from Specimen-6 and Specimen-7 for different axial load levels on HP220x57 section demonstrate that the higher axial load level, the more number of cycles until fracture as shown in Figure 7.39.
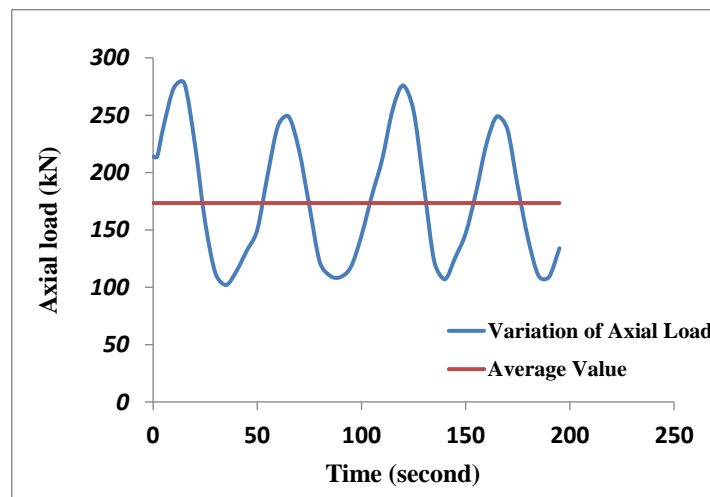
Figure 7.35. Average value of axial load.

171
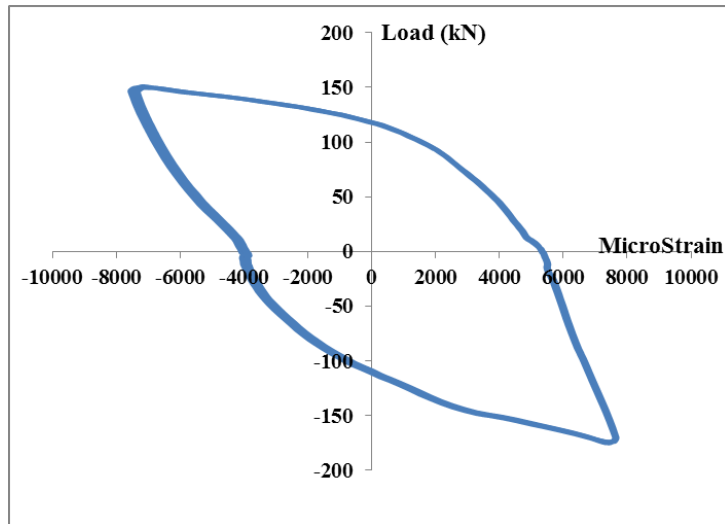
Figure 7.36. HP220x57 pile specimen-7 Lateral Load- strain Relationship.
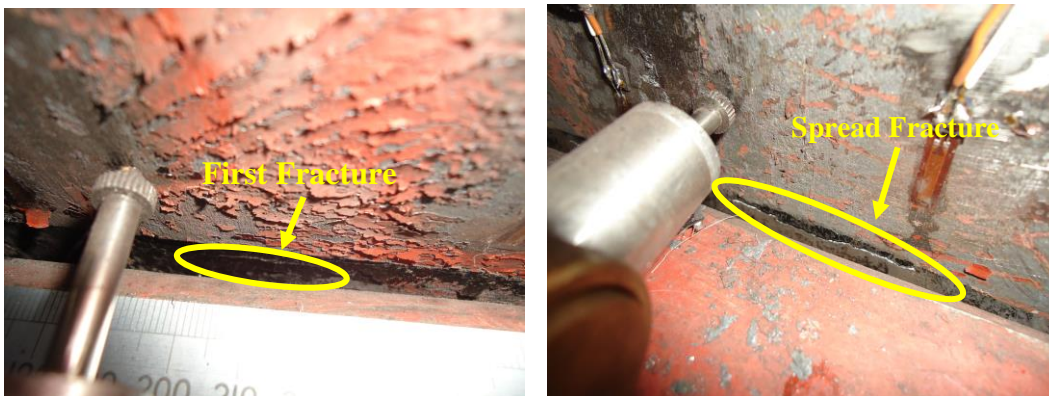
(a)	(b)

Figure 7.37. (a) First fracture, (b) spread fracture.
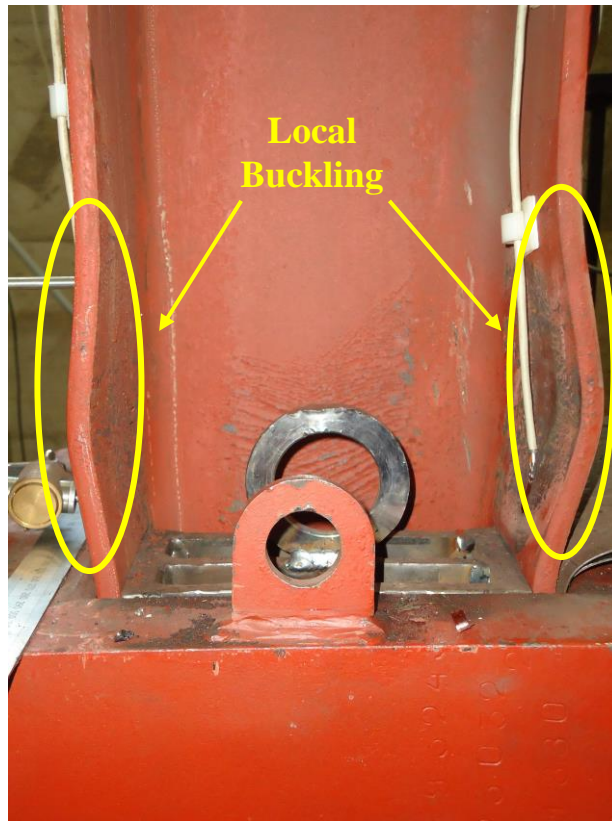
Figure 7.38. Local Buckling.
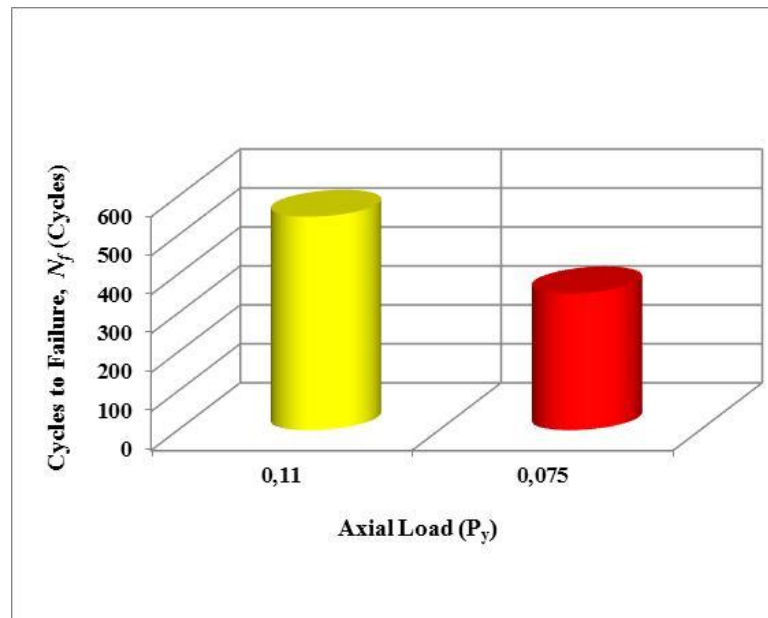
Figure 7.39. Effect of axial loads on HP220X57 steel sections.

173

7.9. Specimen-8: A Maximum Strain of $\varepsilon_a = \pm 5\varepsilon_y$ in Bending about Strong Axis with Axial Load (P=0.16P$_y$)

In the previous two experiments (specimen-6 and specimen-7), the effect of axial load is investigated for (*P=0.11P$_y$ and P=0.075P$_y$*). The results obtained from previous two experiments on HP220x57 section with axial load for *P=0.11P$_y$ and P=0.075P$_y$* demonstrate that 548 and 351 cycles are completed until low cycle fatigue in steel HP220x57 section is reached. In this experiment, different axial load level (*P=0.16P$_y$*) is applied on HP220x57 steel section to investigate the effect of axial load level. For this purpose, the applied axial loads are varied as 410 kN, 312 kN and 360 kN during the push, normal and pull direction. Average value of axial load is determined as 360 kN (*P=0.16P$_y$*). While axial load is applied, lateral displacements are also applied on the push and pull side to obtain five times yield strain (*$\varepsilon_a=\pm 5\varepsilon_y$*). For this purpose, 53 mm and 58 mm lateral displacements are applied on the push and pull side. To reach these displacements, maximum compression and tension forces 158 kN, and 152 kN respectively are applied during the push and pull of first cycle.

The results obtained from experimental test on HP220x57 section demonstrate that first fracture begins 547 cycles. After 547 cycles, fracture begins expansion. Finally, low cycle fatigue occurs when steel HP220x57 section is reached to the 818 cycles.

Consequently, the experimental test results obtained from Specimen-6, Specimen-7 and Specimen-8 for different axial load levels (*P=0.075P$_y$, P=0.11P$_y$ and P=0.16P$_y$*) on HP220x57 section demonstrate that the higher axial load level, the more number of cycles are needed until fracture as shown in Figure 7.40.
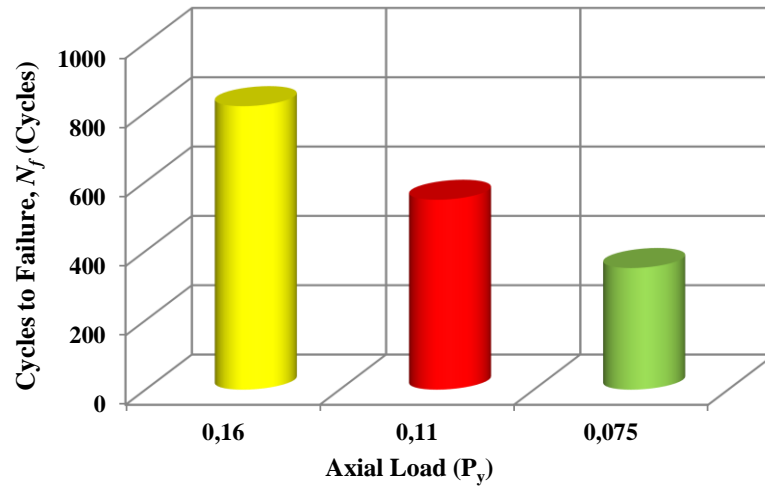
Figure 7.40. Effect of different axial loads on HP220X57 steel sections.

7.10. Specimen-9: A Maximum Strain of $\varepsilon_a = \pm10\varepsilon_y$ in Bending about Strong Axis without Axial Load (P=0 P_y)

This specimen is tested under cyclic lateral load normal to its strong axis; no vertical loads are applied to the pile. Using a servo hydraulic actuator operated in displacement control, the amount of cyclic displacement is controlled such that a maximum strain of 0.015 which is equal to ten times yield strain ($\varepsilon_a=10\varepsilon_y$) is developed. Total 180 mm displacements are applied on the push and pull side to obtain ten times yield strain. To reach these displacements, maximum compression and tension forces 185 kN, respectively are applied during the push and pull of first cycle.

The results obtained from experimental test on HP220x57 section demonstrate that first fracture begins 110 cycles. After 110 cycles, fracture begins expansion. Finally, low cycle fatigue occurs when steel HP220x57 section is reached to the 152 cycles.

7.11. Specimen-10: A Maximum Strain of $\varepsilon_a = \pm10\varepsilon_y$ in Bending about Strong Axis with Axial Load (P=0.075 P_y)

Maximum strain of 0.015 equivalent to ten times yield strain ($\varepsilon_a=10\varepsilon_y$) is developed in this experiment to investigate the effect of axial load together with lateral load under different strain level. 90 mm and 95 mm displacements are applied on the push and pull side to obtain ten times yield strain. Additionally, axial loads are applied as 290 kN, 70 kN and 250 kN during the push, normal and pull direction respectively. Average value of axial load is determined as 170 kN ($P=0.075P_y$). The results obtained from experimental test on HP220x57 section demonstrate that first fracture begins 70 cycles. After 70 cycles, fracture begins expansion. Finally, 95 cycles are completed until low cycle fatigue in steel HP220x57 section is reached.

In this experiment, very big lateral buckling occurred as seen in Figure 7.41. Local buckling of flanges takes place distance of 200 mm from lateral supports as seen in 7.42. The comparison of the five times and ten times yield strain levels together with the similar axial load level reveals that at low strain rates, more permanent deformation occurred as illustrated in Figure 7.43. As a result of this large lateral buckling, fracture starts earlier and also low cycle fatigue in steel HP220x57 occurs at smaller cycles. Additionally, because of this large lateral buckling, strain gauges are not used to measure the strains on the surface of the steel H-piles at the most critical points.

176

Figure 7.41. Local Buckling in steel HP220x57.
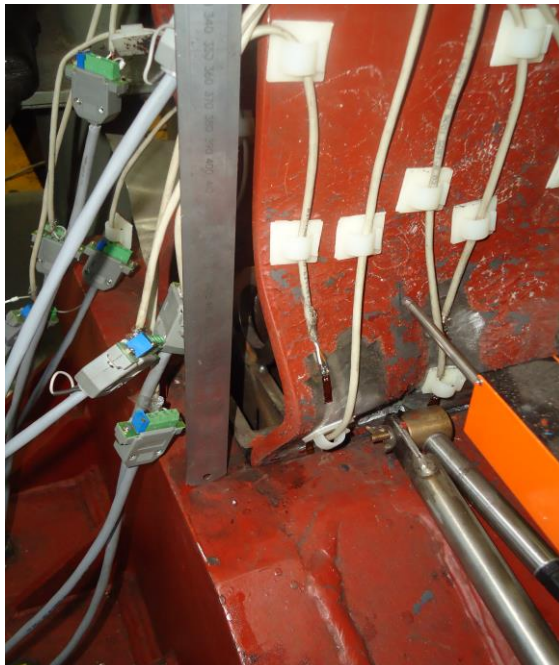
Figure 7.42. Local buckling distance of 200 mm from lateral supports.

(a)

(b)

Figure 7.43. Comparison of the five times yield strain and ten times yield strain with same axial load (P=0.075 P$_y$) , (a) Maximum Strain of $\varepsilon_a = \pm5\varepsilon_y$, (b) Maximum Strain of $\varepsilon_a = \pm10\varepsilon_y$.

7.12. Specimen-11: A Maximum Strain of $\varepsilon_a = \pm 10\varepsilon_y$ in Bending about Strong Axis with Axial Load (P=0.11 P_y)

In this experiment, the level of axial load is changed to compare with results of specimen-6, which have same axial load but different strain level. For this purpose, total 177 mm displacement is applied on the push and pull side to obtain ten times yield strain ($\varepsilon_a = \pm 10\varepsilon_y$). To reach these displacements, maximum compression and tension forces 182 kN, and 175 kN respectively are applied during the push and pull of first cycle. In addition to lateral load, axial loads are also applied as 364 kN, 158 kN and 280 kN during the push, normal and pull direction. Average value of axial load is determined as 250 kN ($P=0.11P_y$). The results obtained from experimental test on HP220x57 section demonstrate that first fracture begins 52 cycles. After 52 cycles, fracture starts to expand. Finally, low cycle fatigue occurs when steel HP220x57 section is reached to the 74 cycles as shown in Figure 7.44. This experiment reveals that low cycle fatigue occurs earlier with effect of axial load with high strain level as seen in Figure 7.45. Additionally, larger local buckling occurs in the higher strain levels as illustrated in Figure 7.46.

Figure 7.44. Fracture occurs on web.
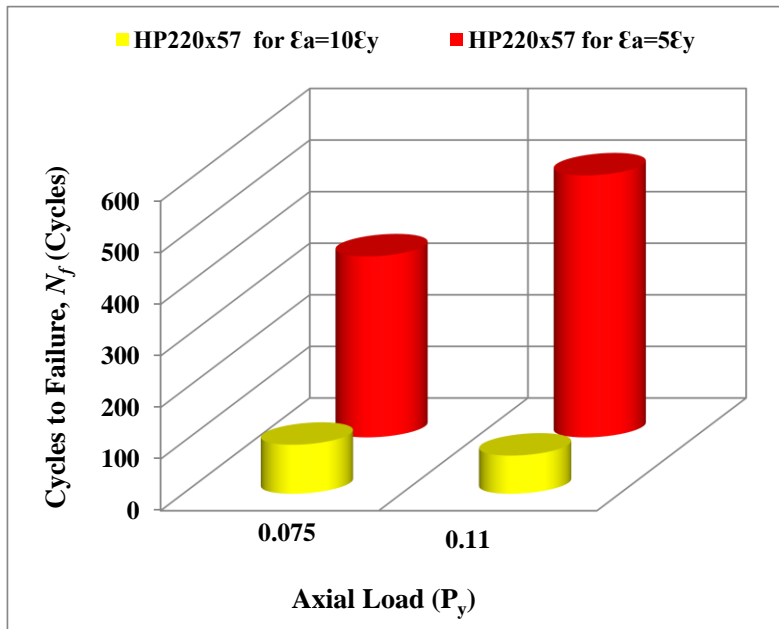
Figure 7.45. Effect of different axial loads with different strain levels on
HP220X57 steel sections.

(a)

(b)

Figure 7.46. Comparison of the five times yield strain and ten times yield strain with same axial load (P=0.11 P_y) , (a) Maximum Strain of $\varepsilon_a = \pm 5\varepsilon_y$, (b) Maximum Strain of $\varepsilon_a = \pm 10\varepsilon_y$.

7.13. Specimen-12: A Maximum Strain of $\varepsilon_a=\pm5\varepsilon_y$ in Bending about Weak Axis without Axial Load (P=0P$_y$)

This specimen is tested under same conditions as specimen-1 to investigate the low cycle fatigue effects in HP steel piles oriented along the weak axis as illustrated in Figure 7.47. Using a servo hydraulic actuator operated in displacement control, the amount of cyclic displacement is controlled such that a maximum strain of 0.0076 which is equal to five times yield strain ($\varepsilon_a=\pm5\varepsilon_y$). For this purpose, total 130 mm displacement is applied on the push and pull side respectively to obtain five times yield strain. Maximum compression and tension forces 50 kN, and 75 kN respectively are applied during the push and pull of first cycle to reach these displacements. The results obtained from experimental test on HP220x57 section oriented along the weak axis demonstrate that first fracture begins 447 cycles. After 447 cycles, fracture starts to expand. Finally, low cycle fatigue occurs when steel HP220x57 section is reached to the 622 cycles. For the strong axis, low cycle fatigue occurs 239 cycle to five times yield strain ($\varepsilon_a=\pm5\varepsilon_y$) as shown in Figure 7.48. As observed from the figure, more cycle is needed to reach low cycle fatigue failure when the piles oriented in weak axis than those oriented in strong axis.
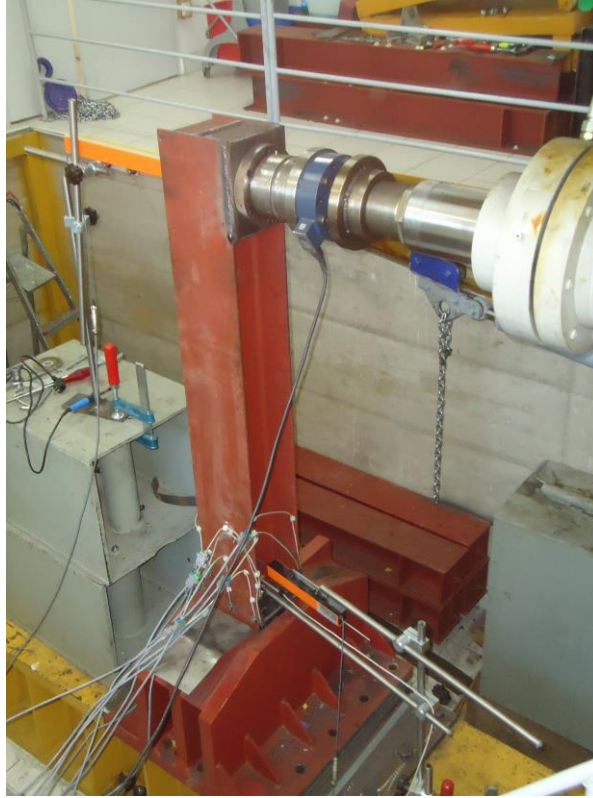
Figure 7.47. Specimen-12 under cyclic lateral load normal to its weak axis.

Figure 7.48. Front view of fracture occurs exactly above the 400 mm-high steel
base fixture.

7.14. Specimen-13: A Maximum Strain of $\varepsilon_a=\pm10\varepsilon_y$ in Bending about Weak Axis with Axial Load ($P=0.11P_y$)

The specimen-13 is tested under same conditions as the specimen-11 to investigate the low cycle fatigue of HP steel pile oriented along the weak axis as observed from the Figure 7.49. Using a servo hydraulic actuator operated in displacement control, the amount of cyclic displacement is controlled such that a maximum strain of 0.0152 which is equal to five times yield strain ($\varepsilon_a=\pm10\varepsilon_y$). For this purpose, displacements are applied on the push and pull side to obtain 10 times yield strain. To reach these displacements, maximum compression and tension forces, respectively are applied during the push and pull of first cycle as illustrated in Figure 7.50. The results obtained from experimental test on HP220x57 section oriented along the weak axis demonstrate that first fracture begins 72 cycles. After 72 cycles, fracture starts to expand as seen in Figure 7.51. Finally, low cycle fatigue occurs when steel HP220x57 section is reached to the 83 cycles. Close view of the fracture may be observed from Figure 7.52. Local buckling is illustrated in Figure 7.53. For the strong axis, low cycle fatigue occurs 508 cycle to five times yield strain ($\varepsilon_a=\pm5\varepsilon_y$). As observed from the figure, more cycle is needed to reach low cycle fatigue failure when the piles oriented in strong axis than those oriented in weak axis.

A few research studies have been found on low cycle fatigue of HP steel pile oriented along the weak axis in the literature. In the earlier research studies conducted by Wasserman, E. (2007) to study orienting the piling for weak axis bending offers the least resistance and facilitates pile-head bending for fixed head conditions. However, due to potential for flange buckling of steel H-piles, the total lateral displacement that can be accommodated is more limited that when piling is oriented for strong axis bending.

In the other research conducted by Yura, J. (1986), for axial load within 60% of the buckling load, the non-dimensionalized weak axis strength is less than that for the strong axis. For low axial load, the weak axis is slightly stronger. At high axial

184

load, the residual stresses more adversely affect the weak axis buckling load. At low axial load, the large shape factor results in significant inelastic nonlinear behavior which does not permit the section to take advantage of its superior plastic capacity.

Yoshida and Maegawa (1978) also mentioned that in addition to local buckling of axially loaded H-columns, member buckling or torsional buckling will take place. Weak axis member buckling for common types of H-columns may take prior to strong axis member buckling or torsional buckling.

Figure 7.49. Specimen-13 under cyclic lateral and axial load normal to its weak axis.
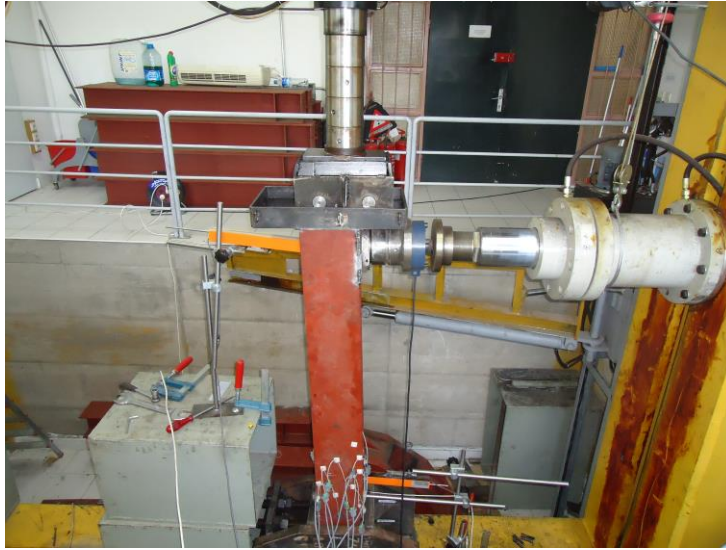
Figure 7.50. Displacements applied on the push side
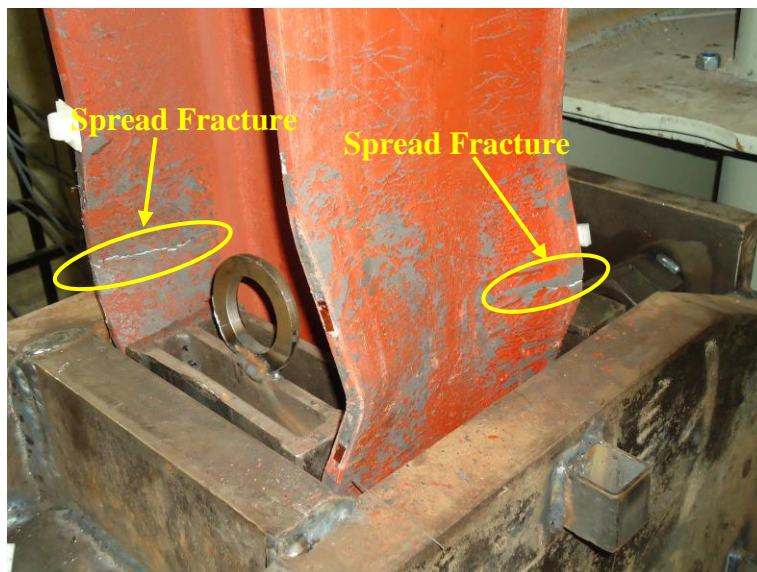
Figure 7.51. Fracture occurs on flanges.

Figure 7.52. Close view of the crack.
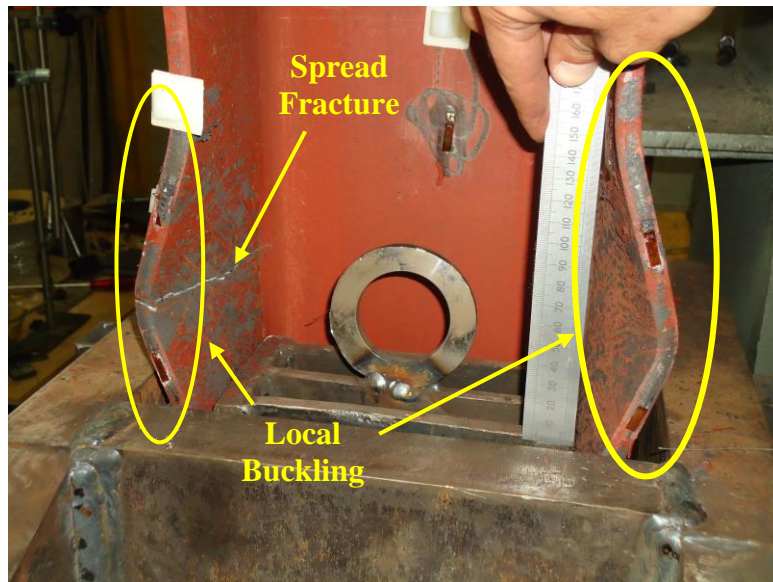
Figure 7.53. Local buckling distance of 200 mm from lateral supports.

7.15. Summary of Experiments for HP 220x 57 Steel Section

Experimental tests of HP220x57 and HP260x75 H-pile specimens are conducted to investigate the effect of several parameters on the low cycle fatigue life of integral bridge steel H-piles subjected to cyclic thermal strains. For this purpose, thirteen cyclic tests of HP220x57 steel sections subjected to strong and weak axes bending are conducted at various strain amplitudes to investigate the effect of strain amplitude and pile bending orientation on the low cycle fatigue performance. Additional tests are conducted to investigate the effect of axial loads on the low cycle fatigue performance of steel H-piles used in integral bridges. It is observed that, as expected, number of cycles to failure is inversely proportional to the strain amplitude. Furthermore, piles oriented to bend about their weak axes are observed to have a better low cycle fatigue performance. The effect of axial load is observed to have a significant effect on the low cycle fatigue performance of steel H-piles in two ways: (i) when the pile is subjected to moderate strain amplitudes (five times the yield strain), the presence of axial load is observed to enhance the low cycle fatigue life of the pile. This mainly due to the fact that, the presence of axial load decreases the amplitude of the tensile strain that results in cracking of the material (it delays the initiation of the crack), (ii) when the pile is subjected to larger strain amplitudes (10 times the yield strain), the presence of axial load is observed to decrease the low cycle fatigue life of the pile. This is mainly due to local buckling of the flange under the effect of compressive stresses from the axial load and high compressive strains due to the effect of bending. Local buckling increases the local curvature and strains. This locally accelerates the cracking of the material.

Table 7.2. Experiments results for HP220x57 Steel Section oriented along the Strong Axis.

Section Type	Load Type	Test Number	Axial load	Strain Amplitude (ε_a)	Number of Cycles	
					First Crack	Fracture
HP 220x57 Strong Axis	*No Axial Load*	1	P=0	$5\varepsilon_y$	145	200
		2	P=0	$5\varepsilon_y$	220	239
		3	P=0	$5\varepsilon_y$	232	285
		4	P=0	$2.5\varepsilon_y$	1695	2134
		9	P=0	$10\varepsilon_y$	110	152
	Axial + Lateral load	5	P=0.11P$_y$	$5\varepsilon_y$	341	508
		6	P=0.11P$_y$	$5\varepsilon_y$	329	548
		7	P=0.075P$_y$	$5\varepsilon_y$	229	351
		8	P=0.16P$_y$	$5\varepsilon_y$	547	818
		10	P=0.075P$_y$	$10\varepsilon_y$	70	95
		11	P=0.11P$_y$	$10\varepsilon_y$	52	74

Table 7.3. Experiments results for HP220x57 Steel Section oriented along the Weak Axis.

Section Type	Load Type	Test Number	Axial load	Strain Amplitude (ε_a)	Number of Cycles	
					First Crack	Fracture
HP 220x57 Weak AXis	*No Axial Load*	12	P=0	$5\varepsilon_y$	447	622
	Axial + Lateral load	13	P=0.11P$_y$	$10\varepsilon_y$	72	83

7.16. Test Results for HP260x75 Section

7.16.1. Specimen-14: A Maximum Strain of $\varepsilon_a=\pm2.5\varepsilon_y$ in Bending about Strong Axis with No Axial Load

To compare the experimental results for different steel H piles, HP 260x75 steel section is tested under same conditions as HP 220x57. For this purpose, first, total 94 mm lateral displacements are applied on the push and pull side to obtain the two and a half times yield strain ($\varepsilon_a=\pm2.5\varepsilon_y$) as shown in Figure 7.54. To reach these displacements, maximum compression and tension forces 105 kN, and 105 kN respectively are applied during the push and pull of first cycle. The results obtained from experimental test on HP260x75 section oriented along the strong axis demonstrate that first fracture begins 1823 cycles. After 1823 cycles, fracture starts to expand as seen in Figure 7.55. Finally, low cycle fatigue occurs when steel HP260x75 section is reached to the 2358 cycles. The comparison of the HP 220x57 steel section and HP 260x75 steel section together with the same yield strain level reveals that low cycle fatigue occurs in the approximate same cycles.
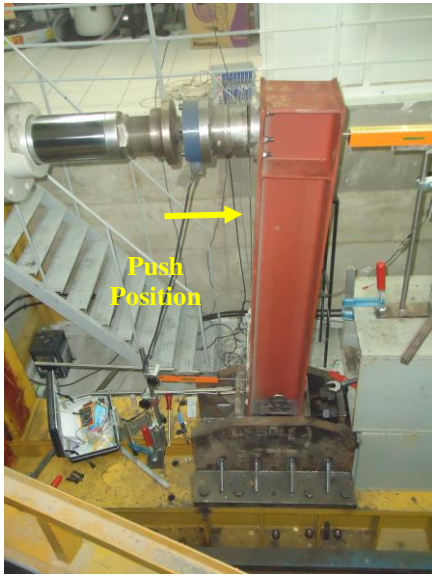
(a)
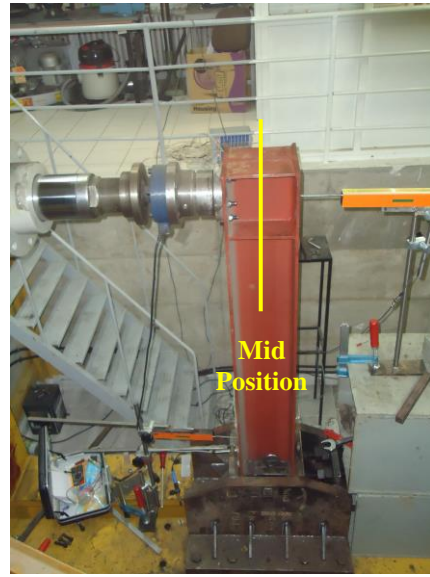
(b)
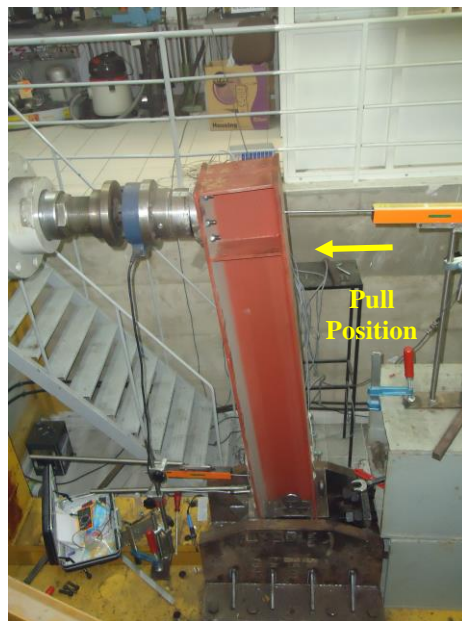
(c)

Figure 7.54. (a) Push direction, (b) Mid-position, (c) Pull direction.
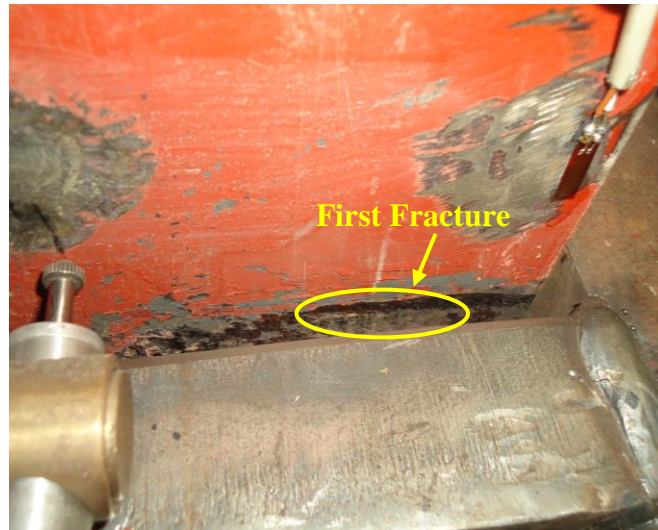
Figure 7.55. First fracture occurs.

7.16.2. Specimen-15: A Maximum Strain of $\varepsilon_a=\pm5\varepsilon_y$ in Bending about Strong Axis with No Axial Load

This specimen subjected to no vertical loads, is tested under cyclic lateral load normal to its strong axis. To obtain five times yield strain ($\varepsilon_a=\pm5\varepsilon_y$), 97 mm lateral displacements are applied on the push and pull side. To reach these displacements, maximum compression and tension forces 230 kN, respectively are applied during the push and pull of first cycle.

The cracks firstly developed in the intersect lines of flanges and webs, and then expanded with the following cycles. Finally the specimen fractured due to the low cycle fatigue when the steel HP 260x75 is reached to 204 cycles.

7.16.3. Specimen-16: A Maximum Strain of $\varepsilon_a=\pm10\varepsilon_y$ in Bending about Strong Axis with No Axial Load

This specimen is tested under cyclic lateral load normal to its strong axis; no vertical loads are applied to the pile. Using a servo hydraulic actuator operated in displacement control, the amount of cyclic displacement is controlled such that a maximum strain of 0.017 which is equal to ten times yield strain ($\varepsilon_a = 10\varepsilon_y$) is developed as shown in Figure 7.56.

Total 230 mm lateral displacements are applied on the push and pull side to obtain ten times yield strain. To reach these displacements, maximum compression and tension forces 225 kN, and 225 kN respectively are applied during the push and pull of first cycle as seen in Figure 7.57. The results obtained from experimental test on HP220x57 section demonstrate that first fracture begins 96 cycles. After 96 cycles, fracture begins expansion. Finally, low cycle fatigue occurs when steel HP220x57 section is reached to the 147 cycles.
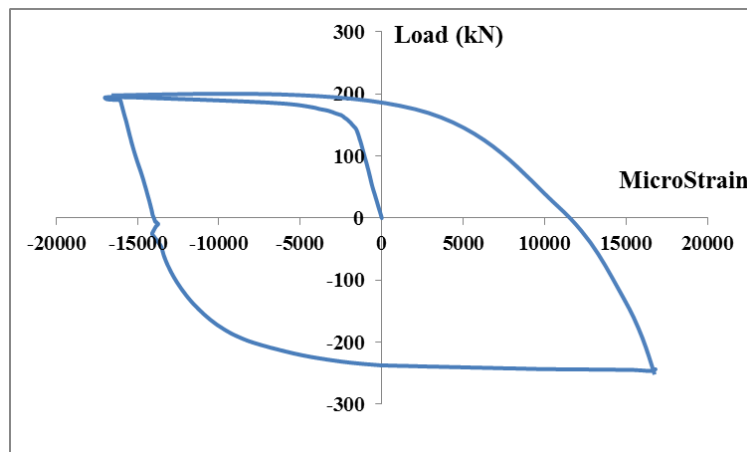
Figure 7.56. HP260x75 pile specimen-16 Lateral Load-strain Relationship.

194

7.16.4. Specimen-17: A Maximum Strain of $\varepsilon_a=\pm15\varepsilon_y$ in Bending about Strong Axis with No Axial Load

This specimen subjected to no vertical loads, is tested under cyclic lateral load normal to its strong axis. To obtain fifteen times yield strain ($\varepsilon_a=\pm15\varepsilon_y$), 125 mm and 125 mm lateral displacements are applied on the push and pull side. To reach these displacements, maximum compression and tension forces 228 kN, and 228 kN respectively are applied during the push and pull of first.

The cracks firstly developed in the intersect lines of flanges and webs, and then expanded with the following cycles. The results obtained from experimental test on HP260x75 section demonstrate that first fracture begins 28 cycles. After 28 cycles, fracture begins expansion. Finally, low cycle fatigue occurs when steel HP2620x75 section is reached to the 61 cycles.

7.16.5. Specimen-18: A Maximum Strain of $\varepsilon_a=\pm20\varepsilon_y$ in Bending about Strong Axis with No Axial Load

This specimen subjected to no vertical loads, is tested under cyclic lateral load normal to its strong axis. To obtain twenty times yield strain ($\varepsilon_a=\pm20\varepsilon_y$), 131 mm and 131 mm lateral displacements are applied on the push and pull side. To reach these displacements, maximum compression and tension forces 245 kN, and 245 kN respectively are applied during the push and pull of first.

The cracks firstly developed in the intersect lines of flanges and webs, and then expanded with the following cycles. The results obtained from experimental test on HP260x75 section demonstrate that first fracture begins 28 cycles. After 14 cycles, fracture begins expansion. Finally, low cycle fatigue occurs when steel HP2620x75 section is reached to the 47 cycles.

7.16.6. Specimen-19: A Maximum Strain of $\varepsilon_a = \pm5\varepsilon_y$ in Bending about Strong Axis with Axial Load (P=0.075P$_y$)

This specimen is tested under cyclic lateral load normal to its strong axis; vertical loads are also applied to the pile to investigate the effect of axial load together with lateral load on HP 260x75 section. Using a servo hydraulic actuator operated in displacement control, the amount of cyclic displacement is controlled such that a maximum strain of 0.0085 which is equal to five times yield strain ($\varepsilon_a = 5\varepsilon_y$), is developed as shown in Figure 7.57. The maximum compression and tension forces 290 kN, and 285 kN respectively are applied during the push of first cycle, and mounted at a height of 1900 mm above the base. In addition, axial loads are also applied as 370 kN, 180 kN and 345 kN during the push, normal and pull direction together with the lateral loads. Average value of axial load is determined as 250 kN (*P=0.075P$_y$*). HP260x75 section under cyclic lateral load and axial load are shown in Figure 7.58. 83 mm and 83 mm lateral displacements are applied on the push and pull side to obtain five times yield strain as shown in Figure 7.59. Before first fracture begins, small lateral buckling started in 64 cycles and then lateral buckling expanded as shown in Figure 7.60. The results obtained from experimental test on HP 260x75 section demonstrate that first fracture begins 115 cycles as shown in Figure 7.61. After 115 cycles, fracture start expanding as shown in Figure 7.62. Finally, low cycle fatigue occurs when steel HP260x75 section is reached to the 145 cycles.

Figure 7.57. HP260x75 pile specimen-19 Lateral Load-strain Relationship.

Figure 7.58. Specimen-19 under cyclic lateral and axial load normal to its Strong axis.
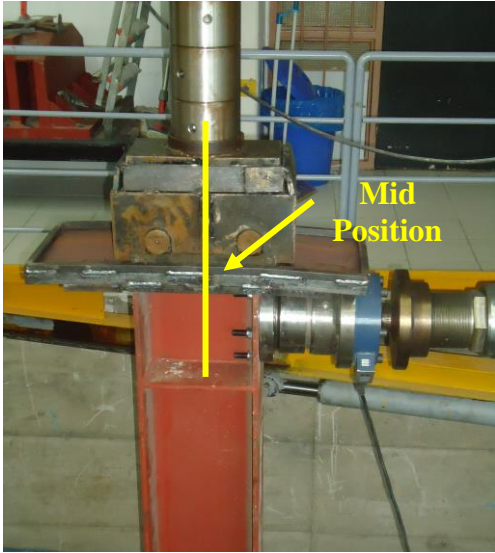
(a)
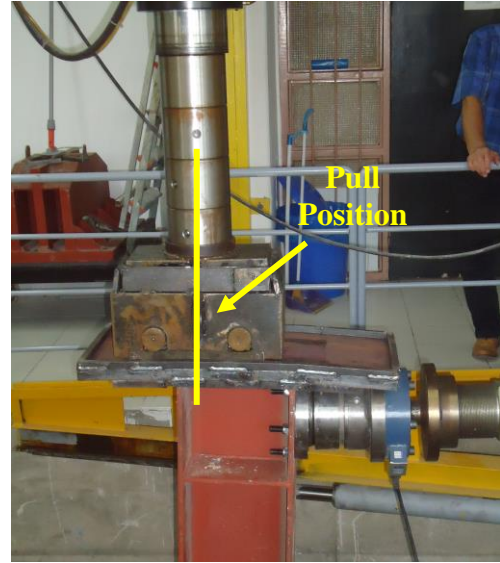
(b)
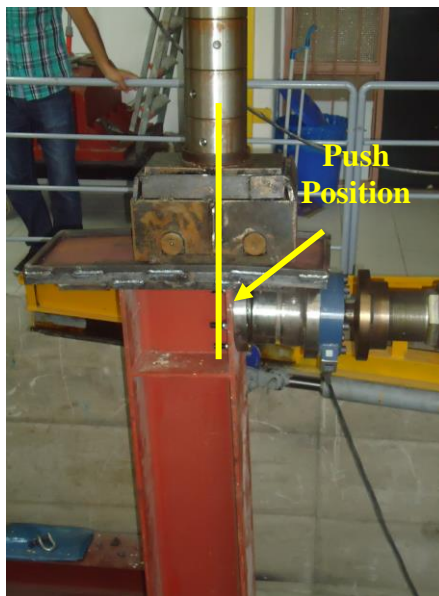
(c)

Figure 7.59. (a) Mid-position, (b) Push direction, (c) Pull direction.

(a)

(b)

(c)

Figure 7.60. Expanding lateral buckling occurring experiment.
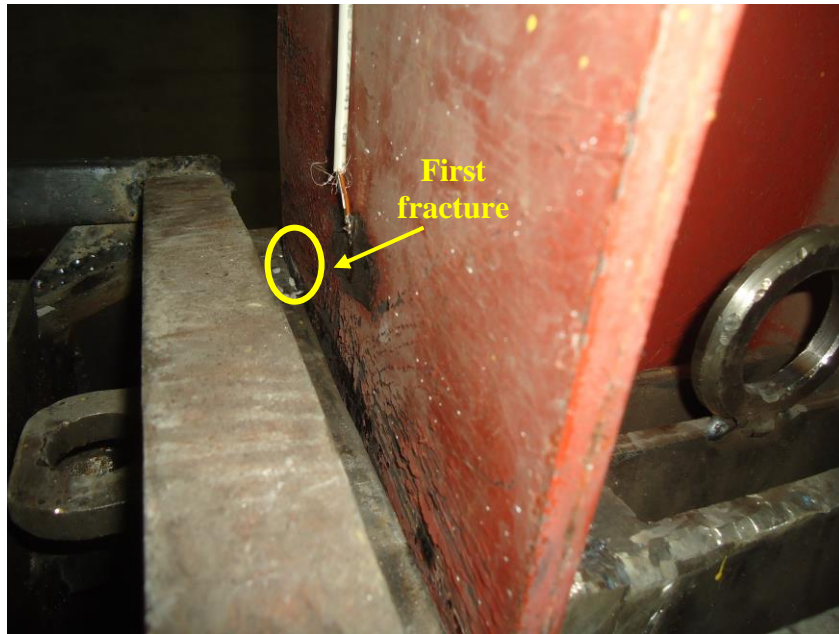
Figure 7.61. First fracture occurs.

Figure 7.62. Spread fracture and close view of the crack.

7.16.7. Specimen-20: A Maximum Strain of $\varepsilon_a=\pm5\varepsilon_y$ in Bending about Strong Axis with Axial Load $(P=0.11P_y)$

In this experiment, the level of axial load is changed to compare with results of specimen-19, which have same strain level but different axial load. For this purpose, 97 mm lateral displacements are applied on the push and pull side to obtain five times yield strain ($\varepsilon_a=\pm5\varepsilon_y$). To reach these displacements, maximum compression and tension forces 305 kN, and 300 kN respectively are applied during the push and pull of first cycle as shown in Figure 7.63. In addition to lateral load, axial loads are also applied as 455 kN, 250 kN and 430 kN during the push, normal and pull direction. Average value of axial load is determined as 360 kN ($P=0.11P_y$). The axial load during the push direction for 107 mm and pull direction for 78 mm is shown in Figure 7.64. The results obtained from experimental test on HP260x75 section demonstrate that first fracture begins 42 cycles. After 42 cycles, fracture starts to expand as shown in Figure 7.65 Finally, low cycle fatigue occurs when steel HP260x75 section is reached to the 89 cycles.

Figure 7.63. HP260x75 pile specimen-20 Lateral Load-strain Relationship.
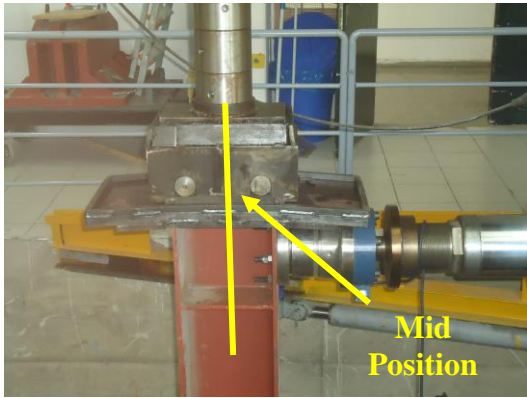
(a)
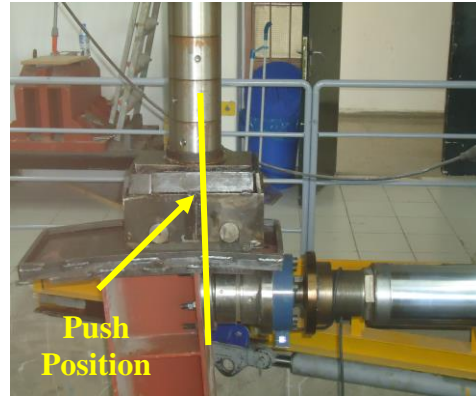
(b)
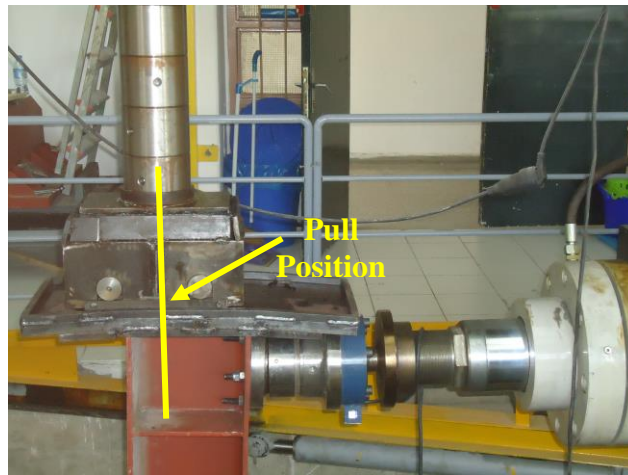
(c)

Figure 7.64. (a) Mid-position, (b) Push direction, (c) Pull direction.
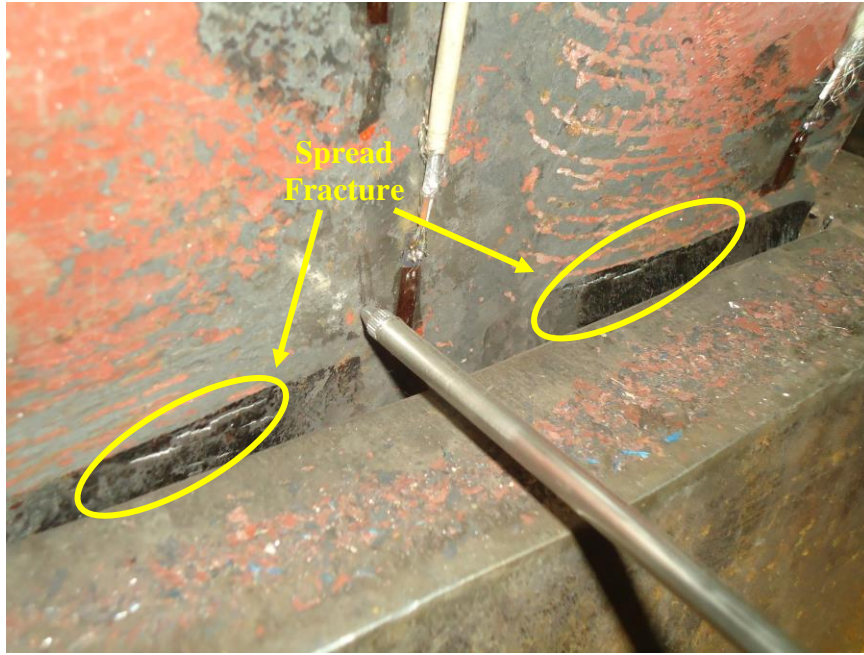
Figure 7.65. Spread fracture after 42 cycles.

In this experiment, lateral buckling occurred as seen in Figure 7.66. Local buckling of flanges takes place exactly above the 400 mm-high steel base fixture as seen in Figure 7.67. As a result of this large lateral buckling, distances of flanges expand from 225 mm to 266 mm as seen in Figure 7.67. Additionally, because of this large lateral buckling, strain gauges are not used to measure the strains on the surface of the steel H-piles at the most critical points.

Figure 7.66. Expanding lateral buckling occurring experiment.
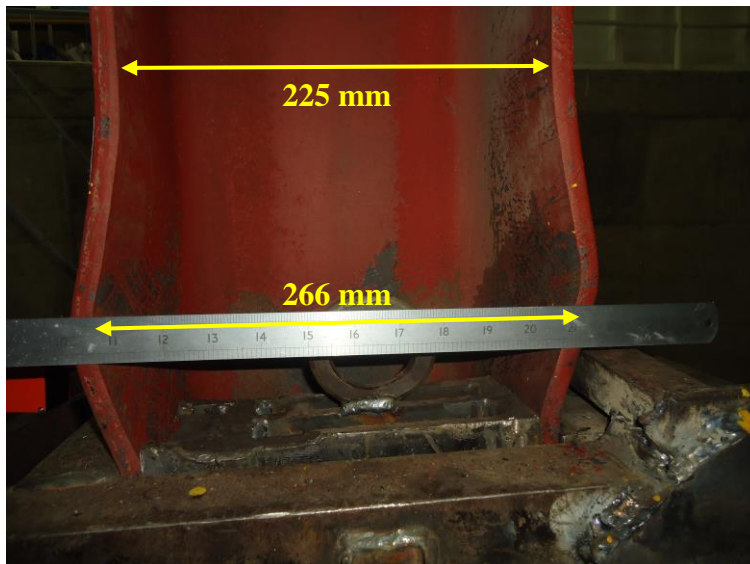
Figure 7.67. Expanding flanges because of lateral buckling

7.16.8. Specimen-21: A Maximum Strain of $\varepsilon_a=\pm5\varepsilon_y$ in Bending about Strong Axis with Axial Load (P=0.16 P_y)

In this experiment, the level of axial load is changed to compare with results of specimen-19 and specimen-20, which have same strain level but different axial load. For this purpose, 80 mm and 80 mm displacements are applied on the push and pull side to obtain five times yield strain ($\varepsilon_a=\pm5\varepsilon_y$). To reach these displacements, maximum compression and tension forces 295 kN, and 300 kN respectively are applied during the push and pull of first cycle. In addition to lateral load, axial loads are also applied as 600 kN, 390 kN and 550 kN during the push, normal and pull direction. Average value of axial load is determined as 530 kN ($P=0.16P_y$). The results obtained from experimental test on HP260x75 section demonstrate that first fracture begins 178 cycles. After 178 cycles, fracture starts to expand. Finally, low cycle fatigue occurs when steel HP260x75 section is reached to the 215 cycles. As observed from the figure 7.68, web begins buckling at the high level axial load. A series of photographs illustrates the crack propagation that occurred in the intersect lines of flanges and webs, and then expanded with the following cycles as seen in Figure 7.69.

Figure 7.68. Web buckling

(a)

(b)

Figure 7.69. Crack propagation

7.16.9. Specimen-22: A Maximum Strain of $\varepsilon_a= \pm5\varepsilon_y$ in Bending about Weak Axis without Axial Load (P=0P$_y$)

The specimen-22 is tested under same conditions as the specimen-15 to investigate the low cycle fatigue of HP steel pile oriented along the weak axis as shown in Figure 7.70. Using a servo hydraulic actuator operated in displacement control, the amount of cyclic displacement is controlled such that a maximum strain of 0.0085 which is equal to five times yield strain ($\varepsilon_a=\pm5\varepsilon_y$) as observed from the Figure 7.71. For this purpose, 51 mm and 53 mm displacements are applied on the push and pull side to obtain five times yield strain. To reach these displacements, maximum compression and tension forces 120 kN, and 112 kN respectively are applied during the push and pull of first cycle. The results obtained from experimental test on HP260x75 section oriented along the weak axis demonstrate that first fracture begins 291 cycles as shown in Figure 7.72-(a). After 291 cycles, fracture starts to expand as seen in Figure 7.72-(b)-(c) and (d). Finally, low cycle fatigue occurs when steel HP260x75 section is reached to the 561 cycles. For the strong axis, low cycle fatigue occurs 204 cycle to five times yield strain ($\varepsilon_a=\pm5\varepsilon_y$). As observed from the figure, more cycle is needed to reach low cycle fatigue failure when the piles oriented in weak axis than those oriented in strong axis.

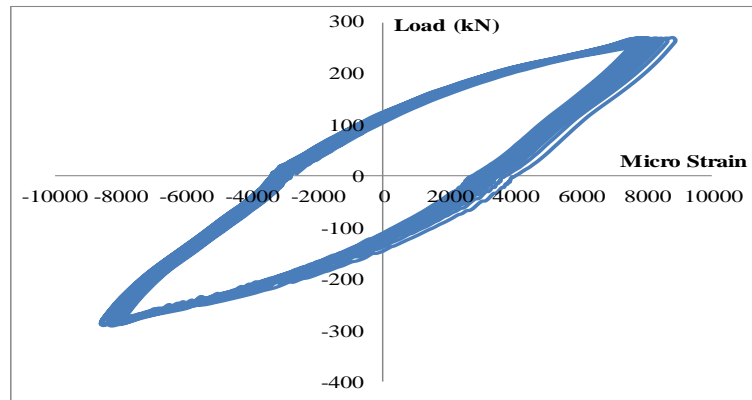**Figure 7.70.** Specimen-21 under cyclic lateral load normal to its Weak axis.
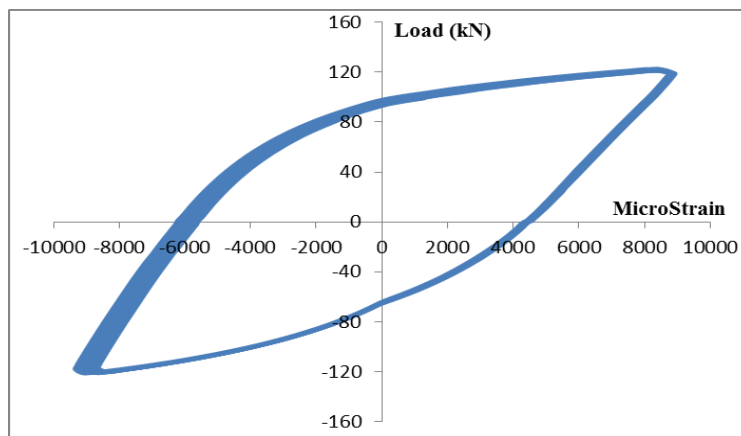
Figure 7.71. HP260x75 pile specimen-21 Lateral Load-strain Relationship for
Weak axis

208
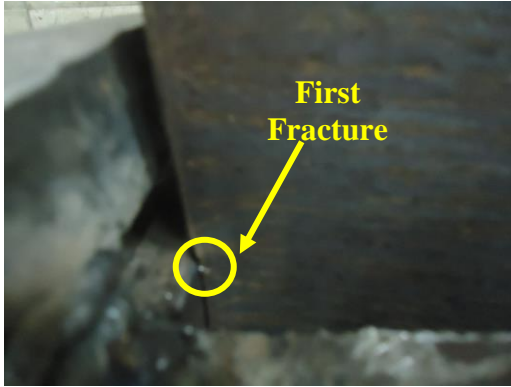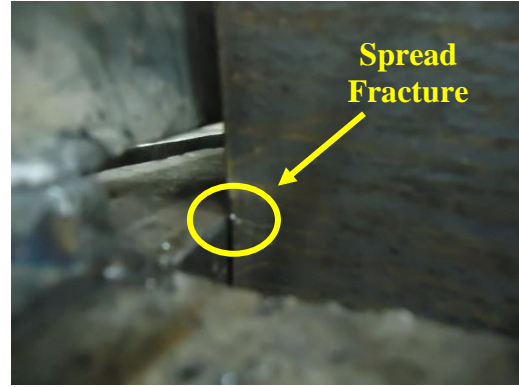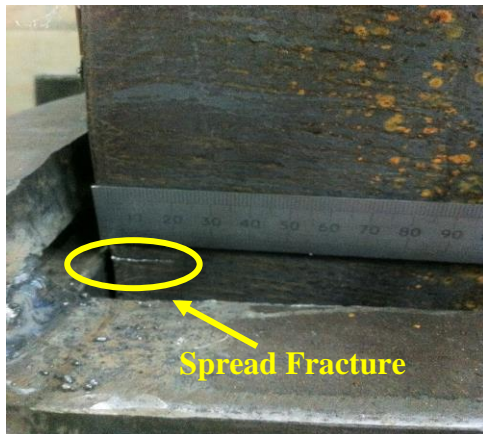
Figure 7.72. (a) First Fracture, (b) Spread Fracture after 377 cycles, (c) Spread Fracture after 407 cycles, (d) Spread Fracture after 441 cycles

7.16.10. Specimen-23: A Maximum Strain of $\varepsilon_a = \pm 10\varepsilon_y$ in Bending about Weak Axis without Axial Load ($P=0P_y$)

The specimen-22 is tested under same conditions as the specimen-16 to investigate the low cycle fatigue of HP steel pile oriented along the weak axis as shown in Figure 7.73. For this purpose, 75 mm and 75 mm displacements are applied on the push and pull side to obtain ten times yield strain for weak axis. To reach these displacements, maximum compression and tension forces 120 kN, and 118 kN respectively are applied during the push and pull of first cycle. Otherwise, 115 mm and 115 mm displacements are applied on the push and pull side to obtain ten times yield strain for strong axis. Additionally, to reach these displacements, maximum compression and tension forces 225 kN, and 225 kN respectively are applied.

(a)   (b)

Figure 7.73. (a) Specimen-16 under cyclic lateral load normal to its Strong axis, (b) Specimen-22 under cyclic lateral load normal to its Weak axis.

In the beginning of the experiment, after 36 cycles, local buckling is seen on the flange of HP260x75 section as seen in Figure 7.74. After 36 cycles, local buckling starts to expand. Because of this reason, low cycle fatigue occurs 121 cycles to ten times yield strain for weak axis.
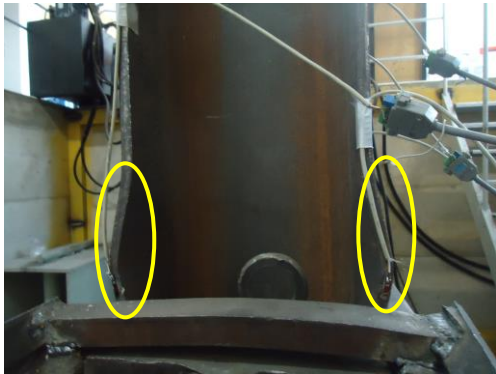
(a)

(b)

(c)

(d)

Figure 7.74. (a) Local buckling after 36 cycles, (b) Spread Fracture, (c) close view of the crack, (d) Fracture complete after 121 cycles.

7.16.11. Specimen-24: A Maximum Strain of $\varepsilon_a=\pm2.5\varepsilon_y$ in Bending about Weak Axis without Axial Load ($P=0P_y$)

This specimen subjected to no vertical loads, is tested under cyclic lateral load normal to its weak axis. To obtain the two and a half times yield strain ($\varepsilon_a=\pm2.5\varepsilon_y$), 38 mm lateral displacements are applied on the push and pull side. To reach these displacements, maximum compression and tension forces 96 kN, and 105 kN respectively are applied during the push and pull of first. The cracks firstly developed in the exterior surface of flanges, and then expanded with the following cycles. The results obtained from experimental test on HP260x75 section demonstrate that first fracture begins 2100 cycles. After 2100 cycles, fracture begins expansion. Finally, low cycle fatigue occurs when steel HP2620x75 section is reached to the 2736 cycles.

7.16.12. Specimen-25: A Maximum Strain of $\varepsilon_a=\pm15\varepsilon_y$ in Bending about Weak Axis without Axial Load ($P=0P_y$)

This specimen which is not subjected to vertical loads is tested under cyclic lateral load normal to its weak axis. To obtain fifteen times yield strain ($\varepsilon_a=\pm15\varepsilon_y$), 90 mm and 91 mm lateral displacements are applied on the push and pull side. To do so, maximum 138 kN compression and 138 kN tension forces are applied during the push and pull of first as shown in Figure 7.75. In the beginning of the experiment, after 3 cycles, it is observed that small lateral buckling occurs on the flange of HP260x75 section as seen in Figure 7.76. After 3 cycles, local buckling starts expanding as seen in Figure 7.76-(c) and (d). While width of the flange is 249 mm in the beginning of the experiment, width of the flange caused by local buckling is 280 mm after 26 cycles as shown in Figure 7.76-(d).
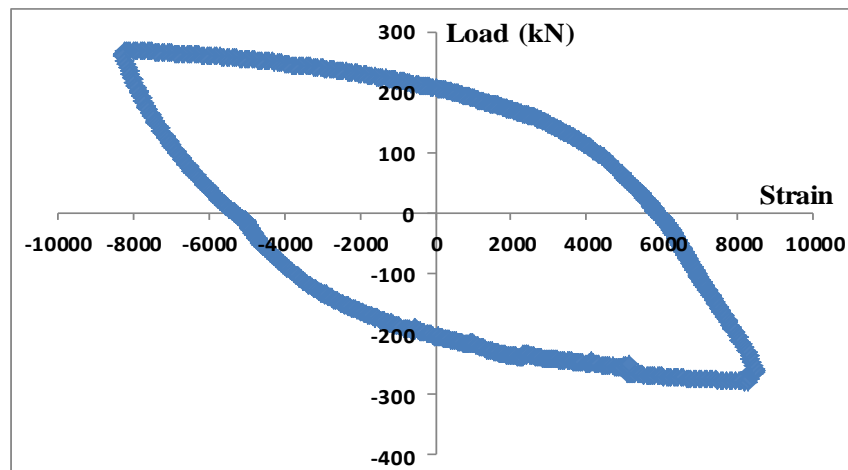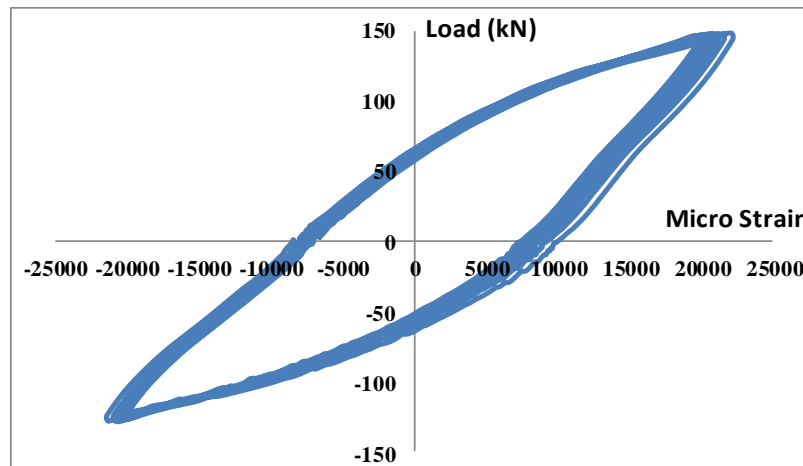
Figure 7.75. HP260x75 pile specimen-24 Lateral Load-strain Relationship

At first, the cracks occur in the interior surface of flanges, and then expand during the following cycles as seen in Figure 7.77 (a) and (b). Finally, low cycle fatigue comes into picture and flanges of steel HP2620x75 section rupture to the 44 cycles as seen in Figure 7.77 (c) and (d).

(a)
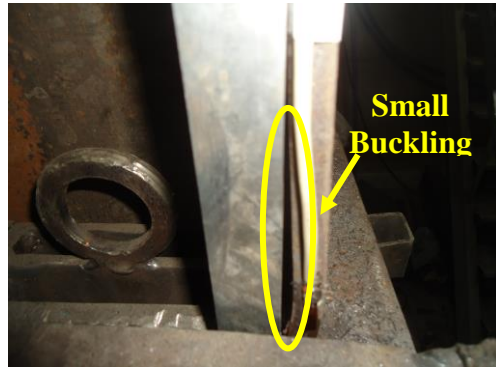
(b)
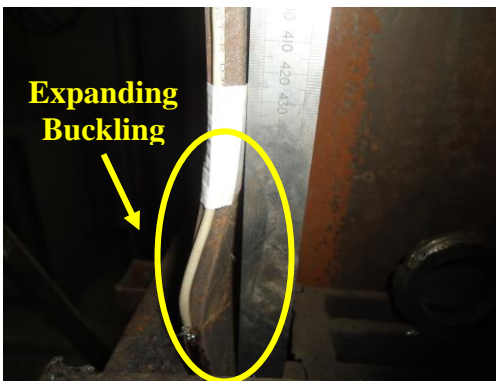
(c)
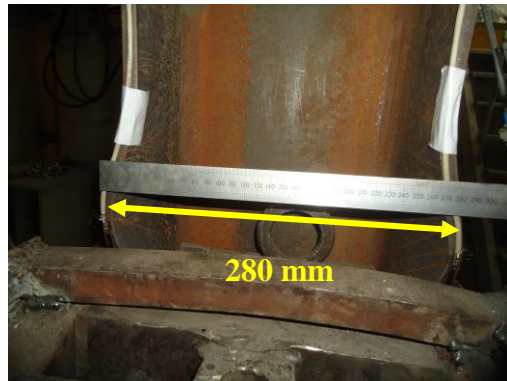
(d)

Figure 7.76. (a) In the beginning of experiment, (b) Local buckling occurring after 3 cycles, (c) close view of the buckling after 17 cycles (d) close view of the buckling after 26cycles

(a)   (b)

(c)   (d)

Figure 7.77. (a) Spread Fracture after 17 cycles, (b) Spread Fracture, (c) close
view of the crack, (d) Fracture complete after 44 cycles.

7.16.13. Specimen-26: A Maximum Strain of $\varepsilon_a=\pm5\varepsilon_y$ in Bending about Weak Axis without Axial Load (P=0.075P$_y$)

The specimen-26 is tested under same loading conditions as the specimen-19 to investigate the low cycle fatigue of HP steel pile oriented along the weak axis and compare to results which is for strong axis and weak axis as observed from the Figure 7.78. Using a servo hydraulic actuator operated in displacement control, the amount of cyclic displacement is controlled to attain a maximum strain of 0.0085 which is equal to five times yield strain ($\varepsilon_a=\pm5\varepsilon_y$). For this purpose, 55 mm and 50 mm displacements are applied on the push and pull side to obtain five times yield strain. To reach these displacements, maximum 138 kN compression and tension forces respectively are applied during the push and pull of first cycle. While it is observed that the local buckling occurs exactly above the 450 mm-high steel base fixture for the weak axis as shown in Figure 7.79-(a), the local buckling occurs exactly above the 550 mm-high steel base fixture for the strong axis as shown in Figure 7.80-(b). The results obtained from experimental test on HP260x75 section oriented along the weak axis demonstrate that first fracture begins 186 cycles. After 186 cycles, fracture starts to expand. Finally, low cycle fatigue occurs when steel HP260x75 section is reached to the 220 cycles. Additionally, it is observed that fracture occurs above 465 mm-high steel base fixture for the weak axis. On the other hand, for the strong axis, fracture occurs exactly above the 450 mm-high steel base fixture. Close view of the fracture may be observed from Figure 7.81-(a).
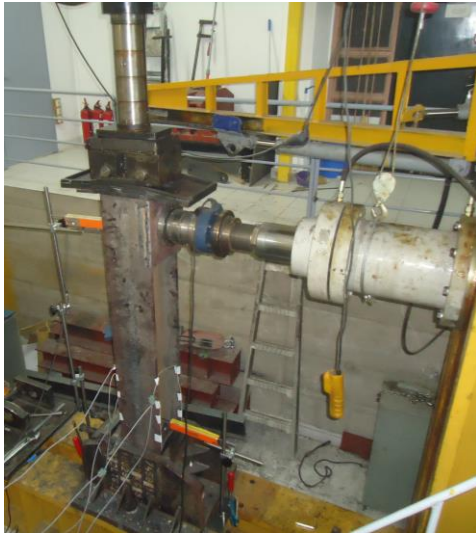
Figure 7.78. (a) Specimen-25 under cyclic lateral and axial load normal to its Weak axis, (b) Specimen-19 under cyclic lateral and axial load normal to its Strong axis.
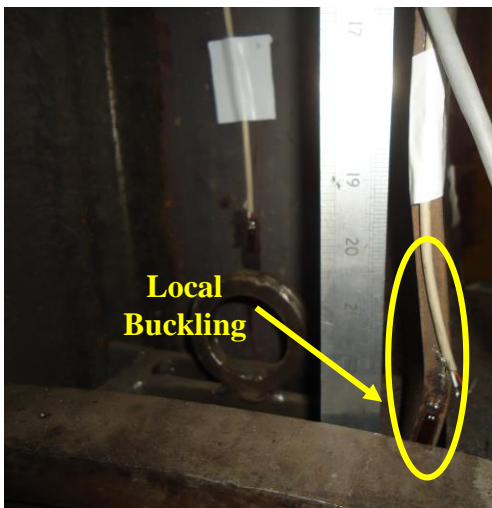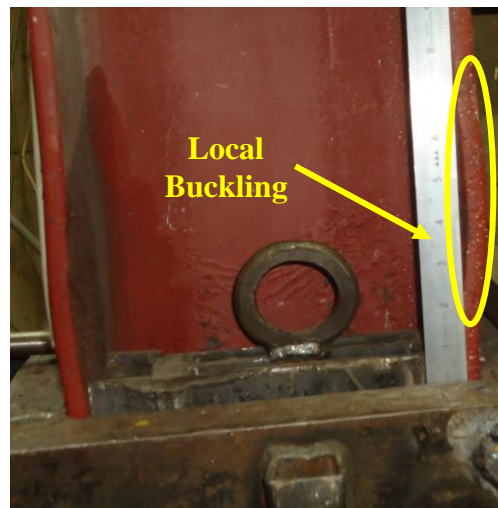
Figure 7.79. (a) Local Buckling occurs in Specimen-25 under cyclic lateral and axial load normal to its Weak axis, (b) Local Buckling occurs in Specimen-19 under cyclic lateral and axial load normal to its Strong axis.

217
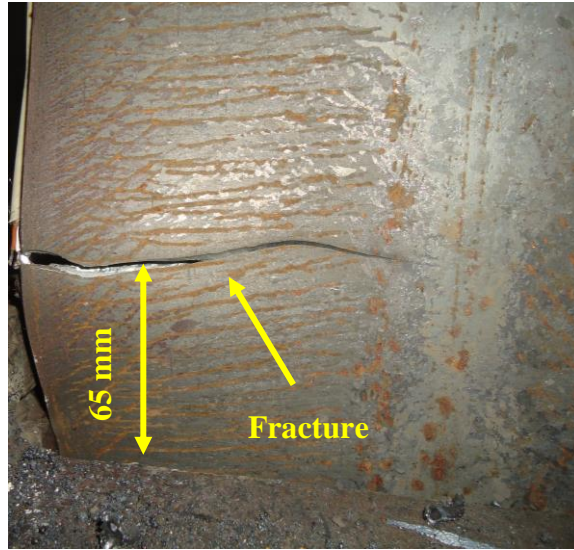
(a)
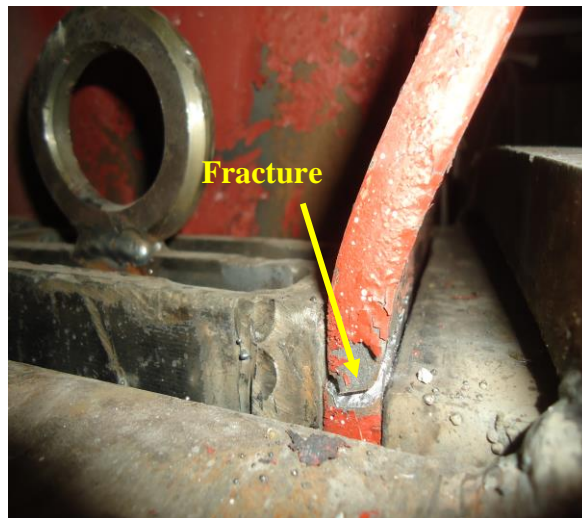
(b)

Figure 7.80. (a) Fracture occurs in Specimen-25 under cyclic lateral and axial load normal to its Weak axis, (b) Fracture occurs in Specimen-19 under cyclic lateral and axial load normal to its Strong axis.

7.17. Summary of Experiments for HP 260x 75 Steel Section

Experimental tests of HP260x75 H-pile specimens are conducted to investigate the effect of several parameters on the low cycle fatigue life of integral bridge steel H-piles subjected to cyclic thermal strains as done for HP220x57 H-pile specimens. For this purpose, thirteen cyclic tests of HP260x75 steel sections subjected to strong and weak axes bending are conducted at various strain amplitudes to investigate the effect of strain amplitude and pile bending orientation on the low cycle fatigue performance. Additional tests are conducted to investigate the effect of axial loads on the low cycle fatigue performance of steel H-piles used in integral bridges. It is observed that, as expected, number of cycles to failure is inversely proportional to the strain amplitude. Furthermore, piles oriented to bend about their weak axes are observed to have a better low cycle fatigue performance. The effect of axial load is observed to have a significant effect on the low cycle fatigue performance of steel H-piles in two ways: (i) when the pile is subjected to moderate strain amplitudes (five times the yield strain), the presence of axial load is observed to enhance the low cycle fatigue life of the pile. This mainly due to the fact that, the presence of axial load decreases the amplitude of the tensile strain that results in cracking of the material (it delays the initiation of the crack), (ii) when the pile is subjected to larger strain amplitudes (10 times the yield strain), the presence of axial load is observed to decrease the low cycle fatigue life of the pile. This is mainly due to local buckling of the flange under the effect of compressive stresses from the axial load and high compressive strains due to the effect of bending. Local buckling increases the local curvature and strains. This locally accelerates the cracking of the material. Consequently, it is also observed that the pile size does not affect the low cycle fatigue performance. That is, piles subjected to the same cyclic flexural strain amplitude and identical axial stress level, exhibit similar low cycle fatigue performance.

Table 7.4. Experiments results for HP260x75 Steel Section oriented along the Strong Axis.

Section Type	Load Type	Test Number	Axial load	Strain Amplitude (ε_a)	Number of Cycles	
					First Crack	Fracture
HP 260x75 Strong Axis	*No Axial Load*	14	P=0	$2.5\varepsilon_y$	1823	2358
		15	P=0	$5\varepsilon_y$	124	204
		16	P=0	$10\varepsilon_y$	96	147
		17	P=0	$15\varepsilon_y$	28	61
		18	P=0	$20\varepsilon_y$	14	47
	Axial + Lateral load	19	P=0.075P$_y$	$5\varepsilon_y$	115	145
		20	P=0.11P$_y$	$5\varepsilon_y$	42	89
		21	P=0.16P$_y$	$5\varepsilon_y$	178	215

Table 7.5. Experiments results for HP260x75 Steel Section oriented along the Weak Axis.

Section Type	Load Type	Test Number	Axial load	Strain Amplitude (ε_a)	Number of Cycles	
					First Crack	Fracture
HP 260x75 Weak Axis	*No Axial Load*	24	P=0	$2.5\varepsilon_y$	2100	2736
		22	P=0	$5\varepsilon_y$	291	561
		23	P=0	$10\varepsilon_y$	46	121
		25	P=0	$15\varepsilon_y$	17	44
	Axial + Lateral load	26	P=0.075P$_y$	$5\varepsilon_y$	186	220

7.18. Effect of Pile Length for HP Steel Section

7.18.1. Specimen-27: A Maximum Strain of $\varepsilon_a=\pm5\varepsilon_y$ in Bending about Strong Axis with No Axial Load for HP 220x57 Specimen Having 1.30 m Length

In this phase of the research study, the effect of pile length for steel H piles is investigated by performing comparable tests on the HP 220x57 sections having same dimensions, but different lengths of piles. For this purpose, the equivalent pile length that will be used in this phase of this research study is determined as 1.30 m for HP220x57. Then, HP section is cut as having 1.30 m length. Cutting process of test specimens from the HP 220x57 section using CNC (Computer Numerical Control) method are mentioned earlier in chapter 4. To investigate the effect of pile length, the HP 220x57 specimen having 1.30 m length is tested under same loading conditions as the specimen-1, specimen-2 and specimen-3 as mentioned in section 7.1. The test set up for the HP 220x57 section having 1.3 m and 1.9 m is shown in Figure 7.81. Using a servo hydraulic actuator operated in displacement control, the amount of cyclic displacement is controlled to attain a maximum strain of 0.0075 which is equal to five times yield strain ($\varepsilon_a=\pm5\varepsilon_y$). To obtain five times yield strain ($\varepsilon_a=\pm5\varepsilon_y$), 58 mm and 58 mm lateral displacements are applied on the push and pull side. To do so, maximum 285 kN compression and tension forces are applied during the push and pull of first. On the other hand, 70 mm lateral displacements and maximum 160 kN compression and tension forces respectively are applied on the push and pull side for the HP 220x57 section having 1.9 m as the specimen-1 and the specimen-2. The results obtained from experimental test on HP220x57 section having 1.3 m and 1.9 m demonstrate that it needs more lateral force for the HP 220x57 section having 1.3 m than for the HP 220x57 section having 1.9 m by way of the pile length as shown in Figure 7.82.

After 56 cycles, it is observed that lateral buckling occurs above 420 mm-high steel base fixture for the HP220x57 specimen having 1.30 m length. Furthermore, as seen in Figure 7.83, flange expands about 1.8 mm in the HP220x57 specimen having 1.30 m length. On the other hand, it is seen that flange expands about 1.7 mm in the HP220x57 specimen having 1.90 m length. Consequently, it is clear that pile length does not affect the buckling deformation of the flange.

The results obtained from experimental test on HP220x57 section oriented along the strong axis demonstrate that the cracks firstly begins 87 cycles in the intersect lines of flanges and webs, and then expanded with the following cycles as seen in Figure 7.84. Finally, low cycle fatigue occurs when steel HP220x57 section is reached to the 104 cycles.

(a)

(b)

Figure 7.81. (a) the HP 220x57 specimen having 1.30 m length, (b) the HP 220x57 specimen having 1.90 m length
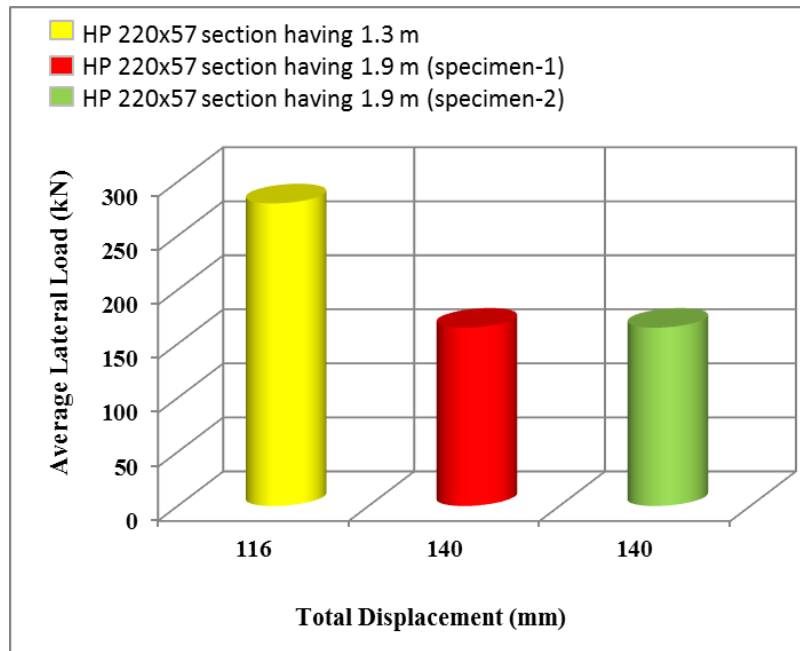
Figure 7.82. Experiment test results for different pile lengths.

(a)   (b)
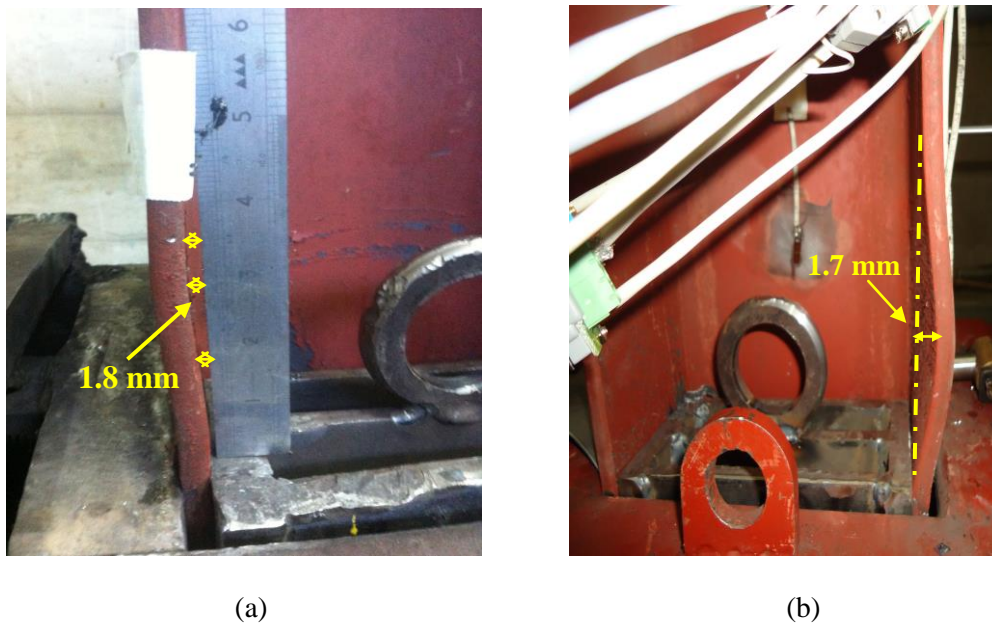
Figure 7.83. (a) Local Buckling occurs in the HP 220x57 specimen having 1.30
m length, (b) Local Buckling occurs in the HP 220x57 specimen
having 1.90 m length
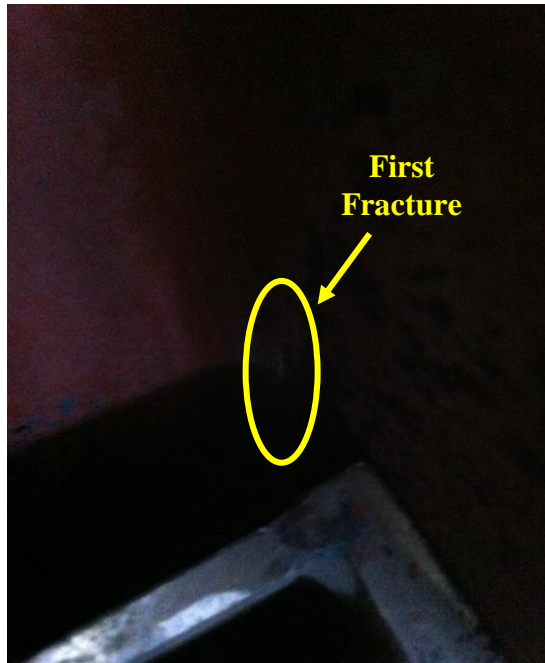
(a)
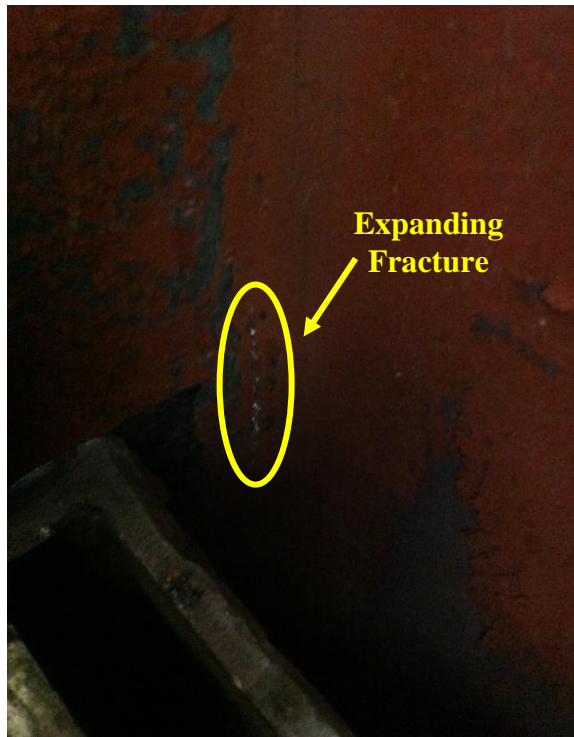
(b)

Figure 7.84. (a) First fracture after 36 cycles, (b) Expanding Fracture

7.18.2. Specimen-28: A Maximum Strain of $\varepsilon_a = \pm 5\varepsilon_y$ in Bending about Strong Axis with No Axial Load for HP 220x57 Specimen Having 1.30 m Length

This specimen is tested before under the same conditions as specimen-16. The lateral actuator is mounted at a height of 1300 mm above the base. In this phase of the experiment, 59 mm and 58 mm displacements are applied on the push and pull side to obtain five times yield strain for the HP 220x57 section having 1.3 m. To reach these displacements, maximum compression and tension forces 280 kN, and 282 kN respectively are applied during the push and pull of first cycle. On the other hand, 70 mm lateral displacements and maximum 160 kN compression and tension forces respectively are applied on the push and pull side for the HP 220x57 section having 1.9 m as the specimen-1 as shown in Figure 7.85. As observed in Figure 7.86, to arrive five times yield strain for the HP 220x57 section having 1.3 m, 50 % more lateral loads is needed than for the HP 220x57 section having 1.9 m.
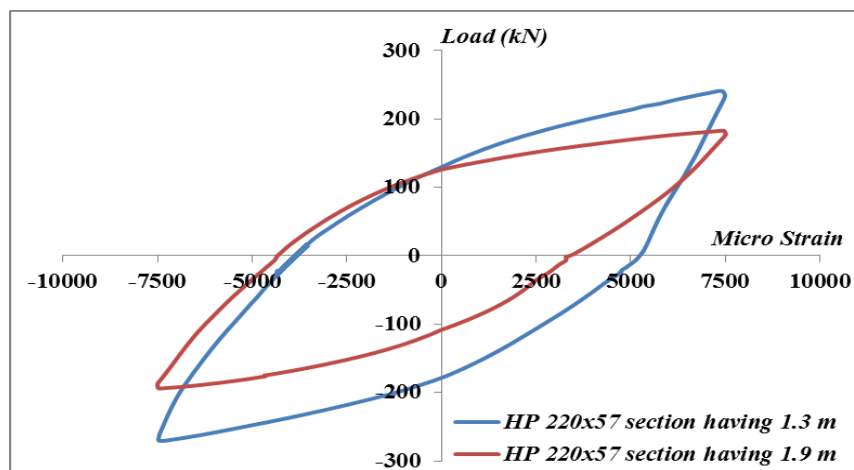
Figure 7.85. HP 220x57 specimen having 1.30 m length and 1.9 m Lateral Load-strain Relationship

The results obtained from experimental test on HP220x57 section having 1.3 m and oriented along the strong axis demonstrate that the cracks firstly begins 68 cycles in the intersect lines of flanges and webs, and then expanded with the following cycles. Finally, low cycle fatigue occurs when steel HP220x57 section is reached to the 117 cycles.

7.18.3. Specimen-29: A Maximum Strain of $\varepsilon_a=\pm5\varepsilon_y$ in Bending about Strong Axis with No Axial Load for HP 220x57 Specimen Having 1.30 m Length

In the previous two experiments (specimen-27 and specimen-28), the effect of pile length is investigated for HP220x57 section having 1.3 m. The results obtained from previous two experiments on HP220x57 section having 1.3 m demonstrate that 104 and 117 cycles are completed until low cycle fatigue in steel HP220x57 section having 1.3 m is reached.

In this experiment, to compare test results (specimen-1, specimen-2, specimen-3 for HP220x57 sections having 1.9 m and specimen-27, specimen-28 for HP220x57 sections having 1.3 m), this experiment is done. For this purpose, the lateral load is applied to obtain a maximum strain of 0.0075 which is equal to five times yield strain ($\varepsilon_a=\pm5\varepsilon_y$). To do so, 59 mm and 59 mm lateral displacements are applied on the push and pull side. To obtain these lateral displacements, maximum 282 kN compression and 280 kN tension forces are applied during the push and pull of first. The results obtained from experimental test on HP220x57 section having 1.3 m demonstrate that the cracks firstly begins 73 cycles in the intersect lines of flanges and webs, and then expanded with the following cycles. Finally, low cycle fatigue occurs when steel HP220x57 section is reached to the 123 cycles. The test results are shown in Table 7.6.

Table 7.6. Effect of pile length

Section Type	Load Type	Pile Length (m)	Test Number	Strain Amplitude (ε_a)	Number of Cycles	
					First Crack	Fracture
HP 220x57 Strong Axis	*No Axial Load*	1.9	1	$5\varepsilon_y$	145	200
			2	$5\varepsilon_y$	220	239
			3	$5\varepsilon_y$	232	285
		1.3	27	$5\varepsilon_y$	87	104
			28	$5\varepsilon_y$	68	117
			29	$5\varepsilon_y$	73	123

7.19. Preventing Local Buckling

As mentioned in earlier section, lateral local buckling occurs at high strain rates. As a result of this large lateral buckling, fracture starts earlier and also low cycle fatigue in steel HP sections takes place at smaller cycles. To prevent lateral local buckling occurring at high strain rates, stiffener is designed and in this experiment, the effect of stiffener designed is investigated at high strain rates. As shown in Figure 7.86, stiffener is established on the steel HP sections. Details of stiffener are seen in Figure 7.87. In this experiment, to investigate the effect of stiffener designed and compare the results, test set up is established as seen in Figure 7.88. Furthermore, details of stiffener are shown on test set up in Figure 7.89. As seen in the details, 7 mm thickness source is used to refuse breaking. Thickness of the stiffener is taken as 10 mm as thickness of the flange.

As mentioned earlier in the section 7.11, 95 mm and 90 mm displacements are applied on the push and pull side to obtain ten times yield strain ($\varepsilon_a=\pm10\varepsilon_y$) with the axial load. To reach these displacements, maximum compression and tension forces 182 kN, and 175 kN respectively are applied during the push and pull of first cycle. In addition to lateral load, axial loads are also applied as 364 kN, 158 kN and 280 kN during the push, normal and pull direction. Average value of axial load is determined as 250 kN ($P=0.11P_y$). The results obtained from experimental test on HP220x57 section demonstrate that first fracture begins 52 cycles. After 52 cycles, fracture starts to expand. Finally, low cycle fatigue occurs when steel HP220x57 section is reached to the 74 cycles. This experiment reveals that low cycle fatigue occurs earlier with effect of axial load with high strain level. Additionally, larger local buckling occurs in the higher strain levels.

To compare the effect of stiffener designed, ten times yield strain ($\varepsilon_a=\pm10\varepsilon_y$) with the axial load is reached on HP220x57 section as mentioned in the section 7.11. For this reason, the 90 mm and 90 mm displacements are applied on the push and pull side. Consequently, lateral load-strain relationship is obtained as seen in Figure 7.90.

The results obtained from experimental test on HP220x57 section having stiffener designed demonstrate that the cracks firstly begins 69 cycles, and then expanded with the following cycles. Finally, low cycle fatigue occurs when steel HP220x57 section is reached to the 97 cycles as shown in Figure 7.91. Furthermore, the effect of stiffener is seen in Figure 7.92. Lateral buckling does not occur in so far as effect of stiffener. On the other hand, as mentioned in section 7.11, low cycle fatigue occurs when steel HP220x57 section is reached to the 74 cycles. As seen from the test results in Figure 7.93, stiffener is so effective to prevent the lateral buckling. Thus, the effect of fatigue on HP steel section decreases and service life of HP section increase more than 20%.

Using the strain gauge attachment on the stiffener, strain values causing lateral loads and axial load are obtained on the stiffener. The strain values show that strain occurring on the stiffener is one percent of the strain occurring on the HP steel specimen. Additionally, at the end of the experiment, it is seen that stiffener at high strain levels works very well because of the thickness source. It shows that thickness source is so important as much as stiffener.

Actuator

Load Cell#1-1

LVDT#2-1

100 mm

Ball Joint

Centerline of Actuator

10 mm thick Steel Bar

Stand

1800 mm

LVDT

500 mm

10 mm

Stand

Strain Gauges

Steel Frame

Lateral Supports

Actuato

Centerline of Actuator

120 mm

LVDT#2-1

HP 220x57

48 mm

48 mm

10 mm

Detail-A

500

Strain Gauge

10

Strain Gauges

Lateral Support

Steel Frame
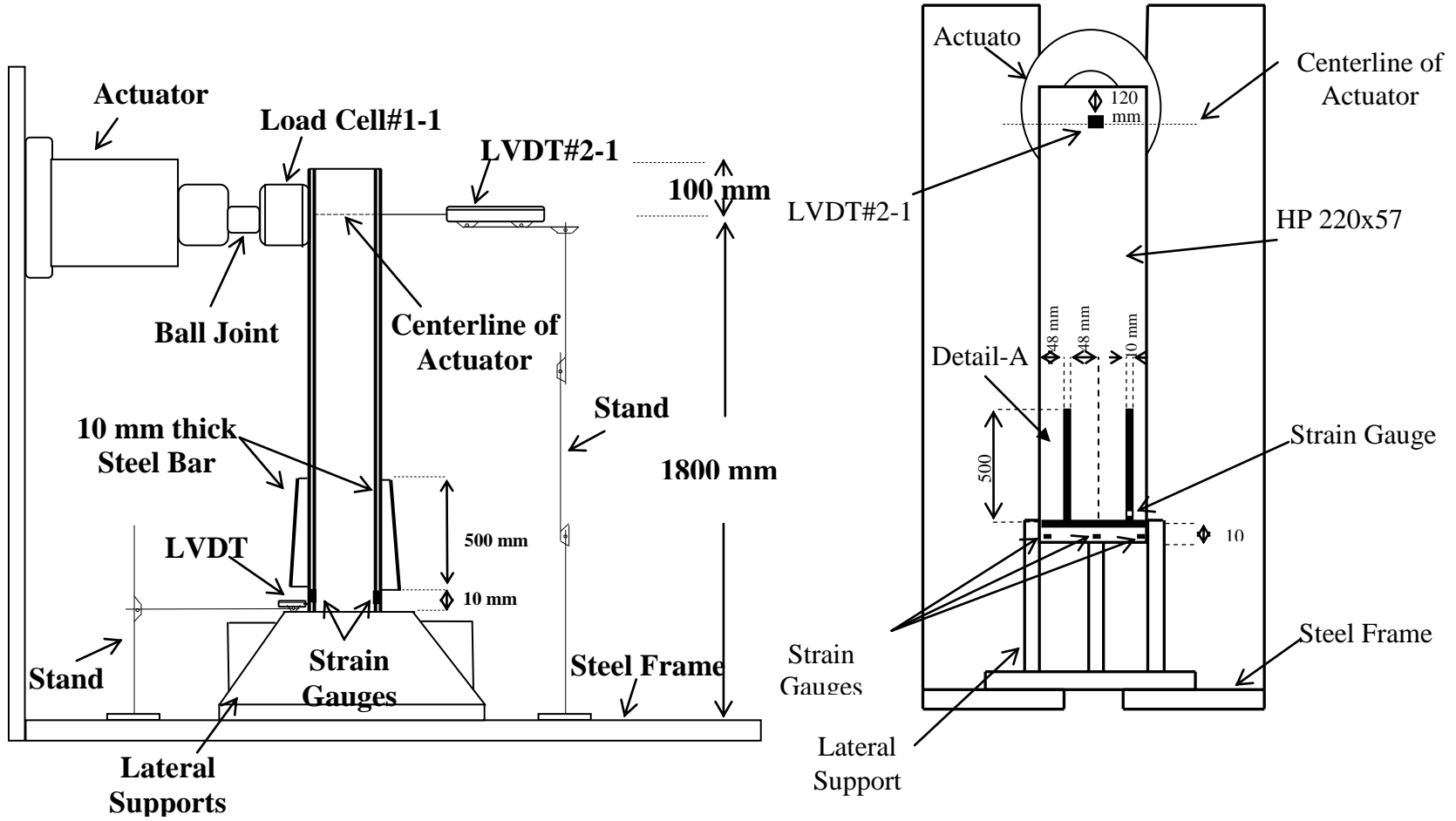
Figure 7.86. Stiffener designed
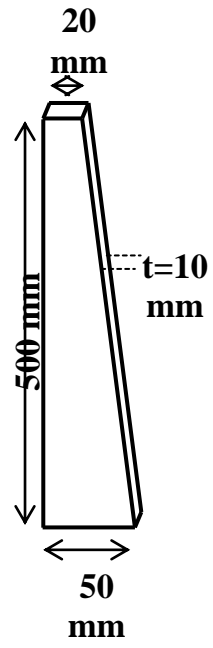
Figure 7.87. Detail-A
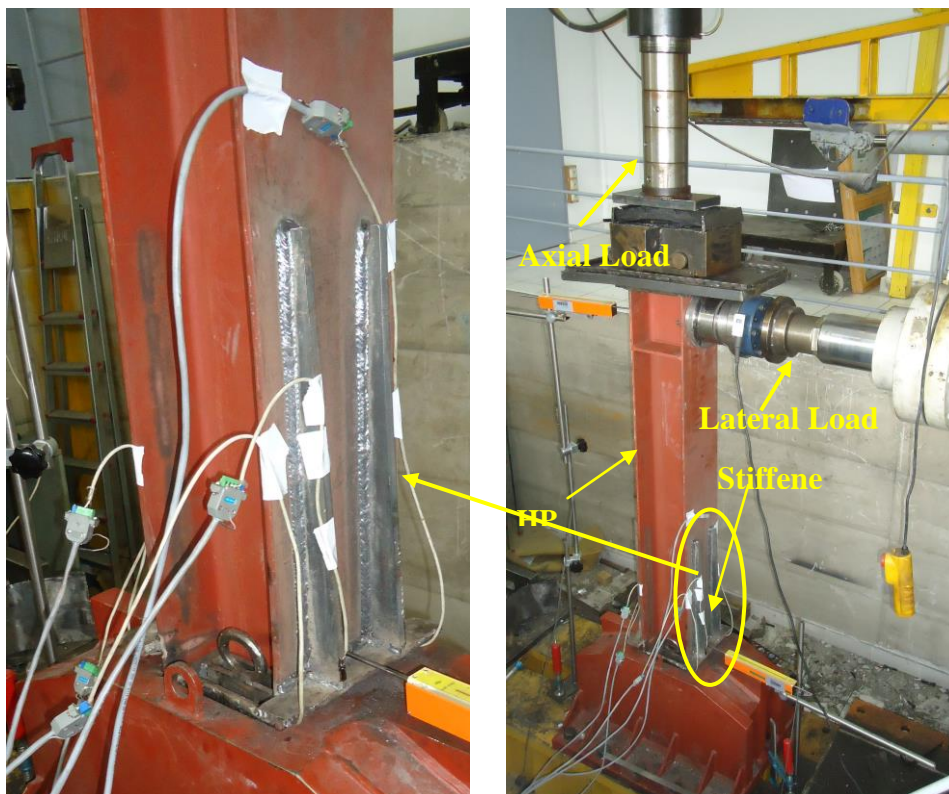
Figure 7.88. Test set up

Figure 7.89. Stiffener details
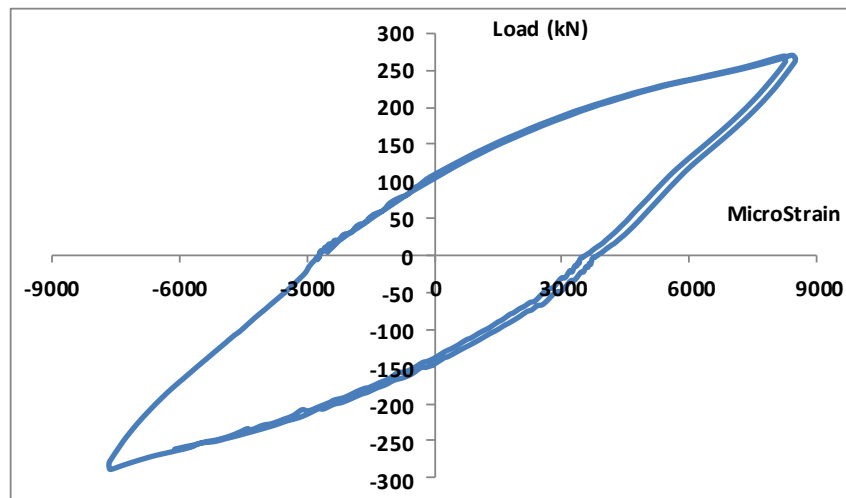
Figure 7.90. Lateral Load-strain Relationship

Figure 7.91. Spread Fracture after 97 cycles

235

Figure 7.92. Effect of stiffener designed after 97 cycles

<p style="text-align: center;">(a)</p>

<p style="text-align: center;">(b)</p>

Figure 7.93. (a) HP 220x57 Strong Axis for $10\varepsilon_y$ (P=0.11P$_y$) without stiffener, (b) HP 220x57 Strong Axis for $10\varepsilon_y$ (P=0.11P$_y$) with stiffener

7.20. The Effect of Small Strain Cycles in the Piles within the Amplitude of the Large Strain Cycles

Due to seasonal (summer and winter) temperature changes, one dominant cyclic lateral displacement of steel H-piles at the abutments occurs each year. Additionally, due to daily and/or weekly temperature fluctuations, numerous smaller cyclic lateral displacements also occur. This is confirmed by research studies and by the strain vs. time records of instrumented steel H-piles for integral bridges until now. Although bridge engineers have already confirmed that smaller cyclic lateral displacements also occur, there is neither a research nor an experimental study in the literature about the effect of small cycle lateral displacements in the steel H piles. In this phase of the research study, the effect of small cyclic lateral displacements of steel H-piles due to daily and/or weekly temperature fluctuations is investigated.

7.20.1. Specimen-31: Effect of Beta (β=0.3) with a Maximum Strain of $\varepsilon_a=\pm5\varepsilon_y$ in Bending about Strong Axis with No Axial Load for HP220x57 Section

As mentioned earlier in the section 7.1, the effect of one dominant cyclic lateral displacement of steel HP220x57 section is investigated. However, the effect of the small cycle lateral displacements within the amplitude of the large strain cycles on HP steel specimen has not been taken into account in the earlier experiments. In this phase of the research study, the effect of small cyclic lateral displacements on HP220x57 section is considered together with the amplitude of the large strain cycles as seen in Figure 7.94. The cyclic displacement of steel H-piles based on loading and unloading due to small cycles is also shown in Figure 7.95.
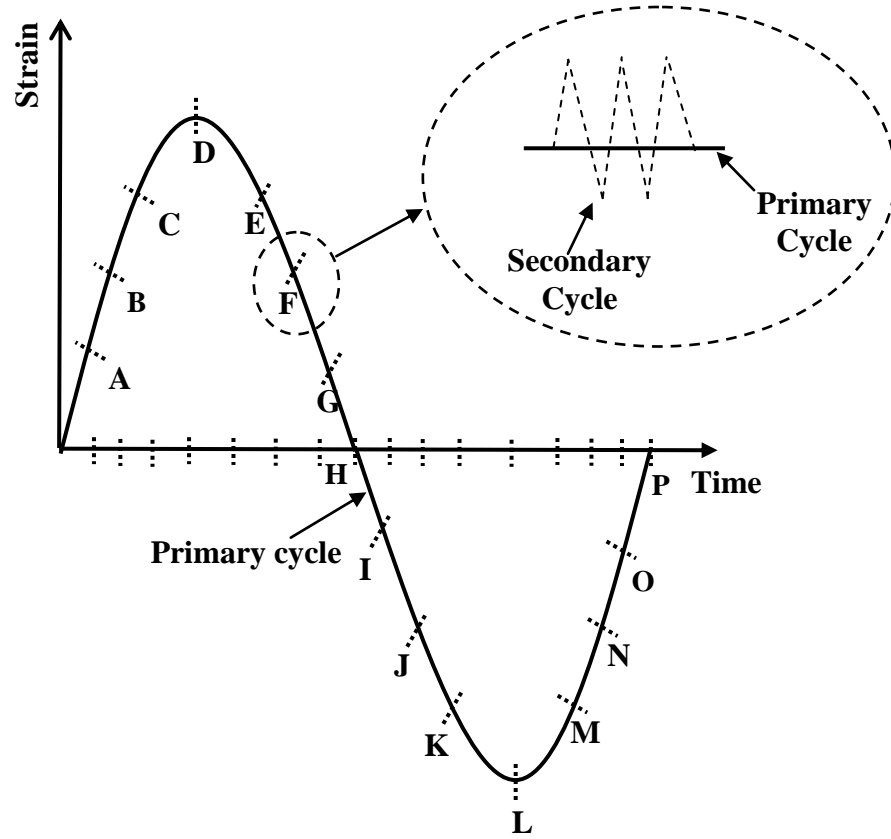
Figure 7.94. Loading and unloading due to small cycles on strain vs. time
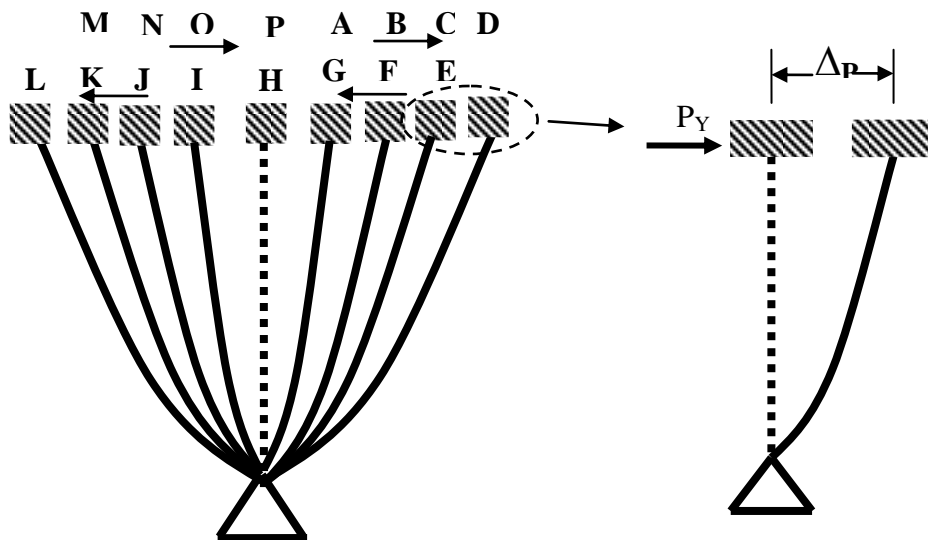
Figure 7.95. The cyclic displacement of steel H-piles based on Loading and

unloading due to small cycles

To investigate the effect of β=0.3 with a maximum strain of ε_a=±5ε_y in bending about strong axis with no axial load on HP220x57 section, one dominant cyclic lateral displacement is divided 17 section as seen in Figure 7.96. Furthermore, in the each section, small cycles are applied three times. To reach the maximum strain of ε_a=±5ε_y in bending about strong axis with no axial load on HP220x57 section, 64 mm displacement is applied in the push and pull direction. Additionally, to observe the effect of β, cyclic lateral displacements (Δ_p) are applied as 19 mm on the push and pull direction on HP220x57 section in each small cycle point as seen in Figure 7.97. Thus, in each small cycle, the value of β=0.3 is added to one dominant cyclic lateral displacement.
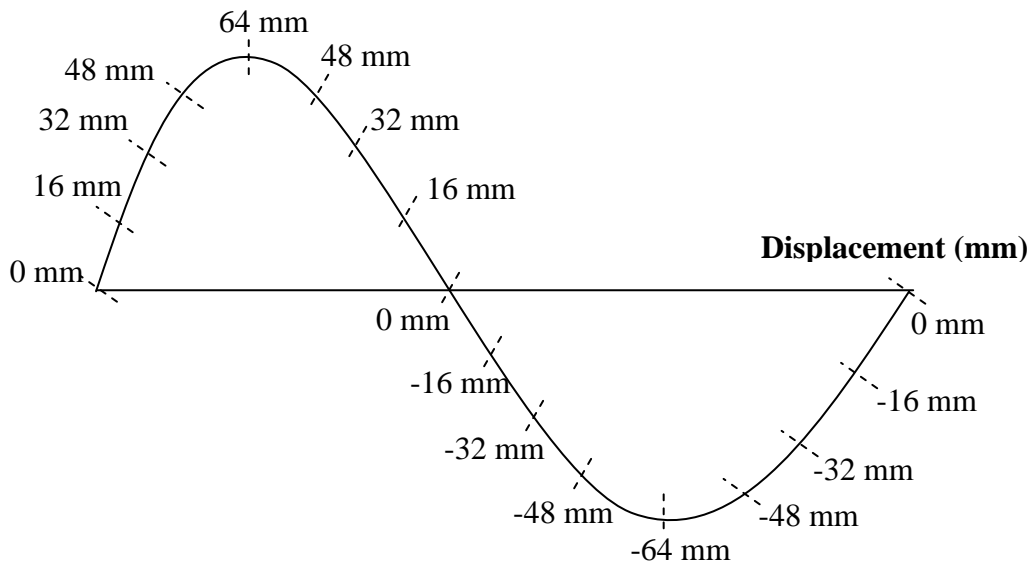
Figure 7.96. The point of the small cycles applied

As shown in Figure 7.98, the actuator is located exactly 105 mm before the experiment. And then, 19 mm cyclic lateral displacements are applied on the push and pull direction in the each step as shown in Table 7.7. At the end of the loading process, about 52 smaller strain cycles per year as qualitatively is provided.

240

Figure 7.97. HP220x57 section

Table 7.7. Displacement point of Actuator for large and small cycles

Step Number	Displacement point of Actuator	
	Large cycle	*Small cycle (±19 mm)*
1	105	124-86
2	121	140-102
3	137	156-118
4	153	172-134
5	169	188-150
6	153	172-134
7	137	156-118
8	121	140-102
9	105	124-86
10	89	108-70
11	73	92-54
12	57	76-38
13	41	60-22
14	57	76-38
15	73	92-54
16	89	108-70
17	105	124-86

The results obtained from experimental test on HP220x57 section having the effect of β demonstrate that the cracks firstly begins 152 cycles on the flange surfaces, and then expanded with the following cycles. Finally, low cycle fatigue occurs when steel HP220x57 section is reached to the 193 cycles. The test results are shown in Table 7.8. Furthermore, as observed in Figure 7.98-(a), local buckling occurs on HP steel specimen having the small cycle lateral displacements within the amplitude of the large strain cycles. Because of this lateral local buckling, flange expands about 11 mm. On the other hand, it is clear that steel HP220x57 section which does not have the small cycle lateral displacements within the amplitude of the large strain cycles is exposed to lateral local buckling as seen in Figure 7.98-(b). At the end of this lateral local buckling, flange expands about 6 mm. Consequently, it is concluded that low cycle fatigue on HP steel sections having the small cycle lateral displacements within the amplitude of the large strain cycles occurs earlier than HP steel sections which does not have the small cycle lateral displacements within the amplitude of the large strain cycles. Moreover, it is seems that width of lateral local buckling and size on HP steel sections having the small cycle lateral displacements within the amplitude of the large strain cycles are bigger than that on HP steel sections which does not have the small cycle lateral displacements within the amplitude of the large strain cycles.

(a)

(b)

(c)

(d)

(e)

(f)

Figure 7.98. Crack propagation during the loading and unloading
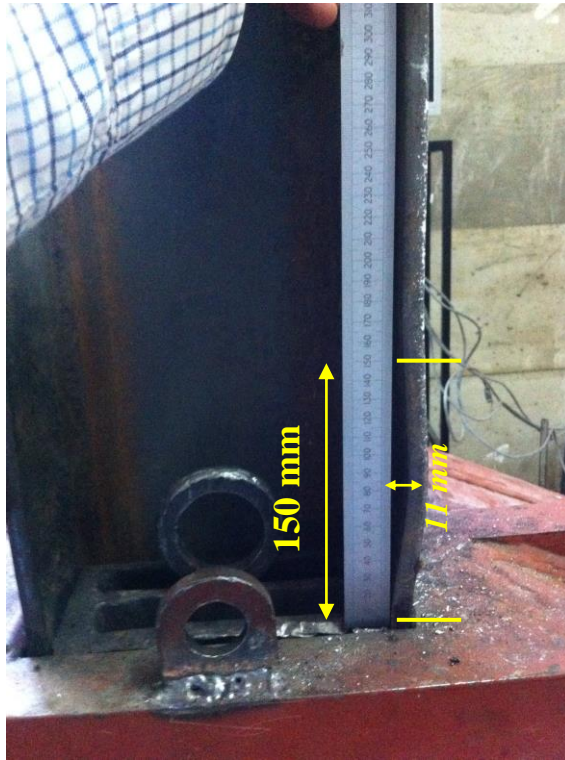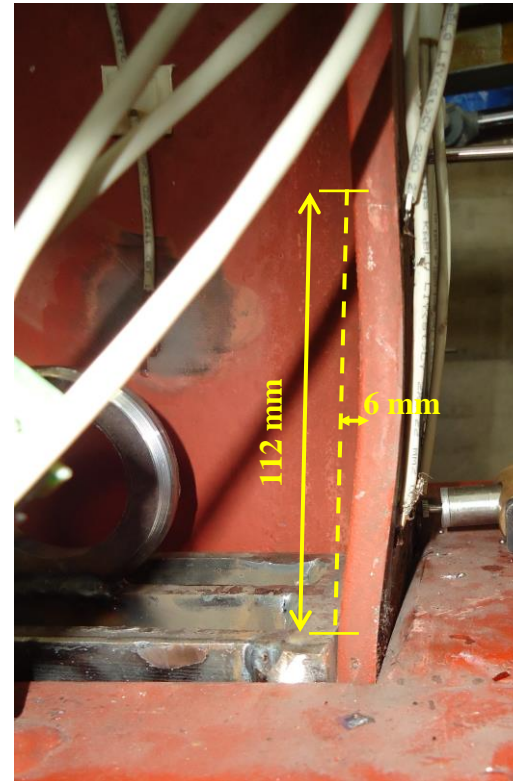
Figure 7.99. (a) Local buckling on HP220x57 section with β effect, (b) Local buckling on HP220x57 section without β effect

7.20.2. Specimen-32: Effect of Beta (β=0.15) with a Maximum Strain of $\varepsilon_a=\pm5\varepsilon_y$ in Bending about Strong Axis with No Axial Load for HP220x57 Section

In this experiment, effect of β is investigated for β=0.15 and also compared with results of specimen-31 and specimen-2, which have same strain level but different β value. To investigate the effect of β=0.15 with a maximum strain of $\varepsilon_a=\pm5\varepsilon_y$ in bending about strong axis with no axial load on HP220x57 section, one dominant cyclic lateral displacement is divided 17 section as done in earlier section. Additionally, cyclic lateral displacements (Δ_p) are applied as 9.6 mm on the push and pull direction on HP220x57 section in each small cycle point as seen in Table 7.8. The actuator is located exactly 105 mm before the experiment. And then, 9.6 mm cyclic lateral displacements are applied on the push and pull direction in the each step as shown in Figure 7.100. At the end of the loading process, about 52 smaller strain cycles per year as qualitatively is provided.

Table 7.8. Displacement point of Actuator for large and small cycles

Step Number	Displacement point of Actuator	
	Large cycle	Small cycle (±9.6 mm)
1	105	114.6-95.4
2	121	130.6-111.4
3	137	146.6-127.4
4	153	162.6-143.4
5	169	178.6-159.4
6	153	162.6-143.4
7	137	146.6-127.4
8	121	130.6-111.4
9	105	114.6-95.4
10	89	98.6-79.4
11	73	82.6-63.4
12	57	66.6-47.4
13	41	50.6-31.4
14	57	66.6-47.7
15	73	82.6-63.4
16	89	98.6-79.4
17	105	114.6-95.4

The results obtained from experimental test on HP220x57 section having the β=0.15 value demonstrate that the cracks firstly begins 191 cycles on the flange surfaces as shown in Figure 7.101, and then expanded with the following cycles. Finally, low cycle fatigue occurs when steel HP220x57 section is reached to the 247 cycles. Consequently, it is concluded once more that low cycle fatigue on HP steel sections having the small cycle lateral displacements within the amplitude of the large strain cycles occurs earlier than HP steel sections which does not have the small cycle lateral displacements within the amplitude of the large strain cycles. In addition to this conclusion, it is also seems that effect β decreases the low cycle fatigue life of the steel HP section. While the value of β increases, life of the steel HP section decreases as shown in Figure 7.102.
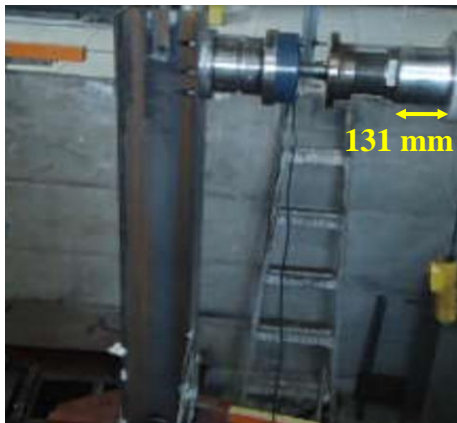
(a) Loading and Unloading 131-111 mm in Step-2 and Step-8
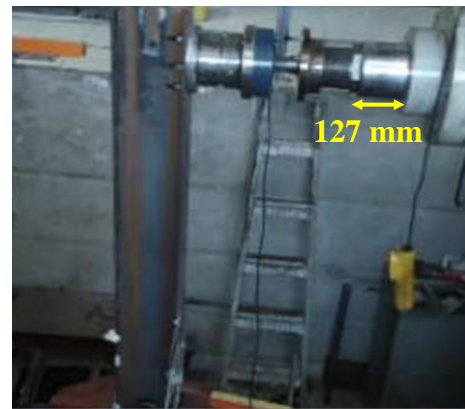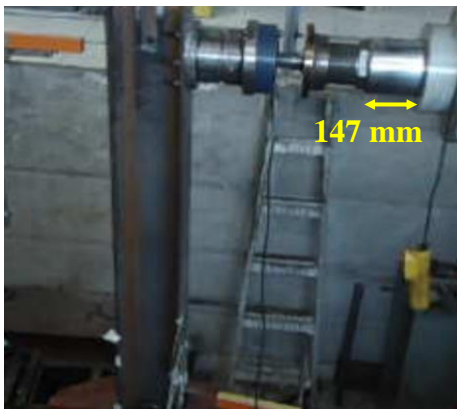
(b) Loading and Unloading 147-127 mm in Step-3 and Step-7

(c) Loading and Unloading 163-143 mm in Step-4 and Step-6

Figure 7.100. Displacement points of Actuator for large and small cycles
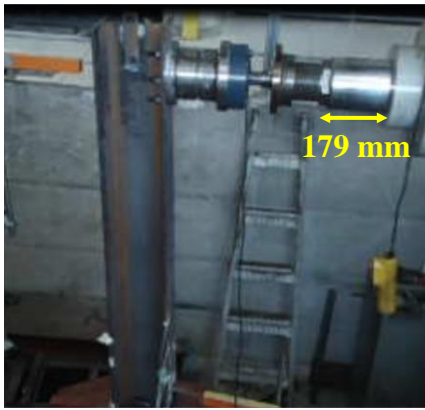
(d) Loading and Unloading 179-159 mm in Step-5
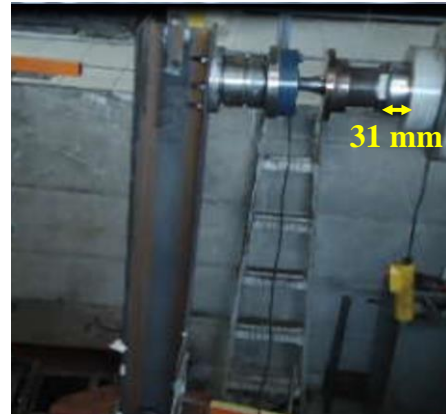
(e) Loading and Unloading 51-31 mm in Step-13

(f) Loading and Unloading 67-47 mm in Step-14 and Step-12

Figure 7.101. (Continued)

248
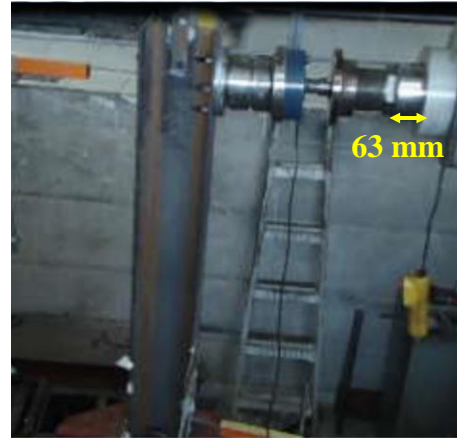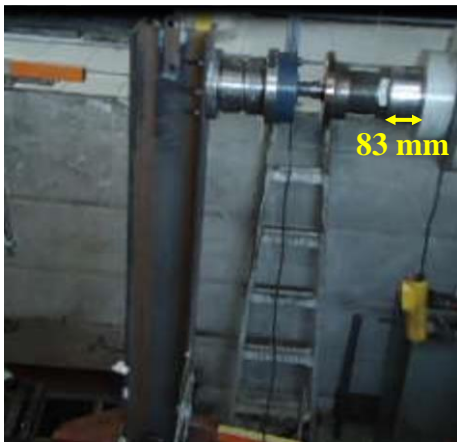
(g) Loading and Unloading 83-63 mm in Step-15 and Step-11

(h) Loading and Unloading 99-79 mm in Step-16 and Step-10

(i) Loading and Unloading 115-95 mm in Step-17 and Step-9

Figure 7.102. (Continued)
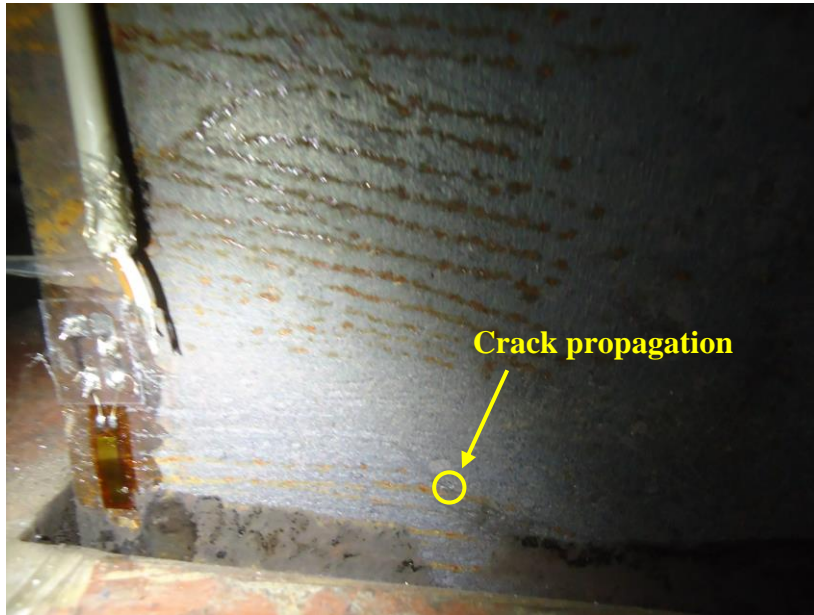
Figure 7.103. Crack propagation on HP steel sections having the small cycle lateral displacements
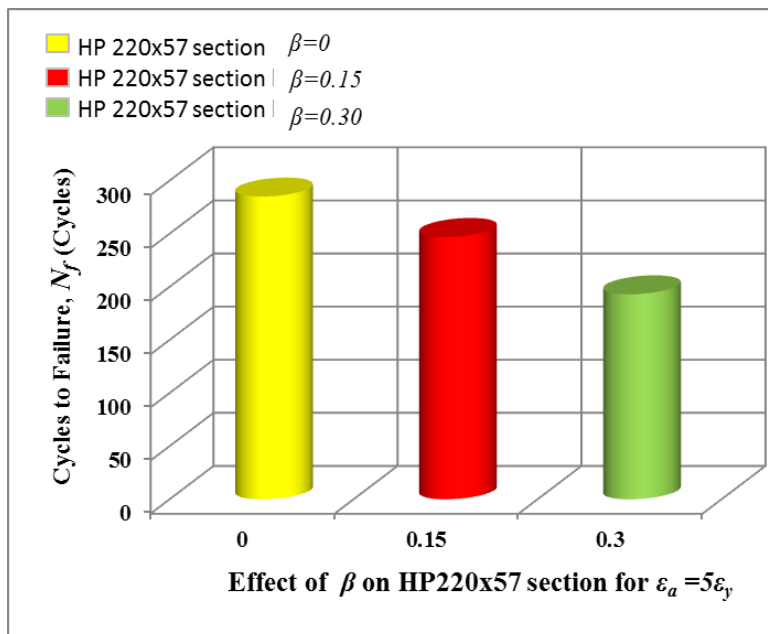
Figure 7.104. Effect of β on HP steel section

7.20.3. Specimen-33: Effect of Beta (β=0.15) with a Maximum Strain of $\varepsilon_a=\pm10\varepsilon_y$ in Bending about Strong Axis with No Axial Load for HP220x57 Section

In the previous two experiments (specimen-32 and specimen-33), the effect of β is investigated on HP220x57 section with a maximum strain of $\varepsilon_a=\pm5\varepsilon_y$ in bending about strong axis with no axial load. In this step of the test, the effect of β is also investigated for HP220x57 section with a maximum strain of $\varepsilon_a=\pm10\varepsilon_y$ in bending about strong axis with no axial load and is compared the test results earlier performed for HP220x57 section with a maximum strain of $\varepsilon_a=\pm5\varepsilon_y$. For this purpose, one dominant cyclic lateral displacement is divided 17 sections as mentioned earlier, and then in the each section, small cycles are applied three times. The actuator is located exactly 139 mm before the experiment. To reach the maximum strain of $\varepsilon_a=\pm10\varepsilon_y$ in bending about strong axis with no axial load on HP220x57 section, 90 mm displacement is applied in the push and pull direction as seen in Figure 7.103. Additionally, to observe the effect of β, cyclic lateral displacements (Δ_p) are applied as 13.5 mm on the push and pull direction on HP220x57 section in each small cycle point as shown in Table 7.9. Thus, in each small cycle, the value of β=0.15 is added to one dominant cyclic lateral displacement. At the end of the loading process, about 52 smaller strain cycles per year as qualitatively is provided.

The results obtained from experimental test on HP220x57 section having the β=0.15 value demonstrate that the cracks firstly begins 45 cycles on the flange surfaces as shown in Figure 7.104, and then expanded with the following cycles. Finally, low cycle fatigue occurs when steel HP220x57 section is reached to the 74 cycles as shown in Figure 7.105. As mentioned earlier in section-9, low cycle fatigue occurs at 152 cycles on HP steel section which does not have the small cycle lateral displacements within the amplitude of the large strain cycles. On the other hand, low cycle fatigue occurs earlier in this experiment as mentioned above.

As observed in Figure 7.106, local buckling occurs on HP steel specimen having the small cycle lateral displacements within the amplitude of the large strain cycles. Because of this lateral local buckling, flange expands about 23 mm. On the other hand, it is clear that steel HP220x57 section which does not have the small cycle lateral displacements within the amplitude of the large strain cycles is exposed to lateral local buckling as seen in Figure 7.106. At the end of this lateral local buckling, flange expands about 13.7 mm.

Consequently, it is concluded that low cycle fatigue on HP steel sections having the small cycle lateral displacements within the amplitude of the large strain cycles occurs earlier than HP steel sections which does not have the small cycle lateral displacements within the amplitude of the large strain cycles. In other words, it is also seems that effect β reductions the low cycle fatigue life of the steel HP section. While the value of β increases, life of the steel HP section decreases. Moreover, it is seems that width of lateral local buckling and size on HP steel sections having the small cycle lateral displacements within the amplitude of the large strain cycles are bigger than that on HP steel sections which does not have the small cycle lateral displacements within the amplitude of the large strain cycles.
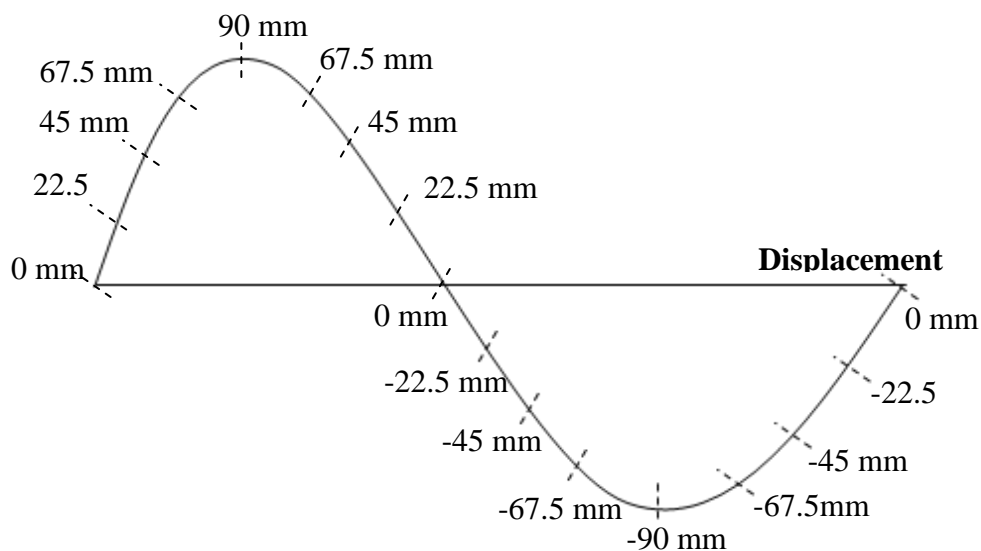
Figure 7.105. The point of the small cycles applied

Table 7.9. Displacement point of Actuator for large and small cycles

Step Number	Displacement point of Actuator	
	Large cycle	Small cycle (±13.5 mm)
1	139	153-125
2	162	175-148
3	184	198-170
4	206	220-192
5	229	242-215
6	206	220-192
7	184	198-170
8	162	175-148
9	139	153-125
10	116.5	130-103
11	94	108-80
12	71.5	85-58
13	49	62.5-35
14	71.5	85-58
15	94	108-80
16	116.5	130-103
17	139	153-125
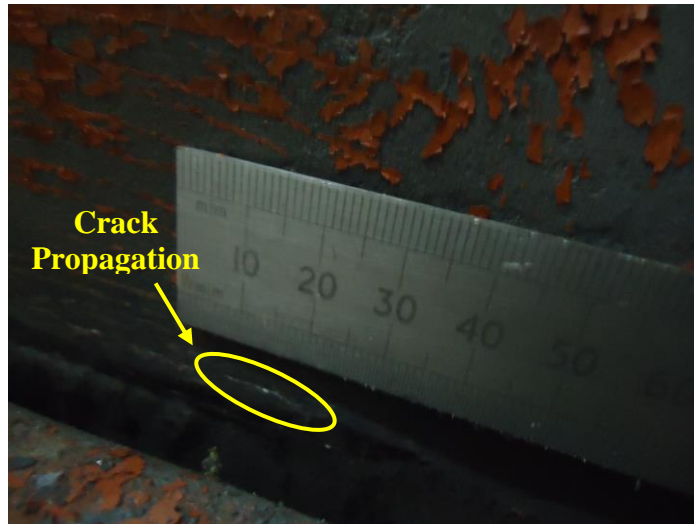
Figure 7.106. Crack propagation

Figure 7.107. Low cycle fatigue
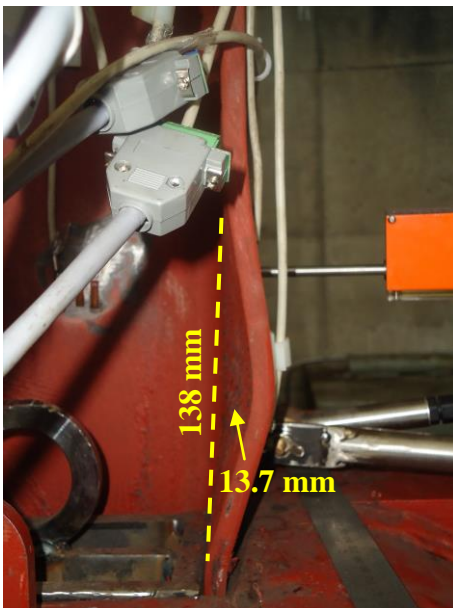
(a)
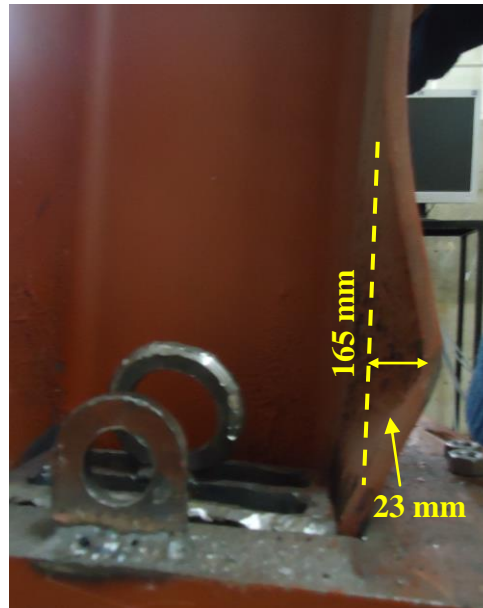
(b)

Figure 7.108. (a) Local buckling on HP220x57 section without β effect, (b) Local buckling on HP220x57 section with β effect

7.20.4. Specimen-34: Effect of Beta (β=0.15) with a Maximum Strain of $\varepsilon_a=\pm10\varepsilon_y$ in Bending about Strong Axis with Axial Load (P=0.075P$_y$) for HP220x57 Section

In the previous three experiments (specimen-31, specimen-32 and specimen-33), the effect of beta (β) is investigated for different strain values. However, the effect of axial load together with beta (β) on HP 220x57 steel section has not been investigated until now. In this experiment, effect of β with the axial load is investigated for β=0.15 and also compared with results of specimen-10 which have same strain level and axial load but different β value. For this purpose, one dominant cyclic lateral displacement divided 17 sections as mentioned earlier and small cycles in the each section are applied. The actuator is located exactly 140 mm before the experiment. To reach the maximum strain of $\varepsilon_a=\pm10\varepsilon_y$ in bending about strong axis with axial load (P=0.075P$_y$) on HP220x57 section, 92 mm displacement is applied in the push and pull direction as seen in Figure 7.107.

Additionally, to observe the effect of β, cyclic lateral displacements (Δ_p) are applied as 14 mm on the push and pull direction on HP220x57 section in each small cycle point as shown in Table 7.10. Thus, in each small cycle, the value of β=0.15 is added to one dominant cyclic lateral displacement. At the end of the loading process, about 52 smaller strain cycles per year as qualitatively is provided. The results obtained from experimental test on HP220x57 section having the β=0.15 value demonstrate that the cracks firstly begins 14 cycles on the flange surfaces as shown in Figure 7.108, and then expanded with the following cycles. Finally, low cycle fatigue occurs when steel HP220x57 section is reached to the 47 cycles as shown in Figure 7.109. As mentioned earlier in section-10, low cycle fatigue occurs at 95 cycles on HP steel section which does not have the small cycle lateral displacements within the amplitude of the large strain cycles. On the other hand, low cycle fatigue occurs earlier in this experiment as mentioned above.
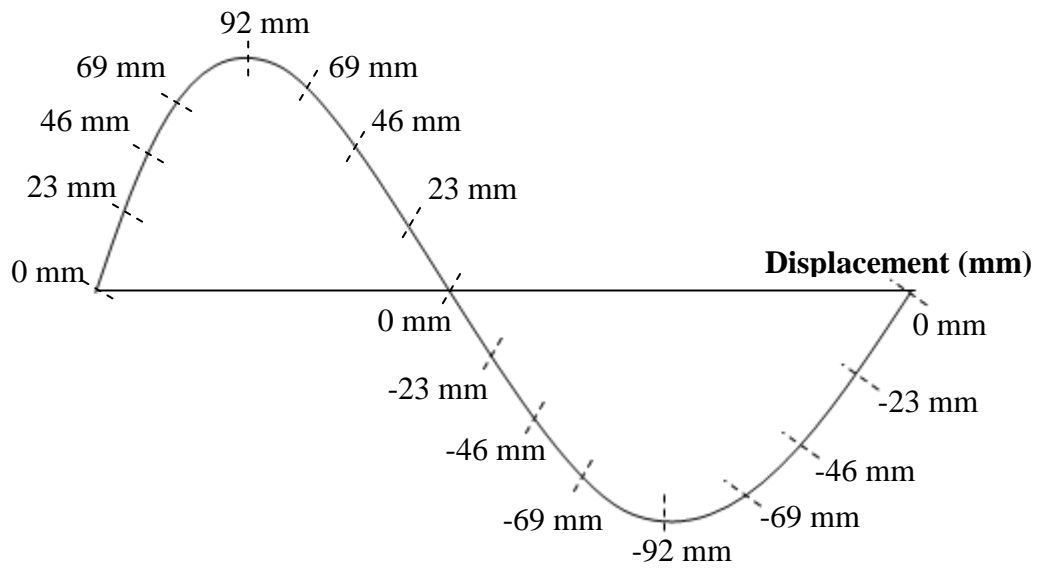
Figure 7.109. The point of the small cycles applied

Table 7.10. Displacement point of Actuator for large and small cycles

Step Number	Displacement point of Actuator	
	Large cycle	Small cycle (±13.5 mm)
1	140	154-126
2	163	177-149
3	186	200-172
4	209	223-195
5	232	246-218
6	209	223-195
7	186	200-172
8	163	177-149
9	140	154-126
10	117	131-103
11	94	108-80
12	71	85-57
13	48	62-34
14	71	85-57
15	94	108-80
16	117	131-103
17	140	154-126

(a)

(b)

Figure 7.110. Crack propagation on HP 220x57 steel section having axial load together with beta (β)

During the experiment, it is observed that lateral local buckling takes place exactly above the 450 mm-high steel base fixture on each flange of HP steel specimen for the strong axis. Because of this lateral local buckling, flange expands as shown in Figure 7.109 and Figure 7.110. On the other hand, it is clear that steel HP220x57 section which does not have the small cycle lateral displacements within the amplitude of the large strain cycles is exposed to lateral local buckling as seen in Figure 7.111. At the end of this lateral local buckling, flange expands extremely. Consequently, it is observed that the effect of beta (β) has same local buckling effects in the high strain value with axial load on HP220x57 steel section.
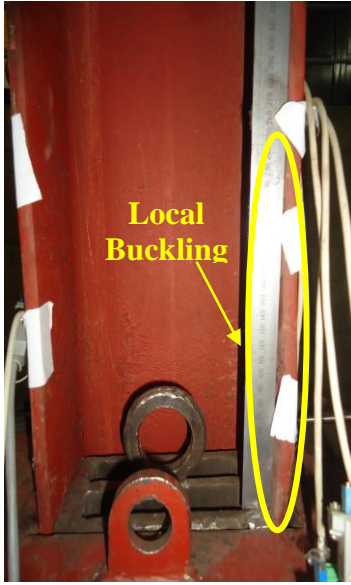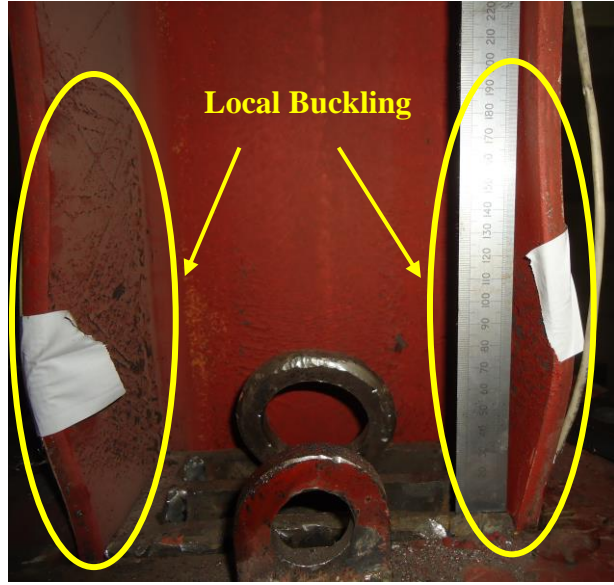
(a)   (b)

(c)

Figure 7.111. Local buckling step

(a)

(b)

(c)

(d)

Figure 7.112. Local buckling step on HP220x57 specimen
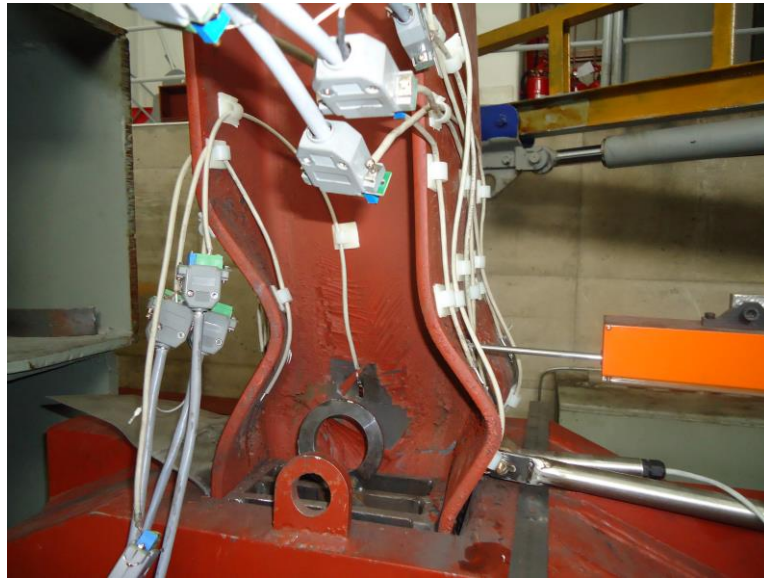
(a)

(b)

Figure 7.113. (a) Local buckling on HP220x57 section without β effect, (b) Local buckling on HP220x57 section with β effect

Table 7.11. Effect of Small+Large Cycle

Section Type	Axial load	Test Number	Effect of β	Strain Amplitude (ε_a)	Number of Cycles	
					First Crack	Fracture
HP 220x57 Strong Axis	P=0	31	0.3	$5\varepsilon_y$	152	193
		32	0.15	$5\varepsilon_y$	191	247
		33	0.15	$10\varepsilon_y$	45	74
	P=0.075P$_y$	34	0.15	$10\varepsilon_y$	14	34

CHAPTER 8

FINITE ELEMENT MODEL OF EXPERIMENTAL WORKS

Nonlinear finite element models (FEM) of the steel H-pile specimens that is used in the experimental part of this research study are developed using the computer program ANSYS to compare between the experimental test results and ANSYS' results. For this purpose, a sensitivity FEM study is performed to establish a FE model that best represents the actual behavior of the steel H-pile specimens, as in actual experimental test set up. Comparisons between FE model predictions and experimental test results are made in terms of fatigue life in the steel H-pile specimens for various lateral and axial load values.

In the finite element model, a structure is divided into small and simple elements. The finite elements used in the model are composed of 10-node high-order tetrahedron elements. Every node has three degrees of freedom: translations in the nodal x, y and z directions. The element has a quadratic displacement behavior and is well suited to modeling irregular meshes.

For the contact elements, CONTA174 is used to represent contact and sliding between 3-D "target" surfaces and a deformable surface. The element is applicable to 3-D structural and coupled field contact analyses. This element is located on the surfaces of 3-D solid or shell elements with mid-side nodes. It has the same geometric characteristic as the solid or shell element face, to which it is connected. Contact occurs when the element surface penetrates one of the target segment elements on a specific target surface.

For the target elements, TARGE170 is used to represent various 3-D "target" surfaces for the associated contact elements. The contact elements themselves

overlay the solid, shell or line elements describing the boundary of a deformable body and are potentially in contact with the target surface, defined by TARGE170. This target surface is discretized by a set of target segment elements and is paired with its associated contact surface via shared real constant set.

Mesh size and type are important for accurate stress values. For this purpose, Tetrahedrons meshing option is chosen because the obtained mesh has a better size distribution across the model. Selected meshing type, tetrahedron mesh, divides various sizing mesh starting with 250 mm. When the stress values are stable, this mesh sizing can be applicable for FEM analysis. The maximum stress value in the HP section remains nearly constant for both 50 mm and 25 mm mesh sizes (526 MPa and 529MPa, respectively). Thus, the mesh sizes are input manually and taken as 25 mm within contact regions and 50 mm within the rest of the model. Consequently, an accurate simulation of the nonlinear behavior is obtained. The number of elements for the whole structure is 7886 and number of nodes is 15325.

Material properties are extracted from material library, which covers standard concrete, steel and has the ability to create user defined custom materials for non-standard applications. In the nonlinear FEM, the main material model used in this structure is steel. Nonlinear material model is used for steel HP sections with Young's modulus of 200,000 MPa, Poisson's ratio 0.3, tensile yield stress 305 MPa and tensile ultimate stress 460 MPa for the HP220x57 steel section. On the other hand, tensile yield stress 350 MPa is used for the HP260x75 steel section.

Contact surfaces in ANSYS allow representing a wide range of different types of interaction between components in a model. In the present finite element model, there exists contact between HP section and the plates of the steel base fixture. Thus, it is important to investigate the nature of interaction between two contacting bodies (HP section and connection plates) and the ANSYS solution procedure to understand the simulation of the contact behavior. Contact between the HP section and the connection plates is surface-to-surface contact type. This

contact type is established when a surface of one body comes in contact with the surface of another body. This contact type is commonly used for arbitrary bodies that have large contact areas. In this study, frictionless contact is chosen between the HP section and connection plates. Gaps can form in the model between contacting bodies. For the remainder of the model, bonded contact is chosen (for the contact with the side plates of the steel base fixture). Asymmetric contact is usually the most efficient way to model face-to-face contact for solid bodies. In this study, asymmetric contact is chosen between two contact surfaces of the model. In this study, the augmented lagrangian method is chosen because it usually leads to better conditioning and is less sensitive to the magnitude of contact stiffness.

Before proceeding to the solution, analysis options should be defined including boundary conditions, analysis type and stepping controls. Analysis setting is about the load to be applied to the structure, including load steps, load magnitude and load direction. For a static structural analysis, there can be one or several load steps. Furthermore, for each load step, several sub-steps might be required to make the solution converge better and results more accurate. The total number of steps, number of sub-steps for the initial step and maximum allowable number of sub-steps are set to 10, 10 and 100 sub-steps, respectively. A maximum lateral and axial force are applied to the structure. Having 10 steps, at each step incremental load is applied to the structure. Additionally, the software uses the Newton-Raphson iterative algorithm for the solution of equations.

Correct definition of boundary conditions is of great importance in the finite element analysis and, depending on the structure, can greatly affect the behavior. Fixed Support means that any movement of the body is restrained, is defined below surfaces of the structure.

To compare between FE model predictions and experimental test results in terms of fatigue life in the steel H-pile specimens for various lateral and axial load values, fatigue damage model are defined in ANSYS.

8.1. Fatigue Life Prediction

There are several different methods that have been used in the literature to estimate the fatigue life of a structure. The type of approach consists many factors, such as type of material, types of deformation, and mode of cyclic loading. The fracture mechanics approach is one of the examples. Fracture mechanics takes into account propagation of a single dominant crack through an otherwise undamaged material. This technique is more appropriate for modeling cracks in brittle material where plasticity is negligible. If material is subject of plastic deformation or distributed damage, a fracture mechanics approach is not the best technique to model damage and cracks. In this case, a crack is extended by growth, joining, and the interconnection of micro-cracks and voids distributed all over the stressed regions. Therefore, the use of a continuum damage model is more appropriate. Continuum damage modeling approaches have been classified into several groups: stress-based, strain-based, and energy-based approaches. In the case of steel, available models are stress-based and strain-based. Since the piles in our case experience plastic deformation and thus experience low-cycle fatigue, a strain based model is selected as the fatigue model.

8.1.1. Stress Based Approach

The stress life method (also referred to as the S-N method) is the first approach used in try to understand and quantify metal fatigue. The S-N method is still widely used in design application. The basis of the S-N method is S-N diagram, which is a plot of alternating stress, S, versus cycles to failure, N. Millions of cycles might be require to cause failure at lower loading levels, so horizontal axis in usually plotted logarithmically. The S-N method works very well in situations including constant amplitude loading and long fatigue lives. However, The S-N method does not work well in low cycle applications, where the applied strains have a significant plastic component due to high load levels. For these applications a strain life analysis is more appropriate.

8.1.2. Strain Based Approach

The strain life is based on the observation that in many components the response of the material in the critical locations is strain or deformation dependent. When load levels are low, stresses and strains are linearly related. Thus, in this range, load-controlled and strain-controlled test results are correlative. Early fatigue research demonstrates that damage is subject to plastic deformation or strain. In the strain life approach the plastic stain or deformation is directly measured and quantified. The stress life approach does not account for plastic strain. At long lives, where plastic strain is negligible and stress and strain are easily related, the strain life and stress life approaches essentially the same. Though most engineering structures and components are designed such that the insignificant loads stay elastic, stress concentration often reasons plastic strains to develop in the vicinity of notches. The strain life method accepts that smooth specimens tested under strain control can simulate fatigue damage at the notch roof of an engineering component. This method can be used high strain/ low cycle situations and can be more easily concluded to situations involving complicated geometries. Since the piles in our case experience plastic deformation and thus experience low-cycle fatigue, a strain based model is selected as the fatigue model.

Having made all the above mentioned definitions, the finite element model is ready for solution.
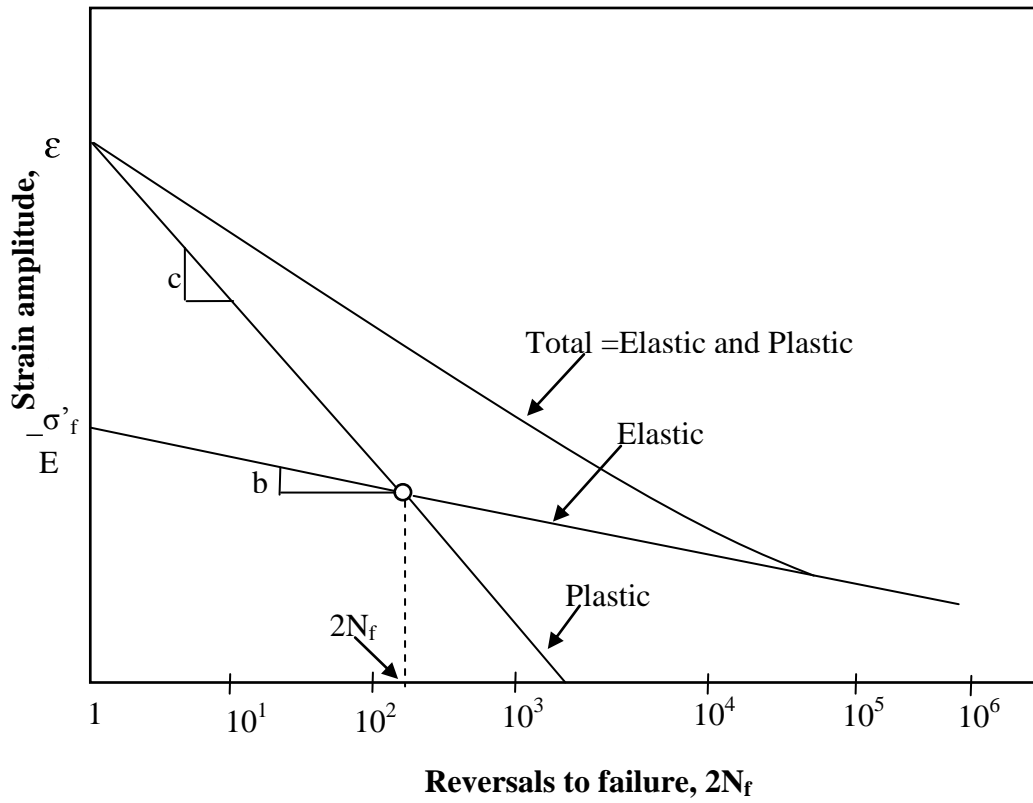
Figure 8.1. Strain-Life Curves Showing the Total, Elastic and Plastic

Components

268

8.2. Comparison between Test Result and FEM Results

8.2.1. Comparison-1: A Maximum Strain of $\varepsilon_a = \pm 5\varepsilon_y$ in Bending about Strong Axis with No Axial Load

As mention earlier, to obtain the five times yield strain ($\varepsilon_a = \pm 5\varepsilon_y$), 70 mm and 72 mm lateral displacements were applied on the push and pull side. To reach these displacements, maximum compression and tension forces 160 kN, and 165 kN respectively were applied during the push and pull of first. To compare experiment results with the finite element model, finite element model is constructed similarly according to actual HP220x57 steel specimen oriented in strong axis bending in the test set up. For this reason, a lateral pressure is implemented over the entire top surface of the HP220x57 steel section in the ANSYS software to apply the lateral load on the top of the HP220x57 steel specimen and then finite element model is solved based on above procedure explained in detail. Based on the FE analysis results, strain values for HP 220x57 steel sections are obtained as seen in Figure 8.2. Finite element analysis results show that maximum strain in the piles occurs in the flange of the HP 220x57 steel specimen right above the 465 mm-high steel base fixture. Because of this reason, comparison between the FEM and experiment results is made at this point.

It is seems that strain value obtained from the ANSYS solution are confirmed by the experimental results while HP steel specimen is push and pull to under the same lateral displacement and the same lateral loads. From the comparison shown in Figure 8.3, it shows that the fatigue cracks obtained from ANSYS model is in close agreement with the fatigue cracks obtained from experiment test set up. This indicates that the actual behavior of HP220x57 steel specimen oriented in strong axis bending under lateral loading can be accurately predicted by the FEM approach. In addition to that, using the FEM, fatigue life of HP220x57 steel specimen oriented in strong axis bending under same lateral loads is investigated. In the experiment, the fatigue life of the HP220x57 steel specimen oriented in strong axis bending under lateral loading for the five times yield strain ($\varepsilon_a \pm 5\varepsilon_y$) is

obtained 285 cycles. On the other hand, in the FEM, the fatigue life of the HP220x57 steel specimen is obtained 292 cycles as seen in Figure 8.4. Furthermore, it is observed from experiment that crack occurs in the flange of the HP 220x57 steel specimen right above the 465 mm-high steel base fixture. In addition to experiment test result, from the comparison shown in Figure 8.5, it shows that fatigue occurs in the same location in right above the 465 mm-high steel base fixture.

(a)   (b)
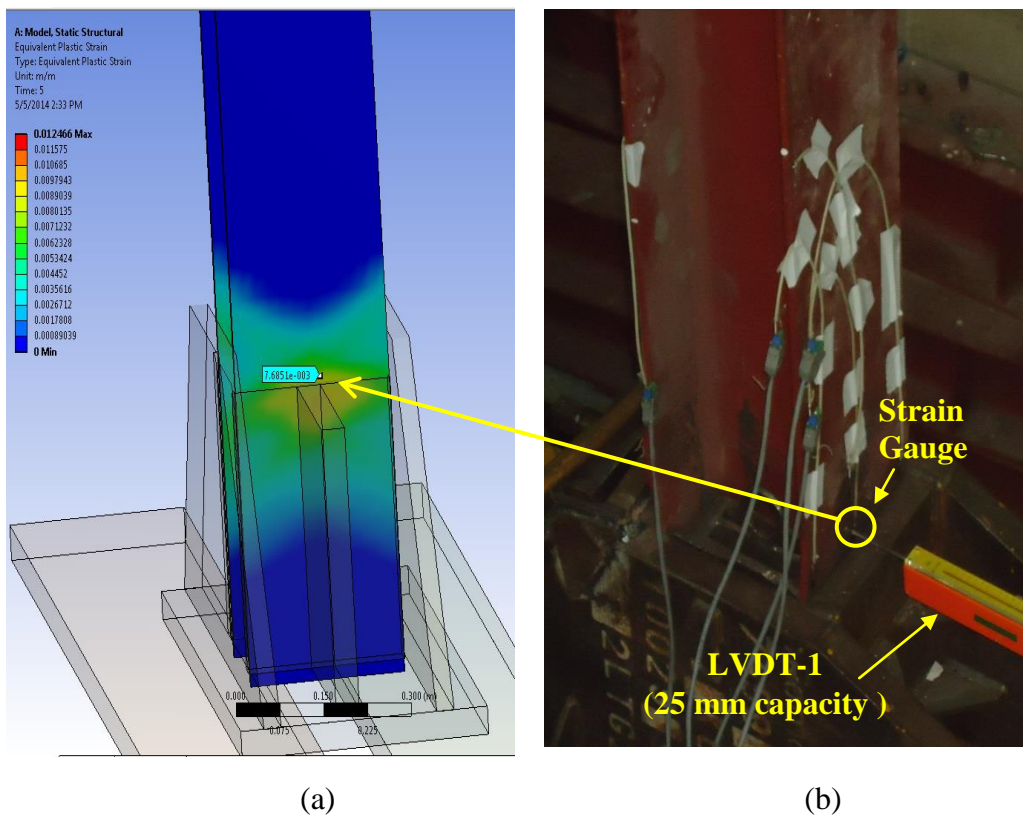
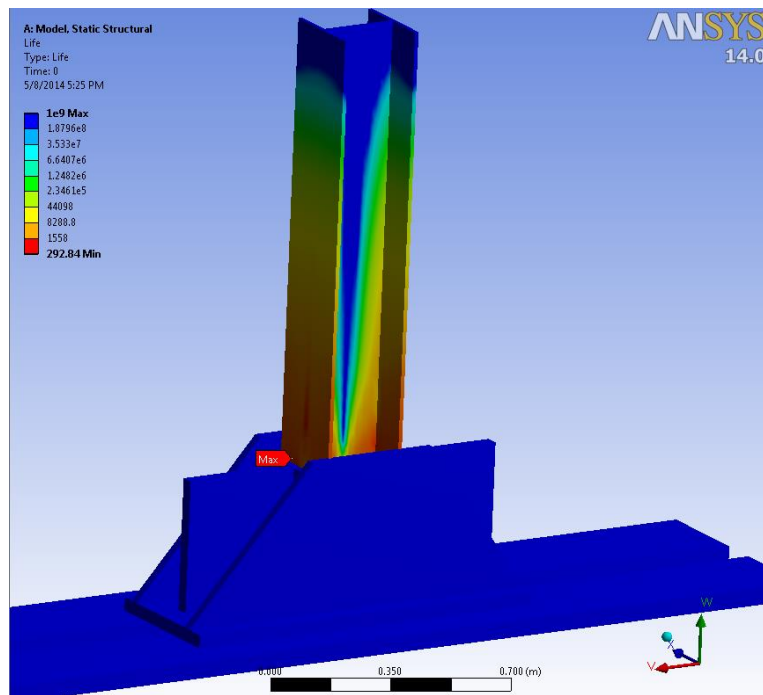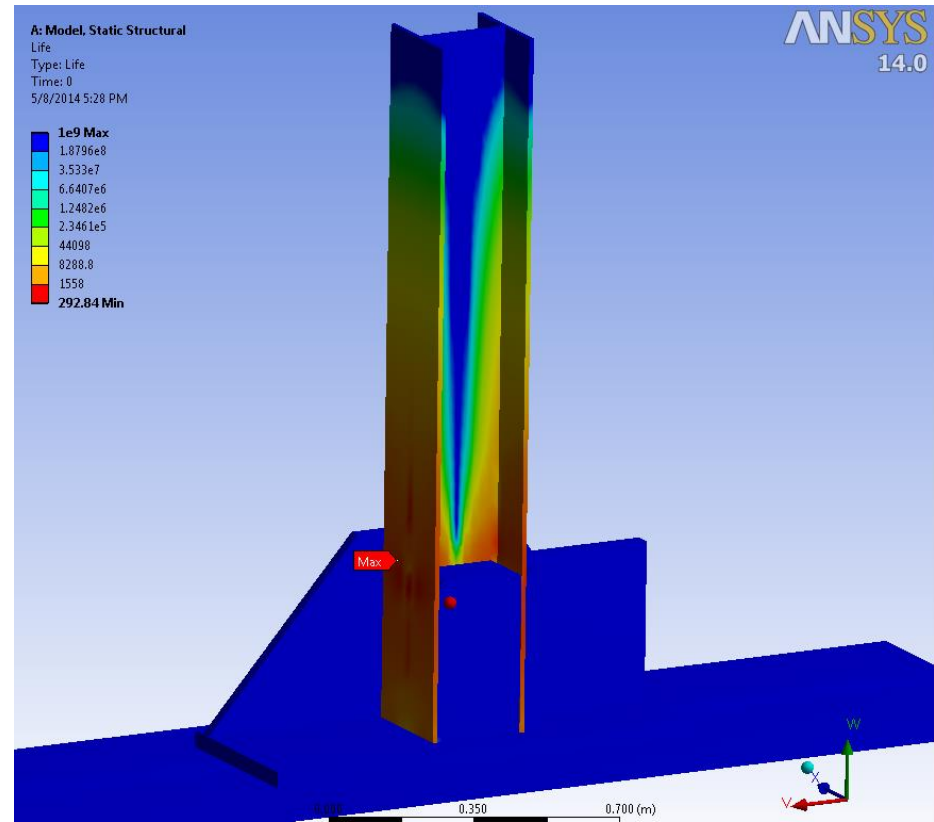**Figure 8.2.** (a) Finite Element Model, (b) Experiment test set up

Figure 8.3. Fatigue life of the HP220x57 steel section on FEM

(a) (b)

Figure 8.4. (a) Crack Propagation on Test Set Up, (b) Crack Location due to Fatigue Life

8.2.2. Comparison-2: A Maximum Strain of $\varepsilon_a=\pm5\varepsilon_y$ in Bending about Strong Axis with Axial Load ($P=0.11P_y$)

To compare experiment results with the finite element model for the HP220x57 steel specimen under the axial load, finite element model is constructed similarly according to actual HP220x57 steel specimen oriented in strong axis bending in the test set up. Therefore, a lateral pressure is implemented over the entire top surface of the HP220x57 steel section in the ANSYS software to obtain a maximum strain of 0.0075 which is equal to five times yield strain ($\varepsilon_a=\pm5\varepsilon_y$) as applied in test set up. To do so, 60 mm lateral displacements are applied on the push and pull side in the FEM as in the experiment test set up. Additionally, an axial load is also applied over the entire top surface of the HP220x57 steel section in the ANSYS software as seen in Figure 8.5. Average value of axial load is applied as 250 kN ($P=0.11P_y$) for the FEM.

In the experimental test set up, to reach the maximum strain of 0.0075 which is equal to five times yield strain ($\varepsilon_a=\pm5\varepsilon_y$), maximum compression and tension forces 176 kN respectively were applied during the push and pull of first. On the other hand, in the FEM, to reach the five times yield strain, maximum compression and tension forces 205 kN respectively are obtained during the push and pull side. Based on the FE and experiment test results, lateral deformations are shown in Figure 8.6. As seen in Figure 8.6, same deformation value is obtained to reach five times yield strain. Five times yield strain obtained in FEM as shown in Figure 8.7.

As seen in this experiment, local buckling of flanges occurred exactly above the 425 mm-high steel base fixture as seen in Figure 8.8-(a). In addition to experimental part, it is seems that same local buckling takes place accurately above the 425 mm-high steel base fixture in FEM as seen in Figure 8.8-(b). Finally, the results obtained from experimental test on HP220x57 section demonstrate that first fracture begins 341 cycles. After 341 cycles, fracture start to expand and then, low cycle fatigue occurs when steel HP220x57 section is

reached to the 548 cycles. On the other side, in the FEM, low cycle fatigue takes place when steel HP220x57 section is reached to the 585 cycles.

Form the comparison shown in Figure 8.9, it shows that the fatigue life obtained from ANSYS model is in close agreement with the fatigue life obtained from the experiment test set up. This indicates that the actual behavior of HP220x57 steel specimen oriented in strong axis bending under lateral and axial loading can be accurately predicted by the FEM approach.
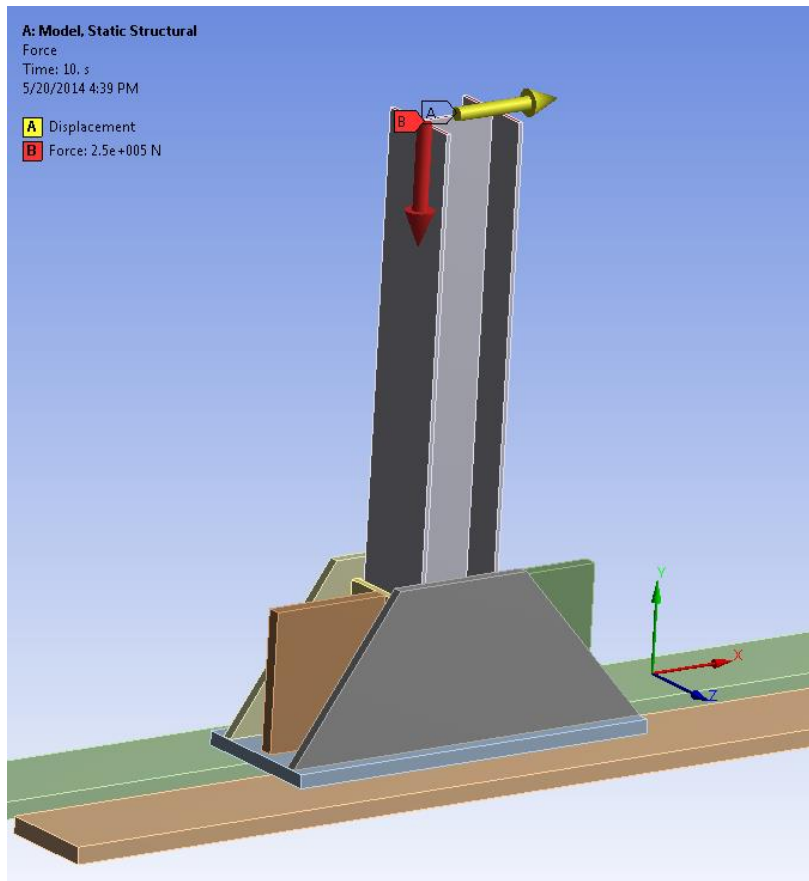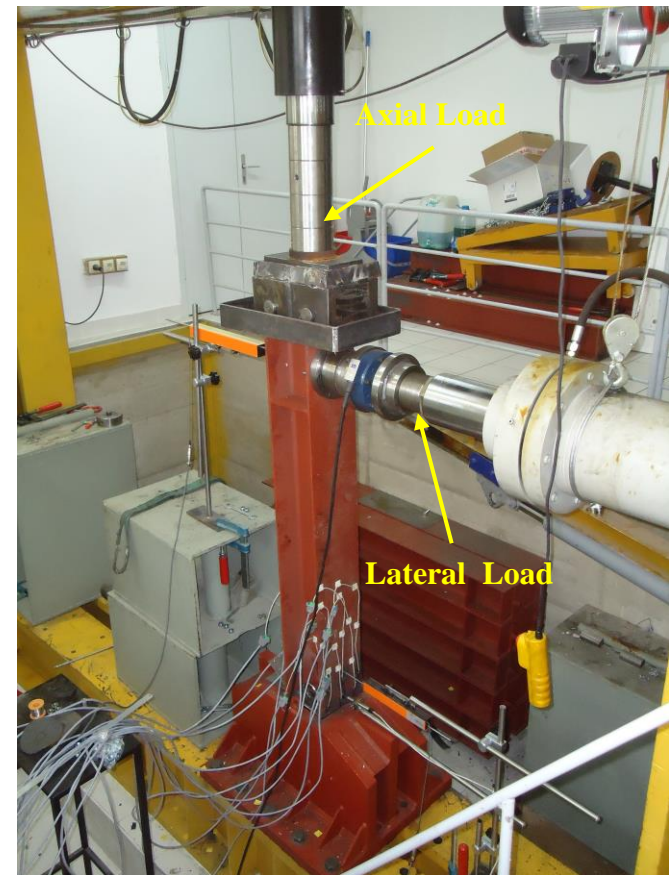
(a)   (b)

Figure 8.5. (a) Applied axial and lateral load in FEM, (b) Applied axial and lateral load in test set up
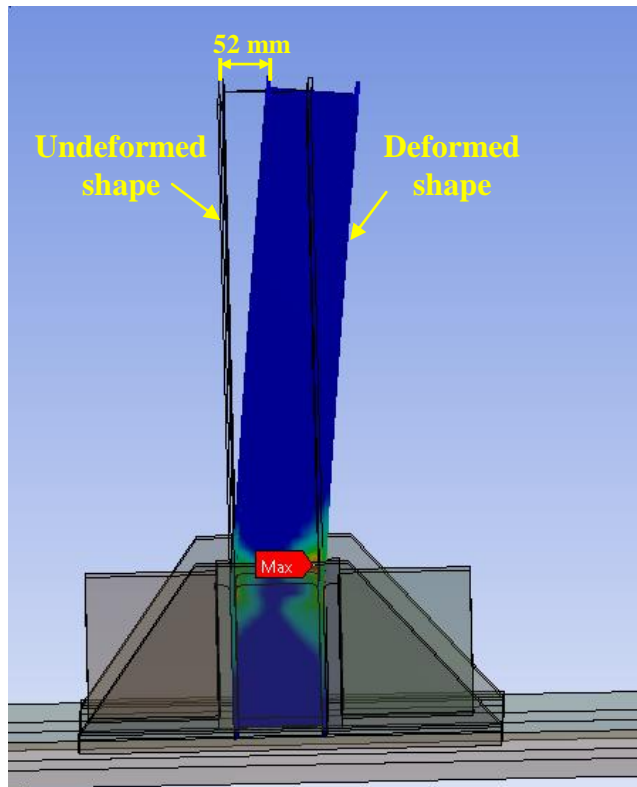
(a)
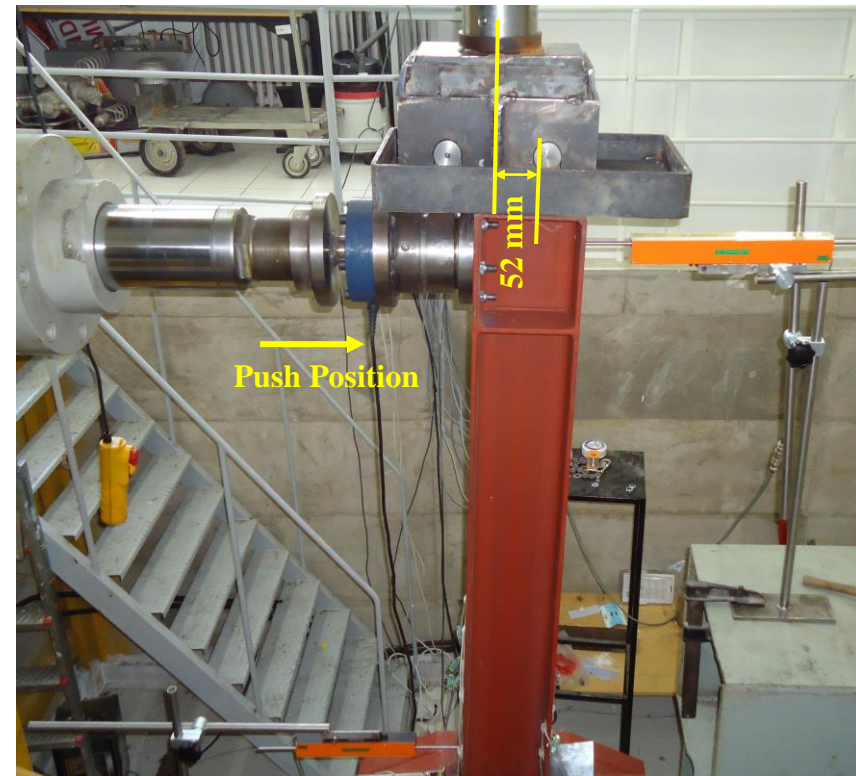
(b)

Figure 8.6. (a) Deformed shape under lateral and axial load in FEM, (b) deformed shape under lateral and axial load in test set up
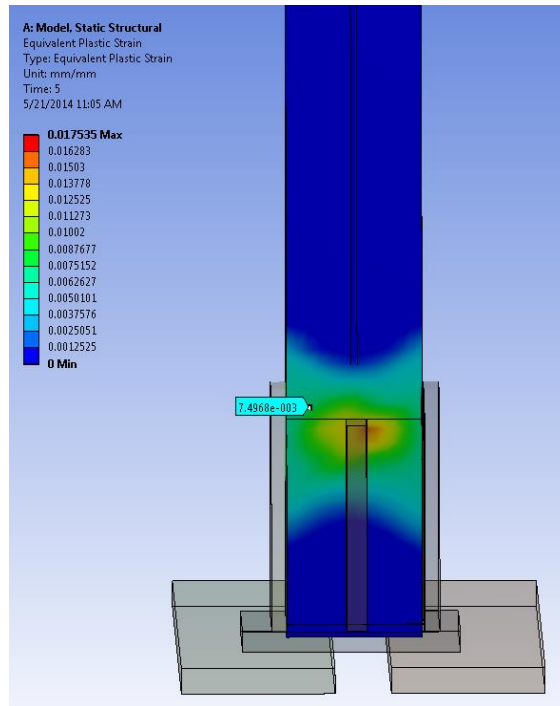
Figure 8.7. Equivalent plastic strain on HP 220x57 steel specimen in FEM
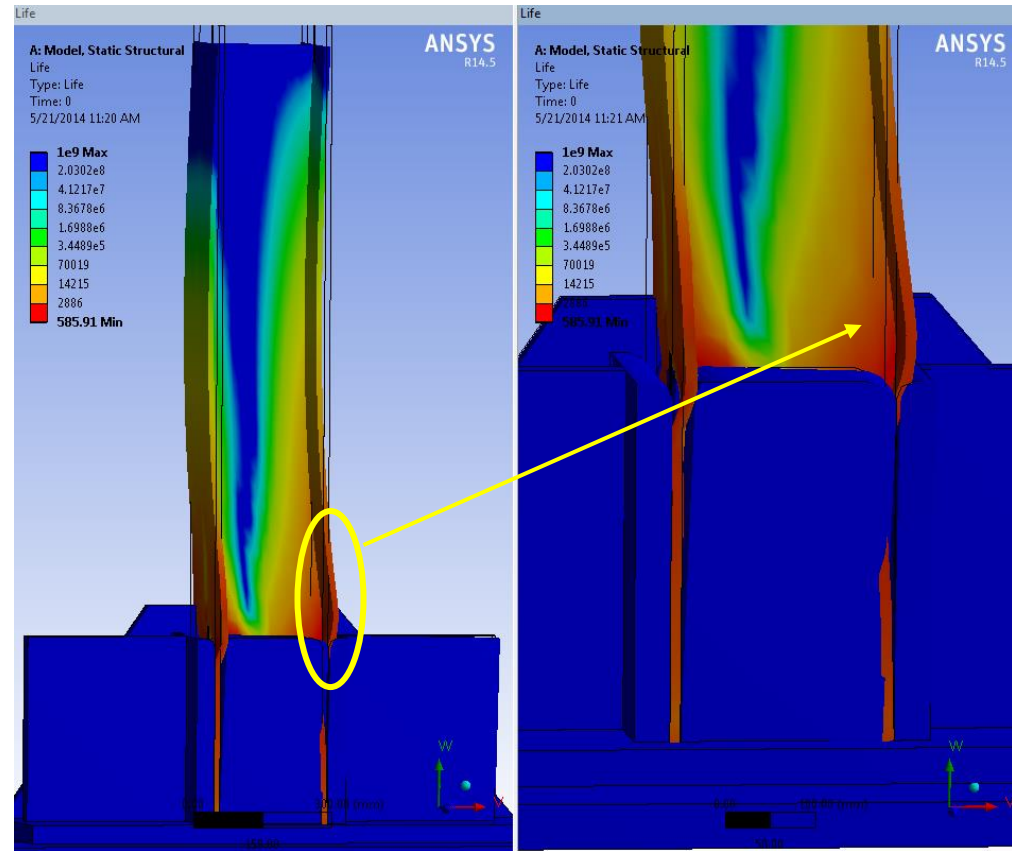
Figure 8.8. (a) Local buckling in the experiment test set up, (b) Local buckling due to low cycle fatigue in FEM
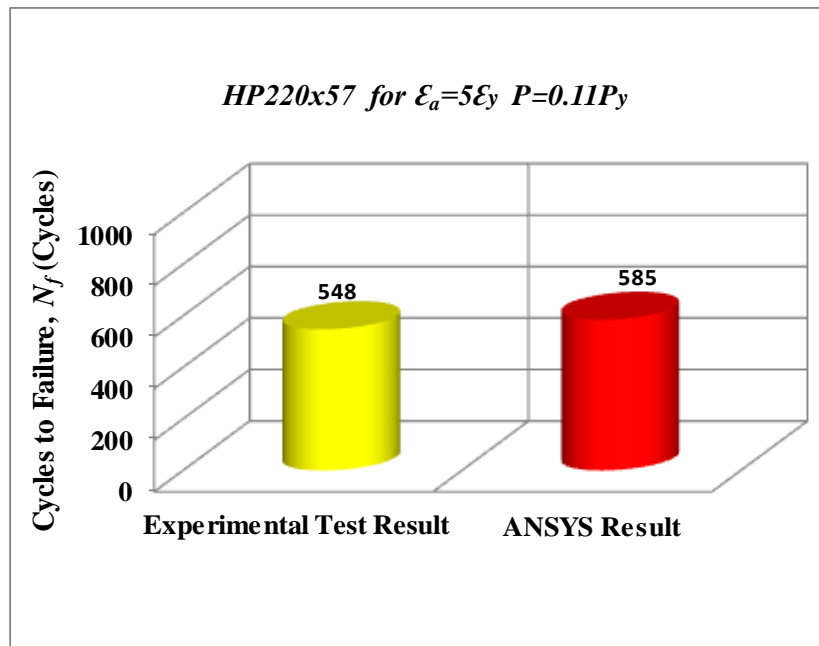
Figure 8.9. Experimental and FE model test results

8.2.3. Comparison-3: A Maximum Strain of $\varepsilon_a = \pm5\varepsilon_y$ in Bending about Strong Axis with Axial Load (P=0.075P$_y$)

The other comparison between the FE model and experimental test results is done on the HP220x57 section with axial load for *P=0.075P$_y$*. As mentioned earlier in section 7.8, to reach a maximum strain of 0.0075 which is equal to five times yield strain ($\varepsilon_a=\pm5\varepsilon_y$) with axial load *P=0.075P$_y$*, 60 mm and 65 mm lateral displacements are applied on the push and pull side in the experiment test. Furthermore, to reach these displacements, maximum compression and tension forces 178 kN, and 182 kN respectively are applied during the push and pull of first cycle. To compare the experimental test results with the FE model results, same lateral displacements and axial load are applied on the HP220x57 steel section in FEM as seen in Figure 8.10.
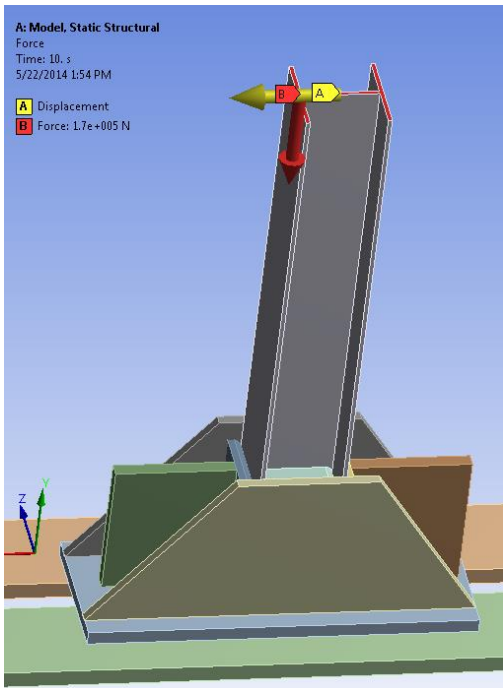
(a)   (b)

Figure 8.10. (a) Applied axial and lateral load in FEM, (b) Applied axial and lateral load in test set up

And consequently, as seen in Figure 8.11, in the push and pull direction, same lateral displacements as in the experimental test set up are applied in the FEM and then five times yield strain resulting from these lateral displacements on the HP220x57 steel section is obtained in Figure 8.12.

As mentioned earlier in section 7.8, the results obtained from experimental test on HP220x57 section demonstrate that first fracture begins 229 cycles. After 229 cycles, fracture start to expand and then, low cycle fatigue occurs when steel HP220x57 section is reached to the 351 cycles. On the other side, in the FEM, low cycle fatigue takes place when steel HP220x57 section is reached to the 319 cycles. Furthermore, as seen in Figure 8.13, it is seems that starting point of crack takes place accurately above the 400 mm-high steel base fixture in FEM as occurs in experimental test set up. The reasons explained in detail above shows that the fatigue life obtained from ANSYS model is in close agreement with the fatigue life obtained from the experiment test set up.
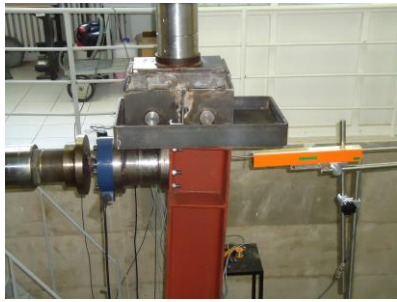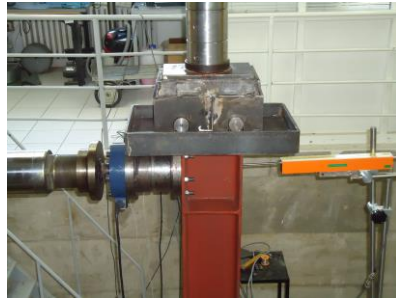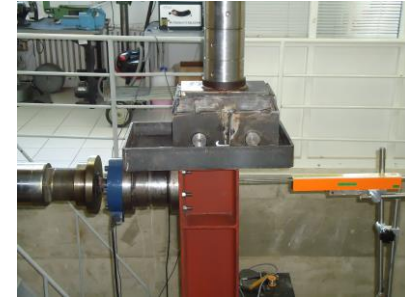
Figure 8.11. (a) Mid-position in FEM, (b) Push direction in FEM, (c) Pull direction in FEM, (d). Mid-position in experimental test set up, (e) Push direction in experimental test set up, (f) Pull direction in experimental test set up
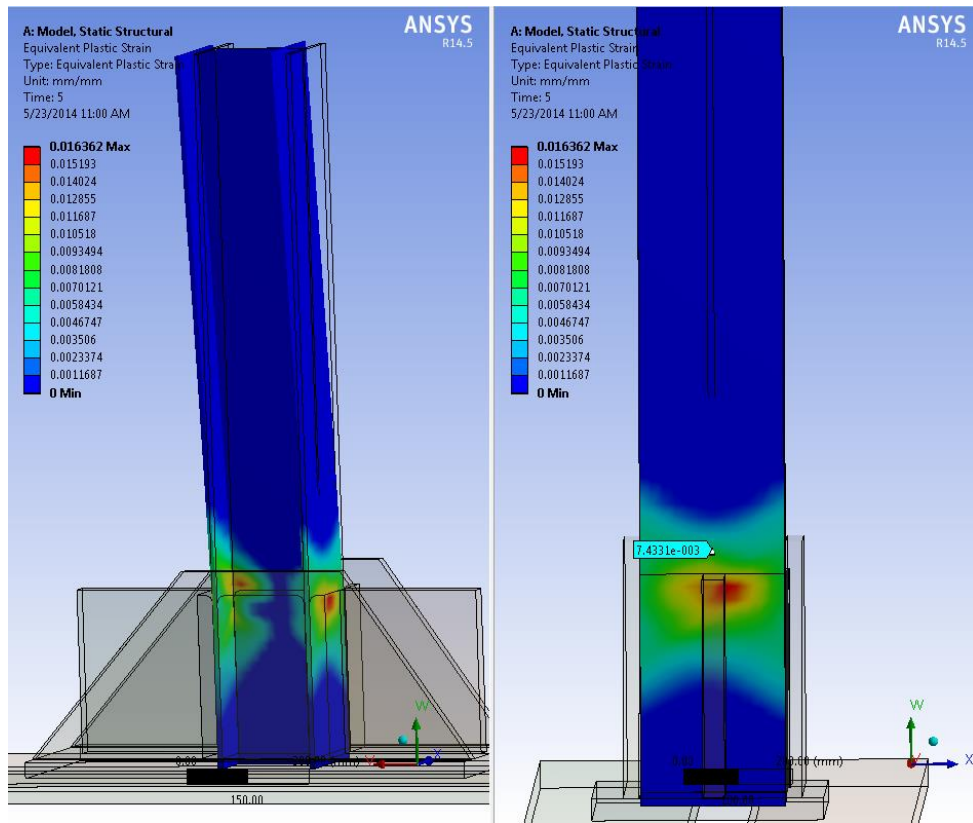
Figure 8.12. Equivalent plastic strain on HP 220x57 steel specimen with axial
load in FEM
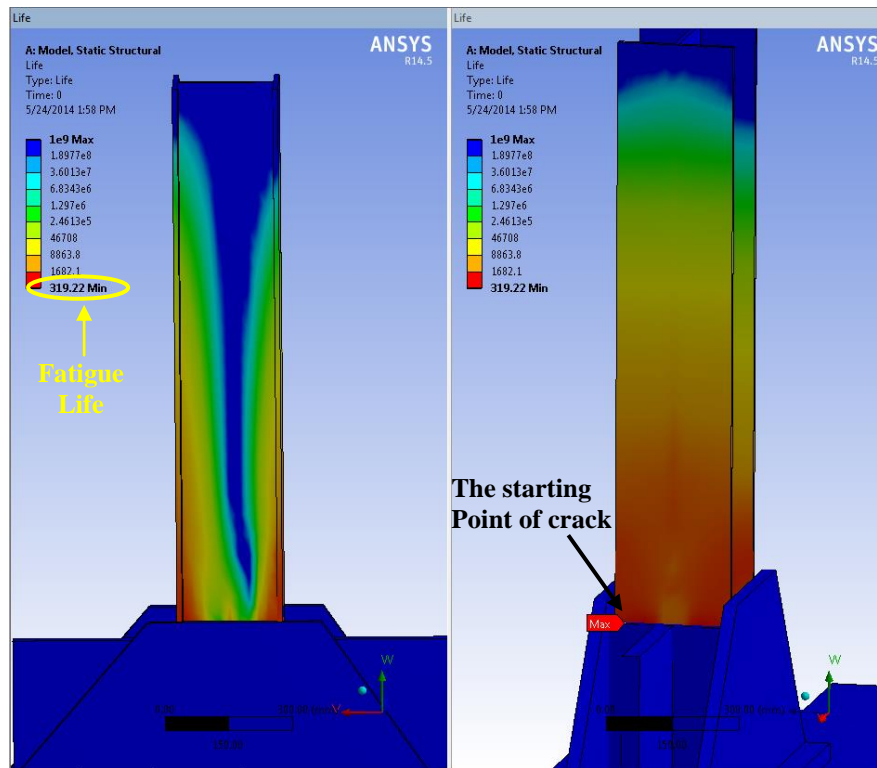
(a)
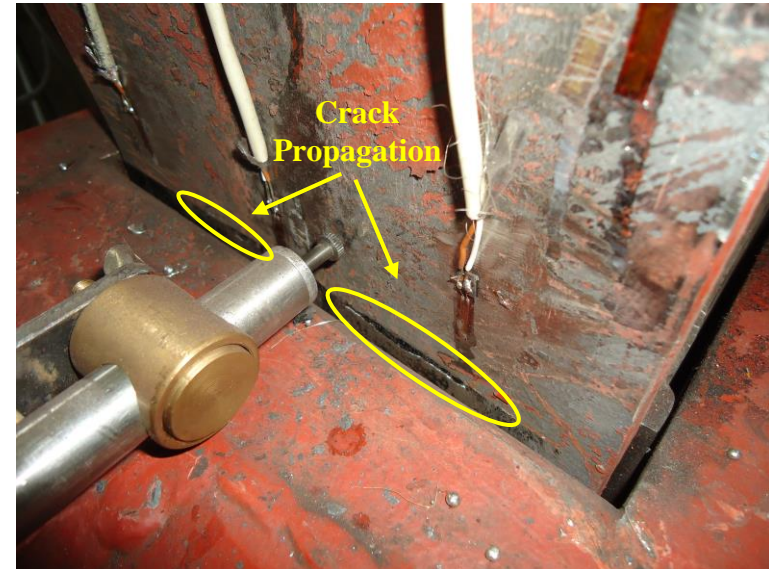
(b)

Figure 8.13. (a) Fatigue life and the starting point of crack in FEM, (b) the starting point of crack in experimental test set up

8.2.4. Comparison-4: A Maximum Strain of $\varepsilon_a=\pm10\varepsilon_y$ in Bending about Strong Axis without Axial Load ($P=0P_y$)

To investigate the differences between the FEM and experimental test results in the high strain values on the HP220x57 steel section, finite element model is constructed similarly according to actual HP220x57 steel specimen oriented in strong axis bending in the test set up. As mentioned earlier, total 180 mm displacements are applied on the push and pull side to obtain ten times yield strain in the experimental test set up as shown in Figure 8.14. Furthermore, to reach these displacements, maximum compression and tension forces 165 kN, and 160 kN respectively are applied during the push and pull of first cycle. To model the test set up in ANSYS software, same displacement are applied on the HP220x57 steel section. At the end of this displacements on the push and pull direction, it is seems that a maximum strain of 0.015 which is equal to ten times yield strain ($\varepsilon_a=\pm10\varepsilon_y$) without axial load $P=0.P_y$ is obtained as shown in Figure 8.15.

As mentioned earlier, the results obtained from experimental test on HP220x57 section demonstrate that first fracture begins 110 cycles. After 110 cycles, fracture start to expand and then, low cycle fatigue occurs when steel HP220x57 section is reached to the 152 cycles. On the other side, in the FEM, low cycle fatigue takes place when steel HP220x57 section is reached to the 167 cycles. Furthermore, as seen in Figure 8.16, it is seems that starting point of crack takes place accurately above the 400 mm-high steel base fixture in FEM as occurs in experimental test set up. The reasons explained in detail above shows that the fatigue life obtained from ANSYS model is in close agreement with the fatigue life obtained from the experiment test set up as seen in the earlier comparisons.
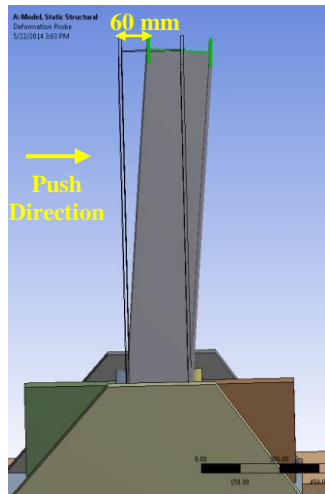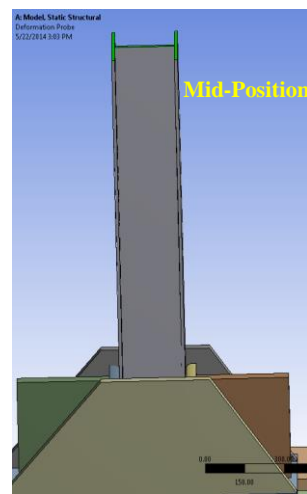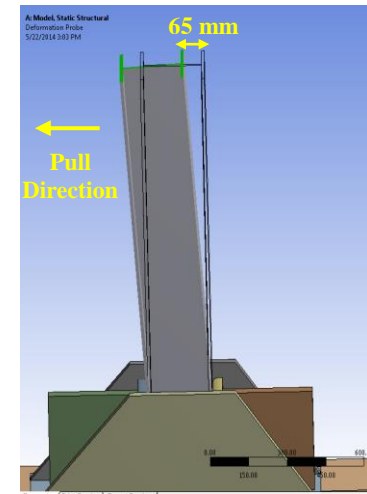
Figure 8.14. (a) Push and Pull direction in the experimental test set up, (b) Push and Pull direction in the FEM
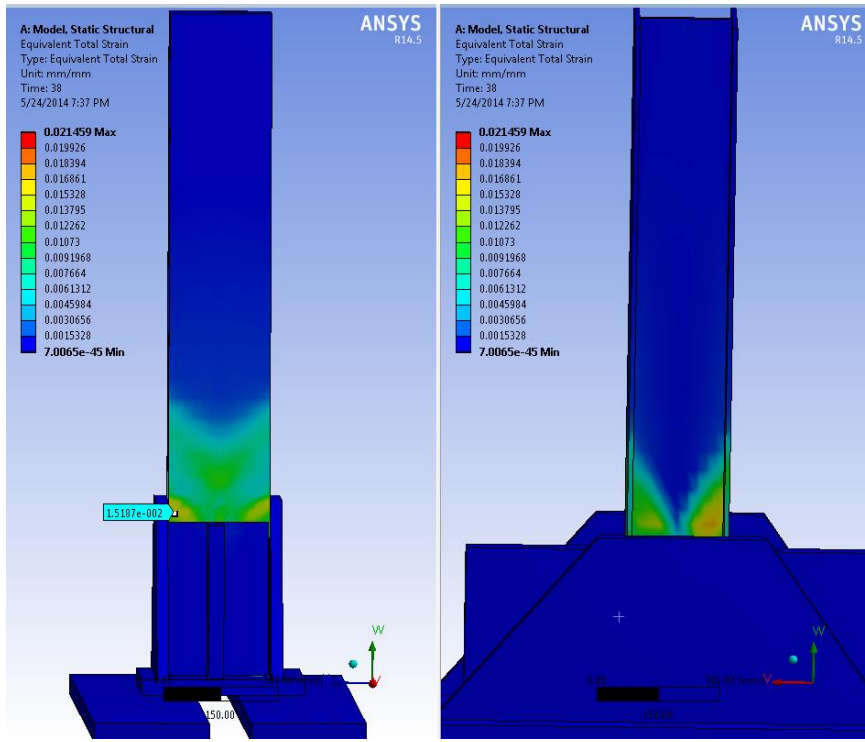
Figure 8.15. Equivalent plastic strain on HP 220x57 steel specimen with axial
load in FEM
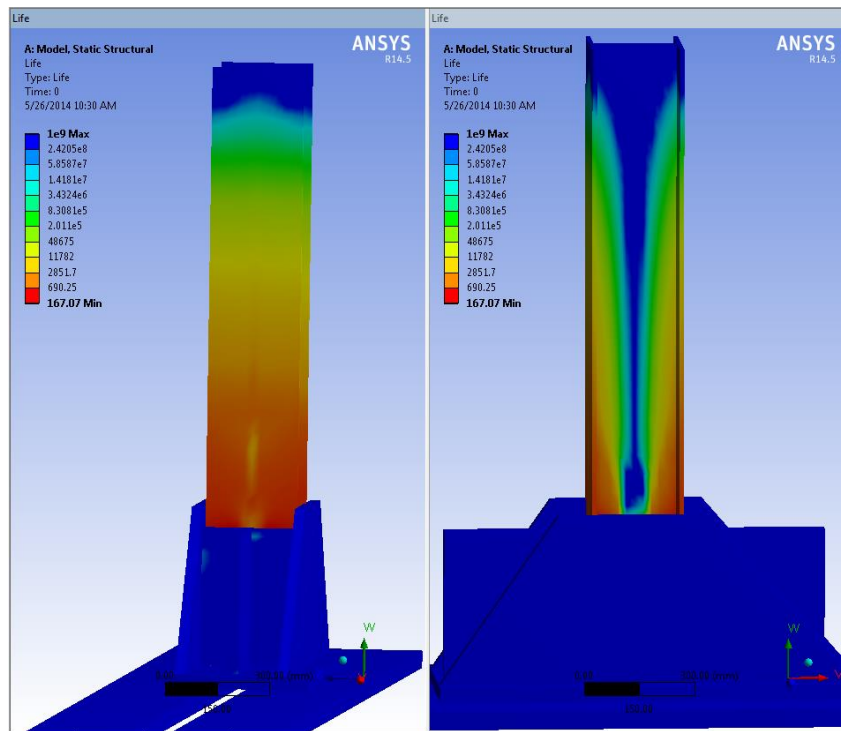
Figure 8.16. Fatigue life in FEM

287

8.2.5. Comparison-5: A Maximum Strain of $\varepsilon_a=\pm5\varepsilon_y$ in Bending about Strong Axis without Axial Load ($P=0P_y$)

To compare the experimental test and FEM results for different steel H piles, finite element model is constructed similarly according to actual HP260x75 steel specimen oriented in strong axis bending in the test set up as constructed earlier according to actual HP220x57 steel specimen. As mentioned earlier, 97 mm lateral displacements are applied on the push and pull side. To reach these displacements, maximum compression and tension forces 220 kN, and 240 kN respectively are applied during the push and pull of first cycle in the experimental test set up. To model the test set up in ANSYS software, same displacement are applied on the HP260x75 steel section. At the end of this displacements on the push and pull direction, it is seems that a maximum strain of 0.0085 which is equal to ten times yield strain ($\varepsilon_a=\pm5\varepsilon_y$) without axial load $P=0.P_y$ is obtained as shown in Figure 8.17. On the other hand, in the FEM, to reach the ten times yield strain without axial load on the HP260x75 steel section, maximum compression and tension forces 270 kN, and 270 kN respectively are applied during the push and pull of first cycle. As a consequence, it is seems that same displacements are obtained under these lateral forces.

The results obtained from experimental test on HP260x75 section demonstrate that first fracture developed in the intersect lines of flanges and webs, and then expanded with the following cycles. After first fracture, fracture start to expand and then, low cycle fatigue occurs when steel HP260x75 section is reached to the 204 cycles. On the other hand, in the FEM, low cycle fatigue takes place when steel HP260x75 section is reached to the 235 cycles as seen in Figure 8.18. In addition to fatigue life, it is also obtained damage result defined as the design life divided by the available life in FEM as seen in Figure 8.19. A damage of greater than 1 indicates the part will fail from fatigue before the design life is reached. Furthermore, it is seems from damage result in Figure 8.19 that starting point of crack takes place accurately above the 400 mm-high steel base fixture in the intersect lines of flanges and webs in FEM as occurs in experimental test set up.

The reasons explained in detail above shows that the fatigue life obtained from ANSYS model is in close agreement with the fatigue life obtained from the experiment test set up as seen in the earlier comparisons.
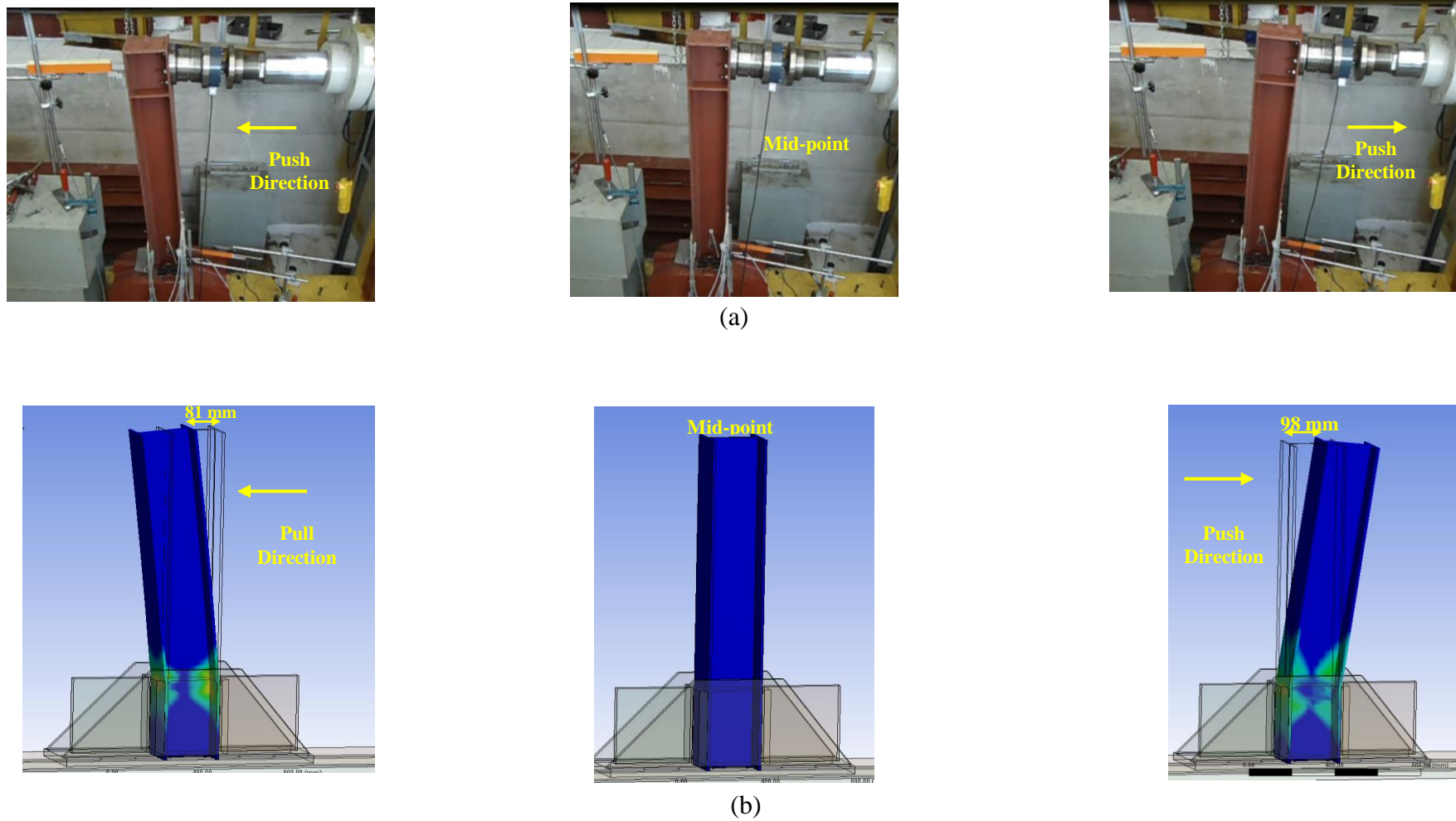

Figure 8.17. Equivalent plastic strain on HP 260x75 steel specimen without axial load in FEM

Figure 8.18. Fatigue life, Shear Stress and Deformation in FEM
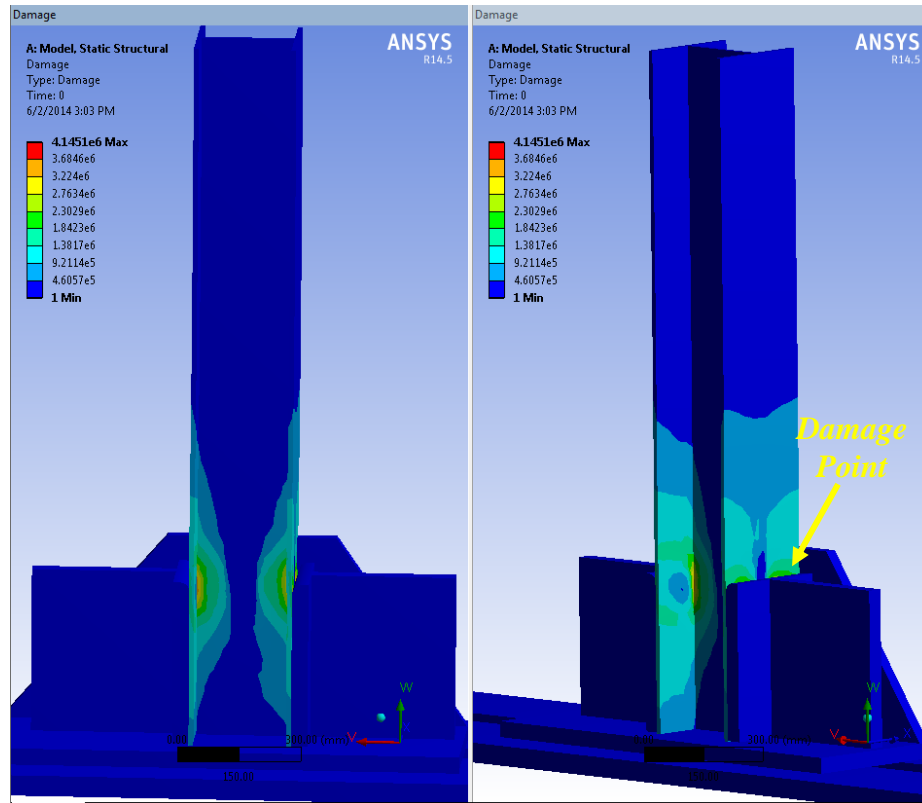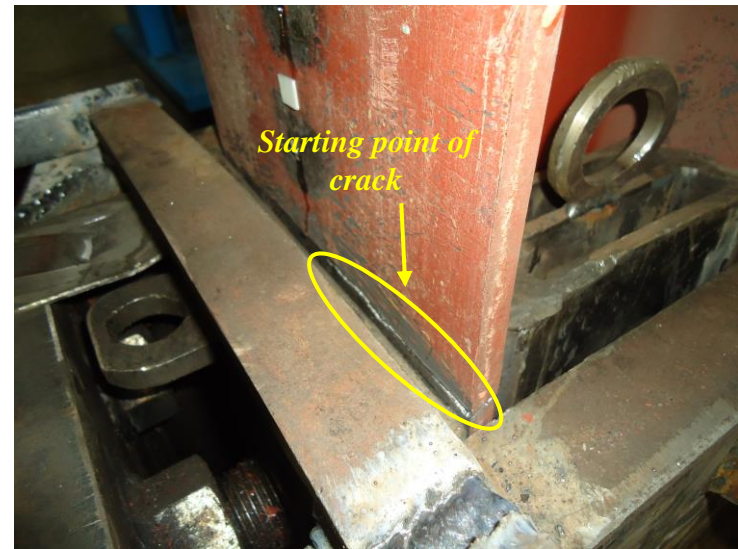
(a)   (b)

Figure 8.19. (a) Damage result in FEM, (b) starting point of crack
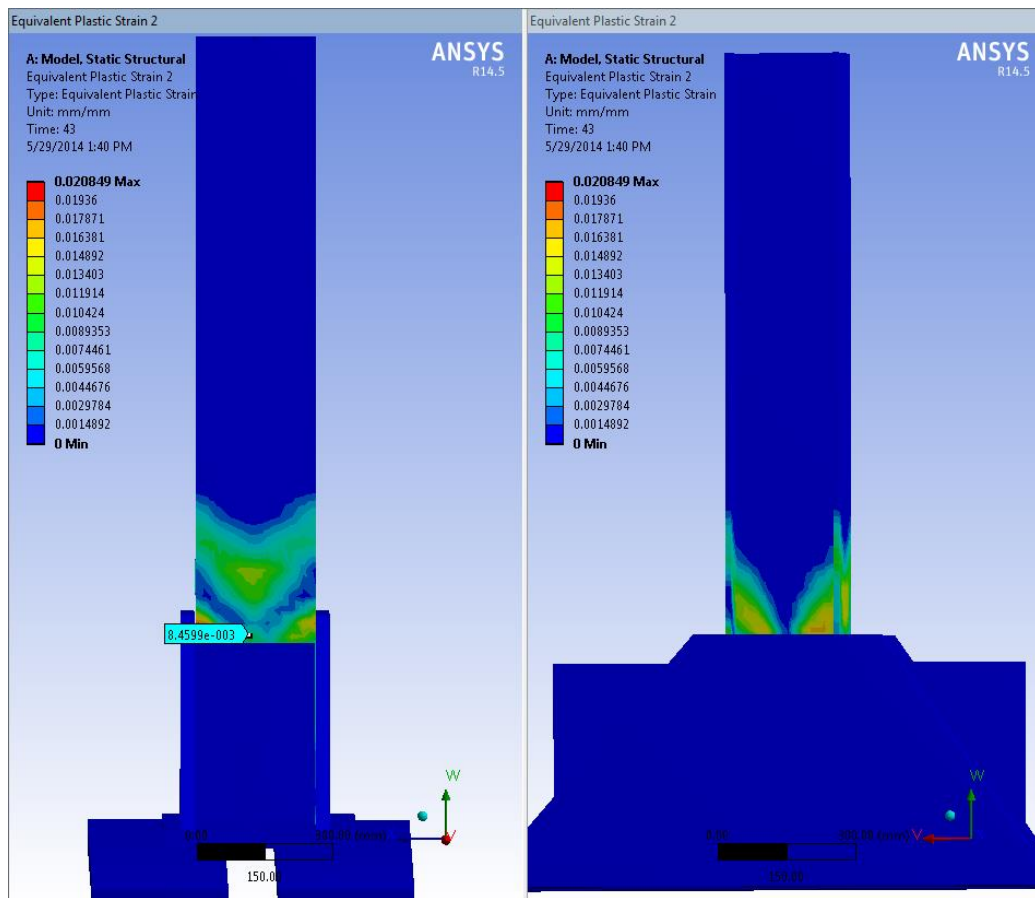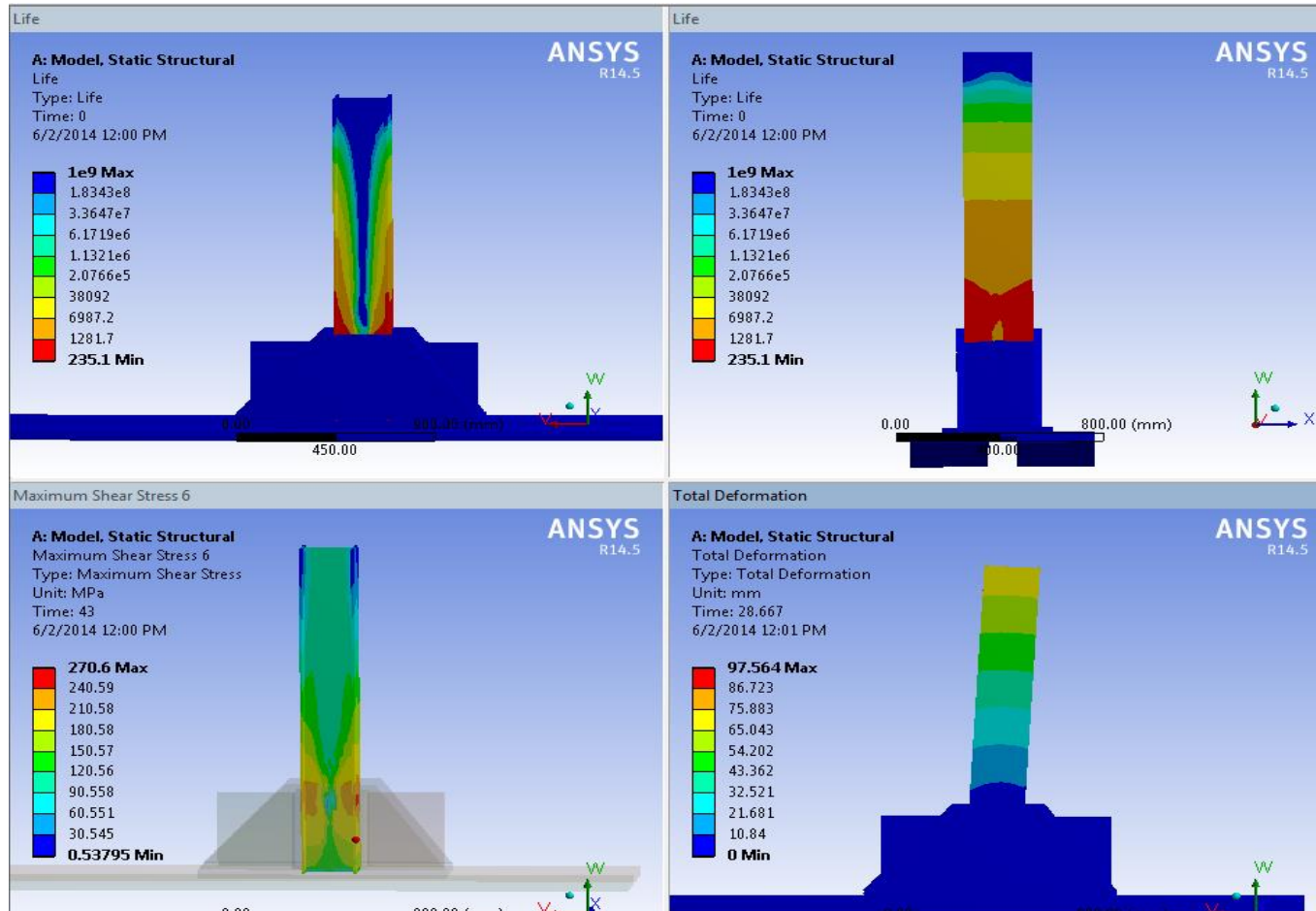
8.2.6. Comparison-6: A Maximum Strain of $\varepsilon_a=\pm5\varepsilon_y$ in Bending about Strong Axis with Axial Load ($P=0.16P_y$)

As mentioned earlier, 80 mm displacements are applied on the push and pull side to obtain ten times yield strain in the experimental test set up. Furthermore, to reach these displacements, maximum compression and tension forces 280 kN, and 310 kN respectively are applied during the push and pull of first cycle. In addition to lateral load, axial loads are also applied as 600 kN, 390 kN and 550 kN during the push, normal and pull direction. Average value of axial load is determined as 530 kN ($P=0.16P_y$). To model the test set up in ANSYS software, same lateral and axial loads are applied on the HP260x75 steel section. At the end of these loads on the push and pull direction, it is seems that same lateral displacements are obtained as shown in Figure 8.20. Furthermore, a maximum strain of 0.0085 which is equal to five times yield strain ($\varepsilon_a=\pm5\varepsilon_y$) with axial load $P=0.16P_y$ is obtained in FEM as obtained in test set up.

As mentioned earlier in the experimental test set up, the results obtained from experimental test on HP260x75 section demonstrate that first fracture begins 178 cycles. After 178 cycles, fracture starts to expand. Finally, low cycle fatigue occurs when steel HP260x75 section is reached to the 215 cycles. As observed from the Figure 8.21, web begins buckling at the high level axial load. A series of photographs illustrates the crack propagation that occurred in the intersect lines of flanges and webs, and then expanded with the following cycles as seen in Figure 8.22.

On the other hand, in the FEM, low cycle fatigue takes place when steel HP260x75 section is reached to the 227 cycles as seen in Figure 8.23. In addition to fatigue life, it is also obtained damage result. Furthermore, it is seems from damage result in Figure 8.23 that starting point of crack takes place accurately occurred in the intersect lines of flanges and webs in FEM as occurs in experimental test set up. In addition to fatigue life, as seen in Figure 8.24, local

buckling occurs in same point accurately above the 500 mm-high steel base fixture on flanges in FEM as occurs in experimental test set up. As a result of this large lateral buckling, distances of flanges expand 5 mm as seen in Figure 8.24.
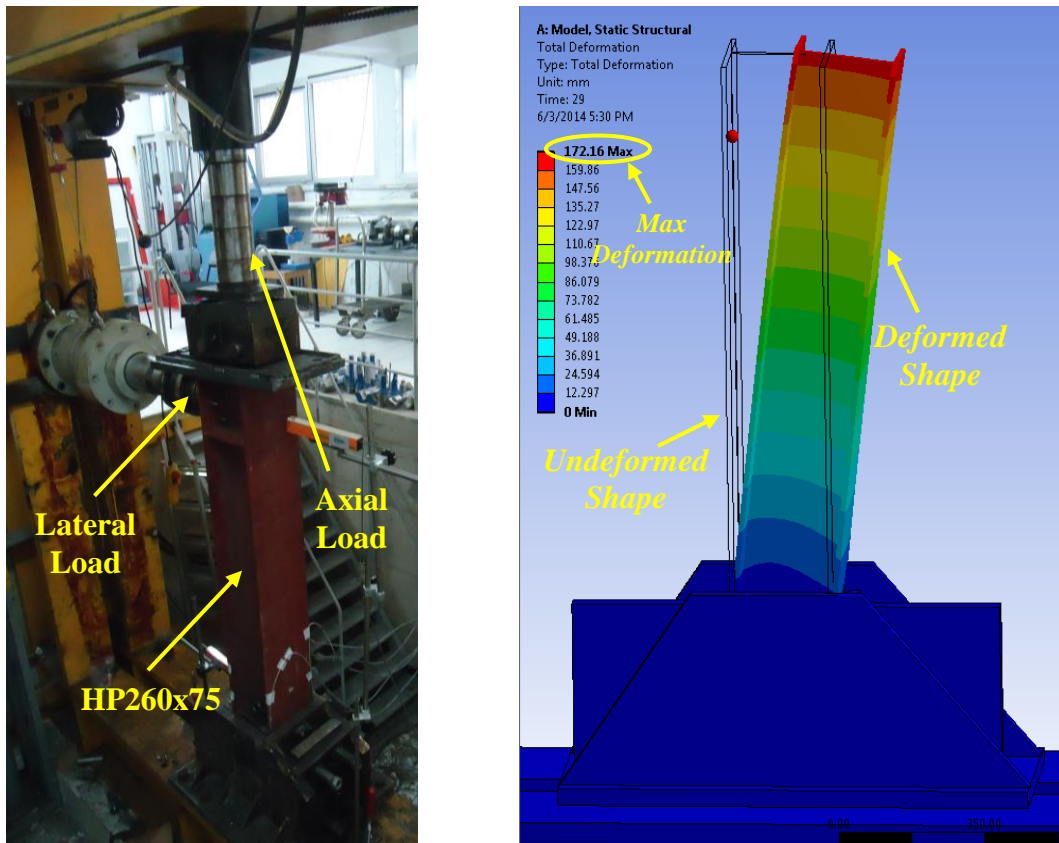
(a) (b)

Figure 8.20. (a) Applied axial and lateral load in FEM, (b) Applied axial and lateral load in test set up
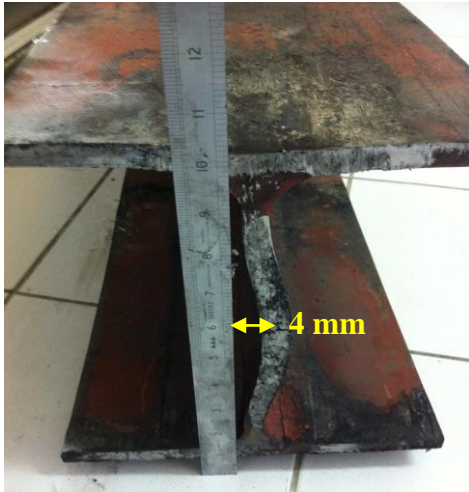
Figure 8.21. **(**a) Web buckling, (b) Crack propagation
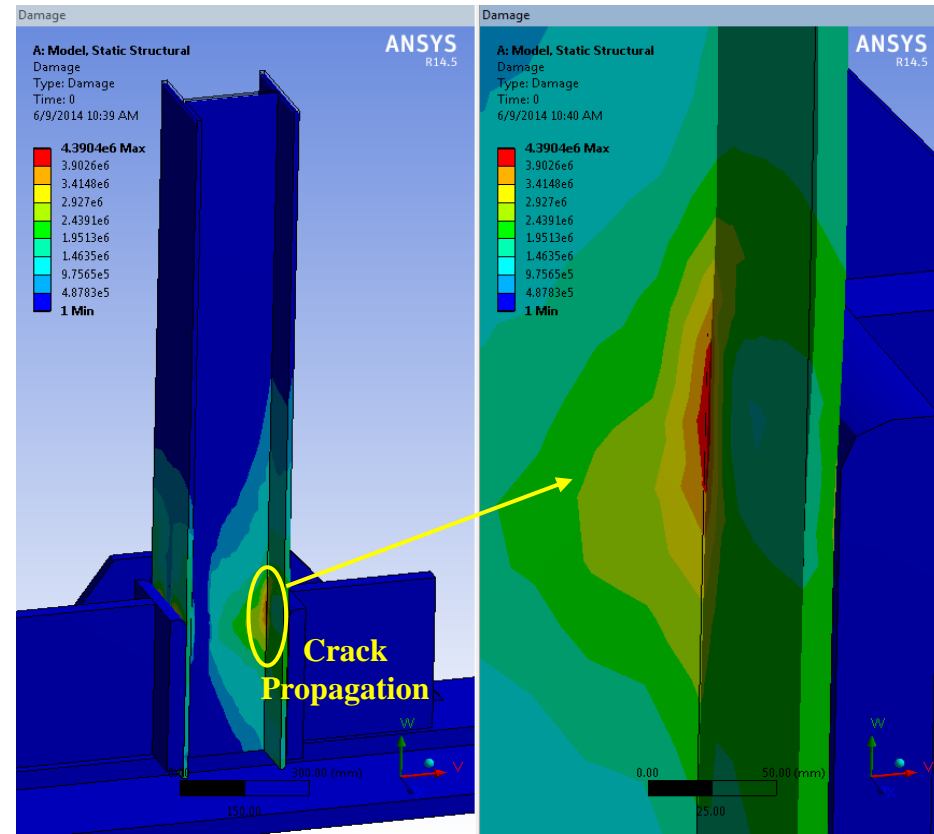
(a)   (b)

Figure 8.22. (a) Crack Propagation that occurred in the intersect lines of flanges and webs in the test set up, (b) Crack Propagation that occurred in the intersect lines of flanges and webs in the FEM
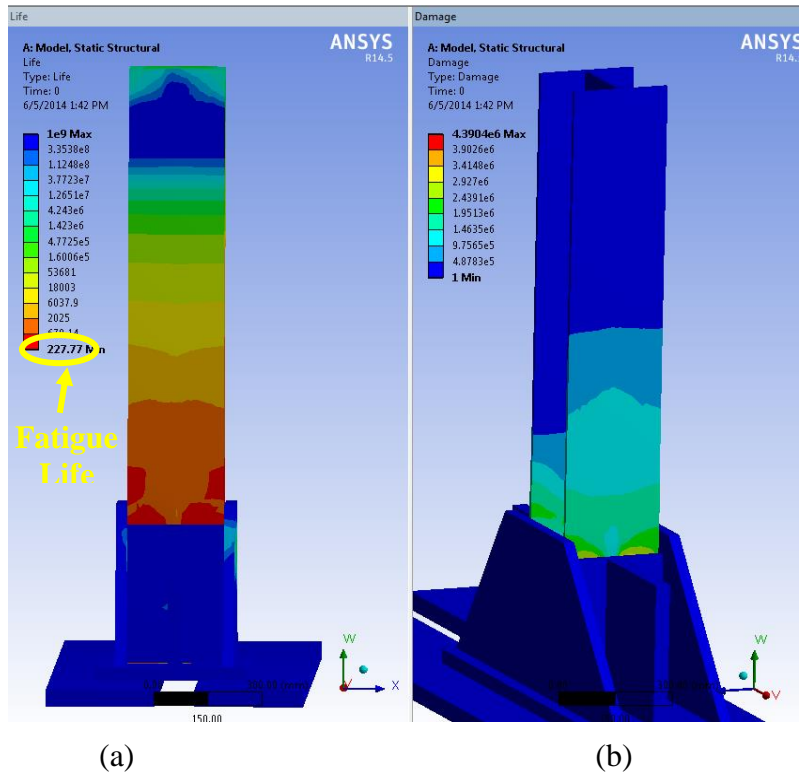
Figure 8.23. (a) Fatigue life in FEM, (b) Damage result in FEM
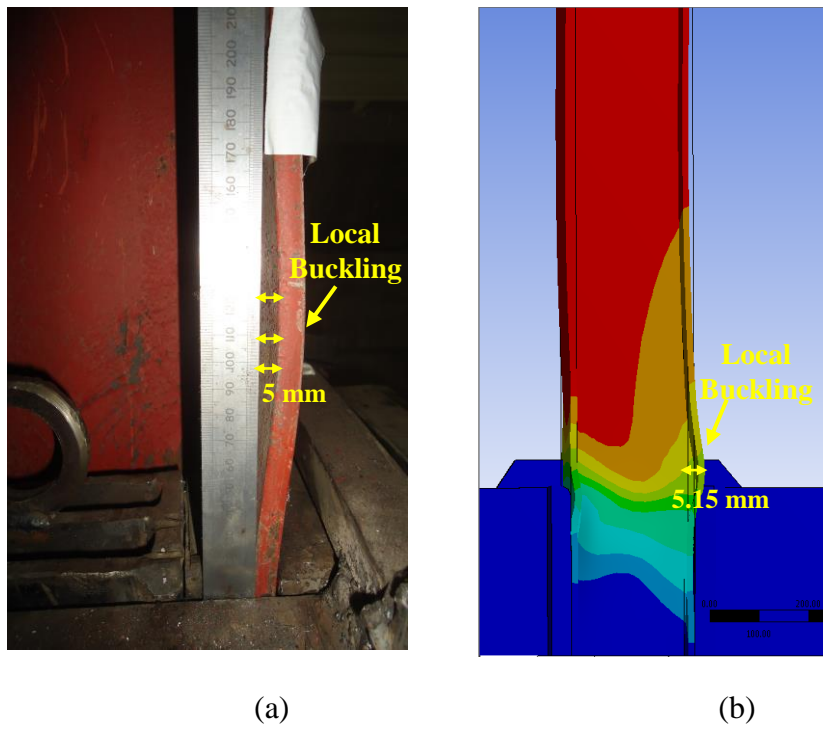
Figure 8.24. (a) Local buckling in test set up, (b) Local buckling in FEM

296

8.2.7. Comparison-7: Effect of Beta (β=0.15) with a Maximum Strain of ε_a=±10ε_y in Bending about Strong Axis with Axial Load (P=0.075P$_y$) for HP220x57 Section

As mentioned earlier, effect of β is investigated for β=0.15 in the experimental test set up and also compared with results of specimen-31 and specimen-2, which have same strain level but different β value. To investigate the effect of β=0.15 with a maximum strain of ε_a=±10ε_y in bending about strong axis with no axial load on HP220x57 section, one dominant cyclic lateral displacement is divided 17 section. Additionally, cyclic lateral displacements (Δ_p) are applied as 13.5 mm on the push and pull direction on HP220x57 section in each small cycle point. At the end of the loading process, about 52 smaller strain cycles per year as qualitatively is provided. On the other hand, same lateral and axial loads are applied on the HP260x75 steel section to model the test set up in ANSYS software. To do so, cyclic lateral displacements as shown in Table 8.1 are applied on the push and pull direction in the each step as seen in Figure 8.25.

Table 8.1. Displacement point of Actuator for large and small cycles

Step Number	Displacement point of Actuator	
	Large cycle	*Small cycle (±13.5 mm)*
1	140	154-126
2	163	177-149
3	186	200-172
4	209	223-195
5	232	246-218
6	209	223-195
7	186	200-172
8	163	177-149
9	140	154-126
10	117	131-103
11	94	108-80
12	71	85-57
13	48	62-34
14	71	85-57
15	94	108-80
16	117	131-103
17	140	154-126

At the end of these loads on the push and pull direction, it is seems that same lateral displacements are obtained in ANSYS software as done in experimental test set up. Furthermore, ten times yield strain ($\varepsilon_a=\pm 10\varepsilon_y$) with axial load $P=0.075P_y$ is obtained in FEM as obtained in test set up.

As mentioned earlier in section 7.20.4, the experimental test set up, the results obtained from experimental test on HP220x57 section demonstrate that first fracture begins 14 cycles. After 14 cycles, fracture starts to expand. Finally, low cycle fatigue occurs when steel HP220x57 section is reached to the 34 cycles. Furthermore, as observed from the Figure 8.26, web begins buckling at the high level axial load. On the other hand, in the FEM, low cycle fatigue takes place when steel HP260x75 section is reached to the 66 cycles as seen in Figure 8.27. In addition to fatigue life, it is also obtained damage result as shown in Figure 8.28. It is seems from damage result that starting point of crack takes place accurately occurred in the intersect lines of flanges and webs in FEM as occurs in experimental test set up. Additionally, as seen in Figure 8.28, settlement takes place in the middle of the web where is in same point accurately above the 500 mm-high steel base fixture in the experiment test set up due to local buckling. This settlement is also seen in FE model, ANSYS as occurs in experimental test set up.

The result of fatigue life distribution on the web of the steel HP220x57 section is shown in Figures 7.20.4. In this figure, x-coordinate gives the calculated points at location of web. It can be seen from Figure 8.29 that the damage initiation becomes earlier in the middle of the web. Thus, fatigue occurs earlier at this point then at the other points of the web, where local failure and progressive rupture may occur under high axial load level on the steel HP220x57 section. As a result of this damage initiation, it leads to the occurrence of steel HP220x57 section failure.
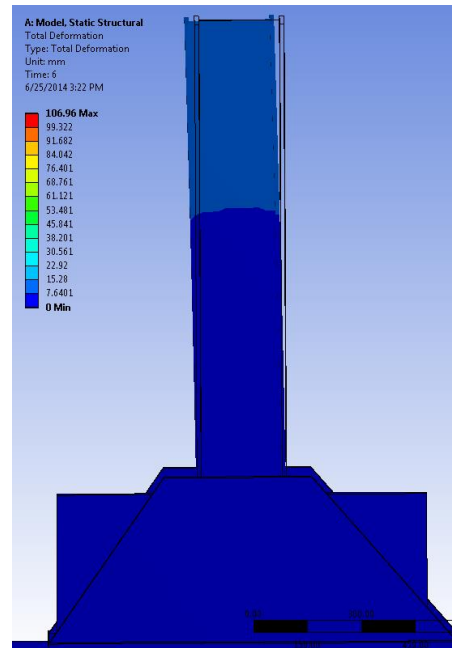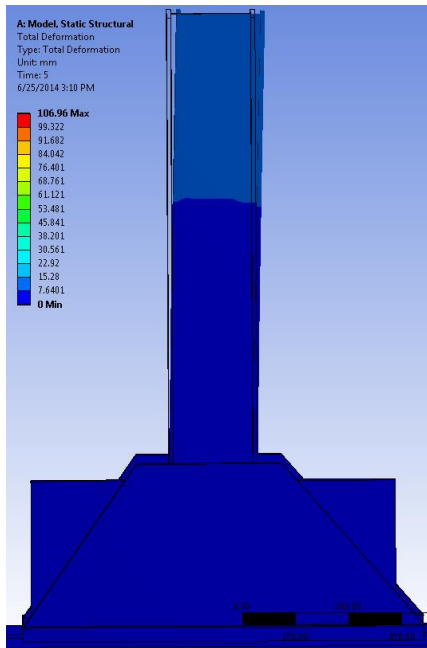
(a) Loading and Unloading 154-126 mm in Step-1 and Step-9
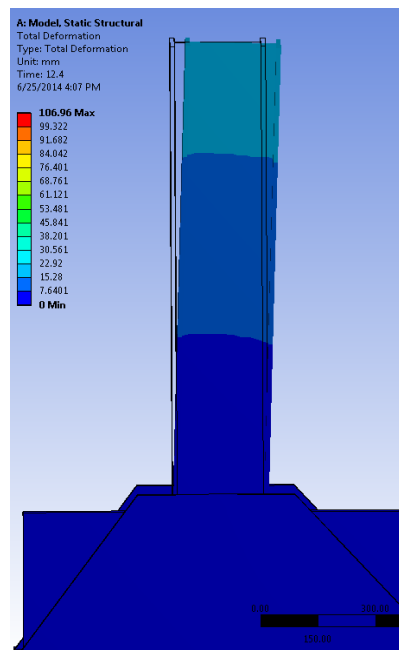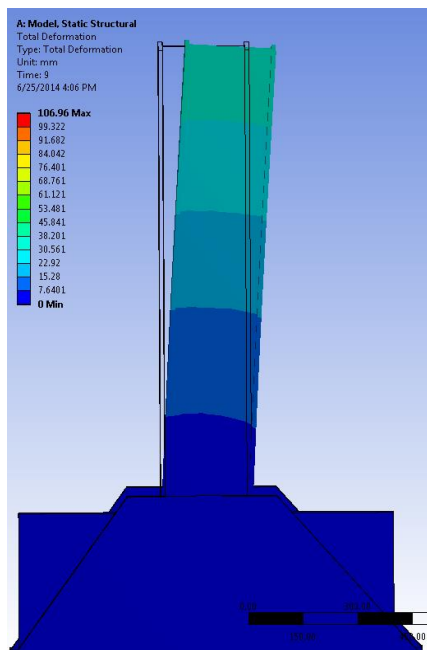
(b) Loading and Unloading 177-149 mm in Step-2 and Step-8

Figure 8.25. Displacement points of Actuator for large and small cycles

299
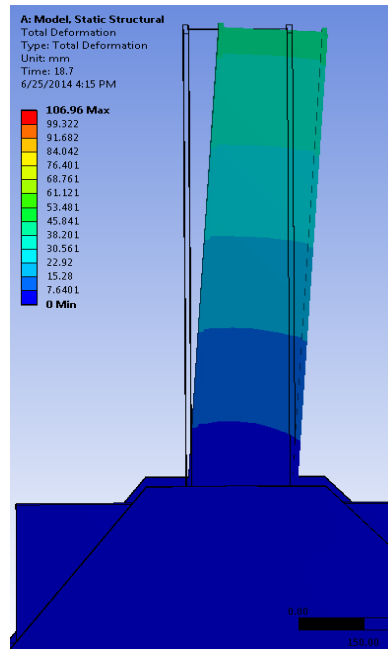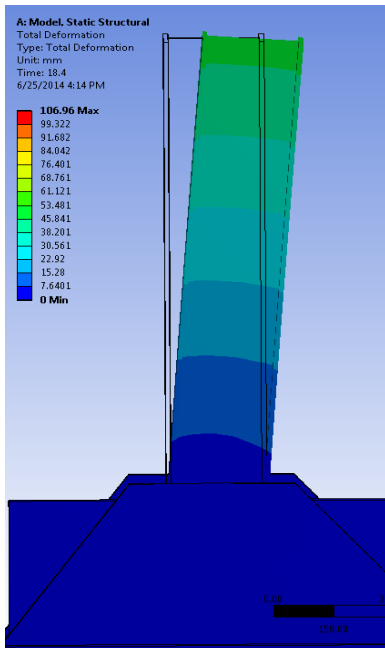
(c) Loading and Unloading 200-172 mm in Step-3 and Step-7
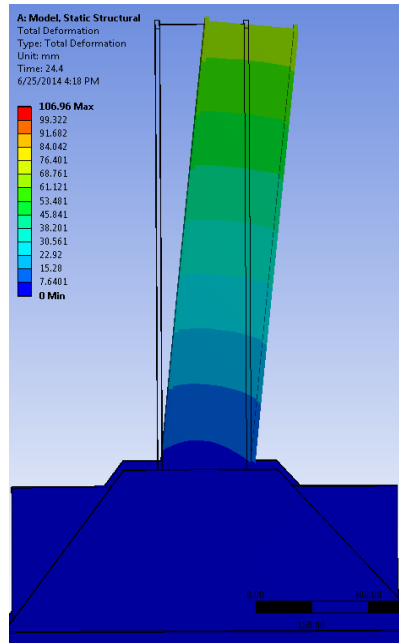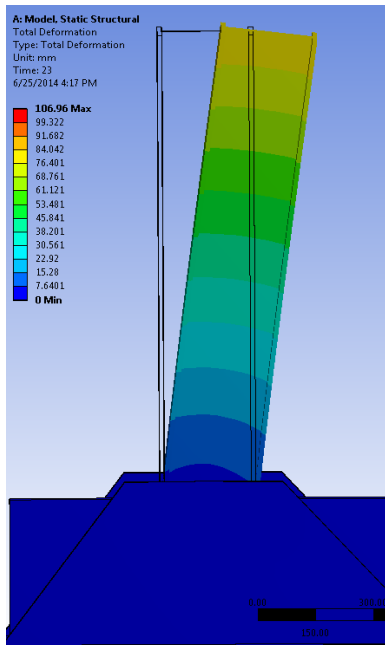
(d) Loading and Unloading 223-195 mm in Step-4 and Step-6

Figure 8.26. (Continued)

300
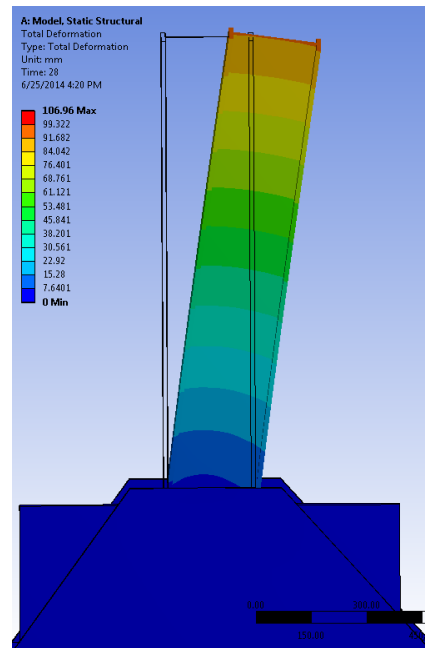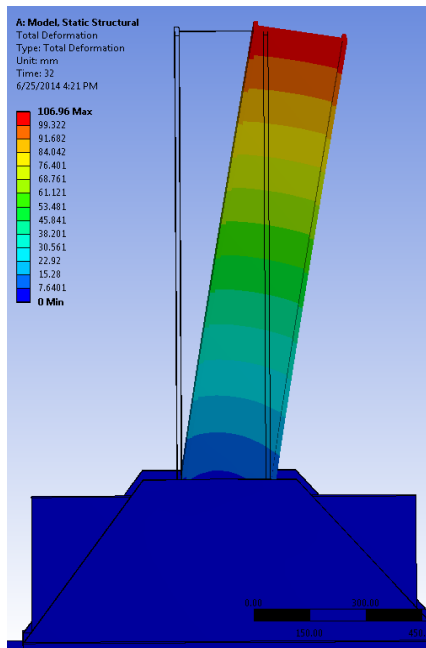
(e) Loading and Unloading 246-218 mm in Step-5
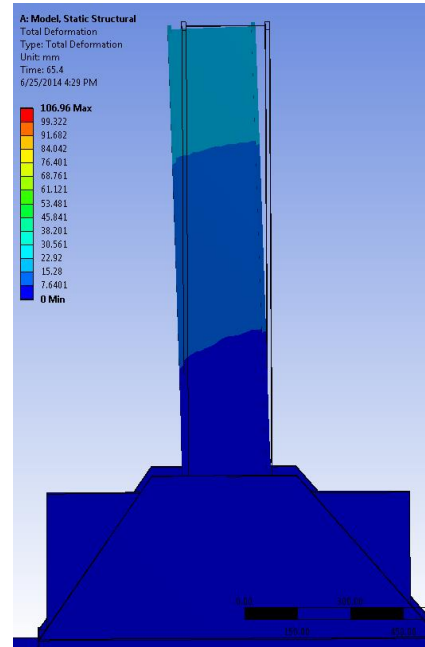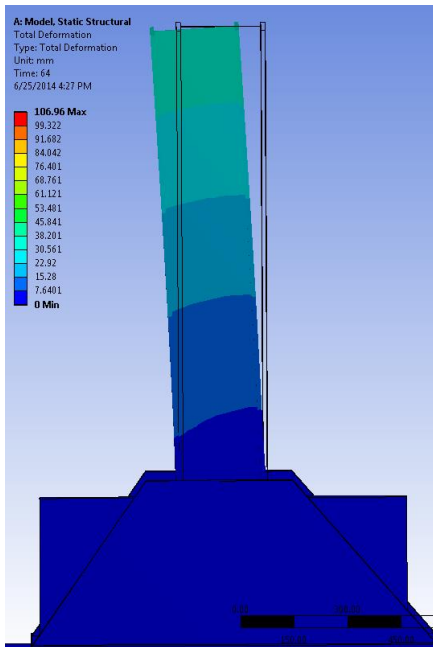
(f) Loading and Unloading 131-103 mm in Step-10 and Step-16

Figure 8.27. (Continued)
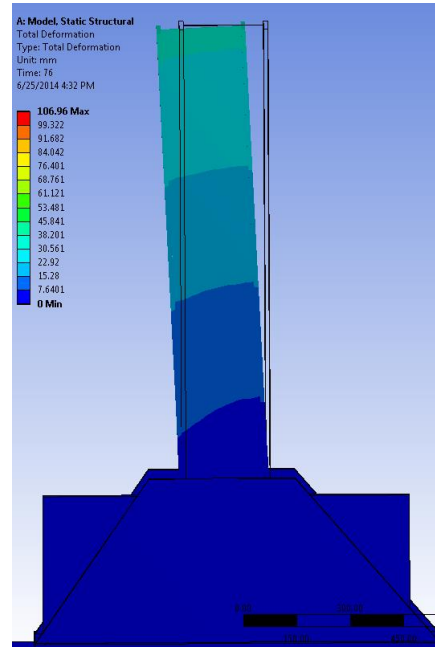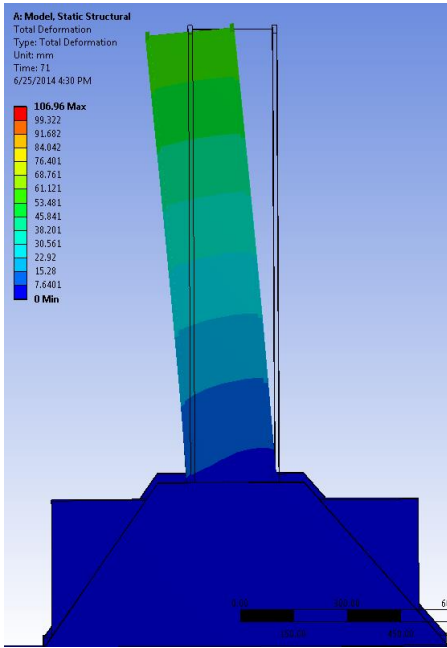
(g)   Loading and Unloading 108-80 mm in Step-11 and Step-15
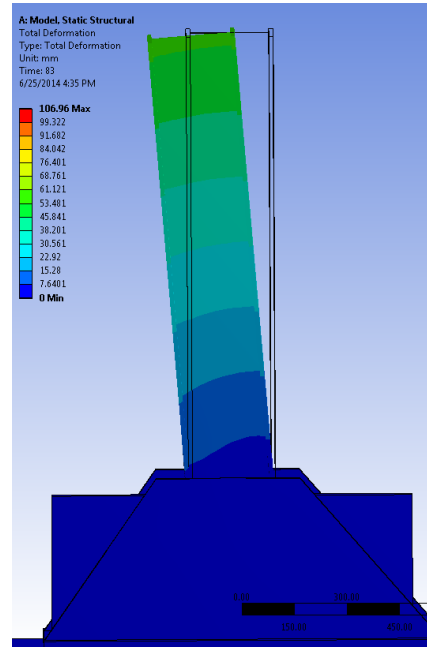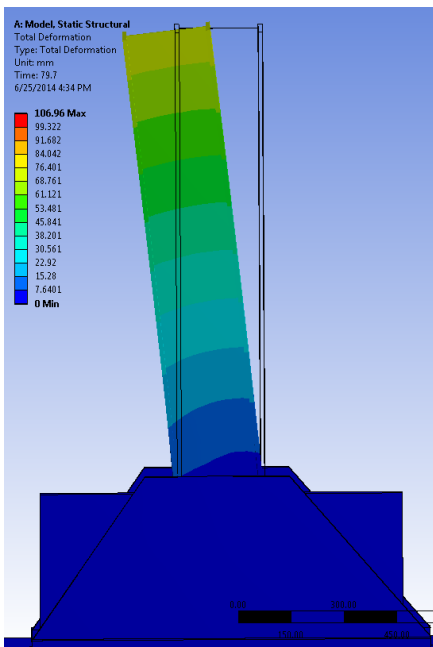
(h) Loading and Unloading 85-57 mm in Step-12 and Step-14

Figure 8.28. (Continued)

302
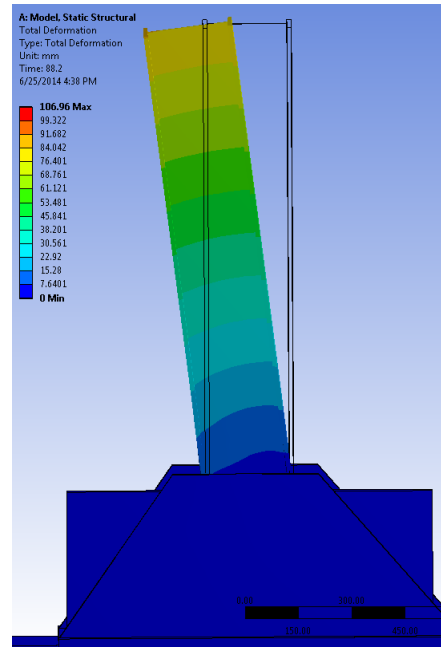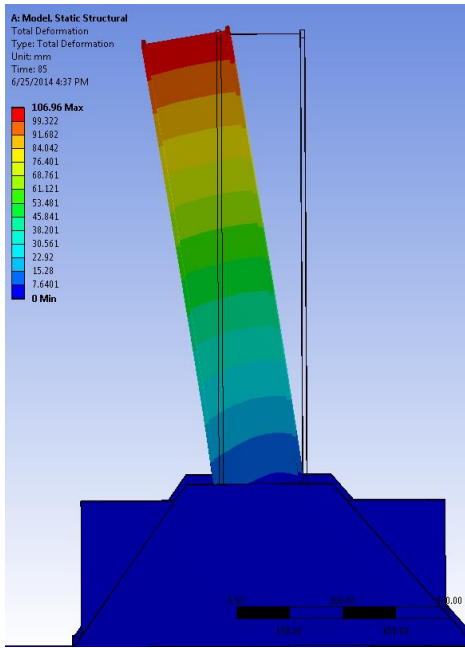
(h) Loading and Unloading 62-34 mm in Step-13

Figure 8.29. (Continued)
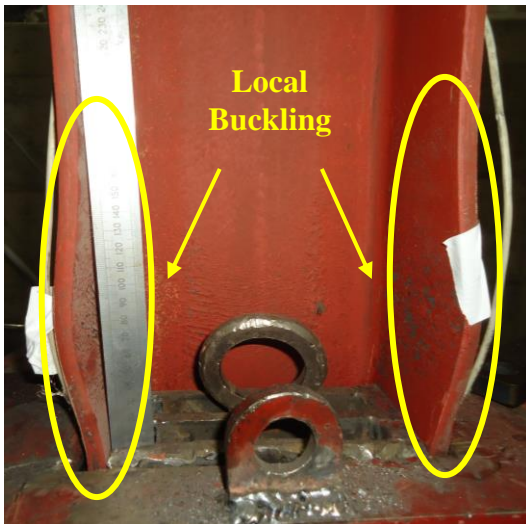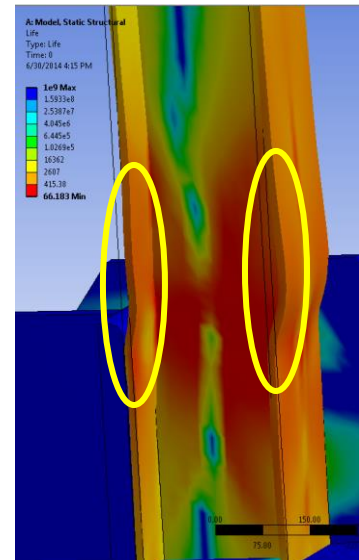
(a)   (b)

Figure 8.30. (a) Local buckling in test set up, (b) Local buckling in FEM
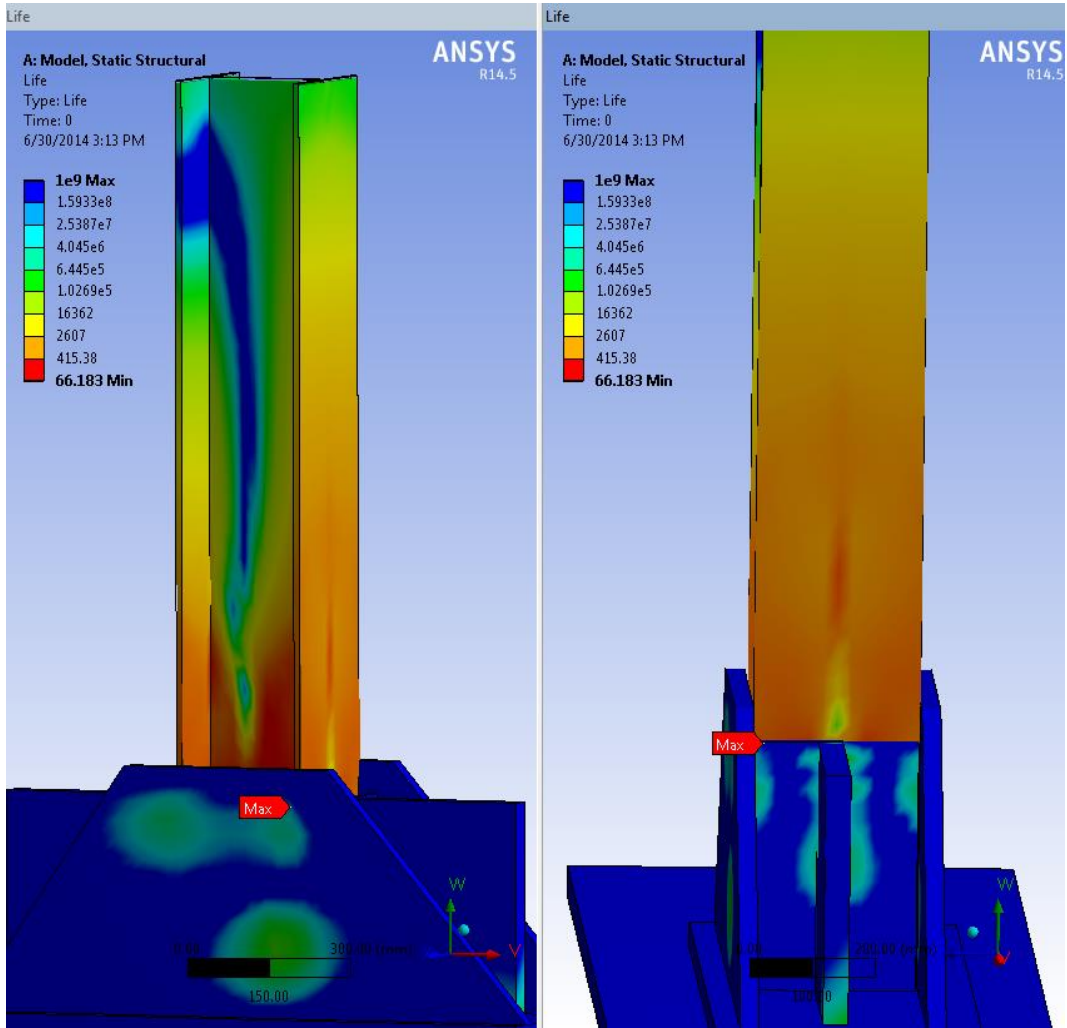
Figure 8.31. Fatigue life in FEM,

304
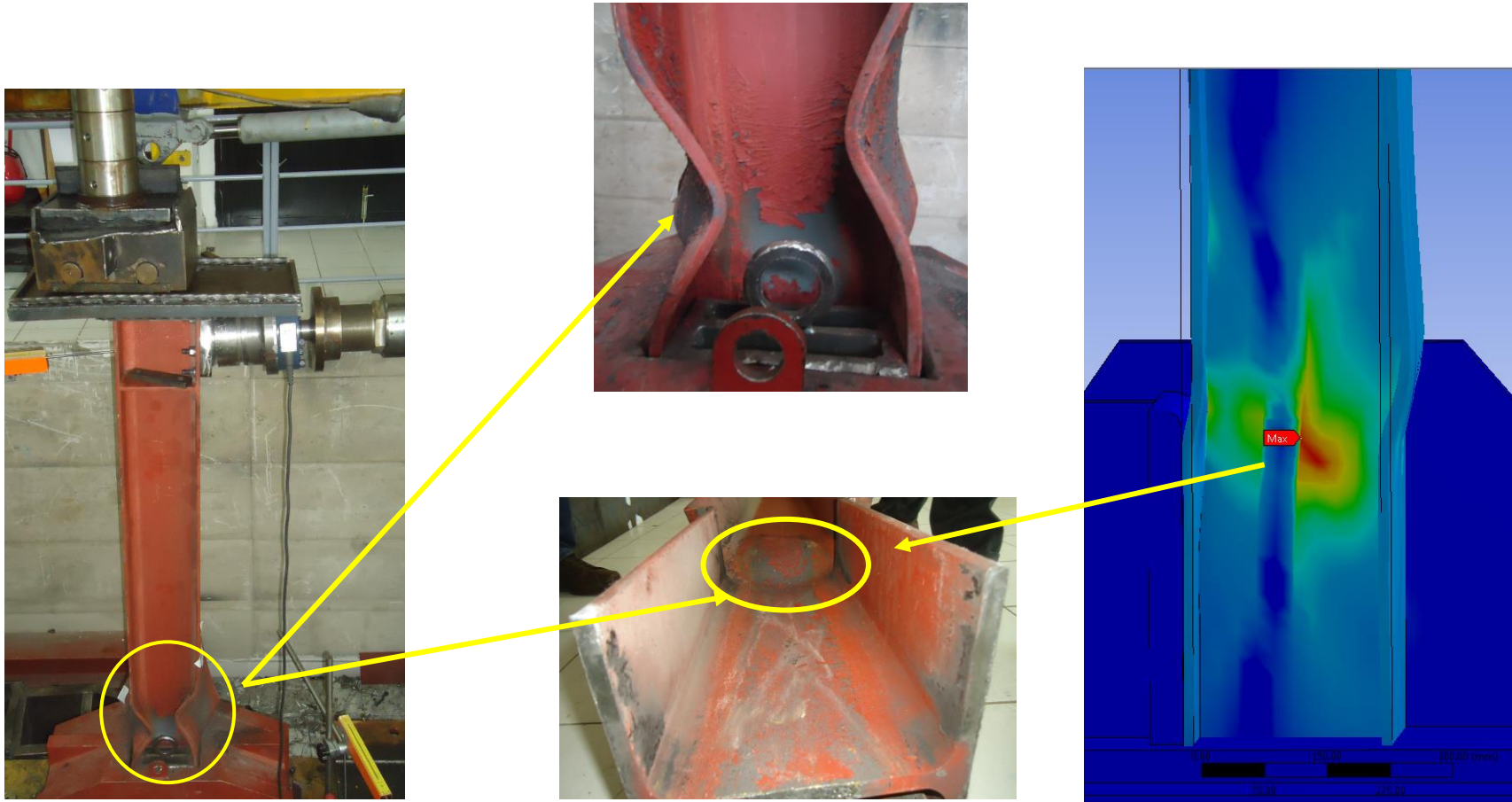
Figure 8.32. Settlement occurs in middle of the web (a) in the experiment test set up, (b) in FEM
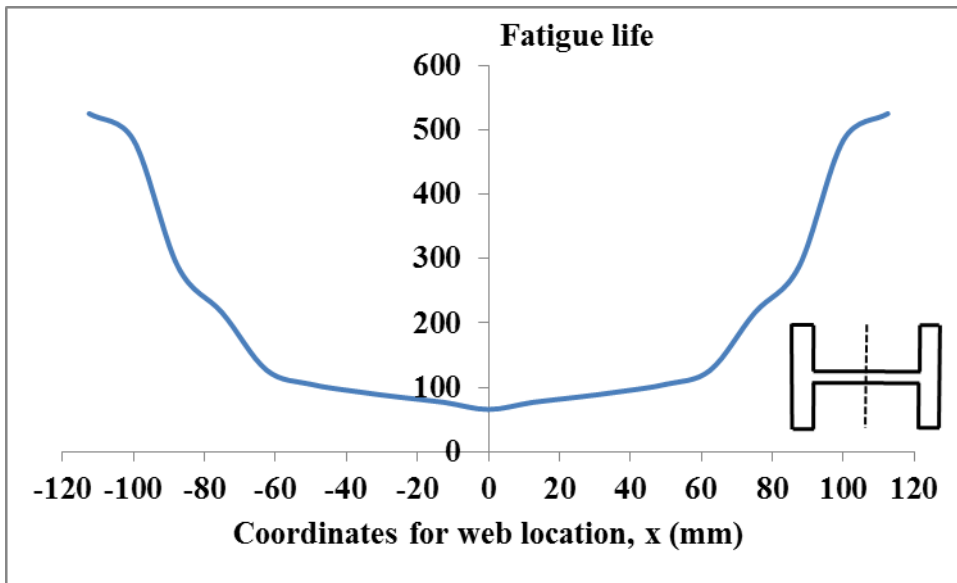
Figure 8.33. Fatigue life distribution on the web of the steel HP220x57 section

CHAPTER 9

SUMMARY AND CONCLUSIONS

In this thesis, a cycle counting technique is developed to accurately predict the cyclic thermal effects on integral bridge piles. Thus, the field measurements obtained for existing integral bridges are used to determine the amplitude and the number of temperature induced cycles on steel H-piles in integral bridges. Using the obtained measurements, the number of large strain cycles per year due to seasonal temperature changes and the number and relative amplitude (relative to the amplitude of large displacement/strain cycles, i.e. β=small strain amplitude / large strain amplitude) of small strain cycles per year due to daily or weekly temperature changes are determined. Additionally, the number of small cycles between the maximum and minimum cycle above and/or under the large strain is counted. Using the available data on the number and amplitude of temperature induced displacement-strain cycles, a new cycle counting method is developed to determine the number and amplitude of large and small displacement/strain cycles.

The calculated number of large and small amplitude cycles and their relative amplitude are employed in a strain versus number-of-cycles-to-failure equation together with Miner's rule to study the low cycle fatigue performance of steel H piles in several existing integral bridges with field test results. It is observed that small amplitude cycles do not have a very significant effect on the low cycle fatigue life of steel H-piles in integral bridges.

As part of the preparation for the experimental test set up, static pushover analyses of two existing symmetrical integral bridges are conducted to calculate the equivalent pile length at the abutments for integral bridges subjected to cyclic

thermal loading. The calculated equivalent pile length is used to determine the length of the pile specimens used in the test. For this purpose, the piles, *HP220X57* and *HP260X75* that are used in the experimental study are separately assumed for each bridge to obtain the equivalent pile length for the experimental test set up. Orientation of the piles for bending about their strong and weak axes is also considered in the analyses. The soil stiffness is anticipated to affect the equivalent pile length. Accordingly, four different soil stiffnesses are included in the analyses. However, the average of the results from all the analyses cases is used to determine the equivalent pile length for the experimental test set up. Based on the pushover analyses results, the average equivalent pile length that is used in the experimental part of this research study is determined as 1.35 m for both HP220x57 and HP260x75.

Additionally, nonlinear finite element models of the steel H-pile used in the experimental part of this research study is developed using the computer program ANSYS to identify potential problems that may be encountered during testing and to improve the test apparatus if necessary. Then, the numerical model of these test specimens is subjected to a loading similar to that is used in the experimental testing and analyzed. As a result of these finite element analyses, it is revealed that high axial stress concentrations occur around the contact surfaces of the HP steel section and the 400 mm-high plate of the steel base fixture. To prevent such high stress concentrations so as to simulate the real boundary conditions as if the pile is embedded in concrete, steel blocks are used between flanges of the HP section within the steel base fixture and the finite element model is modified accordingly. In the case of the modified finite element model, the presence of the steel blocks between the flanges of the HP section within the steel base fixture results in a more even distribution of stresses simulating the real case of pile embedded in concrete abutment.

Further numerical studies are conducted to estimate the displacement of the steel H-pile specimens required to determine the stroke of the actuator for the experimental test setup. For this purpose, first the moment-curvature relationships

(MCR) of the steel HP sections used in the experimental testing are obtained for both strong and weak axis bending under an axial load that ranges between 0 to 60 percent of the axial yield capacity, P_y, of the steel H-pile section The calculated moment-curvature relationships are employed in moment-area method to obtain the inelastic displacement of the steel H-pile specimens as a function of maximum flexural strain. The obtained inelastic displacement versus maximum flexural strain relationships are then used to determine the stroke of the actuator for a predetermined strain level. This allowed us to determine (i) if the stroke capacity of the actuator is adequate for a given strain level, (ii) the level of displacement expected for an assumed strain level while setting up the test at the initial stage.

Subsequently, experimental tests of HP220x57 and HP260x75 H-pile specimens are conducted to investigate the effect of several parameters on the low cycle fatigue life of integral bridge steel H-piles subjected to cyclic thermal strains. For this purpose, thirteen cyclic tests of HP220x57 steel sections subjected to strong and weak axes bending are conducted at various strain amplitudes to investigate the effect of strain amplitude and pile bending orientation on the low cycle fatigue performance. Additional tests are conducted to investigate the effect of axial loads on the low cycle fatigue performance of steel H-piles used in integral bridges. It is observed that, as expected, number of cycles to failure is inversely proportional to the strain amplitude. Furthermore, piles oriented to bend about their weak axes are observed to have a better low cycle fatigue performance. The effect of axial load is observed to have a significant effect on the low cycle fatigue performance of steel H-piles in two ways: (i) when the pile is subjected to moderate strain amplitudes (five times the yield strain), the presence of axial load is observed to enhance the low cycle fatigue life of the pile. This mainly due to the fact that, the presence of axial load decreases the amplitude of the tensile strain that results in cracking of the material (it delays the initiation of the crack), (ii) when the pile is subjected to larger strain amplitudes (10 times the yield strain), the presence of axial load is observed to decrease the low cycle fatigue life of the pile. This is mainly due to local buckling of the flange under the effect of compressive stresses from the axial load and high compressive strains due to the effect of bending.

Local buckling increases the local curvature and strains. This locally accelerates the cracking of the material. Further tests conducted on the larger steel HP260x75 H-pile sections yielded similar behavior. Moreover, it is also observed that the pile size does not affect the low cycle fatigue performance. That is, piles subjected to the same cyclic flexural strain amplitude and identical axial stress level, exhibit similar low cycle fatigue performance.

Additional tests are conducted on piles with stiffeners welded to the flanges to delay local buckling and hence, to improve the low cycle fatigue performance of the piles under axial load and large amplitude strains. It is observed that stiffening the flanges of the H-pile in the region of maximum flexural strain enhanced its low cycle fatigue life more than 20%.

Further tests are conducted to investigate the effect of equivalent pile length or moment gradient on the low cycle fatigue performance of steel H-piles. It is observed that larger moment gradient (or shorter equivalent length of pile) has an adverse effect on the low cycle fatigue performance of steel H-piles.

Tests are also conducted to investigate the effect of small amplitude strain cycles combined with large amplitude strain cycles on the low cycle fatigue performance of the steel H-piles. First, the effect of small amplitude strain cycles (ratio of small to large strain amplitude is taken and 0.15 and 0.30) is investigated using an HP220x57 steel section without the presence of axial load. It is observed that the small amplitude strain cycles do not have a significant effect on the low cycle fatigue performance of the steel H-piles. This confirms the earlier analytical observations.

In the last phase of this study, nonlinear finite element models of the steel H-pile specimens that is used in the experimental part of this research study are developed using the computer program ANSYS to numerically simulate the low cycle fatigue performance of the steel H-piles. For this purpose, first a sensitivity

finite element study is performed to establish a finite element model that best represents the actual behavior of the steel H-pile specimens, as in actual experimental test set up. Comparisons between finite element model predictions and experimental test results are made in terms of low cycle fatigue life in the steel H-pile specimens for various lateral and axial load values. Form the comparison, it is seen that the fatigue life obtained from ANSYS model is in close agreement with the fatigue life obtained from the experiment test set up. This indicates that the actual behavior of HP steel specimen under lateral and axial loading can be accurately predicted by the FEM approach.

RECOMMENDATIONS FOR FUTURE WORK

In this research study, two non-compact HP sections; HP220x57 and HP260x75 are selected for experimental testing. These sections were selected based on their common use as integral bridge piles as well as their availability from the manufacturer. In future studies experimental low cycle fatigue tests may be conducted on compact HP sections. Furthermore, tests on steel H piles embedde3d in representative reinforced concrete abutment section may be conducted to more realistically investigate the damage and fatigue life of steel H-piles due to cyclic loading induced by temperature variations. In addition various structural details of abutment-pile connections may be studied experimentally to enhance the fatigue life of steel H-piles.

REFERENCES

Aref A., Alampalli S., He Y., *Composite Structure*, Performance of a Fiber Reinforced Polymer Web Core Skew Bridge Superstructure Part I: Field Testing and Finite Element Simulations, 2004.

Arsoy S., Experimental and Analytical Investigations of Piles and Abutments of Integral Bridges, 2000

Arsoy S., Duncan J.M., Barker R.M., *Journal of Bridge Engineering, Vol.9, No. 2,*Behavior of a Semiintegral Bridge Abutment under Static and Temperature-Induced Cyclic Loading., 2004.

Arsoy S., Duncan J.M., *Transportation Research Record, n 1849, 03-2633, p 91-97,* Effect of Bridge-Soil Interaction on Behavior of Piles Supporting Integral Bridges*, 2003.*

Ayman A. Shama, John B. Mander, Blaise A. Blabac, Stuart S. Chen., Eartquake Spectra, Volume 18, No. 1, Pages 121-142, Seismic Investigation of Steel Pile Bents:I. Evaluation of Performance, 2002.

Ayman A. Shama, John B. Mander, Blaise A. Blabac, Stuart S. Chen., *Earthquake Spectra, Volume 18, No. 1, Pages 143-16,* Seismic Investigation of Steel Pile Bents II. Retrofit and Vulnerability Analysis, 2002.

Abendroth R.E., Greimann L.F (*1990*)., *Journal of Geotechnical Engineering, Vol. 116, No. 4*, Pile Behavior Established from Model Tests, 1990.

Abendroth R.E., Greimann L.F. *Thesis*, Field Testing of Integral Abutments. Final Report

Arockiasamy M., Butrieng N., Sivakumar M.*, Journal of Bridge Engineering, Vol. 9, No. 5,* State-of-the-Art of Integral Abutment Bridges: Design and Practice, 2004.

Arockiasamy M., Sivakumar M., *Practice Periodical on Structural Design and Construction, Vol. 10, No. 3,* Time-Dependent Behavior of Continuous Composite Integral Abutment Bridges, 2005.

315

Budkowska B.B., Szymczak C. , *Computers and Structures Vol. 52, No. 5, pp. 931-938,* Effect of Varying Length of Pile Undergoing Torsion, 1994.

Dicleli M., *Engineering Structures*; 22 (3):230-45, A Rational Design Approach for Prestressed-Concrete-Girder Integral Bridges, 2000.

Dicleli M, Suhail M. Albhais, Maximum Length of Integral Bridges Supported on Steel H-Piles Driven in Sand. Department of Civil Engineering and Construction, Bradley University, Peoria, IL, 2003.

Dicleli M., Albhaisi S.M., Performance of Abutment-Backfill System under Thermal Variations in Integral Bridges Built on Clay. Department of Civil Engineering and Construction, Bradley University, Peoria, IL, 2004.

Dicleli M, Albhaisi SM., *Journal of Constructional Steel Research*; *60(2):161-182,* Effect of Cyclic Thermal Loading on the Performance of Steel H-Piles in Integral Bridges with Stub-Abutments, 2004.

Dicleli M., *Advanced in Structural Engineering, Vol.7, No.8,* Analytical Prediction of Thermal Displacement Capacity of Integral Bridges Built on Sand,* 2004.

Dicleli M., *Journal of Bridge Engineering, Vol.10, No. 3,* Integral Abutment-Backfill Behavior on Sand Soil-Pushover Analysis Approach, May 2005.

Faraji S., Ting J.M., Crovo D.S.*, Journal of Geotechnical and Geoenvironmental Engineering, Vol. 127, No. 5,* Ernst H. Nonlinear Analysis of Integral Bridges: Finite-Element Model, 2001.

French C., Huang J., Shield C., *Final Report,* Behavior of Concrete Integral Abutment Bridges, 2004.

Greimann L.F., Wolde-Tınsae A.M., Yang P.S., *Transportation Research Record, n 90, p 64-72,* Skewed Bridges with Integral Abutments, 1983.

Greinmann L.F., Yang Pe-Shen, Wolde-Tinsae A.M., *Journal of Structural Engineering, Vol. 112, No. 10,* Nonlinear Analysis of Integral Abutment Bridges, 1986.

Girton D.D., Hawkinson T.R., Greinmann L.F., *Journal of Structural Engineering, v117, n 7, Jul, p 2117-2134,* Validation of Design Recommendations for Integral-Abutment Piles, 1991.

Greinmann L.F.,Yang Pe-Shen, Wolde-Tinsae A.M., *Journal of Structural Engineering, Vol. 114, No. 8,* End-Bearing Piles in Jointless Bridges, 1998.

Jorsenson, James L., *Transportation Research Record, n 903, p 72-79,* Behavior of Abutment Piles in an Integral Abutment in Response to Bridge Movements, 1983.

Khodair Y.A., Hassiotis S.*, Computers and Geotechnics 32 201-209,* Analysis of Soil-Pile Interaction in Integral Abutment, 2005.

Kunin J., Alampalli S., *Journal of Performance of Constructed Facilities, Vol. 14, No. 3,* Integral Abutment Bridges: Current Practice in United States and Canada, 2000.

Mander J.B., Panthaki F.D., Kasalanati A., Steel. *Journal of Materials in Civil Engineering, Vol. 6, No. 4,* Low-Cycle Fatigue Behavior of Reinforcing, 1994.

Steinberg E., Sargand S.M., Bettinger C., *Journal of Bridge Engineering, Vol. 9, No.6,* Forces in Wingwalls of Skewed Semi-Integral Bridges., 2004.

Sandford, Thomas C., Elgaaly M., *Transportation Research Record, n 1415, p 1-11,* Skew Effects on Backfill Pressures at Frame Bridge Abutments, 1993.

Tlustochowicz G., Thesis, Optimized Design of Integral Abutments for Three Span Composite Bridge, 2005.

Yoshida H. and Maegawa K., *Journal of Structural Mechanics, 6(1), 1-27*, Local and Member Buckling of H-Columns, 1978.

Wasserman, E.P., *Seismic Bridge Workshop*, Integral Abutment Design,1st US-Italy, 2007.

CURRICULUM VITAE

PERSONAL INFORMATION

Surname, Name   : Karalar, Memduh
Nationality   : Turkish (T.C.)
Date of Birth and Place : 18.10.1980, Adana
Marital Status   : Bekar
e-mail   : memduh@metu.edu.tr

EDUCATION

Degree	Institution	Year of Graduation
PhD.	METU, Engineering Sciences Dept.	2014
BSc.	Çukurova University, Civil Engineering Dept.	2002
High School	Adana Erkek High School, Adana	1997

WORK EXPERIENCE

Year	Enrollment	Place
1. 2005-2014,	Research Assistant,	Department of Engineering Sciences, Middle East Technical University (METU), Ankara, Turkey
2. 2012,	Visitor Graduated Researcher,	Civil and Environmental Engineering, University of Nevada, Reno (UNR), Reno, Nevada, USA

FOREIGN LANGUAGES

1. Advanced English.

PUBLICATIONS

1. Dicleli, M. and **Karalar, M**., "Optimum Characteristic Properties of Isolators with Bilinear Force-Displacement Hysteresis for Seismic Protection of Bridges", Soil Dynamics and Earthquake Engineering, Elsevier Science, Vol. 31, No. 7, pp. 982-995, 2011.

2. **Karalar, M.,** Padgett, J.E., Dicleli M., "Parametric Analysis of Optimum Isolator Properties for Bridges Susceptible to Near-Fault Ground Motions", Engineering Structures, Elsevier Science, Vol. 40 (2012) pp. 276–287.

3. Pekcan, G., Itani, A., **Karalar, M**. Seismic Code Requirements for the Design of Nonstructural Components, Earthquake Spectra, In press

2. Proceedings in Symposiums, Conferences, and Congresses

2.1. International Proceedings

1. Dicleli, M. and **Karalar, M**., "Low Cycle Fatigue Performance Of Integral Bridge Steel H-Piles Subjected To Earthquakes", 9th International Conference on Short and Medium Span Bridges, Hyatt Regency Calgary, Alberta, Canada, July 15 - 18, 2014.

2. **Karalar M**. and Dicleli M, "Analytical and Experimental Research on Low Cycle Fatigue Performance of Integral Bridge Steel H-Piles under Seismic Displacement Reversals", The Seventh National Seismic Conference on Bridges & Highways, Oakland, California, USA, MAY 20-22, 2013.

3. **Karalar, M**., Padgett, J.E., Dicleli M., "Selection of Seismic Isolation Properties for Bridges in Near Fault Regions", 9th International Congress on Advances in Civil Engineering, Karadeniz Technical University, Trabzon, Turkey, 27-30 September 2010.

4. **Karalar M**. and Dicleli M, "Development of a New Cycle Counting Method for Cyclic Thermal Strains in Integral Bridge Piles", 9th International Congress on Advances in Civil Engineering, Karadeniz Technical University, Trabzon, Turkey, 27-30 September 2010.

5. **Karalar M.** and Dicleli M, "Improved Effective Damping Equation for Equıvalent Linear Analysis of Seismic-Isolated Bridges", 9th US National and 10th Canadian Conference on Earthquake Engineering: Reaching Beyonda Borders, Toronto, Canada, Jully 25-29, 2010.

6. **Karalar M**. and Dicleli M, "Optimum Selection of Isolator Proporties for Effective Mitigation of Seismic Risk for Bridges", 9th US National and 10th Canadian Conference on Earthquake Engineering: Reaching Beyonda Borders, Toronto, Canada, Jully 25-29, 2010.

7. **Karalar M**. and Dicleli M, "Development of a New Cycle Counting Method for Cyclic Thermal Strains in Integral Bridge Piles", The Fifth International Conference on Bridge Maintenance, Safety and Management, Philadelphia,PA, USA, Jully 11-15, 2010.

8. **Karalar M**. and Dicleli M, "Estimation of Optimum Isolator Parameters for Effective Mitigation of Seismic Risk for Bridges", The Fifth International Conference on Bridge Maintenance, Safety and Management, Philadelphia,PA, USA, Jully 11-15, 2010.

9. **Karalar M**. and Dicleli M, "Effect of Near-Field Ground Motion and Isolator Proporties on the Performance of Seismic-Isolated Bridges", TC4 Satellite Conference of Earthquake Geotechnical Engineering, Alexandria,Egypt, 2-3 October,2009.

10. **Karalar M.** and Dicleli M, "Effect of Soil-Structure Interaction on the Seismic Response of Bridges with Isolation Bearings", TC4 Satellite Conference of Earthquake Geotechnical Engineering, Alexandria,Egypt, 2-3 October,2009.

11. Dicleli M and **Karalar M.**, "Optimal Isolator Parameters for Economical Mitigation of Seismic Risk for Highway Bridges", Proceedings of the Seventh US Conference and Workshop on Lifeline Earthquake Engineering, ASCE Technical Council on Life Line Earthquake Engineering Monograph, Long Beach, California, USA, June 28-July 1, 2009

12. **Karalar M**. and Dicleli M, "Performance Based Design of Seismic Isolated Bridges in Near-Fault Zones Using Elastic-Gap Devices", Proceedings of the Seventh US Conference and Workshop on Lifeline Earthquake Engineering, ASCE Technical Council on Life Line Earthquake Engineering Monograph, Long Beach, California, USA, June 28-July 1, 2009.

13. **Karalar M**. and Dicleli M, "Economical Seismic Retrofitting of Chevron Braced Steel Frames Based on Averting Brace Buckling ", WCCE-ECCE-TCCE Joint Conference on Earthquake & Tsunami, Istanbul - Turkey, 22 - 24 June 2009.

14. Dicleli M, Calik, E.E. and **Karalar M**., "Analytical Simulation of Cyclic Behavior of Steel Braces under Seismic Loads", WCCE-ECCE-TCCE Joint Conference on Earthquake & Tsunami, Istanbul - Turkey, 22 - 24 June 2009.

15. Dicleli M and **Karalar M**., "Optimization of Isolation Bearing Parameters for Effective Mitigation of Seismic Risk for Bridges", 26th Annual International Bridge Conference, Pittsburg, Pennsylvania, USA, June 14 - 17, 2009.

TEACHING EXPERIENCES

2005-2013

Course/Teaching Assistant

Department of Engineering Sciences,

Middle East Technical University (METU),

Ankara, Turkey

· ES202 Mathematics for Engineers

· ES223 Statics and Strength of Materials

· ES224 Strength of Materials

· ES225 Engineering Mechanics

· ES361 Computing Methods in Engineering

SCHOLARSHIPS, AWARDS and HONOURS

1. International Scientific Fellowship Program, Scientific Fellowship and Grant Programs (BIDEB), The Scientific and Technological Research Council of Turkey (TUBITAK), Turkey.

Place; San Francisco,USA

Date (Duration); May 21-25, 2013 (1 week)

2. International Scientific Publication Awards, Development Foundation, Middle East Technical University (METU), Turkey.

in 2011, 2012

3. International Scientific Publication Awards, The Scientific and Technological Research Council of Turkey (TUBITAK), Turkey.

in 2011, 2012

Computer Skills

- ✓ SolidWorks
- ✓ SAP 2000
- ✓ ANSYS Workbench
- ✓ Nonlin
- ✓ Microsoft

Professional Experience

University of Nevada, Reno as a visitor researcher (8 months)

Site Engineer Assistant, June 2000 - Sept. 2000, ALARKO Co., Adana, Turkey.

Site Engineer Assistant, June 2001 - Sept. 2001, ALARKO Co., Adana, Turkey.

Site Engineer Assistant, 2002 - 2003, LİMAK Co., Kahramanmaraş, Turkey.